



HAL
open science

Metal-seeded lithium niobate nanoparticles as hybrid nanozymes for mimicking bioactivity

Ana Maria Pablo Sainz Ezquerro

► **To cite this version:**

Ana Maria Pablo Sainz Ezquerro. Metal-seeded lithium niobate nanoparticles as hybrid nanozymes for mimicking bioactivity. Other. Ecole Centrale de Lyon; RMIT University (Melbourne), 2023. English. NNT : 2023ECDL0014 . tel-04125607

HAL Id: tel-04125607

<https://theses.hal.science/tel-04125607v1>

Submitted on 12 Jun 2023

HAL is a multi-disciplinary open access archive for the deposit and dissemination of scientific research documents, whether they are published or not. The documents may come from teaching and research institutions in France or abroad, or from public or private research centers.

L'archive ouverte pluridisciplinaire **HAL**, est destinée au dépôt et à la diffusion de documents scientifiques de niveau recherche, publiés ou non, émanant des établissements d'enseignement et de recherche français ou étrangers, des laboratoires publics ou privés.



N° d'ordre NNT : 2023ECDL0014

**THESE de DOCTORAT DE L'ÉCOLE CENTRALE DE LYON membre de
l'Université de Lyon**

**En cotutelle internationale avec Royal Melbourne
Institute of Technology (RMIT)**

Ecole Doctorale N° 160
Electronique, Electrotechnique et Automatique

Spécialité de doctorat : Ingénierie pour le vivant

Soutenue publiquement le 30/03/2023, par :

Ana María Pablo Sainz-Ezquerria

Metal-Seeded Lithium Niobate Nanoparticles as Hybrid Nanozymes for Mimicking Bioactivity

Devant le jury composé de :

| | | | | |
|-----------------------|------------|-------------------------------|--|---------------------|
| Pr. AMIENS | Catherine | Professeure des Universités | Université de Toulouse III | Rapporteure |
| Pr. MILLOT | Nadine | Professeure des Universités | Université de Bourgogne | Rapporteure |
| Dr. COMESAÑA HERMO | Miguel | Chargé de Recherches | CNRS-Université Paris Cité | Examineur |
| Dr. GEANTET | Christophe | Directeur de recherche | CNRS-Université de Lyon | Président du jury |
| Dr. MONNIER | Virginie | Maîtresse de conférences, HDR | École Centrale de Lyon | Directrice de thèse |
| Pr. BANSAL | Vipul | Professeur | Royal Melbourne Institute of Technology | Directeur de thèse |
| Dr. CHEVOLOT | Yann | Directeur de recherches | École Centrale de Lyon | Invité |
| Dr. RAMANATHAN | Rajesh | Professeur associé | Royal Melbourne Institute of Technology | Invité |

Table of contents

| | |
|---|----------|
| Table of contents..... | III |
| List of Figures..... | IX |
| List of Tables..... | XVII |
| Glossary..... | XIX |
| Acknowledgments..... | XXIII |
| General introduction..... | 1 |
| Chapter 1: State of the art..... | 5 |
| 1.1 . Artificial enzymes: Nanozymes..... | 6 |
| 1.1.1 . Concept of Nanozyme..... | 6 |
| 1.1.2 . Enzyme mechanism and kinetics applied to Nanozymes..... | 8 |
| 1.1.2.1 . Enzyme activities in Nanozymes: oxidoreductases..... | 8 |
| 1.1.2.2 . Kinetics and catalytic mechanism of Nanozymes..... | 11 |
| 1.1.2.3 . Specificity for the catalytic mechanism of Nanozymes..... | 13 |
| 1.1.3 . Noble metal nanoparticles as Nanozymes..... | 13 |
| 1.1.3.1 . Size..... | 14 |
| 1.1.3.2 . Composition and crystallinity..... | 15 |
| 1.1.3.3 . pH and temperature..... | 15 |
| 1.1.3.4 . Presence of other chemical species..... | 16 |
| 1.1.3.5 . Surface coating..... | 16 |
| 1.1.3.6 . Light..... | 17 |
| 1.1.3.7 . Combination of materials..... | 18 |
| 1.1.4 . Metal nanoparticles on metal oxides as Nanozymes..... | 18 |
| 1.1.4.1 . Classic metal/metal oxide catalysts mechanisms..... | 19 |
| 1.1.4.2 . The metal-semiconductor (metal oxide) junction in catalysis..... | 19 |
| 1.1.4.3 . Hybrid Nanoparticles: Effect of Metal/Metal Oxide Junctions in Classic Redox Catalysis..... | 21 |

| | |
|--|-----------|
| 1.1.4.4 . Hybrid nanoparticles: Metal/Metal-Oxide Junctions Effect on Photocatalysis | 22 |
| 1.1.4.5 . Synergetic effect in Metal/Metal Oxide hybrid nanoparticles for enhanced Nanozyme activity | 24 |
| 1.1.4.6 . Peroxidase and Oxidase Hybrid Nanozymes..... | 24 |
| 1.1.4.7 . Catalase Hybrid Nanozymes..... | 25 |
| 1.1.4.8 . Superoxide Dismutase Hybrid Nanozymes | 27 |
| 1.1.4.9 . Hybrid Nanozymes light interaction..... | 27 |
| 1.1.5 . Synthesis and characterization methods of Metal/Metal Oxide Nanozymes..... | 28 |
| 1.1.6 . LiNbO ₃ /Metal hybrid NPs as Nanozymes | 34 |
| 1.1.6.1 . LiNbO ₃ properties and synthesis | 35 |
| 1.1.6.2 . Metal Seeds Synthesis | 37 |
| 1.2 . Metal Nanozyme ROS activity | 39 |
| 1.2.1 . ROS boosted production for oxidant therapeutics | 41 |
| 1.2.1.1 . Antimicrobial activity | 42 |
| 1.2.1.2 . Tumour-cell therapy..... | 43 |
| 1.2.2 ROS scavenging for antioxidant therapeutics..... | 45 |
| 1.2.2.1 . Internal agent protection | 45 |
| 1.2.2.2 . External agent protection | 46 |
| 1.3 . Objectives | 46 |
| Chapter 2: Characterization techniques..... | 49 |
| 2.1 . Transmission electron microscopy (TEM) | 50 |
| 2.2 . Dynamic Light Scattering (DLS)..... | 53 |
| 2.3 . Laser Doppler Velocimetry and Electrophoresis..... | 54 |
| 2.4 . Inductively coupled plasma atomic emission spectroscopy (ICP-AES)..... | 56 |
| 2.5 . UV-Vis spectrophotometry | 57 |
| 2.5.1 . Light matter-interactions..... | 57 |
| 2.5.2 . UV-Visible spectrophotometric techniques used in this work | 59 |

| | |
|--|-----------|
| 2.5.3 . UV-Vis instruments used in this work..... | 61 |
| 2.5.3.1 . UV-Vis absorption spectroscopy: nanoparticles surface plasmon resonance | 62 |
| 2.5.3.2 . UV-Vis well plate reader: study of nanoparticles catalytic activity, singlet oxygen production and bacterial growth..... | 62 |
| 2.5.3.3 . UV-Vis absorbance spectroscopy: optical band gap determination | 63 |
| 2.6 . X-ray and Ultraviolet photoelectron spectroscopy (XPS/UPS)..... | 64 |
| 2.7 . Fluorescence spectroscopy..... | 65 |
| 2.8 . Conclusion | 67 |
| Chapter 3: Synthesis and Characterization of Hybrid Nanozymes..... | 69 |
| 3.1 . Materials and methods | 69 |
| 3.1.1 . Chemicals..... | 69 |
| 3.1.2 . Synthesis of LiNbO ₃ nanoparticles (LN NPs) | 70 |
| 3.1.3 . Polymer Adsorption onto LN NPs..... | 70 |
| 3.1.4 . Synthesis of LN Coated with Noble Metal Seeds..... | 71 |
| 3.1.5 . Synthesis of TiO ₂ NPs Coated with Noble Metal Seeds..... | 72 |
| 3.1.6 . Structural Characterization of NPs | 73 |
| 3.2 . Results and Discussion | 73 |
| 3.2.1 . Characterization of the starting building blocks of LN/Au and LN/Pt hybrid NPs (LN NPs, LN@BPEI, AuSeeds, PtSeeds) | 73 |
| 3.2.2 . Characterization of LN/Au and LN/Pt Hybrid Nanoparticles | 76 |
| 3.2.3 . Attempt to produce LN/Ag hybrid NPs..... | 79 |
| 3.2.4 . Reproducibility and ageing | 81 |
| 3.2.5 . TiO ₂ /metal Hybrid Nanoparticles | 82 |
| 3.3 . Conclusion | 84 |
| Chapter 4: Nanozyme activity of LN/Au and LN/Pt hybrid nanoparticles as peroxidase mimics. Optimization and elucidation of their catalytic mechanism..... | 85 |
| 4.1 . Materials and Methods for Peroxidase Mimics Characterization..... | 86 |
| 4.1.1 . Chemicals..... | 86 |

| | |
|---|------------|
| 4.1.2 . Peroxidase-Mimics of LN/Au and LN/Pt Optimization and Characterization..... | 86 |
| 4.1.3 . Mechanism elucidation | 87 |
| 4.1.3.1 . Optical Band Gap..... | 87 |
| 4.1.3.2 . ROS characterization | 88 |
| 4.2 . Optimization of the peroxidase mimics of LN/Au NPs and LN/Pt NPs..... | 88 |
| 4.2.1 . LN/Au and LN/Pt Peroxidase-Mimics Optimization. | 89 |
| 4.2.2 . Synergetic effect of AuSeeds and PtSeeds on the surface of LN. | 98 |
| 4.2.3 . Ageing and reproducibility across batches | 99 |
| 4.2.4 . TiO ₂ /Au and TiO ₂ /Pt hybrid NPs as peroxidase-mimics..... | 100 |
| 4.3 . Calculation of the enzymatic kinetic parameters | 101 |
| 4.4 . Mechanistic elucidation | 106 |
| 4.4.1 . Synergetic effect in the band structure..... | 106 |
| 4.4.2 . Metal Seeds and BPEI effect | 114 |
| 4.4.3 . ROS characterization | 117 |
| 4.5 . Conclusion | 122 |
| Chapter 5: Nanozyme ROS production/ scavenging and their interaction with bacteria | 123 |
| 5.1 . Materials and Methods for Bacterial culture and ROS characterization | 124 |
| 5.1.1 . Chemicals..... | 124 |
| 5.1.2 . Microbial Culture of <i>E. coli</i> . and Nanozymes under Oxidative Stress..... | 124 |
| 5.2 . <i>E. coli</i> growth interaction with Nanozymes and nanoparticles..... | 126 |
| 5.3 . <i>E. coli</i> growth interaction with Nanozymes and H ₂ O ₂ | 128 |
| 5.3.1 . <i>E. coli</i> growth response to increasing concentration of H ₂ O ₂ | 128 |
| 5.3.2 . <i>E. coli</i> growth response to H ₂ O ₂ and Nanoparticles | 129 |
| 5.3.3 . <i>E. coli</i> growth response to H ₂ O ₂ and Nanozyme | 131 |
| 5.4 . <i>E. coli</i> interaction with Nanozymes and UV | 134 |
| 5.4.1 . Optimization of the UV exposure time..... | 135 |

| | |
|---|------------|
| 5.4.2 . <i>E. coli</i> growth interaction with Nanoparticles and UV light | 136 |
| 5.4.3 . <i>E. coli</i> growth interaction with Nanozymes and UV light..... | 138 |
| 5.5 . <i>E. coli</i> interaction with Nanozymes, UV light and H ₂ O ₂ | 142 |
| 5.5.1 . <i>E. coli</i> growth interaction with Nanoparticles, H ₂ O ₂ and UV light..... | 142 |
| 5.5.2 . <i>E. coli</i> growth response to H ₂ O ₂ and UV with Nanozymes..... | 144 |
| 5.6 . Effect of oxidative-stress treatments as a function of material..... | 146 |
| 5.7 . Conclusion | 150 |
| Conclusion and prospects..... | 151 |
| Bibliography | 157 |
| Appendix..... | 179 |
| Batch-to-batch synthesis reproducibility | 179 |
| TiO ₂ NPs characterization..... | 180 |
| TiO ₂ /Au synthesis for different volume ratios..... | 180 |
| Calculation of metal seeds in one LN NP | 181 |
| Number of surface metal atoms calculation..... | 181 |
| Indirect band gaps | 182 |
| XPS/UPS characterization of TiO ₂ , and TiO ₂ /Au..... | 183 |
| Résumé de la thèse en français | 187 |

List of Figures

| | |
|---|----|
| Figure 1.1. Timeline of Nanozyme development. Extracted from Wu <i>et al.</i> [30]. | 8 |
| Figure 1.2. Michaelis-Menten graph. Velocity of a reaction catalysed by an enzyme as a function of substrate concentration. Extracted from Nelson <i>et al.</i> [35]. | 12 |
| Figure 1.3. Different ways for modifying metal Nanozyme's enzymatic activity. | 14 |
| Figure 1.4. LSPR effect for spherical metal nanoparticles. | 17 |
| Figure 1.5 Energy level diagram of a metal-semiconductor junction at different stages of contact: not in contact, in contact and at equilibrium in Schottky junction (left) and Ohmic contact (right). Φ_m , metal work function; ϕ_s , semiconductor work function; χ_s , the electron affinity of the semiconductor; E_{vac} , vacuum energy; E_c minimum energy of the semiconductor conduction band; E_v , maximum energy of the semiconductor valence band; $E_{F,m}$, Fermi level of the metal and $E_{F,s}$, Fermi level of the semiconductor; ϕ_{SB} , Schottky barrier; V_{BB} , valence band bending. Extracted from Zhang and Yates [97]. | 20 |
| Figure 1.6. (A) Electron-hole recombination processes in semiconductor particles upon light excitation. Extracted from Zhang and Yates [97]. (B) Schematic diagram of metal deposition induced charge separation due to the creation of a Schottky barrier between metal and semiconductor. (C) Schematic diagram of plasmon-induced charge separation on the semiconductor-metal junction under light excitation and the possible redox reactions accompanying it. B and C are extracted from Jing <i>et al.</i> [121]. | 23 |
| Figure 1.7. Peroxidase and oxidase hybrid Nanozyme ROS-mediated mechanism. | 25 |
| Figure 1.8. Catalase mimics energy diagrams of each reaction step in A) Pd Nanosheets and B) Pd@TiO ₂ . Extracted from Chongchong Wang <i>et al.</i> [134]. | 26 |
| Figure 1.9. Scheme of the structures of the different hybrids containing metal oxide (grey) and noble metal (red). From left to right, (A) Dumbbell-like, (B) Janus nanoparticles, (C) Core-Shell, and (D) Seed Decoration. It has to be pointed out that the Janus nanoparticle is just a representation of a two-sided hybrid nanoparticle, but the structures for this are endless. | 28 |
| Figure 1.10. Dumbbell-like hybrid nanoparticles synthesis route. Adapted from Yu <i>et al.</i> [113]. | 29 |
| Figure 1.11. Scheme of different approaches for synthesising seed-decorated hybrid nanoparticles. | 31 |
| Figure 1.12. Second harmonic generation in non-linear LN NPs. | 36 |
| Figure 1.13. Mechanism of particle nucleation and growth in wet-chemical methods according to LaMer's model. Extracted from Khan <i>et al.</i> [197]. | 38 |
| Figure 1.14. Nanozyme mediated ROS reactions examples: production and scavenging. | 39 |
| Figure 1.15. Mechanism for Au/g-C ₃ N ₄ NPs for antibacterial activity under (A) light and (B) dark conditions. Extracted from Hongda Zhang <i>et al.</i> [207]. | 42 |
| Figure 1.16. Ag/CeO ₂ SOD-mimics Nanozyme with antibacterial properties. Extracted from Li <i>et al.</i> [137]. | 43 |
| Figure 1.17 Oxidoreductase activities of Nanozymes against cancer cells. S represents a substrate, and P is the oxidized product. CAT is catalase activity, SOD is superoxide dismutase, GSH is glutathione, GPx is glucose peroxidase, POD is peroxidase, OXD is oxidase and SDT is sonodynamic therapy. Extracted from Li <i>et al.</i> [228]. | 44 |
| Figure 2.1. TEM coupled to EDS operating display. | 51 |
| Figure 2.2. EDS principle. | 52 |

| | |
|--|----|
| Figure 2.3. Electrical double layer around a negatively-charged particle, surrounded by positively-charged species in the Stern layer and the diffusion layer. Extracted from Tengku Mohd <i>et al.</i> [235]. | 55 |
| Figure 2.4. ICP-AES scheme. Extracted from Cherevko and Mayrhofer [236]. | 56 |
| Figure 2.5. Interaction of light with (A) metal nanoparticle, (B) molecule, (C) semiconductor and (D) bacteria. | 57 |
| Figure 2.6. Electronic transitions in semiconductors. (A) Direct band gap transition. (B) Indirect band gap transition. | 58 |
| Figure 2.7. (A) Tauc's plot for the direct band gap energy calculation. The linear part extrapolated to the x-axis intersection provides a value of a direct band gap of 3.41 eV. Extracted from Yogamoorthy <i>et al.</i> [245]. (B) Tauc plot for the indirect band gap energy calculation. The linear part extrapolated to the x-axis intersection provides a value of indirect band gap of 3.05 eV. Extracted from Maheu <i>et al.</i> [246]. | 61 |
| Figure 2.8. UPS and XPS spectra diagram. Extracted from Roland [251]. | 64 |
| Figure 2.9. Fluorescent electronic transitions scheme. | 66 |
| Figure 3.1. Scheme of the layer-by-layer synthesis method for LN/Au and LN/Pt hybrid NPs. | 69 |
| Figure 3.2. TEM image and TEM diameter lognormal distribution of (A, A1) LN NPs, (B, B1) LN@BPEI, (C, C1) AuSeeds and (D, D1) PtSeeds. | 74 |
| Figure 3.3. UV-Vis absorption spectra of AuSeeds (black) and PtSeeds (red). | 75 |
| Figure 3.4. TEM images and corresponding diameter of noble metal seeds deposited onto LN fitted to a lognormal distribution for LN/Au (A-A1, B-B1, C-C1) and LN/Pt (D-D1, E-E1) NPs. LN/Au NPs and LN/Pt NPs were prepared with the following metal seeds to LN ratios: 30 for LN/Au1 (A, A1), 100 for LN/Au2 (B, B1), 200 for LN/Au3 (C, C1), 10 for LN/Pt1 (D, D1) and 60 for LN/Pt2 (E, E1). | 76 |
| Figure 3.5. (A) STEM image of LN/Au3 with corresponding EDS chemical maps of (A1) Au, (A2) Nb and (A3) Au and Nb merged on the same image. (B) STEM image of LN/Pt2 with corresponding EDS chemical maps of (B1) Pt, (B2) Nb and (B3) Pt and Nb merged on the same image. | 78 |
| Figure 3.6. HRTEM image and facets characterization of metal seeds: (A) AuSeeds on LN/Au3 and (B) PtSeeds on LN/Pt2. In both cases, LN-bound Au and Pt have an expected well-defined face centred cubic (fcc) structure. | 79 |
| Figure 3.7. TEM images of AgSeeds (A), log normal fitted diameter distribution of AgSeeds (B), LN/Ag1 hybrid nanoparticles (C) and LN/Ag2 hybrid nanoparticles (D). | 79 |
| Figure 3.8. (A) TEM images of AuSeeds aged for more than one year. (B and C) TEM images of two independent batches of LN/Au3 and (D) LN/Au3 aged for more than one year. (E) TEM images of PtSeeds aged for more than one year. (F and G) TEM images of two independent batches of LN/Pt2 and (H) LN/Pt2 aged for more than one year. | 82 |
| Figure 3.9. (A) TiO ₂ /Au Nanoparticles TEM image. (B) TiO ₂ /Pt Nanoparticles TEM image. | 83 |
| Figure 4.1. (A) Time-dependent kinetics of the LN/Au Nanozyme mediated oxidation of TMB. TMB + LN/Au allowed to test the oxidase activity, TMB + H ₂ O ₂ and LN/Au were negative controls, (B) measurement of the absorbance maximum at an incubation time of 38 min for LN/Au peroxidase reaction using different substrates (ABTS, OPD and TMB). All the experiments were carried out at 37 °C and pH 4 (acetate buffer). | 89 |
| Figure 4.2. Catalase mimics of Au-based Nanozymes after 38 minutes. Control experiment, H ₂ O ₂ +Buffer (A). AuSeeds catalase mimics, H ₂ O ₂ +AuSeeds+Buffer; [Au] = 27 μM (B). LN/Au catalase mimics, H ₂ O ₂ +LN/Au; [Au] = 27 μM; [LiNbO ₃] = 182 μM (C). For all the samples, the measurements were performed in the presence of H ₂ O ₂ (29.7 mM) at pH 4 (acetate buffer) and 37°C. All the concentrations are in the reaction well. | 90 |

- Figure 4.3.** The absorbance spectrum after the completion of TMB oxidation shows peaks at 450 nm and 650 nm due to the formation of yellow and blue products, respectively. The schematic of the TMB oxidation reaction is also provided. 91
- Figure 4.4.** Normalized absorbance at 450 nm and 650 nm at 37 °C and pH 4 (acetate buffer) for the completed reaction with TMB, the absorbance corresponds to the maximum reached after 38 minutes of reaction time. 91
- Figure 4.5.** Measurement of the absorbance maximum (reaction time 38 min) for LN/Au peroxidase reaction using TMB substrate, (A) at pH 4 as a function of temperature, (B) at 37°C as a function of pH. (B, insert) The colour difference between the reaction at pH 2 and pH 4..... 92
- Figure 4.6.** Optimization of the quantity of LN/Au Nanozyme. (A) Peroxidase activity kinetics at different concentrations of Nanozymes (concentrations are given in number of NPs/mL) and (B) plot of the absorbance at 650 nm of oxidized TMB as a function of NPs concentration after 7 min of reaction. All reactions were carried out at $[H_2O_2] = 29.7$ mM, $[TMB] = 167$ μ M, 37 °C and pH 4 (acetate buffer). 93
- Figure 4.7.** (A) Normalized absorbance at 650 nm after 5 min of reaction for two different concentrations of Pt in LN/Pt. (B) Time-dependent kinetics of the LN/Pt Nanozyme mediated oxidation of TMB under different conditions. TMB + LN/Pt allowed to test the oxidase activity, TMB + H_2O_2 and LN/Pt were negative controls. (C) Normalized absorbance at 450 nm and 650 nm at 37 °C and pH 4 for the completed reaction with TMB; the absorbance corresponds to the maximum reached at 5 minutes..... 94
- Figure 4.8.** Catalase mimics of Pt-based NanoZymes after 5 minutes. Control experiment, H_2O_2 +Buffer (A). PtSeeds catalase-mimics, H_2O_2 +PtSeeds+Buffer; $[Pt] = 2.8$ μ M (B). LN/Pt catalase-mimics, H_2O_2 +LN/Pt+Buffer; $[Pt] = 2.8$ μ M; $[LiNbO_3] = 14.5$ μ M (C). For all the samples, the measurements were performed in the presence of H_2O_2 (29.7 mM) at pH 4 (acetate buffer) and 37°C. All the concentrations are in the reaction well..... 95
- Figure 4.9.** Measurement of the absorbance maximum at a duration of 4 min 20 s for LN/Pt peroxidase reaction using TMB substrate, (A) at pH 4 as a function of temperature, and (B) at 37 °C as a function of pH. (C, insert) The colour difference between the reaction at pH 2 and pH 4. 96
- Figure 4.10.** Comparison of the peroxidase-mimic activity of (A) LN/Au (red) and (B) LN/Pt (red) with potentially leached ions from these hybrid nanoparticles (black) and the non-catalysed reaction (blue) measured with TMB at pH 4 and 37 °C..... 97
- Figure 4.11.** (A) The peroxidase-mimic activity of LN/Au (red) compared to its individual constituents. The concentration of the Nanozymes is: $[Au] = 27$ μ M; $[LiNbO_3] = 182$ μ M, corresponding to 3.9×10^{11} NPs/mL and 40 AuSeeds per LN. (B) The peroxidase-mimic activity of LN/Pt (red) compared to its individual constituents. The concentration of the Nanozymes is: $[Pt] = 2.8$ μ M; $[LiNbO_3] = 14.5$ μ M, corresponding to 2.8×10^{10} hybrid NPs/mL and 73 PtSeeds per LN in the reaction well. For both LN/Au and LN/Pt, the measurements were performed in the presence of TMB (167 μ M) and H_2O_2 (29.7 mM) at pH 4 and 37°C..... 98
- Figure 4.12.** (A) Comparison of the peroxidase-mimicking activity of LN/Au synthesised in two independent batches and one aged for more than one year, as evaluated after 38 min of reaction while employing TMB (167 μ M) and H_2O_2 (29.7 mM) at pH 4 and 37°C. The concentration of the Au is constant across the batches (27 μ M). For LN/Au, $[LiNbO_3] = 182$ μ M; for LN/Au-2, $[LiNbO_3] = 184$ μ M and for LN/Au old, $[LiNbO_3] = 163$ μ M based on the independent ICP-MS measurements. (B) Comparison of the peroxidase-mimicking activity of LN/Pt synthesised in two independent batches and one aged for more than one year, as evaluated after 5 min of reaction while employing TMB (167 μ M) and H_2O_2 (29.7 mM) at pH 4 and 37°C. The concentration of Pt is constant across the batches (2.8 μ M). For LN/Pt, $[LiNbO_3] = 14.5$ μ M; for LN/Pt-2, $[LiNbO_3] = 19.2$ μ M and for LN/Pt old; $[LiNbO_3] = 14.5$ μ M..... 100
- Figure 4.13.** (A) Peroxidase mimics TiO_2 /Au hybrids compared to LN/Au, TiO_2 and the non-catalysed reaction. The concentrations are: $[Au] = 2.7$ μ M, $[TiO_2] = 498$ μ M in TiO_2 /Au and TiO_2 and $[Au] = 2.7$

μM , $[\text{LiNbO}_3] = 16.6 \mu\text{M}$ in LN/Au. (B) Peroxidase mimics TiO_2/Pt hybrids compared to LN/Pt, TiO_2 and the non-catalysed reaction. The concentrations are: $[\text{Pt}] = 2.8 \mu\text{M}$, $[\text{TiO}_2] = 279 \mu\text{M}$ in TiO_2/Pt and TiO_2 and $[\text{Pt}] = 2.8 \mu\text{M}$, $[\text{LiNbO}_3] = 14.5 \mu\text{M}$ in LN/Pt. For A and B, control experiments were $\text{TMB} + \text{H}_2\text{O}_2 + \text{Buffer}$. For all the reactions, substrate concentrations were $[\text{TMB}] = 167 \mu\text{M}$ and $[\text{H}_2\text{O}_2] = 29.7 \text{ mM}$, and it was performed at pH 4 and 37°C 101

Figure 4.14. Michaelis-Menten plots and equations for the best fit for the LN/Au and LN/Pt Nanozymes. LN/Au curve fitting at different (A) H_2O_2 (0-29.7 mM) and (B) TMB (0-200 μM) concentrations. LN/Pt curve fitting at different (C) H_2O_2 and (D) TMB concentrations. To obtain the curves, the velocity of each reaction was calculated by converting the absorbance values at 650 nm into concentration values using Beer-Lambert law (molar extinction coefficient of TMB at 650 nm is $39000 \text{ L}\cdot\text{mol}^{-1}\cdot\text{cm}^{-1}$) and then plotting the first derivative at the beginning of the reaction (linear part of the reaction). The fittings were obtained using the Michaelis-Menten enzyme kinetic model with a Levenberg Marquardt iteration algorithm in OriginPro 2016 software. 103

Figure 4.15. Relative increase of steady kinetic parameters of hybrids over Seeds. LN/Au increase over AuSeeds with H_2O_2 as a substrate (A). LN/Au increase over AuSeeds with TMB as a substrate (B). LN/Pt increase over PtSeeds with H_2O_2 as a substrate (C). LN/Pt increase over PtSeeds with TMB as a substrate (D)..... 105

Figure 4.16. Normalized absorbance spectra (A) and Tauc plot for direct band gap (B) were obtained from the percentage of transmittance of LN (black), LN@BPEI (red), AuSeeds (blue) and LN/Au (green). Normalized absorbance spectra (C) and Tauc plot for direct band gap (D) obtained from the percentage of transmittance of LN (black), LN@BPEI (red), PtSeeds (blue) and LN/Pt (green). 107

Figure 4.17. Normalized absorbance spectra (A) and Tauc plot for direct band gap (B) were obtained from the percentage of transmittance of TiO_2 (black), TiO_2/Au (red) and TiO_2/Pt (blue)..... 109

Figure 4.18. UPS analysis of Ag (A) and Au (B) foils. Insert: zoom on Ag (A) and Au (B) electron density. The UPS spectra (black) and their first derivatives (red) are represented. 110

Figure 4.19. (A) UPS spectrum of LN NPs (red curve). The black curve is the 2nd derivative of the red curve used to identify the inflection points (arrow, 3 eV). (B) XPS spectrum of LN NPs focused on the region of Nb 3d peak at 205.8 eV (arrow). 111

Figure 4.20. (A) UPS analysis and (B) zoom in the Fermi Level (FL) of LN NPs (red curve), LN@BPEI NPs (green curve), LN/Au NPs (black curve) and Au foil (blue curve). 112

Figure 4.21. Absolute band structure position for LN NPs (blue), LN@BPEI (green), LN/Au (black), TiO_2 NPs (red) and TiO_2/Au (purple). Absolute VB_{max} positions were obtained by UPS and E_g (band gap) was obtained by UV-Vis. 114

Figure 4.22. TEM images of AuSeeds (old) (A), AuSeeds (old)+BPEI (B, B1), PtSeeds (old) (C) and PtSeeds (old)+BPEI (D, D1). 115

Figure 4.23. (A) Peroxidase-mimics of AuSeeds old+BPEI (red) and AuSeeds old (black) (B) Peroxidase-mimics of PtSeeds old+BPEI (red) and PtSeeds old (black). (B, insert) Zoom on the activity of PtSeeds old+BPEI and PtSeeds. Experiment conditions: $[\text{H}_2\text{O}_2] = 29.7 \text{ mM}$, $[\text{TMB}] = 167 \mu\text{M}$, $[\text{Au}] = 27 \mu\text{M}$, $[\text{Pt}] = 2.8 \mu\text{M}$, pH 4 and 37°C 116

Figure 4.24. (A) The reaction of terephthalic acid (TA) with OH^\bullet producing 2-hydroxyterephthalic acid. (B) The reaction of dihydroethidium (DHE) with $\text{O}_2^{\bullet-}$ producing 2-hydroxyethidium. (C) The reaction of 9,10-Anthracenediyl-bis(methylene)dimalonic acid (ABDA) with $^1\text{O}_2$ producing the correspondent endoperoxide. λ_{exc} is excitation wavelength, λ_{em} is fluorescent emission wavelength, λ_{max} is the absorption maximum. 118

Figure 4.25. (A, B) Fluorescent (F) intensity of the reaction of TA and the possible OH^\bullet generated by the Nanozymes at different times using $[\text{TA}] = 1 \text{ mM}$. (C, D) Fluorescent (F) intensity of the reaction of DHE and the possible $\text{O}_2^{\bullet-}$ generated by the Nanozymes at different times using $[\text{DHE}] = 0.01 \text{ mM}$. (E, F) % Absorbance (A) reduction of the reaction of ABDA and the possible $^1\text{O}_2$ generated by the Nanozymes at different times using $[\text{ABDA}] = 0.2 \text{ mM}$. (A, C, E) $[\text{Au}] = 11 \mu\text{M}$; $[\text{LN}] = 78.1 \mu\text{M}$. (B,

| | |
|--|-----|
| D, F) [Pt] = 1.1 μ M; [LN] = 7.6 μ M. For all the systems, the reactions were done at pH 4 with acetate buffer and [H ₂ O ₂] = 29.7 mM. | 120 |
| Figure 5.1. <i>E. coli</i> colony incubation and preparation process. | 125 |
| Figure 5.2. Bacterial growth over time and relative increase to control in the Au (A, A1) and the Pt system (B, B1). Control, <i>i.e.</i> , bacteria without any treatment (black), LN NPs (blue), LN@BPEI (green), metal Seeds (pink), and hybrid Nanozymes (red) are shown. Concentrations are [Au] = 1 μ M, [Pt] = 1 μ M and [LiNbO ₃] = 7 μ M. | 126 |
| Figure 5.3. Induced relative bacterial growth upon deposition of the metal seeds onto LN@BPEI measured after 1.5 h of incubation. The data represents relative change in the bacterial populations upon deposition of either Au or Pt Seeds on LN@BPEI compared to the respective AuSeeds and PtSeeds. | 128 |
| Figure 5.4. H ₂ O ₂ cytotoxicity at different concentrations after 3 h, from 0 mM (control) to 100 mM. | 129 |
| Figure 5.5. Normalized number of bacteria without Nanoparticles (black), with LN NPs (blue), or LN@BPEI (green) grown over time in the absence (solid line) and presence of H ₂ O ₂ (dashed line) (A). Relative change in the bacterial population for different treatment groups on exposure to H ₂ O ₂ after 1.5 h (B) and 3 h (C). Concentrations were: [LiNbO ₃] = 7 μ M; [H ₂ O ₂] = 1 mM. | 130 |
| Figure 5.6. H ₂ O ₂ induced relative cell growth in bacteria untreated and treated with LN NPs and LN@BPEI. The data represents relative change in the bacterial populations with reference to each of the specific treatment group upon treatment with H ₂ O ₂ compared to non-H ₂ O ₂ treated controls. | 131 |
| Figure 5.7. Bacterial growth over time without Nanoparticles (black), with LN NPs (blue), LN@BPEI (green), AuSeeds (pink), LN/Au (red), either non-treated (solid line) or treated with H ₂ O ₂ (dashed line) (A). Bacterial growth over time without Nanoparticles (black), with LN NPs (blue), LN@BPEI (green), PtSeeds (pink), LN/Pt (red), either non-treated (solid line) or treated with H ₂ O ₂ (dashed line) (B). Relative increase in the treatment groups to control (non-treated) after 1.5 h (C) and 3 h (D). Concentrations were: [LiNbO ₃] = 7 μ M; [Au] = 1 μ M; [Pt] = 1 μ M; [H ₂ O ₂] = 1 mM. | 132 |
| Figure 5.8. H ₂ O ₂ induced relative cell growth in bacteria untreated and treated with LN NPs, LN@BPEI, AuSeeds, LN/Au, PtSeeds and LN/Pt. The data represents relative change in the bacterial populations with reference to each of the specific treatment group upon treatment with H ₂ O ₂ compared to non- H ₂ O ₂ treated controls. | 133 |
| Figure 5.9. Band gap edge wavelengths of the different materials compared to UV-irradiation lamp (302 nm)..... | 134 |
| Figure 5.10. Intensity of light as a function of distance from the lamp. | 135 |
| Figure 5.11. Percentage of cell death as a function of exposure time to UV light ($\lambda_{\text{max}} = 302$ nm, 1 mW/cm ²). | 135 |
| Figure 5.12. Bacterial growth over time without Nanoparticles (black), with LN NPs (blue), LN@BPEI (green) either in the absence (solid line) or presence of UV (dashed line) (A). Relative increase to control (non-treated) after 1.5 h (B) and 3 h (C). Concentration was: [LiNbO ₃] = 7 μ M. | 136 |
| Figure 5.13. The percentage of UV-induced relative cell growth for the non-treated bacteria and those treated with LN and LN@BPEI NPs at 1.5 h and 3 h. The data represents relative change in the bacterial populations with reference to each of the specific treatment group upon their UV exposure. | 137 |
| Figure 5.14. Bacterial growth over time without Nanoparticles (black), with LN NPs (blue), LN@BPEI (green), AuSeeds (pink), LN/Au (red) either non-treated (solid line) or treated with UV (dashed line) (A). Bacterial growth over time without Nanoparticles (black), with LN NPs (blue), LN@BPEI (green), PtSeeds (pink), LN/Pt (red) either non-treated (solid line) or treated with UV (dashed line) (B). Relative increase to control (non-treated) after 1.5 h (C) and 3 h (D). Concentrations were: [LiNbO ₃] = 7 μ M; [Au] = 1 μ M; [Pt] = 1 μ M. | 138 |

| | |
|---|-----|
| Figure 5.15. Percentage of induced relative cell growth for the non-treated bacteria and those treated with LN and LN@BPEI NPs, AuSeeds, LN/Au, PtSeeds and LN/Pt at 1.5 h and 3 h. The data represents relative change in the bacterial populations with reference to each of the specific treatment group upon their UV exposure. | 140 |
| Figure 5.16. (A, B) Fluorescent (F) intensity of the reaction of terephthalic acid and the possible OH [•] generated by the Nanozymes, [TA] = 1 mM. (C, D) Fluorescent (F) intensity of the reaction of dihydroethidium (DHE) and the possible O ₂ ^{•-} generated by the Nanozymes, [DHE] = 0.01 mM. (E, F) % Absorbance (A) reduction of the reaction of ABDA and the possible ¹ O ₂ generated by the Nanozymes, [ABDA] = 0.2 mM. (A, C, E) [Au] = 11 μM; [LN] = 78.1 μM. (B, D, F) [Pt] = 1.1 μM; [LN] = 7.6 μM. For all the systems, the reactions were done in MilliQ. UV light irradiation λ _{max} = 302 nm, 1 mW/cm ² . Panels A, C, and E correspond to Au-based Nanozymes, while panels B, D and F correspond to Pt-based Nanozymes. | 141 |
| Figure 5.17. Bacterial growth over time without Nanoparticles (black), with LN NPs (blue), LN@BPEI (green) either non-treated (solid line) or treated with H ₂ O ₂ and UV (dashed line) (A). Relative increase to control (non-treated) after 1.5 h (B) and 3 h (C). Concentration were: [LiNbO ₃] = 7 μM; [H ₂ O ₂] = 1 mM. | 143 |
| Figure 5.18. Percentage of induced relative cell growth for the non-treated bacteria and those treated with LN and LN@BPEI NPs at 1.5 h and 3 h. The data represents relative change in the bacterial populations with reference to each of the specific treatment group upon their simultaneous exposure to UV+H ₂ O ₂ | 144 |
| Figure 5.19. Bacterial growth over time without Nanoparticles (black), with LN NPs (blue), LN@BPEI (green), AuSeeds (pink), LN/Au (red) either non-treated (solid line) or treated with H ₂ O ₂ and UV (dashed line) (A). Bacterial growth over time without Nanoparticles (black), with LN NPs (blue), LN@BPEI (green), PtSeeds (pink), LN/Pt (red) either non-treated (solid line) or treated with H ₂ O ₂ and UV (dashed line) (B). Relative increase to control (non-treated) after 1.5 h (C) and 3 h (D). Concentrations were: [LiNbO ₃] = 7 μM; [Au] = 1 μM; [Pt] = 1 μM; [H ₂ O ₂] = 1 mM. | 145 |
| Figure 5.20. H ₂ O ₂ and UV induced relative cell growth in bacteria untreated and treated with LN NPs, LN@BPEI, AuSeeds, LN/Au, PtSeeds and LN/Pt. The data represents relative change in the bacterial populations with reference to each of the specific treatment group upon their simultaneous exposure to UV+H ₂ O ₂ | 146 |
| Figure 5.21. Response to NPs treatment of the bacteria relative to control at 1.5 h in the presence of various external oxidative stress stimuli. No treatment (A), treated with LN NPs (B), treated with LN@BPEI NPs (C). | 147 |
| Figure 5.22. Response to Au-based Nanozymes treatment of the bacteria relative to control at 1.5 h in the presence of various external oxidative stress stimuli. No treatment (A), treated with AuSeeds (B), treated with LN/Au (C). | 148 |
| Figure 5.23. Response to Pt-based Nanozymes treatment of the bacteria relative to control at 1.5 h in the presence of various external oxidative stress stimuli. No treatment (A), treated with AuSeeds (B), treated with LN/Au (C). | 149 |
| Figure A1. (A) TEM image of an independent batch of AuSeeds. (B) TEM image of independent batch of LN/Au1. (C) TEM image of an independent batch of LN/Au2. (D) TEM image of an independent batch of PtSeeds. (E) TEM image of independent batch of LN/Pt1. | 179 |
| Figure A2. X-Ray diffractogram of commercial TiO ₂ (Degussa P25). | 180 |
| Figure A3. EDS atomic percentage of Ti and Au for three different TiO ₂ /Au hybrid NPs. | 180 |
| Figure A4. (A) Tauc plot for indirect band gap obtained from the percentage of transmittance of LN (black), LN@BPEI (red), AuSeeds (blue) and LN/Au (green) (B) Tauc plot for indirect band gap (B) obtained from the percentage of transmittance of LN (black), LN@BPEI (red), PtSeeds (blue) and LN/Pt (green). (C) Tauc plot for indirect band gap obtained from the percentage of transmittance of TiO ₂ (black), TiO ₂ /Au (red) and TiO ₂ /Pt (blue). | 182 |

Figure A5. (A) UPS analysis on TiO₂. (insert: Calculation of the V_{bmax} and reminiscent Fermi Level of Ag foil). (B) Ti 2p core level of TiO₂ corresponding to Ti⁴⁺..... 184

Figure A6. (A) UPS analysis on TiO₂-Au. (insert: Calculation of the V_{Bmax}). (B) Au 4f core level and (C) Ti 2p core level of TiO₂-Au..... 185

List of Tables

| | |
|--|-----|
| Table 1.1. Reactions catalysed by the most common oxidoreductase mimic Nanozymes. M^n is a metal centre in its reduced form, and M^{n+1} is its oxidized form. | 9 |
| Table 1.2. Comparative table for the synthesis of seed-decorated hybrid metal-metal oxide nanoparticles. Colour code: green (advantage), yellow (disadvantage), red (important disadvantage). | 34 |
| Table 1.3. Compilation of metal nanoparticles activities towards therapeutics. | 40 |
| Table 2.1. Summary of UV-Vis spectrophotometric techniques. | 63 |
| Table 2.2. Comparative table of UPS and XPS photoelectron spectroscopies..... | 65 |
| Table 3.1. The ratios of noble metal seeds to LN NPs and volumes of AuSeeds, PtSeeds and AgSeeds used to prepare noble metal seeded-LN NPs, starting from a 0.35 g/L LN@BPEI NPs dispersion and 0.037 g/L, 0.036 g/L and 0.020 g/L of AuSeeds, PtSeeds, and AgSeeds, respectively..... | 72 |
| Table 3.2. The ratios of noble metal seeds to TiO ₂ NPs and volumes of AuSeeds and PtSeeds used to prepare noble metal seeded-TiO ₂ NPs, starting from a 0.35 g/L LN@BPEI NPs dispersion and 0.037 g/L and 0.036 g/L of AuSeeds and PtSeeds, respectively..... | 73 |
| Table 3.3. TEM diameter, hydrodynamic diameter, and zeta potential values of LN NPs, LN@BPEI NPs, AuSeeds and PtSeeds. | 74 |
| Table 3.4 TEM diameter of metal seeds onto LN@BPEI, hydrodynamic diameter, zeta potential values of LN/Au and LN/Pt NPs measured in water, and molar percentage of noble metal content in LN/Au and LN/Pt determined by EDS. | 77 |
| Table 3.5. TEM diameter of AgSeeds and AgSeeds onto LN@BPEI, hydrodynamic diameter and zeta potential values of AgSeeds and LN/Ag measured in water, and molar percentage of noble Ag content in LN/Ag determined EDS..... | 80 |
| Table 3.6. Data was collected from multiple samples for LN/Au and LN/Pt, including samples aged more than 1 year (old). TEM diameter of metal seeds onto LN@BPEI, zeta potential values of LN/Au and LN/Pt NPs measured in water, and molar percentage of noble metal content in LN/Au and LN/Pt determined by EDS. In parenthesis, it is included the average of the same parameters of the sample presented before (Table 3.3 , Table 3.4)..... | 81 |
| Table 3.7. TEM diameter of metal seeds onto TiO ₂ , hydrodynamic diameter and zeta potential values of TiO ₂ /Au and TiO ₂ /Pt NPs measured in water..... | 83 |
| Table 4.1. Buffer preparation table showing the expected pH, final measured pH and the type of buffer used. | 87 |
| Table 4.2. Apparent steady-state kinetic parameters for LN/Au, AuSeeds, LN/Pt and PtSeeds for driving a peroxidase-mimic reaction..... | 104 |
| Table 4.3. Direct band gap energies of the different materials obtained from extrapolation in the Tauc plot. | 108 |
| Table 4.4. Direct band gap energies of the different materials obtained from extrapolation in the Tauc plot. | 109 |
| Table 4.5. Work function ϕ and valence band maximum (VB _{max}) values for the samples determined by XPS/UPS analysis..... | 113 |
| Table 4.6. TEM diameters obtained for fresh and old samples of AuSeeds and PtSeeds, and for old samples of AuSeeds and PtSeeds after BPEI addition..... | 115 |
| Table 5.1. Direct band gap energies and corresponding wavelengths of the different materials. | 134 |

Table 5.2. Summarization of the percentage of induced relative bacterial growth upon treatment with different sources of oxidative stress (H_2O_2 , UVB, H_2O_2 +UVB). The data represents relative change in the bacterial populations with reference to each of the specific treatment group upon their exposure to sources of oxidative stress. All numbers are expressed in percentage. Green indicates enhanced viability compared to control, red means worsened viability and yellow means that the viability is similar to the control. 150

Table A1. Indirect band gap energies of the different materials obtained from extrapolation in the Tauc plot. 183

Table A2. Work function ϕ and valence band maximum (VB_{max}) values for the samples determined by XPS/UPS analysis. The absolute energy of the valence band maximum is equal to the sum of VB_{max} relative to the Fermi level and the Ag foil work function (4.2 eV as determined previously). 185

Glossary

| | |
|-----------------------|--|
| ABTS | 2,2'-Azino-Bis(3-Ethylbenzothiazoline-6-Sulfonic Acid) |
| TMB | 3,3',5,5'-Tetramethylbenzidine |
| ABDA | 9,10-Anthracenediyl-Bis(Methylene)Dimalonic Acid |
| ADP | Adenosine Diphosphate |
| ATP | Adenosine Triphosphate |
| V_{BB} | Band Bending Energy |
| E_g | Band Gap |
| BPEI | Branched Polyethyleneimine |
| BSA | Bovine Serum Albumin |
| CAT | Catalase |
| K_{cat} | Catalytic Constant or Turnover Number |
| K_{eff} | Catalytic Efficiency |
| CFU | Colony Forming Units |
| CB | Conduction Band |
| CSNPs | Core-Shell Nanoparticles |
| CTAB | Cetyltrimethylammonium Bromide |
| DMSN | Dendritic Mesoporous Silica |
| DFT | Density Functional Theory |
| DHE | Dihydroxyethidine |
| DMSO | Dimethyl Sulfoxide |
| DBNPs | Dumbbell-Like Nanoparticles |
| DLS | Dynamic Light Scattering |
| χ_s | Electron Affinity |
| EELS | Electron Energy Loss Spectroscopy |
| EDX, EDS | Energy Dispersive X-Ray Spectroscopy |
| E | Enzyme |
| <i>E. Coli</i> | <i>Escherichia Coli</i> |
| ELISA | Enzyme-Linked Immunosorbent Assay |
| FL | Fermi Level |
| FAD/FADH ₂ | Flavine Adenine |
| GOx | Glucose Oxidase |
| GPx | Glucose Peroxidase |
| GO | Graphene Oxide |

| | |
|-----------------------|---|
| HOMO | Highest Occupied Molecular Orbital |
| HRTEM | High-Resolution Transmission Electron Microscopy |
| HCN | Hollow Carbon Shell |
| HRP | Horseradish Peroxidase |
| ICP-AES | Inductively Coupled Plasma Atomic Emission Spectroscopy |
| IBD | Inflammatory Bowel Disease |
| IUPAC | International Union of Pure and Applied Chemistry |
| JNPs | Janus-Shaped Nanoparticles |
| KE | Kinetic Energy |
| LDV | Laser Doppler Velocimetry |
| LN/Ag | LiNbO ₃ NPs Coated with BPEI and AgSeeds |
| LN/Au | LiNbO ₃ NPs Coated with BPEI and AuSeeds |
| LN/Pt | LiNbO ₃ NPs Coated with BPEI And PtSeeds |
| LiNbO ₃ | LN |
| LSPR | Localized Surface Plasmon Resonance |
| LUMO | Lowest Unoccupied Molecular Orbital |
| V _{max} | Maximum Velocity |
| MSN | Mesoporous Silica |
| M | Metal |
| MOF | Metal Organic Framework |
| MOFs | Metal-Organic Frameworks |
| K _m | Michaelis-Menten Constant |
| k | Momentum |
| NCs | Nanocrystals |
| NPs | Nanoparticles |
| NIR | Near Infrared |
| NAD/NADH ⁺ | Nicotine Adenine |
| NLO | Non-Linear Optics |
| NB | Nutrient Broth |
| OAm | Oleylamine |
| OPD | O-Phenylenediamine |
| OD | Optical Density |
| OXD | Oxidase |
| POD | Peroxidase |
| PDT | Photodynamic Therapy |

| | |
|-------------------|---|
| PDT | Photodynamic Therapy |
| PES | Photoemission Spectroscopy |
| PTT | Photothermal Therapy |
| PAA | Polyacrylic Acid |
| PEI | Polyethyleneimine |
| POMD | Polyoxometalate with Wells–Dawson Structure |
| P | Product |
| RT | Radiotherapy |
| ROS | Reactive Oxygen Species |
| STEM | Scanning Transmission Electron Microscopy |
| $\phi_{\Sigma B}$ | Schottky Barrier |
| SHG | Second Harmonic Generation |
| SDNPs | Seed-Decorated Nanoparticles |
| SC | Semiconductor |
| SDT | Sonodynamic Therapy |
| <i>S. aureus</i> | <i>Staphylococcus Aureus</i> |
| S | Substrate |
| SOD | Superoxide Dismutase |
| SPR | Surface Plasmon Resonance |
| TA | Terephthalic Acid |
| THPC | Tetrakis(Hydroxymethyl)Phosphonium |
| TEM | Transmission Electron Microscopy |
| TME | Tumour Microenvironment |
| UPS | Ultraviolet Photoelectron Spectroscopy |
| UV-Vis | Ultraviolet-Visible |
| VB | Valence Band |
| v | Velocity of the Reaction |
| VOC | Volatile Organic Compounds |
| ϕ | Work Function |
| WHO | World Health Organisation |
| XPS | X-Ray Photoelectron Spectroscopy |

Acknowledgments

I would like to take this opportunity to express my appreciation and gratitude to all the people who were involved and helped me during this challenging yet wonderful journey that is my PhD. I deeply appreciate their encouragement, support, advice, and patience.

First and foremost, I would like to thank Pascal Ray, the current director of École Centrale de Lyon, and Frank Debouck, the former director of École Centrale de Lyon, for the opportunity to conduct my thesis at École Centrale de Lyon during my tenure as a PhD student. In addition, I would like to thank the former and current directors of the Institute des Nanotechnologies de Lyon: Dr. Catherine Bru-Chevallier, Dr. Christian Seassal, Dr. Bruno Masenelli, and Dr. Ségolène Callard.

Thank you to all the members of my jury for reading and evaluating the quality of my research. I am grateful to the two reviewers, Prof. Catherine Amiens, and Prof. Nadine Millot, who carefully responded in writing to my manuscript. Your comments and remarks were carefully read, taken into account and aided in the enhancement of my research. I also thank Dr. Christophe Geantet for being the president of my jury and helping me understand the catalysis-related questions I had during my PhD course. I would like to thank Dr. Miguel Comesaña Hermo for his questions and comments that clarified some points of my thesis and promoted a stimulating scientific discussion.

I am very grateful to my supervisory team. They have guided me through my PhD and supported me during the difficult times and struggles caused by the Covid-19 pandemic.

I want to thank my supervisor, Dr. Virginie Monnier, for her caring nature, academic guidance, support, and inspiration throughout my PhD. She gave me the opportunity to pursue this journey, and it has been an honor to have worked under her supervision. She guided me through all my experiments, allowing me to grow independently. I also want to thank her for showing me what a PhD supervisor should be. I appreciate her trust in me to teach practical work and supervise an undergraduate student.

All my sincere appreciation goes to Dr. Yann Chevolut, who co-supervised my PhD at École Centrale de Lyon. His concern and support throughout my candidature will never be forgotten. Thank you, especially for teaching me how to structure a report and for asking incisive

questions that made me rethink my research. He has been an example of what a head group should be, always caring for the well-being of all PhD candidates.

I am extremely thankful to my supervisor at RMIT, Prof. Vipul Bansal, for allowing me to work with him. His extensive knowledge in multidisciplinary areas has been inspiring and serves as an example for me. Although it seemed impossible due to the Covid-19 pandemic, we finally met in person, and I was able to witness how he analyzes a problem and provides immediate solutions.

Finally, I would like to thank Dr. Rajesh Ramanathan, my co-supervisor at RMIT, for his patience and time. His constant strive for perfection has been an example for me. It was a pleasure to work side-by-side at RMIT.

I acknowledge Prof. Arnan Mitchell and Dr. Christian Grillet for making the ECLAUSion project possible and for choosing me as one of the candidates. The ECLAUSion project has received funding from the European Union's Horizon 2020 research and innovation program under the Marie Skłodowska-Curie grant agreement No 801512. We acknowledge the support of the International Associated Laboratory in Photonics between France and Australia (LIA ALPhFA).

I would like to acknowledge all my colleagues who became friends at École Centrale de Lyon. These colleagues have shared with me the misfortunes and joys of doing a PhD, from the endless lunch breaks and coffee times to all the celebrations. I am extremely grateful to Antonin for his patience and for teaching me French. I will always appreciate Paule's advice and caring personality. Thanks to Oleh for showing me what endurance means and also for all the laughs. Thanks to Panteha for all her generosity and joy. Harris has taught me the limits of my patience but has also been a reliable friend and has provided me with useful scientific advice. Greta was my partner in crime in Australia and has been a valuable resource during my PhD; she has shown me that programming is accessible to everyone. I thank Marko for his spontaneity and for helping me to take things less seriously. Thanks, Jesús, for always playing reggaeton and making me feel at home at all the parties. I want to thank Gaukhar for the joy she has always transmitted to me.

I would also like to thank all the people who took part in my PhD. Isabel Nabeth has always made sure that my chemicals arrive on time. Dr. Nicolas Blanchard taught me how to operate the TEM microscope autonomously. Dr. Eric Puzenat taught me how to properly operate a UV-

Vis spectrometer to perform optical band gap measurements. Dr. Samantha Richardson helped me with all the administrative tasks at RMIT. I am grateful to all the people who assessed my work: Dr. Catherine Larose, Dr. Cecile Jamois, Dr. Lathe Jones, and Dr. James Tardio.

I would also like to thank my colleagues at RMIT. Although the experience was short, it was intense, and I learned a lot from all of you: Anupriya, Aviraj, Yule, Wilson, Sanje, and Satnam. I want to especially thank Mr. Shakil Polash for his intensive culture cell course, and Dr. Pabudi Weerathunge for her thoughtful comments. Mrs. Sanjana Naveen Prasad for her patience. Dr. Wenyue Zou for her availability. Thanks to Pyria Rose Divina Mariathomas for helping me from a distance to implement the Nanozyme-mimics experiments in ECL. Without her help, this PhD would not have been possible. I will always be grateful to Dr. Piyumi Balapitiya Liyanage for her time helping me with the aptamer experiments and all her help during my stay at RMIT.

I want to acknowledge Prof. María del Puerto Morales, Prof. Carmen Barrientos Benito, and Dr. Marco Sanna for taking the time to write recommendation letters that allowed me to enter this PhD program. I would also like to thank Dr. Daniel Nižňanský for introducing me to the world of nanoparticles and trusting me to do my first internship at his laboratory in Charles University in Prague. I will always remember him as a smiling, caring, and patient person.

I would like to thank my closest friends. You are the family I choose, and you've shown it throughout these years. María, thank you for talking with me, knowing me better than anyone, giving me the most valuable advice, and supporting me throughout this PhD. You have shown me what sorority means and that love comes in many ways. Rubén, thank you for making my stay in Melbourne easier by taking care of me and being supportive, especially during my hangovers. Lucía, thank you for keeping me connected to Spain. Cristina, thank you for helping me with one of the best decisions I made. Valentina, thank you for all your advice and for simply being my "way out" when I am tired of speaking French or English and understand all the struggles of being an ex-pat. Miguel Ángel, Sonia, Alba, Ali, Manu, and all the rest, thank you for being there and grounding me during all the calls and trips.

I would also like to thank Julien. I greatly appreciate your support during my PhD. You have made the biggest effort to try to understand me. You dried my tears and gave me strength during my stay in France. I have been able to put problems into perspective and enjoy uncertainty

thanks to you. You have been and continue to be patient with me. You have shown me that I am strong. You make me feel at home in France. I keep learning to love by your side.

Finally, I would like to thank my family. Isabel, my aunt, thank you for helping me with my English skills throughout the PhD and supporting me in my expat journey. My grandpa, Javier, is always surprised by all my achievements. My grandpa, Francisco, would be proud of his grandkid for being a PhD. My grandma, Bruni, might not understand many things right now, but I know she's already proud of me. My cat, Roc, thank you for your companionship through all the long evenings working from home. My sister, Sol, thank you for your care and concern, and for standing by me, especially as she was my first student. I am especially grateful to my parents. They have always supported me in my career and encouraged me to be a scientist since I asked for a chemistry game for Christmas at the age of 8. I am very grateful to my father for all his calls and support. During this PhD, he has shown me how deeply he cares for me and all the efforts he has made since I began my PhD. I want to thank my mother for always encouraging me. I want to thank her for taking care of me from so far. She knows that this has not been a simple journey. She has made it easier through her loving support.

General introduction

Nanozymes are nanomaterials that mimic natural enzymes. Recently, they have been positioned as a new emerging technology that has attracted particular attention over the last decade [1]. Nanozymes, compared to natural and artificial enzymes, offer great value in terms of price and, especially, allow multi-functionalization due to their tunability in shape, size, type of material, type of coating or even the modulation of their physical properties through external stimuli such as light. These qualities make them attractive to be used in many different environmental and bio-related applications [2].

Nanozyme-based sensors are one of the most appealing applications. The combination of Nanozymes with antibodies and antigens allows immunological analysis, especially in enzyme-based detection techniques such as enzyme-linked immunosorbent assay (ELISA) [3]. Aptamers, *i.e.* single-stranded DNA or RNA molecules that bind specifically to a target, are also attractive for the functionalization of Nanozymes as they reduce costs and diversify the types of targets that can be detected [4], [5]. Moreover, they have shown outstanding properties in one of the most critical calls of the World Health Organisation (WHO): point-of-care devices. Point-of-care Nanozyme-based sensors fulfill the criteria required by WHO of affordable, fast, sensitive, specific, user-friendly, equipment-free, robust and delivered to the end users [6].

Nanozyme therapeutic applications are useful in many areas. For instance, some Nanozymes increase the production of reactive oxygen species (ROS) and thus induce oxidative stress, which is beneficial in antimicrobial applications or tumour cell treatment. On the contrary, other Nanozymes relieve the overexpression of ROS, reducing oxidative stress. Their use has been reported in anti-inflammatory processes or to decrease tumour micro-environment hypoxia. The latter application is not only beneficial to avoid healthy-cell apoptosis but also to ensure the correct functioning of external therapies requiring oxygen, such as photodynamic

therapy or radiotherapy [7]. Related to this, light interaction can be used to stimulate Nanozyme performance in therapeutics.

Among Nanozymes, noble metal-based Nanozymes have been widely used, and their synthesis methods and ease of functionalization and modification make them attractive candidates. Likewise, their Nanozyme-mimic properties have been established. They have shown different enzyme mimics as peroxidases, oxidases, catalases and superoxide dismutases, which are tunable depending on intrinsic factors such as composition or shape and extrinsic factors such as light or pH [8].

Catalytic activity is highly dependent on the size, and the best performances have been shown for metal nanoparticles with diameters below 5 nm [9]. However, this can provoke an opposite effect: their aggregation and the loss of their catalytic activity. To overcome this, their deposition over metal oxides has been widely used in classic oxidoreduction catalysis [10]. Additionally, their combination with metal oxide nanoparticles has resulted in a synergetic effect: properties of both materials are combined with an extra benefit, an increased catalytic performance due to charge transfer processes, band structure stabilization and defect creation [11].

Among metal oxides, LiNbO_3 has not yet been investigated in combination with metal nanoparticles as Nanozyme. Our group already investigated the synthesis of LiNbO_3/Au hybrid nanoparticles composed of LiNbO_3 nanoparticles (LN NPs), AuSeeds (Au nanoparticles below 5 nm diameter) using branched polyethyleneimine as a chemical link [12]. Based on this, this work aims to prove the applicability of $\text{LiNbO}_3/\text{metal}$ nanoparticles as Nanozymes by extending the synthesis to other materials. We want to confirm the presence of a synergetic effect arising from the material combination. Additionally, we aim to prove their applicability in ROS-related applications.

Chapter 1 presents the basic concepts of Nanozymes and the advantages of using metal-based ones. We also introduce the theory behind the catalytic synergetic effect between metal-metal oxide nanomaterials and their application in enzyme mimics. Then, we present the state-of-the-art of metal-based Nanozymes in ROS boosting and scavenging therapeutic applications with a special focus on metal-metal oxide hybrid Nanozymes and light interaction. Finally, the objectives of the thesis are outlined.

Chapter 2 overviews the different characterization techniques and the principles behind them. The techniques for the characterization of nanoparticles are transmission electron microscopy (TEM), including the variations with scanning TEM (STEM), high-resolution TEM (HRTEM), energy dispersive X-ray spectroscopy (EDS or EDX). Other characterization techniques are dynamic light scattering (DLS), laser doppler velocimetry and electrophoresis (zetammetry), UV-vis spectroscopy and inductively coupled plasma atomic emission spectroscopy (ICP-AES). The techniques for Nanozyme activity characterization and mechanistic elucidation are UV-vis spectroscopy, fluorescent spectroscopy and X-ray and UV photoelectron spectroscopy (XPS/UPS). Finally, Nanozymes and their building blocks interaction with microbial growth is studied through optical density measurements.

Chapter 3 presents the synthesis and characterization of the potential hybrid Nanozymes. Initially, we detail the synthesis protocols of the starting building blocks of the hybrid nanoparticles, *i.e.*, LN NPs, LN@BPEI (LiNbO₃ NPs coated with branched-polyethyleneimine) and metal seeds (Au, Pt and Ag). Subsequently, the synthesis of the hybrid nanoparticles is presented. The characterization of the building blocks and the hybrid nanoparticles is discussed in terms of size and colloidal properties.

Chapter 4 presents the optimization of the enzyme mimics of the hybrid nanoparticles. Parameters such as substrate, pH and temperature are varied and adjusted. Their Nanozyme peroxidase activity is established in the optimized conditions and compared to the separated counterparts. Subsequently, we verified if the Nanozymes and the metal Seeds follow the Michaelis-Menten natural enzyme kinetic model. Finally, mechanistic elucidation is carried out through band structure studies, supplementary catalytic studies, and ROS-traps tests.

Chapter 5 focuses on microbial growth studies in the presence of Nanozymes and oxidative stress induced through hydrogen peroxide (H₂O₂) and UV light. Bacteria growth is initially studied in the presence of Nanozymes, followed by the introduction of an optimized quantity of H₂O₂ and UV light irradiation. Finally, the effect of combining the two oxidative stress sources with the Nanozymes is studied.

The manuscript ends with the conclusions and future perspectives of this work.

Chapter 1: State of the art

This chapter aims to provide the state of the art on metal nanoparticles as Nanozymes. Their synthesis will be discussed, as well as their applicability in the field of enzyme mimics. Specifically, we will focus on how their catalytic activity can be improved by loading them on a metal oxide. We will explore the different synthesis of metal-oxide hybrid nanoparticles and the synergetic effect arising from the combination of materials. Moreover, we will review Nanozyme interaction with reactive oxygen species and their application in therapeutics. With the available literature, we will examine the gaps in the field and the motivation of this research work.

1.1. Artificial enzymes: Nanozymes

1.1.1. Concept of Nanozyme

Before the beginning of the discussion, some key concepts should be defined. Bio-entities that catalyze biochemical reactions can be denominated as biocatalysts. There are two types of biocatalysts: enzymes and whole cells (bacteria, fungi, microalgae, and plants, among others). Enzymes are defined by the International Union of Pure and Applied Chemistry (IUPAC) as: "macromolecules, mostly of protein nature, that function as (bio)catalysts by increasing the reaction rates. In general, an enzyme catalyzes only one reaction type (reaction specificity) and operates on only one type of substrate (substrate specificity). Substrate molecules are attacked at the same site (regiospecificity), and only one or preferentially one of the enantiomers of chiral substrates or racemic mixtures is attacked (stereospecificity)" [13].

The high selectivity and catalytic properties of these molecules lead to an increase in the reaction rate of 10^{14} over uncatalyzed reactions [14]. The ability of enzymes to catalyze reactions arises from the significant reduction in activation energy of the transition state [15]. Due to these outstanding properties, enzymes have been used in many industries: pharmaceutical, food processing, detergent, paper and pulp, and the relatively new biofuel industry [16]. However, some limitations remain, such as high cost, the requirement of in-the-range physiological conditions, low stability, no long-term storage, poor substrate versatility and, for medical applications, the tedious purification steps to obtain high purity catalyst [17], [18]. Therefore, tremendous work has been undertaken to replace natural enzymes.

One strategy is to substitute enzymes with other biomolecules which have enzyme-like activity. At the beginning of the 80s, ribozymes, *i.e.* RNA that showed enzymatic properties, were discovered [19]. Since then, other biomolecules have proven these characteristics, such as DNA [20] or antibodies [21]. Another strategy is to replace natural enzymes with artificial ones. Enzymes are macromolecules, each having a specific 3D conformation. This 3D folding defines the topology of the catalytic site(s). Therefore, a possible strategy is to mimic the active site with lower molecular weight molecules. This strategy is advantageous as lower-size molecules can penetrate better into cells [15]. Alternatively, many efforts have been devoted to synthesizing enzyme-mimicking organic polymers, which allows customizing the application and reduce costs. Organic chemists have here an interesting field of application.

Therefore, various approaches, such as molecular imprinted polymers, dendrimeric molecules, organometals and supramolecular structures like cyclodextrins and calixarenes, are promising to mimic natural enzymes [15], [22], [23].

A particular class of artificial enzymes are the newly discovered "Nanozymes", *i.e.*, nanomaterials that mimic enzymes. In the scope of this thesis, we will define a Nanozyme as a material with the following features: organic or inorganic material in which at least one dimension is between 1 to 100 nm (nanomaterial), which has an intrinsic capability to catalyze biochemical reactions as natural enzymes and which follows natural enzymes catalytic mechanism (*e.g.*, Michaelis-Menten kinetics). Some authors named Nanozymes natural enzymes or enzymatic catalytic groups integrated into nanomaterials. However, we will not consider them here as, in these cases, the nanomaterial does not possess intrinsic enzyme mimics.

Concerning Nanozymes as artificial enzymes, they can substitute enzymes and even improve some features with their lower cost, higher stability, capacity of long-term storage, easier manufacturing, better resistance to harsh environments, and possibility of size/composition engineering. They also present many advantages in comparison to other artificial enzymes. First, their activity, selectivity and/or specificity can be adjusted by varying their nanoscale structure (size, morphology, planes, shape, lattice, vacancies or surface chemistry). This is not the case with small organic molecules in which the structure modification causes the loss of enzyme-like activity. Second, one Nanozyme can perform multiple enzyme-like activities, making them much more versatile than other artificial enzymes. Third, due to their nanostructure, they possess several physicochemical properties that may interact with or regulate the enzymatic activity and diversify their applications [24].

Nanomaterials substantially increase the number of active sites due to their high surface-to-volume ratio, making them suitable catalysts. Therefore, not surprisingly, their enzyme-mimic activity was discovered in 1996-1997 for fullerenes, demonstrating superoxide dismutase mimics [25]. Although bulk gold is chemically inert, gold nanoparticles were reported in 2004 to possess oxidase activity [26]. The same year, a small review appeared, presenting for the first time the term "Nanozyme" [27]. This discovery was followed by the finding of superoxide dismutase (SOD) like-activity of nanoceria [28]. A breakthrough was reached in 2007 when Gao *et al.* published a paper in which peroxidase-like activity was reported for magnetite nanoparticles [29]. This study not only presented this new feature of the magnetite

nanoparticles but also opened the field to a wide range of applications since many other nanomaterials have shown similar behavior such as Nano V_2O_5 , graphene, MOFs, and Prussian blue, among others (**Figure 1.1**) [30]. Various nanomaterials have demonstrated to mimic catalase, oxidase, peroxidase, superoxide dismutase (SOD), esterase, nuclease, phosphatase, or protease. Research in the last decade has led to a variety of applications in which they are useful, such as biosensing, degradation of organic compounds in water, cancer therapy and other medical applications, therapeutics imaging or sunscreen [18]. Consequently, Nanozymes were highlighted as one of the IUPAC's Top Ten Emerging Technologies in Chemistry in 2022 [1]. However, since this is a new research area, many aspects remain unknown and extensive investigations are yet needed to fill the gaps between natural enzymes and Nanozymes. Although, for some reactions, Nanozymes can rival the performance of proteins [31], there is room for improvement. Rational design and surface modification are promising ways to reach this.

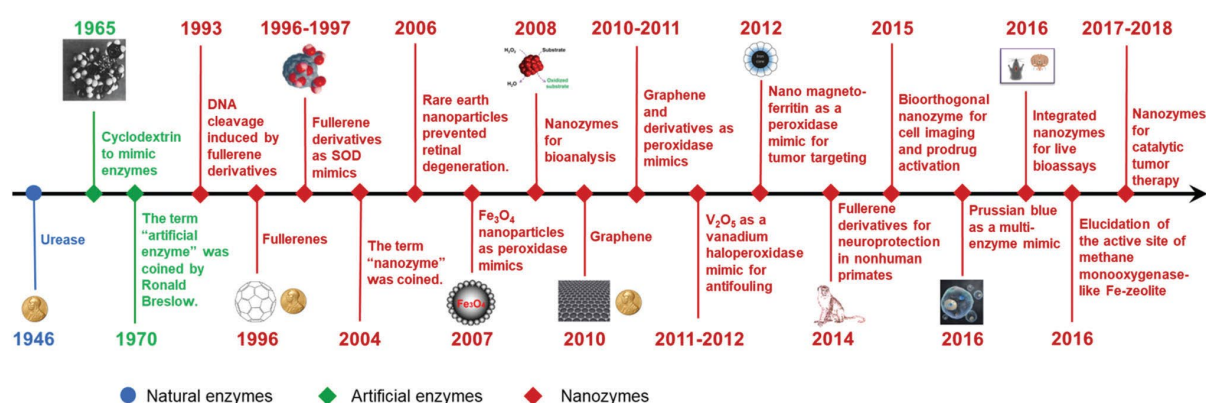


Figure 1.1. Timeline of Nanozyme development. Extracted from Wu *et al.* [30].

1.1.2. Enzyme mechanism and kinetics applied to Nanozymes

As Nanozymes catalyze the same reactions as enzymes and follow their kinetic mechanism, it is essential to understand first some basic concepts of natural enzymes. We will focus this section on oxidoreductase activity as it is the most frequent type of enzymatic mimics found in Nanozymes.

1.1.2.1. Enzyme activities in Nanozymes: oxidoreductases

Enzymes are classified depending on the type of reaction they catalyze. There are oxidoreductases for oxidation-reduction, transferases for reactions involving the transfer of

molecular groups between molecules, hydrolases for hydrolytic cleavage, isomerases for molecular rearrangement, ligases for reactions that bond two molecules and lyases involved in double bond formation and elimination [32]. It has also to be pointed out that some Nanozymes mimic hydrolases such as proteases [33] or nucleases [34]. Among all enzyme reaction types, oxidoreductase activity of Nanozymes is the most studied. Therefore, this section will be focused on oxidoreductase activities: peroxidase, catalase, oxidase, superoxide dismutase (SOD) and sulphite oxidase.

One of the most frequent activities of Nanozymes is peroxidase. Natural peroxidases catalyse reactions involving a peroxide (oxidant) and a second substrate (reductant). They can also be named hydrogen acceptor and donor, respectively. Typically, peroxidase catalyses the oxidation of a substrate with H₂O₂ (**Table 1.1**).

Table 1.1. Reactions catalysed by the most common oxidoreductase mimic Nanozymes. Mⁿ is a metal centre in its reduced form, and Mⁿ⁺¹ is its oxidized form.

| Enzymatic activity | Reaction |
|----------------------|--|
| Peroxidase | $H_2O_2 + AH_2 \rightarrow A + 2H_2O$ |
| Catalase | $2H_2O_2 \rightarrow O_2 + 2H_2O$ |
| Oxidase | $O_2 + AH_2 \rightarrow A + H_2O_2$ $O_2 + 2AH_2 \rightarrow 2A + 2H_2O$ |
| Superoxide Dismutase | $O_2^{\bullet-} + M^{n+1} \rightarrow O_2 + M^n$ $O_2^{\bullet-} + M^n + 2H^+ \rightarrow H_2O_2 + M^{n+1}$ |

Peroxidases naturally participate in many living functions, mainly antioxidant and protective processes. Moreover, horseradish peroxidase (HRP) is a potent tool for many immunological and diagnosis techniques [35]. Nanozymes that show intrinsic peroxidase activity are Fe₃O₄ NPs [29], [36], Pt NPs [37], Co₃O₄ [38], CeO₂ [39] or Au NPs [40]. To assay peroxidase activity in Nanozymes, H₂O₂ and a colourimetric substrate are used. Typically, in the presence of peroxidase activity, Nanozymes will catalyse the oxidation of a molecule by H₂O₂, producing a change of colour. The most common colourimetric substrates are 2,2'-Azino-bis(3-

ethylbenzothiazoline-6-sulfonic acid) (ABTS), o-phenylenediamine (OPD) or 3,3',5,5'-Tetramethylbenzidine (TMB) [41].

Catalase-like activity is another frequent activity found in Nanozymes. Natural catalases accelerate the decomposition of H_2O_2 into H_2O and O_2 (**Table 1.1**). In nature, catalases protect organisms from residual H_2O_2 generated from cellular metabolism [24]. Examples of Nanozymes showing catalase activity are Fe_3O_4 [42], Pt [43] or Co_3O_4 [44] NPs. The most common assay measures the quantity of O_2 generated with an oxygen electrode [44] or the depletion of H_2O_2 at 240 nm [43].

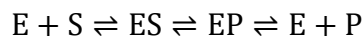
Nanozymes also mimic oxidase activity. Oxidases are enzymes that catalyse the oxidation of a substrate in the presence of O_2 (**Table 1.1**). In nature, oxidases are essential for aerobic organisms as they allow cells to produce energy using O_2 as an oxidant. A notable example is glucose oxidase (GOx) which degrades sugars into simpler metabolites [35]. Some Nanozymes showing peroxidase activity also show oxidase, such as Co_3O_4 NPs modified with Prussian blue [45], leading to the oxidation of colourimetric substrates by O_2 . The assay to determine oxidase activity is the same as for peroxidase, but H_2O_2 is not added in this case. Au NPs, as mentioned before, show glucose oxidase activity [26]. In the case of glucose oxidase, the H_2O_2 generated from glucose oxidation will oxidize TMB (or other colourimetric substrates), producing a change of colour [40].

Superoxidase dismutase (SOD) activity has also been reported in Nanozymes. SOD enzymes catalyse the decomposition of superoxide radicals ($\text{O}_2^{\bullet-}$) into O_2 and H_2O_2 (**Table 1.1**). Indeed, $\text{O}_2^{\bullet-}$ is a by-product of the organism's metabolism and needs to be regulated to avoid cell damage. Most natural superoxide dismutases possess a metal centre (M) working as a reducer or oxidant [35]. Nanozymes showing SOD activity are CeO_2 [46] or Pt NPs [47]. To assess SOD activity, two types of reagents are used: one that produces $\text{O}_2^{\bullet-}$ and another one that detects it through its oxidation leading to the appearance of coloured or fluorescent species. When the Nanozyme is added, $\text{O}_2^{\bullet-}$ is reduced and fewer coloured or fluorescent molecules are produced than without Nanozymes. Thus, comparing the absorbance or fluorescence without Nanozyme and with Nanozyme permits to obtain the SOD-like activity. The most used system is Xanthine/Xanthine oxidase and cytochrome *c*. Xanthine oxidase catalyses xanthine to produce $\text{O}_2^{\bullet-}$, which will cause the oxidation of cytochrome *c* and a concomitant change of colour. When adding SOD-Nanozyme to the system, the change of colour is weaker [48].

1.1.2.2. Kinetics and catalytic mechanism of Nanozymes

One feature of Nanozymes is that they follow the same kinetic mechanism, as natural enzymes: it is a compulsory criterion for a nanomaterial to be a Nanozyme [24]. The natural enzyme (E) binds to the substrate (S), creating the enzyme-substrate (ES) complex. Then, through catalytic reactions, S is converted into the product (P), leading to the EP complex, and finally, P is released from the complex enzyme-product (EP) (**Equation 1.1**). Catalytic reactions mediated by enzymes are saturable. Initially, the velocity increases linearly with the increasing substrate concentration. However, the enzyme saturates when substrate concentration is relatively high [35].

Equation 1.1. Michaelis-Menten mechanism of a reaction catalysed by an enzyme with a single substrate.



Although the Michaelis-Menten model is based on enzymes with one active site, which is not valid for Nanozymes, most of the Nanozymes known to date follow Michaelis-Menten kinetics except for a few exceptions [49]. The kinetic assay to determine if a Nanozyme follows Michaelis-Menten kinetics consists in measuring reaction kinetics as a function of the substrate's concentration. If two or more substrates are involved, like for instance in the case of peroxidases, one substrate concentration will be varied, and those of the others will be kept constant [24].

The Michaelis-Menten model, used to determine the enzyme kinetics, is based on the enzyme saturation at high substrate concentration, reaching the maximum velocity, V_{\max} . As seen in **Figure 1.2**, the substrate concentration at which velocity is half of the maximum velocity ($V_{\max}/2$) is called the Michaelis-Menten constant (K_m) [35].

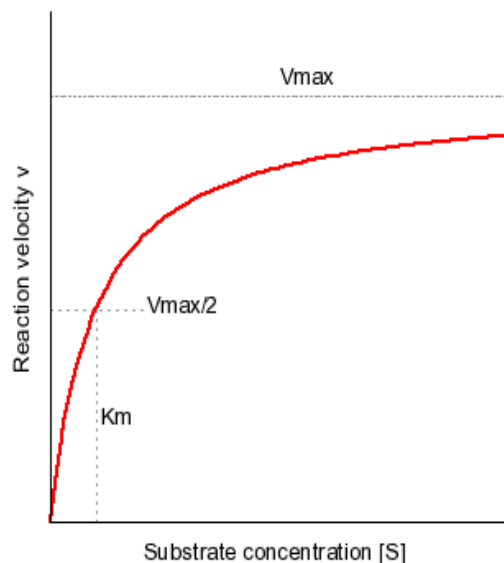


Figure 1.2. Michaelis-Menten graph. Velocity of a reaction catalysed by an enzyme as a function of substrate concentration. Extracted from Nelson *et al.* [35].

The equation on which is based Michaelis-Menten kinetics links the velocity of the reaction (v), the substrate concentration ($[S]$), the maximum velocity (V_{\max}) and K_m (**Equation 1.2**). Initially, the reaction follows first-order kinetics as velocity varies linearly, but the model approximates zero-order kinetics as enzyme saturation is reached. At this point, the maximum number of molecules converted into product per enzyme molecule and per second, called the turnover number (K_{cat}), can be obtained. Moreover, K_m provides qualitative information related to the reaction mechanism: the affinity to the substrate. Low K_m values mean high affinity to a given substrate, while high K_m value indicates low affinity. The previous values give some information about the mechanism of the reaction. For instance, if K_m for H_2O_2 is lower than for TMB in peroxidase assays, the Nanozyme has higher affinity for the former [5]. Another significant coefficient is K_{eff} , the catalytic efficiency: a high K_{eff} value means that an enzyme quickly transforms a substrate into a product (see **Equation 1.2**) [24], [32].

Equation 1.2. Michaelis-Menten kinetics equations: " v " is the velocity of the reaction, " V_{\max} " is the maximum velocity, $[S]$ is the free substrate concentration, " K_m " is the Michaelis-Menten constant, " K_{cat} " is the maximum number of substrate molecules transformed to product, per enzyme and per second, $[E]$ is the enzyme concentration, and K_{eff} is the catalytic efficiency.

$$v = \frac{V_{\max} \cdot [S]}{K_m + [S]}; K_{\text{cat}} = \frac{V_{\max}}{[E]}; K_{\text{eff}} = \frac{K_{\text{cat}}}{K_m}$$

1.1.2.3. Specificity for the catalytic mechanism of Nanozymes

The Michaelis-Menten is a model well suited for systems in which there is a binding site and an active site. Indeed, for a natural enzyme, the substrate binds to the enzyme in the binding site, which may prompt a conformational change of the amino acid chain and traps the substrate in the active site. However, most Nanozymes do not have this flexibility, meaning that the binding and active sites have the same conformation. Thus, the reaction is supposed to be controlled by other parameters.

As mentioned, oxidoreductases are the most common Nanozymes found in the literature. Accordingly, the following discussion will be focused on them. Many different catalytic mechanisms have been proposed for Nanozymes. For instance, in metal oxide Nanozymes, some mechanistic studies have concluded that the reaction is based on a Fenton process for iron-containing Nanozymes (Fe_3O_4 , Fe_2O_3) [50], which means that metal salts initiate the reaction. As another example, in ceria Nanozymes, the leading factor is the oxygen vacancies that favour the adsorption and cleavage of H_2O_2 or O_2 [51]. Mainly, the mechanism requires a valence change of the metal [52]. In metal Nanozymes (Au NPs, Pt NPs, Pd NPs), it is believed that the adsorption of oxygen-containing species onto the metal surface causes their cleavage. Subsequently, non-bonded O atoms subtract H from the substrate (TMB), causing its oxidation [53]–[55]. However, the mechanism is not fully understood and clear. Moreover, many factors can modulate this activity.

In the scope of this thesis, we will now focus on noble metal nanoparticles as Nanozymes.

1.1.3. Noble metal nanoparticles as Nanozymes

Noble metal NPs (in the following, metal NPs will refer to noble metal NPs) have proven their enzyme-mimic properties. Among their advantages are their simple synthesis process and the ease of surface modification which allows a careful tune of their enzyme-mimic properties [56]. Moreover, they have shown high stability and a variety of enzymatic activities such as peroxidase, oxidase, catalase, or superoxide dismutase. Natural enzymes' catalytic activity can be modified by various external factors: pH, temperature, molecules (cofactors, inhibitors) or metal ions. However, modifying the intrinsic structure of the enzyme may cause the loss of its specificity and/or catalytic activity [35]. In the literature, metal Nanozymes' catalytic activity can be modified in many diverse ways (**Figure 1.3**). As for natural enzymes, a change in the

pH, temperature or the presence of metallic ions allows to tune their catalytic activity, in addition to modifications in the structure and morphology of metal Nanozymes. Thus, their size, composition, surface modification or combination with other materials can be used to modulate their enzymatic activity. Moreover, their unique optical properties at the nanoscale allow modifying their activity under light excitation.

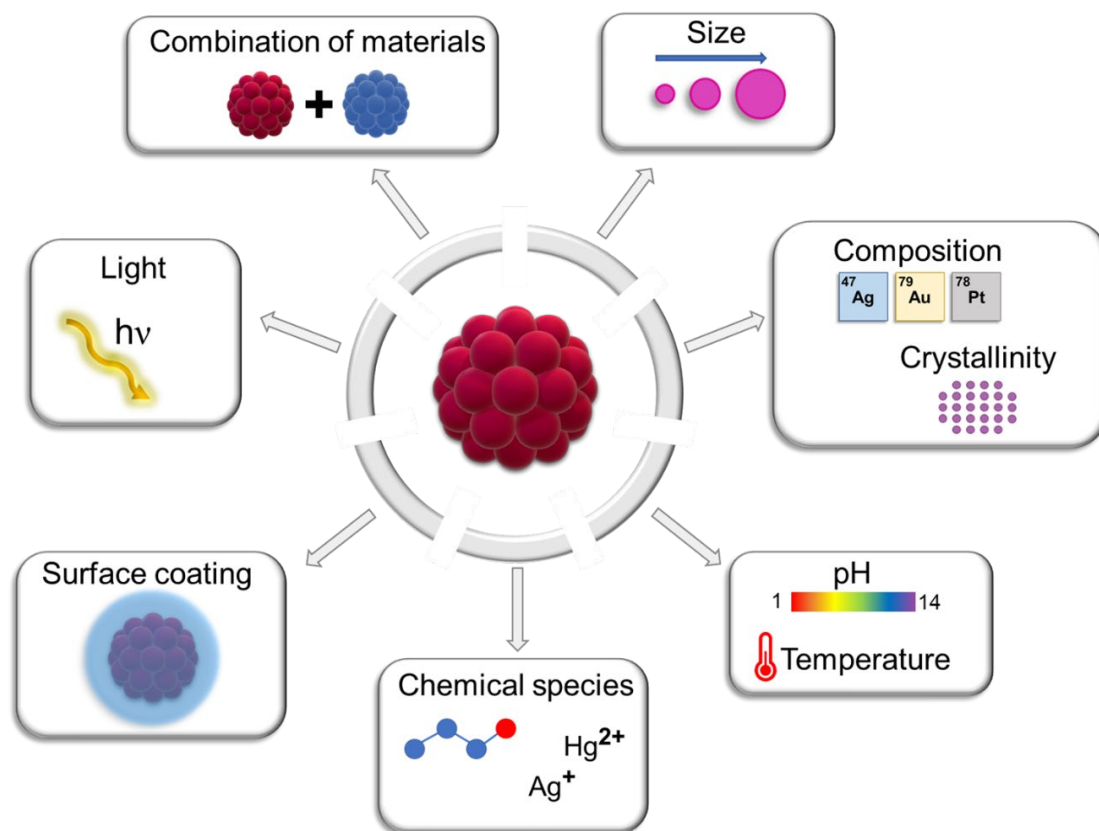


Figure 1.3. Different ways for modifying metal Nanozyme's enzymatic activity.

1.1.3.1. Size

Generally, an efficient catalyst is characterized by a large specific surface area allowing more interactions with the surrounding molecules. Reducing their size has proven to increase the catalytic activity of different Nanozymes [30]. For instance, Au NPs glucose oxidase mimics were tested for different NPs diameters (13, 20, 30, and 50 nm). Their ability to oxidize glucose decreased with increasing diameter [57]. The size-dependent catalytic activity was better evidenced for Au ultra-small nanoparticles (3-5 nm) used as catalyzers in various reactions [9]. Similarly, the oxidase activity of Pt nanoclusters (4 atoms of Pt), and Pt NPs of 5 nm and 30 nm, decreased with the increasing size. The peroxidase-like activity of apoferritin-paired gold

clusters was markedly higher when the size was below 2 nm compared to 6 and 20 nm [58]. The explanation proposed for this increase in activity was that the surface atoms and therefore the active sites increased when NP size decreased [59]. However, below 5 nm decreasing the size can be deleterious for catalytic activity [60], [61].

1.1.3.2. Composition and crystallinity

The composition of the metal Nanozyme can drastically change its properties. Au NPs show intrinsic glucose oxidase activity, which has not been reported in Pt, Pd, Cu or Ag NPs [24]. The studies of (111)-faceted Au, Ag, Pt and Pd Nanozymes show that catalase and peroxidase activities rank as follows: Pd (111) > Pt (111) > Ag (111) > Au (111) [54]. These findings are in agreement with another study in which oxidase activity ranking is Pd (111) > Pt (111) >> Au (111), Ag (111) [62].

Another feature that has proven to be potent parameters for customizing the catalytic activity of the nanoparticles having Nanozyme properties is the crystallinity. Atomic and crystal facet modification can significantly increase or decrease their activity. For instance, Au Nanozymes with (211) crystal facets showed oxidase activity, but for (110) and (111) facets, it was thermodynamically and kinetically disfavored [62]. In a similar study, peroxidase and catalase activities of the (111) facets were less advantageous than for the (110) and (211) facets [54]. An explanation for this may be that the high surface energy of (211) facets presenting more Au atoms with a lower coordination number than (111) facets, facilitates the adsorption of oxygen [24]. These findings are in contrast with the ones obtained for Pd nanocrystals. Theoretical and practical results showed that (111)-faceted Pd nano-octahedrons (lower surface energy) had greater catalase and superoxide dismutase activity than (100)-faceted Pd nano-cubes (higher surface energy) [55].

1.1.3.3. pH and temperature

Metal Nanozymes have pH-dependent catalytic activities. For Pt Nanozymes, peroxidase seems to be favored in acidic pH, whereas catalase activity increases in neutral and alkaline pH [63]. Later it was reported for Au, Ag and Pd as well and confirmed for Pt Nanozyme. In the same work, theoretical studies revealed that pH-switchability strongly depends on hydroxyl

anions (OH^-) pre-adsorption on the surface of the metals, which is only favored under basic pH conditions [54].

Temperature is an essential factor in reaction rate. In Ag Nanozymes, the peroxidase activity increased when heating up to 40 °C and started declining above this temperature [5]. Similarly, Au peroxidase Nanozymes reached their maximum activity at 37 °C [64].

1.1.3.4. Presence of other chemical species

The presence of some chemical species can inhibit or enhance the catalytic activity of the Nanozymes. For instance, Hg^{2+} inhibited the peroxidase activity of both BSA-Pt NPs and BSA-Au clusters [65], [66]. Ag^+ ions quenched BSA-Au and glutathione-functionalized Pd Nanozyme's peroxidase activity [67], [68]. The leading cause seems to be the interaction of Hg^{2+} or Ag^+ with the metal ions in the Nanozymes [65]–[68]. Interestingly, due to alloy formation on the surface, citrate-Au NPs peroxidase activity was increased by Ag^+ , Bi^{3+} and Hg^{2+} [69]. Metal ions are not the only substances that can modify the activity of Nanozymes. ADP (adenosine diphosphate) and ATP (adenosine triphosphate) specifically increased the Au NPs peroxidase activity compared to other biologically present anions (sulfate, carbonate and phosphate) [70].

1.1.3.5. Surface coating

As mentioned before, ultra-small Nanozymes (< 5 nm) generally show the highest catalytic activity. However, smaller nanomaterials lose colloidal stability faster, aggregating, reducing, and even losing their activity [71], [72]. Colloidal stability can be ensured with adapted surface coating. One work evidenced this for Pt NPs. Compared to the naked Pt NPs, chitosan functionalization enhanced catalytic activity. However, oxidase-activity was reduced with citrate-capped Pt NPs and suppressed with BSA or lysozyme coating [73]. In another work, cysteamine-modified Au NPs peroxidase activity was increased by 7-fold compared to citrate-capped ones [74].

The functionalization of Nanozymes with polymers in which 3D configuration varies with temperature allows further catalytic activity modulation. The working principle of this functionalization leads to a temperature-dependent state in which substrates cannot diffuse through Nanozymes, provoking the quenching of their catalytic activity [75]. Moreover, some

polymers are both responsive to temperature and pH, allowing enzyme mimics to be activated or deactivated in Au Nanozymes [76].

1.1.3.6. Light

Metal nanoparticles present an extra property: they can interact with light in a process called Localized Surface Plasmon Resonance (LSPR). Briefly, LSPR is the phenomenon in which the electrical field of light, an electromagnetic wave, causes a concerted oscillation of a metal's free electrons. Indeed, when incident light's wavelength is one order of magnitude higher than the metal nanoparticle diameter, the electric field of the electromagnetic wave polarizes the nanoparticles. The displacement of the electron cloud from its original position produces a Coulombic attraction between nuclei and electrons, provoking a coherent oscillation of the conduction electrons. (**Figure 1.4**). When the incident electromagnetic wave frequency matches the oscillation frequency, a strong absorption of the incident light is observed, which is called the LSPR frequency. The absorbed light is in the UV-Vis region for noble metal nanoparticles (Ag, Au, or Pt NPs). As the size of nanoparticles increases, the wavelength of the oscillation shifts to lower energies, *i.e.*, higher wavelengths [77], [78]. Additionally, the LSPR effect is associated with the apparition of a very intense electric field (plasmonic near-field) at the surface of metal nanoparticles in the direction of incident light polarization [79].

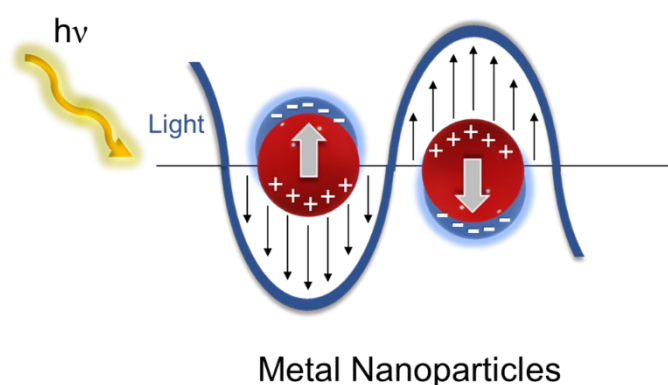


Figure 1.4. LSPR effect for spherical metal nanoparticles.

Consequently, using light, one can originate electrical field hot spots, generating hot nanoparticle electrons to enhance catalytic activity. Au NPs of 15 nm showed enhanced catalytic activity upon illumination with visible light close to their LSPR at 521 nm. It was also

demonstrated that changing the wavelength and the intensity of the light can modulate their catalytic activity [80].

Using the LSPR effect is not the only approach to using light as an external stimulus to increase catalytic activity. A light-sensitive molecule system composed of cyclodextrin and azobenzene was used to functionalize metal nanoparticles. Irradiating with UV light makes it possible to isomerize azobenzene, producing the catalysts' release. Then to inactivate the system, visible light was used [81], [82].

1.1.3.7. Combination of materials

Combining metal Nanozymes with other materials to produce hybrid nanoparticles or alloys may confer additional properties and regulate their catalytic activity. Combining two metals can lead to higher activity. For instance, Xu and colleagues synthesized Au/Cu nanorods with peroxidase mimics. The hybrid nanorods presented increased high-index facets in Au, which enhanced catalytic activity [83]. Another example is AgPd hybrid nanoparticles, which showed a significant improvement in the catalytic activity of Ag NPs [84]. In another work, the control of Au content in AuPt alloy NPs proved to be a potent tool to modulate peroxidase and oxidase activity; the highest the ratio of Pt/Au, the highest catalytic activity was obtained [85]. A combination of metals is not the only strategy. Depositing Au NPs onto carbon nanotubes increased their solubility in water and led to a synergetic peroxidase-mimic effect compared to the separated counterparts [86]. Metal-organic frameworks (MOFs) are also known to possess enzyme mimics. Linking Pt NPs to Fe-MOF increased the stability, and peroxidase activity of Fe-MOF [87]. The combination of metal NPs with metal oxides has gained particular attention in the Nanozyme field due to the possibility of having a synergetic catalytic effect between the two materials [88]. Due to the importance of this result to our work, it will be discussed in more detail in the next section (1.1.4).

1.1.4. Metal nanoparticles on metal oxides as Nanozymes

Combining two materials allows one to merge their properties and eventually get extra benefits from a synergetic effect [89]. Classically, metals dispersed over metal oxides are a well-known system to provide better-performing catalysts. The combination of metal and metal oxide in Nanozymes has also been reported, yet the mechanisms of the synergetic effect are still poorly

reported in the literature. First, we introduce the topic with the classical metal/metal oxide catalysts, *i.e.*, the dispersion of metal particles in bulk metal oxides and the theory behind their improved catalytic properties in redox reactions. We further discuss the dispersion of metal nanoparticles onto metal oxide nanoparticles as catalysts and their use in photocatalysis. Finally, we review the current literature on Nanozyme activity of hybrid nanoparticles and the possible mechanisms of improved enzymatic activity.

1.1.4.1. Classic metal/metal oxide catalysts mechanisms

In catalytic chemistry, the synergetic effects observed from the deposition of metal nanoparticles onto the surface of bulk oxides have been widely studied. In 1989, Haruta and co-workers reported on the catalytic activities of uniformly dispersed gold particles (<10 nm) on the surface of transition metal oxides. Their results showed that Au/ α -Fe₂O₃, Au/Co₃O₄ and Au/NiO significantly increased carbon monoxide and dihydrogen oxidation [90]. Schmal *et al.* also reported an increase in the selectivity for olefin dehydrogenation with Pt/Nb₂O₅ catalysts [91]. Since then, many other works have studied the enhancement in the catalytic activity of noble metals deposited onto oxides for formaldehyde oxidation [92], gas sensing by CO oxidation [93], decomposition of volatile organic compounds (VOCs) [94] or dihydrogen production [95].

1.1.4.2. The metal-semiconductor (metal oxide) junction in catalysis

Two underlying phenomena exist in metal-semiconductor (metal oxide) junctions which may influence catalysis. Initially, in a classic catalyst, the deposition of a highly dispersed metal onto a metal oxide creates a potential barrier, producing the bending of the conduction and valence band to equilibrate the Fermi level of both materials (**Figure 1.5**). The charge transfer then depends on the energies of the materials' work function. The work function of a material is the energy required to release an electron from its surface, and it is defined as the energy difference between the vacuum and the Fermi level. If the work function of the metal (ϕ_m) is higher than the one of the semiconductors (ϕ_s) (*i.e.* Fermi level of the semiconductor is higher than the one of the metal), the transfer occurs from the semiconductor (SC) to the metal, and it is called a Schottky junction. At the interface, a Schottky barrier (ϕ_{SB}) is created, which corresponds to the metal's work function (ϕ_m) minus the electron affinity of the semiconductor (χ_s) (the energy difference between the vacuum and the minimum of the conduction band). On

the contrary, if ϕ_m is smaller than ϕ_s (*i.e.* Fermi level of the metal higher than the one of the oxide), the transfer of electrons occurs from the metal to the oxide, and an Ohmic contact is obtained [96]. In this case, there is no Schottky barrier formation. The change in energy of the bands is called band bending (V_{BB}).

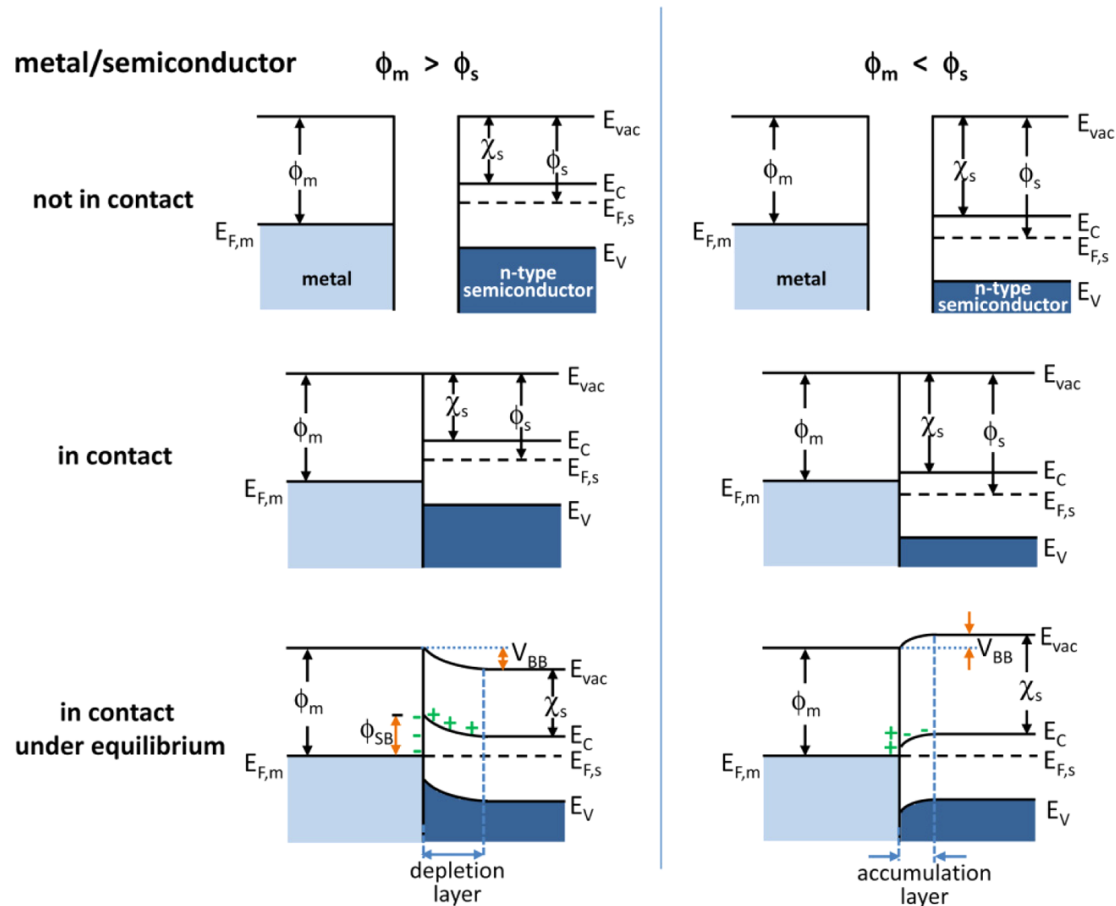


Figure 1.5 Energy level diagram of a metal-semiconductor junction at different stages of contact: not in contact, in contact and at equilibrium in Schottky junction (left) and Ohmic contact (right). Φ_m , metal work function; ϕ_s , semiconductor work function; χ_s , the electron affinity of the semiconductor; E_{vac} , vacuum energy; E_c minimum energy of the semiconductor conduction band; E_v , maximum energy of the semiconductor valence band; $E_{F,m}$, Fermi level of the metal and $E_{F,s}$, Fermi level of the semiconductor; ϕ_{SB} , Schottky barrier; V_{BB} , valence band bending. Extracted from Zhang and Yates [97].

Charge transfer is not the only process involved in metal-metal oxide junctions. Oxygen is released to increase the contact zone, creating oxygen vacancies in the metal oxide close to the interface. The oxygen vacancy creation requires the transfer of two electrons from the semiconductor's valence band (SC) to its conduction band. This process is favoured by the

presence of the metal, which helps stabilize these vacancies by equilibrating their Fermi levels [98]. Thus, the interfacial area is a hot point on the hybrid material, where charge and defects accumulate.

Theoretical works have also proven oxygen vacancies creation. Highly investigated Au/TiO₂ systems for CO oxidation show that O₂ molecule deposits preferentially onto oxygen vacancies near the interface between the two materials, weakening the bond and thus favouring the oxidation [99], [100]. Experimental studies also support these results. Huang *et al.* explained that the enhanced catalytic activity of Pd/TiO₂ catalysts for formaldehyde oxidation eventuated from the defects created by the noble metal onto the surface of the oxide support, favouring the O₂ uptake and dissociation [101]. Indeed, other studies showed that the immobilization of gold clusters on the oxide allows more *d* states of low-coordinated gold atoms to be available, which can enhance the uptake of O₂ [102], [103]. Similarly, H₂O₂ has shown an affinity for these vacancies in different oxides [51].

These above phenomena contribute in two ways to accelerate reactions: the charge transfer process contributes to the reduction of the activation energy and the creation of active sites for the adsorption of reactants in the metal and the metal oxide, which were not present in the separated counterparts [104].

1.1.4.3. Hybrid Nanoparticles: Effect of Metal/Metal Oxide Junctions in Classic Redox Catalysis

Recently, the synergetic effect resulting from the combination of metal nanoparticles with metal oxide nanomaterials has attracted particular attention. Reducing the size of the metal oxide to the nanoscale outcomes in the exponential increase of low-coordinated surface atoms and a decrease in the energetic cost of creating oxygen vacancies. This effect is even more accentuated with the addition of a metal [105]. The measurement of the catalytic activity of metal-metal oxide hybrids has shown an improved catalytic activity for the hybrid nanoparticles, particularly for redox reactions [106]–[108].

Charge transfer and oxygen vacancy creation in metal NPs deposited onto metal oxide support, or metal-metal oxide hybrid nanoparticles, have been theoretically and experimentally tested in classic redox catalysis.

The charge transfer produced by metal-metal oxide junction has been verified through *ab initio* studies in which different metals were coupled with MgO [109]. Density functional theory (DFT) also shows charge transfer and Schottky barrier formation between MgO/Ag and Au/TiO₂ [110], [111]. Experimentally, the charge transfer between metal/metal oxide junctions can be studied by measuring specific physical parameters. Among them, we can cite the surface plasmon shift of nanoparticles, the binding energy shift, or the redox potential. Gold and silver nanoparticles present LSPR in the UV-Vis region; hence the plasmon shift can be easily studied (**section 1.1.3.6**). In some works, a charge transfer happens from the metal to the oxide, resulting in a red shift of LSPR in these nanoparticles, indicating a decrease in the electronic population of the metal nanoparticle [112]–[114]. In the prior work of Zheng *et al.*, the gold's electron density decrease in Fe₃O₄/Au nanoparticles is also supported by a redshift [113]. Indeed, the free electrons of gold can compensate for the charges of the polarized interface. The deposition of Au NPs onto MnO₂ NPs also produced a redshift, and it was more accentuated if the metal oxide was Fe₃O₄ [115]. In a recent work by Liu *et al.*, XPS results strengthen this theory due to the shift of Fe(2p) peak to lower binding energies and Au(4f) to higher binding energies, indicating the loss of electron density of the metal [112]. Pt/Fe₃O₄ presents different results regarding electron transfer. In the report of Buck *et al.*, the Ag/Pt/Fe₃O₄ decrease of XPS binding energy for the platinum elucidates an increase in its electron density [116]. In Wang *et al.* work, the deposition of Pt NPs onto Fe₃O₄ caused sharpened peaks in XPS, and a potential redox shift was observed, decreasing the redox potential of the Fe(II)/Fe(III) redox couple in cyclic voltammetry measurements. This was explained by an electron transfer from Fe to Pt [117].

Oxygen vacancy creation is shown in theoretical studies. Gold nanoparticles deposited on nanoparticle oxide substrates, such as ceria, possess higher catalytic performance as the reaction occurs at the vacancies created by the noble metal onto the crystalline facets of ceria [118].

1.1.4.4. Hybrid nanoparticles: Metal/Metal-Oxide Junctions Effect on Photocatalysis

The synergetic effect is also widely used in classic photocatalysis. Light is a potent modulator of catalytic activity in metal oxide thanks to electron-hole separation [119]. When exciting a metal oxide with photons of the same or more energy than its band gap, it provokes the promotion of electrons from the valence band to the conduction band, which creates a hole (h^+ ,

positive charge) in the conduction band and an electron (e^- , negative charge) in the valence band. Although this favours redox reactions, a significant proportion of electron-hole pairs recombine, leading to energy dissipation by heat generation or light emission (**Figure 1.6A**) [120]. One way of overcoming this is to depose a metal on the oxide. Two phenomena can happen depending on whether the light energy is of the same or higher energy than the semiconductor band gap or if it corresponds to the plasmon band of metal. The first one causes electron-hole separation in the semiconductor and electron transfer to the metal in metal-metal oxide junctions (**Figure 1.6B**). The second one (**Figure 1.6C**) produces a collective excitation of the electrons, provoking hot electrons with higher energy than the Schottky barrier (ϕ_{SB}) to be transferred to the conduction band (hot electron injection), favouring oxidation reactions on the metal and reduction reactions on the semiconductor [97]. In the first scenario (**Figure 1.6B**), oxidation is favoured by the h^+ in the semiconductor and reduction near the metal nanoparticle by the hot electrons. The opposite scenario (**Figure 1.6C**), causes the reduction happening closer to the semiconductor and the oxidation near the metal.

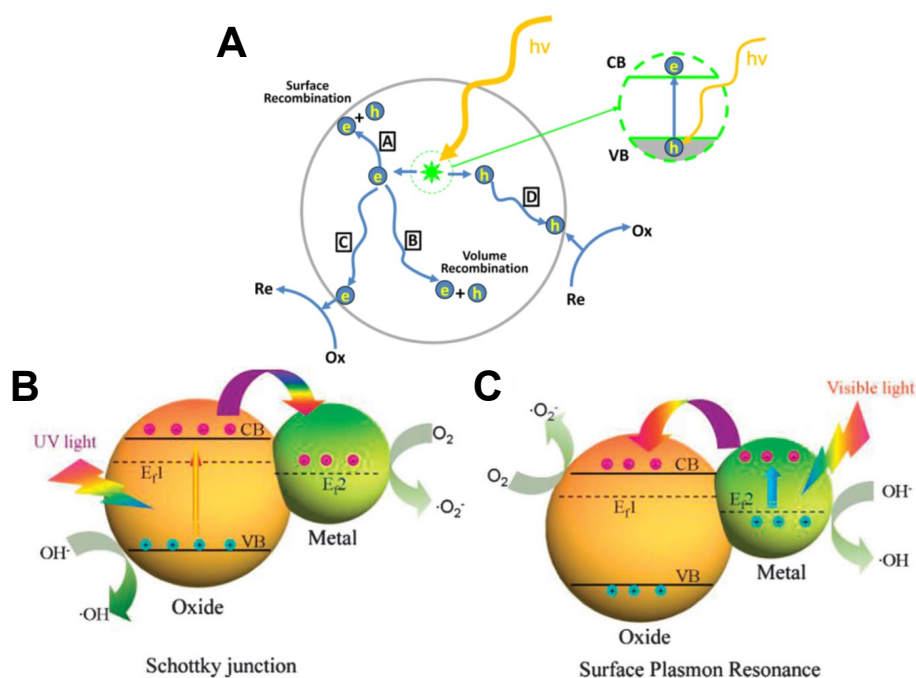


Figure 1.6. (A) Electron-hole recombination processes in semiconductor particles upon light excitation. Extracted from Zhang and Yates [97]. (B) Schematic diagram of metal deposition induced charge separation due to the creation of a Schottky barrier between metal and semiconductor. (C) Schematic diagram of plasmon-induced charge separation on the semiconductor-metal junction under light excitation and the possible redox reactions accompanying it. B and C are extracted from Jing *et al.* [121].

1.1.4.5. Synergetic effect in Metal/Metal Oxide hybrid nanoparticles for enhanced Nanozyme activity

In the previous sections, we reviewed how metal nanoparticles/metal oxide junctions can impact redox reactions. The synergetic effects arise from charge transfer and/or oxygen vacancies creation. These two mechanisms are amplified when using hybrid nanoparticles and can be influenced by photons of specific energy. The field of Nanozymes has also attempted to exploit this synergetic effect by combining two materials. Enzyme-mimicking hybrid nanoparticles (hybrid Nanozymes) have been reported with different oxidoreductase mimics. Moreover, several authors have proposed mechanisms for the better catalytic performance of hybrid nanozymes. In the following sections, we discuss the different oxidoreductase mimics and the proposed mechanisms.

1.1.4.6. Peroxidase and Oxidase Hybrid Nanozymes

Peroxidases are one of the most reported activities. $\text{Fe}_3\text{O}_4/\text{Au}$ and $\text{Fe}_3\text{O}_4/\text{PtPd}$ heterodimers have better peroxidase-mimics than their separated counterparts and a simple mixture of them, which proves the requirement of a chemical link between the materials [88], [122]. Hybrid nanotubes composed of Pd NPs and CeO_2 nanotubes also present a synergetic combination in peroxidase mimics [123]. It is worth mentioning that even though the synergetic effect is not evidenced, hybrid Nanozyme composed of Fe_3O_4 and Pt with peroxidase mimics have surpassed the activity of Horseradish Peroxidase [124]. However, these results should be read carefully as the characterization of the active sites present in Nanozymes is not well established and makes difficult the comparison between natural enzymes and Nanozymes [125].

In peroxidase and oxidase, the most accepted mechanism proposition is the ROS formation and subsequent oxidation of the substrate (**Figure 1.7**), whereas others state the direct oxidation on the surface of the nanoparticles [126], [127]. Liu *et al.* suggested that the $\text{Au}/\text{Co}_3\text{O}_4\text{-CeO}_x$ nanocomposite hybrids with peroxidase mimics could generate $\bullet\text{OH}$ radicals rapidly and stabilize them, which increased the oxidation rate of TMB [128]. Indeed, H_2O_2 is well-known for its affinity for oxygen vacancies in different oxides [51], [129]. Different explanations for this are found across the literature. A study on $\text{Fe}_3\text{O}_4/\text{Au}$ nanoparticles proposed that the cleavage of H-O-O-H structure generated two $\bullet\text{OH}$, systems which were stabilized by the interface created between the two materials [130]. Another work argued that electron-deficient gold nanoparticles stabilised the $\bullet\text{OH}$ radicals [64]. $\bullet\text{OH}$, radicals are not the only ROS

produced by Nanozymes. Pt/C₃O₄ nanoflowers converted dissolved O₂ into singlet oxygen (¹O₂) and superoxide radical (O₂^{•-}) in oxidase mimics. The same hybrid nanoparticles with peroxidase mimics produced [•]OH radicals and ¹O₂ [131].

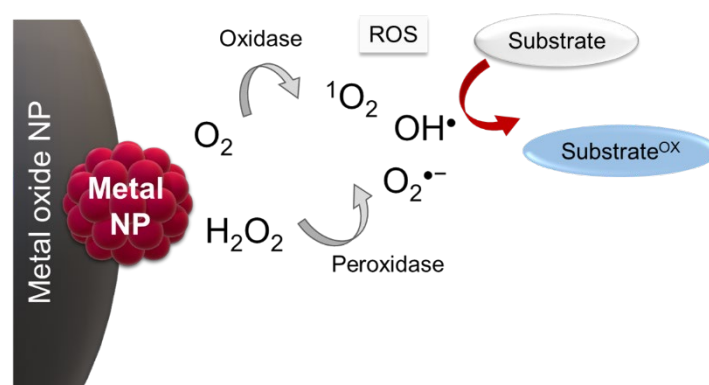


Figure 1.7. Peroxidase and oxidase hybrid Nanozyme ROS-mediated mechanism.

ROS formation is not the only explanation for substrate oxidation [132]. For instance, in Au/CeO₂ core-shell nanoparticles, there was no evidence of the formation of hydroxyl radicals in peroxidase mimics, suggesting that the proximity of the two materials promoted the H₂O₂/H₂O reaction instead of the usual H₂O₂/OH[•] pathway [133]. The findings agree with the results observed in PtNPs@MnO₂ hybrid nanoparticles, where electron spin resonance shows no ROS production for oxidase mimics. Instead, the mechanism is closer to the natural enzyme mechanism: dissolved oxygen and TMB are adsorbed onto the surface. O₂ is the electron acceptor, and TMB is the donor, resulting in the formation of H₂O [127].

1.1.4.7. Catalase Hybrid Nanozymes

Catalase activity was also enhanced through a synergetic effect. For instance, Pd nanosheets modified with TiO₂ NPs showed higher O₂ production in the presence of H₂O₂ than the Pd nanosheets or TiO₂ NPs separated and their simple mixture. In this work, DFT calculations lead to the conclusion that the H₂O₂ decomposition is more thermodynamically and kinetically favourable in the hybrids [134]. A similar effect was observed with PtFe@Fe₃O₄ with both peroxidase and catalase [135]. Au/CeO₂ core-shell nanoparticles showed multienzyme activity: peroxidase, superoxide dismutase and catalase. Peroxidase and superoxide dismutase increased compared to the counterparts, and catalase activity was an exclusive feature obtained from the combination of the materials [133].

Mechanistic studies of catalase activity focus on how H₂O₂ molecules are converted into O₂ and H₂O. This can be done through heterolytic cleavage, *i.e.* H-O bond breaks, or through homolytic cleavage, *i.e.* O-O bond breaks [136]. In the work of Chongchong *et al.*, theoretical *ab initio* studies and XPS measurements show that Pd@TiO₂ hybrid nanoparticles' negative charge distribution is concentrated in Pd nanosheets, whereas TiO₂ surfaces present a positive charge. Further calculations showed that the H₂O₂ cleavage proceeds through homolytic cleavage, and it could happen in the Pd or the TiO₂. The two OH* (* means activated) are transformed into H₂O* and O*, and a second H₂O₂ molecule adsorbs. HO* and HOO* are formed, and O₂ and H₂O are released through hydrogen transfers. Although the mechanism is similar for Pd nanosheets and Pd@TiO₂, the latter shows considerable stabilization and heat release, prompted by the material combination (**Figure 1.8**) [134]. In another work, XPS measurements permitted the elucidation of the mechanism for PtFe@Fe₃O₄ catalase mimics based on the charge transfer between the materials. In this case, the cleavage of the H₂O₂ occurred both heterolytically and homolytically [135].

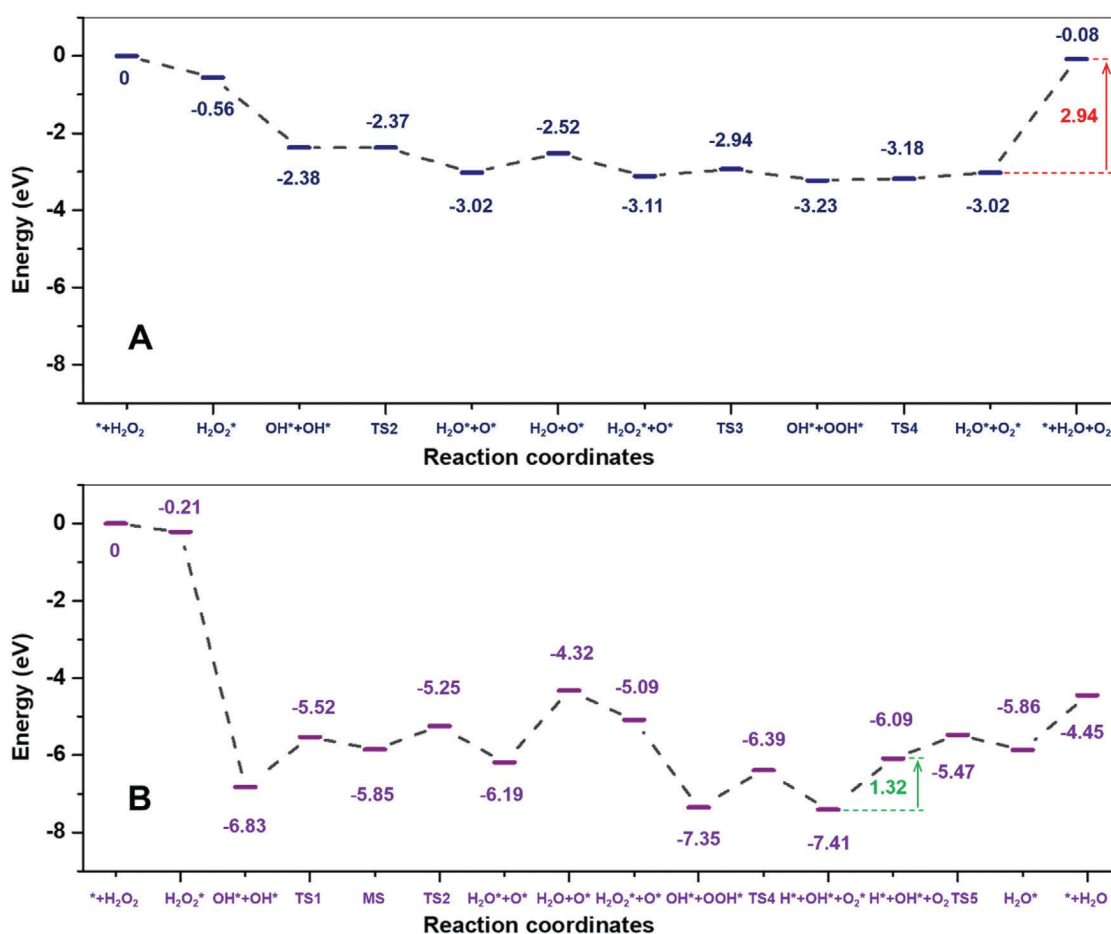


Figure 1.8. Catalase mimics energy diagrams of each reaction step in A) Pd Nanosheets and B) Pd@TiO₂. Extracted from Chongchong Wang *et al.* [134].

1.1.4.8. Superoxide Dismutase Hybrid Nanozymes

Superoxide dismutase exclusive hybrid Nanozymes have been little reported to our knowledge. Ag/CeO₂ nanozyme showed superoxide dismutase as the metal promoted the presence of oxygen vacancies in CeO₂, arising from the Ag-facilitated reduction of Ce⁴⁺ into Ce³⁺ [137]. As mentioned before, Au/CeO₂ core-shell nanoparticles showed catalase, peroxidase and superoxide [133]. Likewise, Pt/Co₃O₄ nanoflowers showed different enzyme mimics depending on the pH: peroxidase, oxidase, catalase, and superoxide dismutase [131]. The presence of bivalent metal cations in CeO₂ and Co₃O₄ appears to be a key feature for SOD-mimics. In addition, the O₂^{•-} decomposition strongly depends on the pH and does not occur at a pH lower than 6. pH-dependence has also been proven in previous works in which Pt NPs ROS scavenging varies with the pH: O₂^{•-} dismutation seems to happen only at neutral pH [138], [139]. SOD-mimicking Nanozymes seem to have a convergence in the type of metal oxide.

A recent work provides insights into the mechanism [140]. Superoxide radicals can decompose through two reactions whose products are O₂ or H₂O₂, with two different potentials. The mechanism leading to one or another depends on the Fermi level position in metal nanomaterials and the conduction band and valence band position in semiconductors.

1.1.4.9. Hybrid Nanozymes light interaction

As mentioned in the previous section (1.1.4.1.3), light interacts with metal oxide and metal nanoparticles and modulates photocatalysis. This has been exploited for Nanozyme applications, but metal-metal oxide junctions (metal-semiconductor) have been little investigated. Some investigations focus on the excitation of the metal to produce hot electrons. For instance, Au@CeO₂ hybrid Nanozyme showed enhanced peroxidase mimics upon excitation with Near Infrared light (NIR). The proposed mechanism was based on the combined effects of photothermal heating and hot electron injection from Au to CeO₂. This latter effect increased the Ce³⁺/Ce⁴⁺ ratio, enhancing ROS production and peroxidase mimics [141]. We can also cite a previously mentioned work, in which PtFe@Fe₃O₄ showed enhanced catalase activity by stimulation with NIR laser, thanks to accelerated excitation of electron-hole pairs in Fe₃O₄ [135]. On the other hand, the light excitation corresponding to the band gap energy has been little investigated in hybrid Nanozymes. SOD-mimicking Ag/CeO₂ Nanozymes

presented a red-shifted band gap compared to CeO₂ alone. This allowed the excitation with a visible-range laser, enhancing the performance of the Nanozymes [137].

1.1.5. Synthesis and characterization methods of Metal/Metal Oxide Nanozymes

Metal/Metal Oxide Nanozymes can be classified by their catalytic activity. Most studies report their peroxidase-mimicking properties, and few publications report their oxidase-like, catalase-like and superoxide-like activities. Nevertheless, there are many different structures in which noble metal and metal oxide are combined, from dumbbell-like structures (DBNPs), Janus-shaped (JNPs), core-shell (CSNPs), and seed decoration (SDNPs), see **Figure 1.9**. Thus, in this section, we chose to present the nanomaterials classified by their structure and the different synthesis methods for each one.

Synthesis of these nanomaterials is mainly characterized by a material's growth on preformed seeds. DBNPs and JNPs are characterized by heterogeneous nucleation at a specific site of the particle, avoiding nucleation at many locations. On the contrary, homogeneous nucleation allows many seeding points. The control of quantities of reactants, temperature and heating method, solvent polarity or surfactants is crucial for determining the final structure [142], [143].

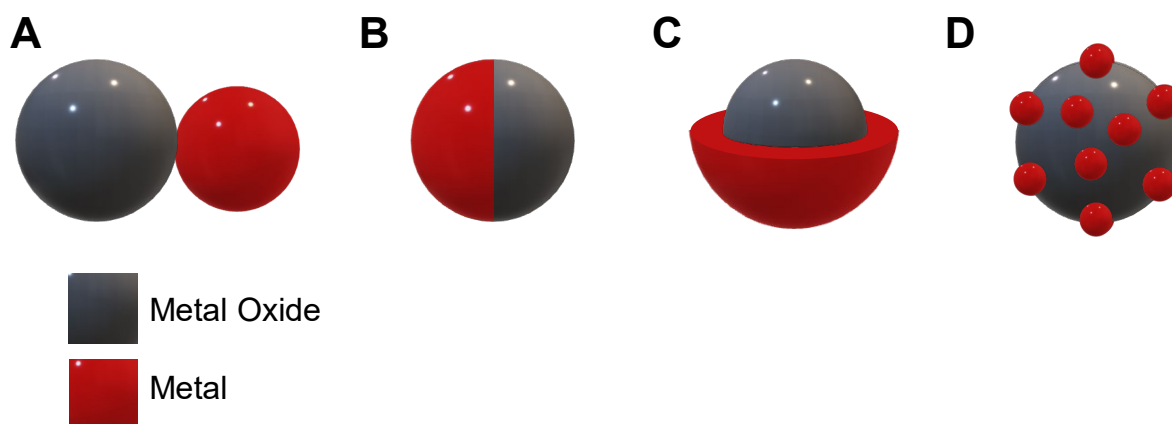


Figure 1.9. Scheme of the structures of the different hybrids containing metal oxide (grey) and noble metal (red). From left to right, (A) Dumbbell-like, (B) Janus nanoparticles, (C) Core-Shell, and (D) Seed Decoration. It has to be pointed out that the Janus nanoparticle is just a representation of a two-sided hybrid nanoparticle, but the structures for this are endless.

The attachment of a "small" nanoparticle onto one of the facets of a "bigger" nanoparticle characterizes dumbbell-like hybrid nanoparticles. One of the most common methods to synthesize this kind of hybrid nanoparticles is a two-step method based on epitaxial growth. DBNPs composed of magnetite (Fe_3O_4), and metal NPs were produced using this standard method (**Figure 1.10**). The first step consists of the reduction of noble-metal salt to obtain a colloid of metal nanoparticles in an organic solvent. In the second step, the hybrid structure is obtained after the decomposition of iron pentacarbonyl ($\text{Fe}(\text{CO})_5$) or iron(III) acetylacetonate ($\text{Fe}(\text{acac})_3$) on the surface of the noble metal nanoparticles with 1-octadecene and a mixture of surfactants, oleic acid (OLA) and oleylamine (OAm), followed by oxidation in the air [113]. Pt- Fe_3O_4 nanoparticles [116] and Pd- Fe_2O_3 with peroxidase mimics were also synthesized [144]. More complex materials have also been reported. PtPd- Fe_3O_4 DBNPs synthesized through this method demonstrated a synergetic effect due to the combination of materials [88].

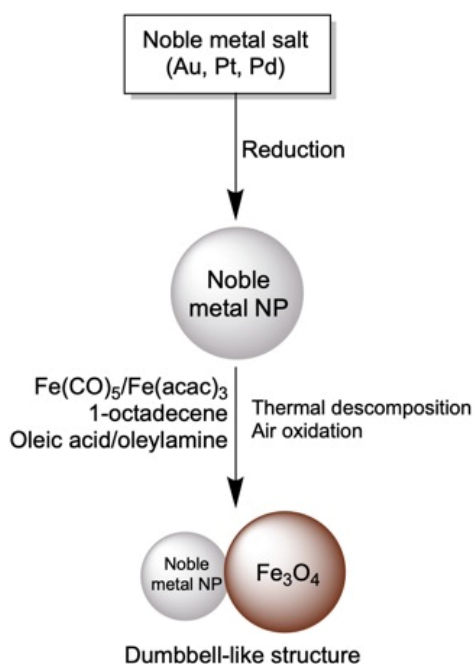


Figure 1.10. Dumbbell-like hybrid nanoparticles synthesis route. Adapted from Yu *et al.* [113].

Although some authors classify Janus nanoparticles (JNPs) separately from DBNPs, we have chosen to treat them as an extended case of DBNPs because the concept of a two-sided nanoparticle is also met in DBNPs [145]–[147]. These nanoparticles are combining two or more parts that differ in their physicochemical properties. Janus nanoparticles are also called anisotropic particles as their properties are not homogeneous. They provide many kinds of possible shapes. Typically they are synthesized by a template-mediated synthesis, like Au-SiO₂ and Ag-Au-SiO₂ nanoparticles [148]. In the work of Zhang *et al.*, gold nanoparticles were

treated with polyacrylic acid (PAA), which worked as the pattern for the deposition of $\text{Ce}(\text{OH})_3$ after adding Ce^{3+} . Subsequently, the nanosystems were coated with SiO_2 to protect them from a calcination treatment. Then the JNPs were released from the silica protection by etching, resulting in the formation of the hybrid. The obtained Au-CeO₂ had a dumbbell-like shape and acted as catalase and SOD-mimics [149]. TiO₂/Pt Nanozyme were also prepared with a Janus configuration. For the synthesis, hollow TiO₂ nanoparticles were placed onto a hydrophilic silicon slide, and then Pt was deposited on the upper side surface of hollow TiO₂. Using vacuum metal sputter deposition and reduction in H₂ atmosphere, Pt NPs were formed on one side of the nanoparticle. These Nanozymes showed catalase mimics [150].

Core-shell nanoparticles are formed of an internal core and a surrounding layer of another material. Metallic NPs covered by an oxide layer, such as Au nanorods coated with Pt NPs and a mesoporous silica shell, showed peroxidase mimics. Au nanorods were prepared from Au NPs through a seeded-growth process, and then K_2PtCl_4 was reduced on their surface with ascorbic acid. They were subsequently functionalized with cetyltrimethylammonium bromide (CTAB) which acted as a template for the deposition of SiO_2 [151]. Some authors have reported Nanozyme oxide-core/metal NPs shells, *i.e.* a shell composed of NPs of the metal [152]. Core-shell Nanozymes composed of an oxide coated with a metal layer have also been reported, for example, $\text{CoO}@\text{Ag}$ [153]. For their synthesis, a one-pot solvothermal method was employed. Initially, $\text{Co}(\text{NO}_3)_2$ was dissolved in glycerin and isopropanol. Then AgNO_3 was added. The reaction system was kept at room temperature for 10 h followed by 6 h at 180 °C. The precipitate was washed with ethanol, and the precursors were calcinated at 400 °C. The synthesis of core-shell $\text{Fe}_3\text{O}_4@\text{Au}$ nanoparticles was done by successive reductions of HAuCl_4 with NaBH_4 onto already formed seed-decorated nanoparticles with an intermediate layer of polyethyleneimine (PEI) [154]. In Kim *et al.* work, direct reduction of the metal precursor on Fe_3O_4 showed that the platinum salt to iron salt ratio influenced the spatial distribution of Pt [124]. When the loading of Pt salts was 7% (w/v), the deposition of platinum led to a shell, whereas, for 30%, a seed-decorated structure was observed. The explanation may be due to the growing and nucleation processes of the two different materials; in particular, lattice mismatch plays a significant role here. A high mismatch is produced between the surfaces favouring seed decoration growing when the amount of noble metal reaches a limit. The last examples can also be defined as metal Seed-decorated oxide nanoparticles.

Nanozymes prepared by metal seed decoration present many advantages, and for the scope of this thesis, we describe their synthesis in more detail. Their structure allows fixing the metal NPs or Seeds on the surface, avoiding aggregation, and thus maximizing the specific surface area of the metal nanoparticles, and providing high density of metal-metal oxide junctions, hotspots for catalysis and for substrates to react [153], [155], [156].

Decoration of metal oxide NPs with metal NPs can be achieved by at least three methods which are described in **Figure 1.11**. The first approach (method 1) consists in functionalizing the preformed oxide nanoparticle with species, such as a polymer [112], small molecules [152] or silica [157]. Afterwards, metal nanoparticles are added and linked to the oxide nanoparticles by weak or strong forces thanks to surface functionalization. The metal oxide is functionalized in the second method (method 2), and the metal cations are added instead of directly anchoring the metal nanoparticles. They are subsequently captured at the surface of oxide nanoparticles and reduced, leading to metal seeds deposited on the oxide nanoparticles. Method 3 consists in directly reducing the metal nanoparticles onto the naked metal oxide nanoparticles (as opposed to method 2) surface. It is worth noting that overloading the noble metal can lead to a raspberry-like hybrid nanoparticle. In this case, the metal oxide nanoparticle is fully covered, leading to a core-shell nanoparticle (previously described).

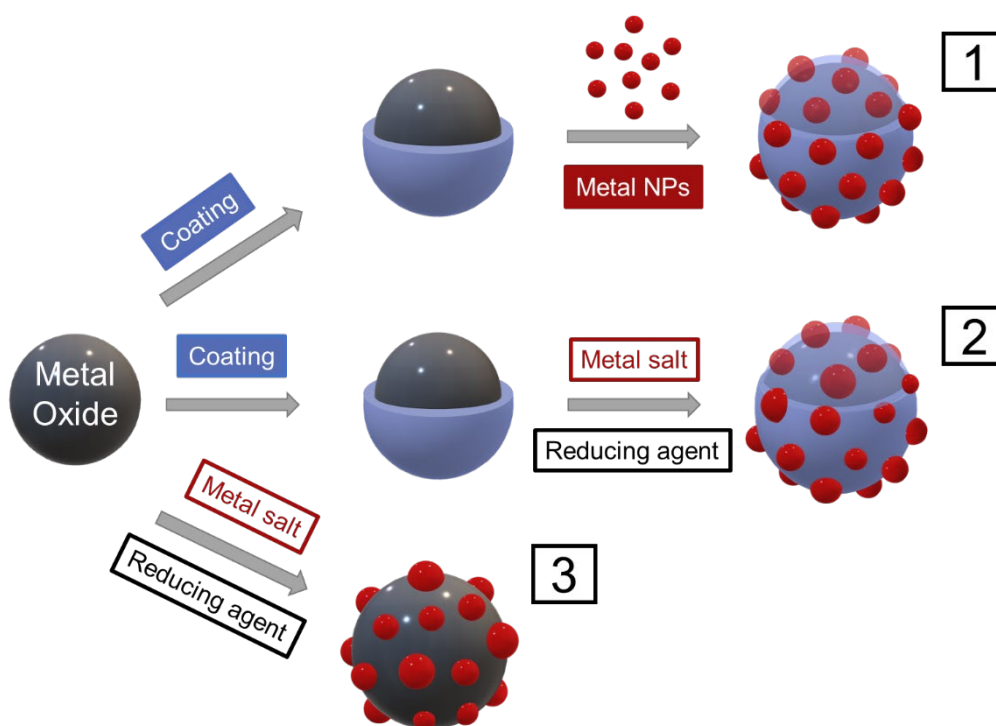


Figure 1.11. Scheme of different approaches for synthesising seed-decorated hybrid nanoparticles.

In method 1, the layer-by-layer synthesis in which both metal oxide and metal are prepared is a standard method for preparing hybrids (method 1, **Figure 1.11**). Nanoparticles of metal oxide and metal nanoparticles can be synthesized independently by conventional methods or directly bought from various suppliers. Consequently, the control of both nanoparticles' size, shape and structure is ensured, and the surface functionalization of one or both NPs ensures the metal NPs' attachment to the metal oxide NPs, but it increases the number of steps in the synthesis. For example, the modification of gold NPs and iron oxide NPs with surfactants of opposite charges allowed the electrostatic linking of the two types of NPs [112]. Another strategy was reported by Bao *et al.* in 2007: the functionalization of oxide nanoparticles with thiol-terminated groups allowed for the successful synthesis of Fe₃O₄-Au hybrid nanoparticles due to the strong affinity between gold and sulfur. Sulfur was introduced at the surface using cysteine to ensure the Au-S bond. The ability to attach gold nanoparticles directly to the amino-functionalized iron oxide was also tested, but the results showed that thiol functionalization was necessary to achieve gold seeding [158]. A few years later, similar work was done in which iron oxide was subsequently functionalized by branched polyethyleneimine (BPEI) [154]. Electrostatic interactions between positively-charged Fe₃O₄@BPEI and negatively-charged AuSeeds were used to achieve the synthesis. Another parameter to control during this synthesis is the amount of metal loading. Liu *et al.* did some experiments regarding the amount of gold nanoparticles added, keeping the iron oxide nanoparticles quantity constant, and *vice versa* [112]. As expected, increasing the gold-to-iron oxide ratio increases the gold loading in the hybrid nanoparticles. Similarly, in previous work, we achieved the attachment and control of the loading of AuSeeds onto LiNbO₃ NPs previously coated with BPEI [12]. The quantity of nanoparticles is not the only parameter to vary, as demonstrated by Goon *et al.* By increasing the PEI quantity, the gold loading on metal oxide NPs increases [154].

Method 2 (**Figure 1.11**) is based on the noble metal salts reduction to form nanoparticles at the surface of functionalized metal oxide nanoparticles. Metal oxide nanoparticles are produced first, similarly to method 1, which ensures the control of their features, whereas metal nanoparticles are synthesized *in situ*, which reduces the number of steps compared to method 1 (from 5 or more to 3 or less). However, it also provokes the loss of control in size and shape over the metal nanoparticle formation. Magnetite and gold [157], [159]–[161], silver [157], or platinum [152], [160], [162] Fe₃O₄ hybrids were synthesized by method 2. Hybrid nanoparticles composed of hematite and gold, platinum, silver or platinum-gold alloy hybrids

were also reported [53]. Also, TiO₂ was functionalized with a polyoxometalate that acted as a reductant to obtain Cu, Ag, Au and Pt hybrids [163].

Small molecules such as dimercaptosuccinic acid for platinum seeding [152], lysine as a general linker for various noble metals [53] or citrate for gold [161] have been used. Another possibility consists in using a polymer such as poly(4-vinylpyridine-co-divinylbenzene) for the attachment of gold cations [159] or polyethyleneimine that can also be used for platinum cations [162]. The importance of the nature of the chemical link between the cation and the iron oxide NPs was demonstrated by Zhang *et al.* [53]. Their results showed a poor distribution of the gold seeds onto the hematite nanoparticles in the absence of lysine. This work compared seeding with different noble metals and showed that Au and Pt seeds have better distribution and are more loaded onto the metal oxide than Ag seeds. Furthermore, the silver seeds are much larger than the two other metals.

A particular case of this method is coating the metal oxide with an inorganic or organic material. Silica layer is widely used, and it is worth mentioning some representative works demonstrating the versatility of this method for synthesizing magnetite-noble metal hybrids [157], [160]. Carbon and nitrated carbon layers for synthesizing Fe₃O₄@PdSeeds were also reported [164]. This synthesis method provided an increased catalytic activity of Fe₃O₄/Pt NPs compared to the Fe₃O₄ [152]; however, as the Pt NPs were synthesized *in situ*, the comparison to the naked Pt NPs was not possible.

Finally, method 3 consists in directly reducing metal cations on the naked surface of the nanoparticles. After synthesizing the initial oxide nanoparticles, the metal cation is added without additional surface modification of the metal oxide NPs after their synthesis. This method has been reported for the synthesis of Fe₃O₄/Au NPs [106], [165], Fe₃O₄/Pt NPs [124], and CeO₂ nanotubes coated with Pd NPs [123] (method 3, **Figure 1.11**) However, in this method, the control over the distribution of the noble metal NPs is lower than in methods 1 and 2, due to the lack of functionalization. Therefore, efforts have been devoted to better monitor this kind of synthesis. For example, Liu *et al.* explored the metal cation injection time to control the growth and dispersion of Au, Pd and Ag on Fe₃O₄, CeO₂ and Mn₃O₄ [165]. The results showed that increasing injection time allowed an increased uniformity in the loading and the production of smaller nanoparticles for the three noble metals.

Interestingly, a recent report focused on one-pot synthesis methods for iron oxide/noble metal hybrids in which the noble metal salts and the iron salts are mixed [165]. More recently, the same group reported that the concentration of gold salts influenced the size of the gold seeds [106].

Regarding the synthesis methods comparison (**Table 1.2**), method 1 allows fine control of the size and shape of the nanoparticles as the nanoparticles are prepared separately. It is suited to compare the separated nanoparticles and the hybrids fully. Moreover, adding an intermediate layer allows for the uniform distribution of the seeds on the core metal oxide nanoparticle. This last feature is also present in method 2, but the size uniformity and control are reduced. In method 3, a significant reduction in the number of steps for the synthesis is achieved, but size control and distribution of the seeds on the surface are difficult. To sum up, as the number of steps decreases, the synthesis control also decreases. For this reason, we have chosen to synthesize the nanoparticles by method 1.

Table 1.2. Comparative table for the synthesis of seed-decorated hybrid metal-metal oxide nanoparticles. Colour code: green (advantage), yellow (disadvantage), red (important disadvantage).

| | Method 1 | Method 2 | Method 3 |
|---|-----------------------------|--------------|--------------|
| Minimum number of synthesis and purification steps | 5 | 4 | 3 |
| Synthesis control | Metal Seeds M. Oxide NPs | M. Oxide NPs | M. Oxide NPs |
| Relative control in the distribution of the metal Seeds | Yes | Yes | No |
| Comparison with the building blocks | Metal Seeds M. Oxide NPs | M. Oxide NPs | M. Oxide NPs |
| Used in this work | ✓ | ✗ | ✗ |

1.1.6. LiNbO₃/Metal hybrid NPs as Nanozymes

As described in **section 1.1.4.2**, metal nanoparticles deposited onto metal oxide nanoparticles show an improvement in catalytic activity due to the synergetic effect. However, the choice of the oxide can change the application and bring different properties to the nanoparticles. For

instance, depositing metal NPs onto Fe₃O₄ or Fe₂O₃ NPs confers magnetic properties, which facilitates their separation [88], [144], the deposition of metals on the surface of CeO₂ causes localized reduction of Ce⁴⁺ into Ce³⁺ which is believed to enhance the catalytic activity [123], [166] and as discussed in the previous section 1.1.4.2 the deposition onto TiO₂ or CuO facilitates photocatalytic processes [167]. Nevertheless, little attention has been paid to non-centrosymmetric oxide nanomaterials. In the following, we will focus on LiNbO₃ as the metal oxide component of hybrid NPs.

1.1.6.1. LiNbO₃ properties and synthesis

LiNbO₃ (LN) has a non-centrosymmetric structure which confers outstanding non-linear optics, pyroelectric and piezoelectric properties, making it ideal for numerous applications in optics, batteries and optical communications [168]–[170].

At the nanoscale, LN NPs present low toxicity and lack phase-matching conditions, making them excellent candidates for bio-imaging and photo-triggered drug delivery [171], [172]. LN NPs' non-linear optical (NLO) properties make them attractive for tissue imaging in the transparent biological windows (700-950, 1000-1350, 1550-1870 nm). When irradiating LN NPs with these wavelengths, two photons with the same frequency ω , are converted by the non-linear material in one single photon of frequency 2ω (**Figure 1.12**) [173]. This process, called Second Harmonic Generation (SHG), provides the possibility to excite LN NPs in the NIR and collect a signal in the visible range. This offers several advantages such as better discrimination between the excitation and the emission wavelengths and easy 3D image reconstruction. In addition, it allows it to operate at higher wavelengths reducing photodamage and better depth tissue imaging [174]. However, NLO properties rapidly decrease under 100 nm particle size, but *in vitro* biological applications requires a size between 10 and 60 nm for optimum cellular uptake [175]. To overcome this, Richter *et al.* combined NLO nanomaterial, KNbO₃, with Au, which leads to an enhancement of the SHG signal. Moreover, this allowed both imaging and treatment (theragnostic) [176], [177].

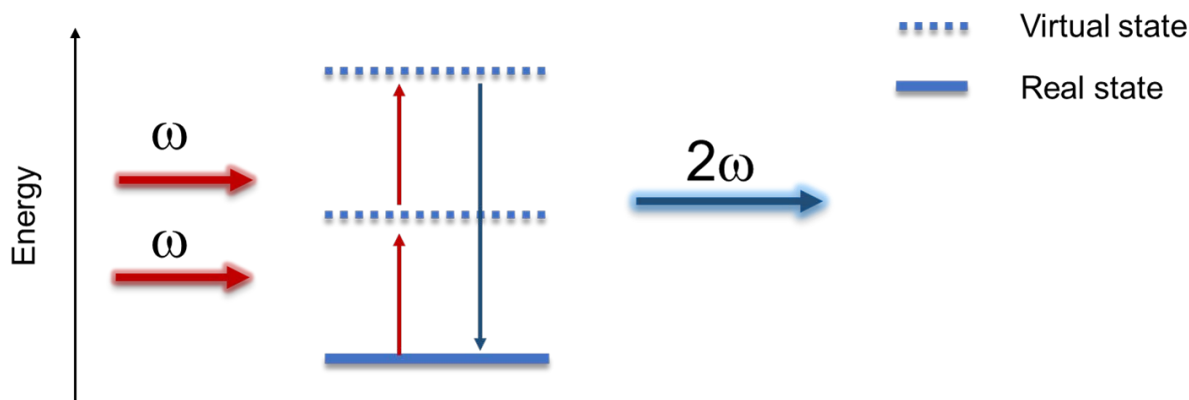


Figure 1.12. Second harmonic generation in non-linear LN NPs.

Other features of LN are their semiconducting properties and ferroelectricity, which enhances catalysis and photocatalysis, especially in redox reactions. These properties favour charge separation and polarization-induced facile adsorption [178]. LN degrades VOCs thanks to its photocatalytic properties. For instance, illuminating LN with UV light ($\lambda < 333$ nm) produces electron/hole separation favouring the production of hydroxyl and superoxide anion radicals leading to the oxidation of organic compounds [179]. Although the presence of oxygen vacancies is anecdotic, preferential oxygen fixation occurs in positively-polarized regions on the LN surface [180], [181]. To our knowledge, there are a few studies that have exploited this. For instance, Cai and co-workers attached glucose oxidase to LN nanotubes to make a glucose biosensor. In this work, they also mentioned that the cause of the lack of studies on LN NPs for catalytic purposes is due to the weak electronic mobility in LN, which makes redox reactions unfavourable [182]. However, the deposition of a metal permits one to overcome this problem thanks to charge separation and defect creation [183], [184]. Additionally, its properties as a semiconductor with a band gap in the UV region might be interesting in modulating its Nanozyme activity under light excitation in combination with metal nanoparticles [185].

Classically, the preparation of LN NPs of this size was achieved by solid-state reaction at 1100 °C, leading to a lack of consistent stoichiometry and the loss of Li_2O component by evaporation. This causes a change in the Nb ions' valence state [186]. More recent methods based on the wet-chemical synthesis also require high temperatures ranging from 400 to 800 °C to calcinate the (Li, Nb) precursors or to produce annealing to obtain crystalline structures, which leads to an increased aggregation [187], [188]. Therefore, milder conditions are needed. Hydrothermal/solvothermal synthesis allows one to obtain the crystalline phase keeping the

temperatures under 300 °C [189]. Indeed, with this method, LN NPs of around 50 nm were recently obtained by dissolving niobium ethoxide in benzyl alcohol with LiOH and triethylamine as surfactant using a maximum reaction temperature of 230 °C [188], [190]. Moreover, we have shown how it is possible to attach branched polyethyleneimine to it and subsequently attach AuSeeds [12]. To our knowledge, LiNbO₃ nanoparticles have not been used in combination with metal nanoparticles or seeds as Nanozyme.

In the next section, we will then detail the available protocols to synthesize noble metal seeds in order to immobilize them onto LN NPs using the seed-decorated hybrid nanostructure.

1.1.6.2. Metal Seeds Synthesis

As discussed in **section 1.1.3.1**, the highest Nanozyme activity was found for metal nanoparticles with diameters ranging between 1 and 5 nm. Indeed metal NPs of that size are often called ultrasmall nanoparticles [191] or seeds [192]. The last terminology is used as they are usually employed for the subsequent reduction of metal salts on them to obtain bigger metal NPs [193] or a shell [12]. One can use top-down or bottom-up approaches for synthesising metal seeds, as for other NPs. In the first method, preformed metal NPs are physically etched (nanolithography, thermolysis) to obtain smaller ones. Although this method allows external control of the process, the resulting NPs do not possess a reproducible structure and surface, which is critical for catalytic properties.

The bottom-up approach to synthesising metal seeds consists of assembling the ions, atoms, or molecules in a controlled way to obtain NPs of a specific size. Most of the bottom-up approaches are based on wet-chemical synthesis. Specifically, for the synthesis of metal nanoparticles, metal ions are reduced, and the size of the nanoparticles is controlled by surfactants [193]–[195]. For our work, it was critical to control the size of the metal seeds to ensure homogeneous catalytic properties. In the 1950s, LaMer and colleagues studied the key stages to control the nucleation and growth of NPs produced in solution [196]. This model comprises three steps schematized in **Figure 1.13**: atom generation, nucleation, and growth. In the reaction media, as atoms start to form due to the addition of reactants, their concentration increases rapidly, passing the solubility concentration and reaching the minimum nucleation concentration. Subsequently, nuclei (or seeds) formation starts, and as a consequence, the atom concentration reaches a maximum and then falls to the minimum nucleation concentration. At this point, the growth phase starts due to the diffusion of additional atoms towards the nuclei's

surface. According to this model, to obtain homogeneous nanoparticles, the nucleation phase should be attained rapidly, and it has to be as short as possible, avoiding the formation of heterogeneous-size nuclei. Moreover, adding surfactants avoids big nanoparticles forming during the growth process, stabilising small nanoparticles and/or counterions by steric and/or electrostatic repulsion to inhibit particle aggregation.

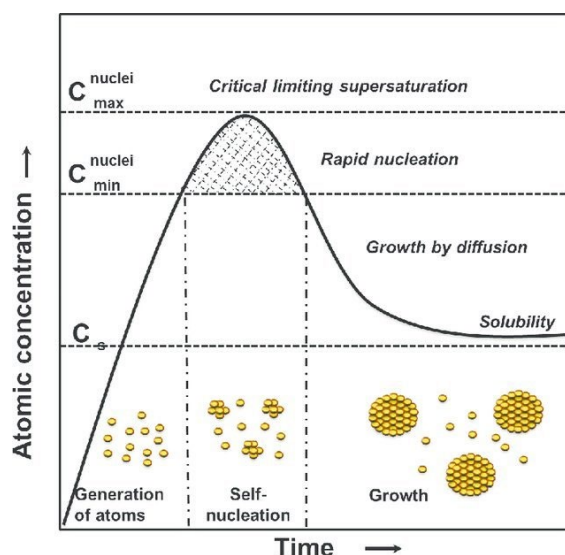


Figure 1.13. Mechanism of particle nucleation and growth in wet-chemical methods according to LaMer's model. Extracted from Khan *et al.* [197].

Numerous synthesis methods for ultrasmall metal seeds can be found in the literature and are summarised in various reviews [191], [198]. In the scope of our work, we need to compare seeds prepared with different metals; thus, the synthesis methods should be equivalent, using the same surfactants and reducers. Duff *et al.* proposed a method to prepare gold seeds using basic media and tetrakis(hydroxymethyl)phosphonium (THPC). The obtained nanoparticles had a diameter below 2 nm and were highly stable in water [199]. This method was successfully applied to the synthesis of other metal nanoparticles with minor modifications: AgSeeds, PtSeeds, PdSeeds or RuSeeds [192], [200].

As a conclusion of **section 1.1**, the Nanozyme concept was presented, and a focus was made on metal nanoparticles as Nanozymes and the strategies to improve their enzymatic activity. Coupling them with a metal oxide in a hybrid nanoparticle appears to be an efficient strategy. The seed-decoration nanostructure was selected as it exhibits several advantages for Nanozyme applications. In the scope of this thesis, LiNbO_3 was chosen as the metal oxide component, while different ultrasmall metal nanoparticles were immobilized on their surface.

Now, we will focus the end of this chapter on the ROS activity of Nanozymes as a potential tool for therapeutic applications.

1.2. Metal Nanozyme ROS activity

As seen in the previous section (1.1.2.1), Nanozyme's main enzymatic activities are peroxidase, oxidase, catalase, and superoxide dismutase, *i.e.*, they are all related to reactive oxygen species (ROS) production or scavenging. ROS are natural intermediates of cell metabolism. They participate in many essential processes: modulation of cell survival and death, differentiation, cell signalling, and inflammation-related processes. Under a physiological state, ROS production and neutralization is a dynamic equilibrium regulated by cells. Enzymes (superoxide dismutase or catalase) and different antioxidants (ascorbic acid, vitamin E or flavonoids) carry out ROS regulation. However, ROS imbalance can seriously harm many signalling mechanisms and causes direct oxidative damage to biomolecules and cell death [201], [202]. Because of that, ROS modulation can be used as a therapeutical tool. For instance, therapies that increase ROS production may damage and kill bacteria or tumour cells, whereas therapies focused on ROS scavenging may help their overexpression and relieve oxidative stress in areas such as ageing or inflammatory processes [202], [203]

In the literature, there are three main interactions between ROS and Nanozymes in living organisms: boosting their production, scavenging and regulating them (**Figure 1.14**) [7], [18]. As seen in **Table 1.1**, peroxidase and oxidase can promote ROS production, whereas catalase and superoxide dismutase mainly scavenge ROS.

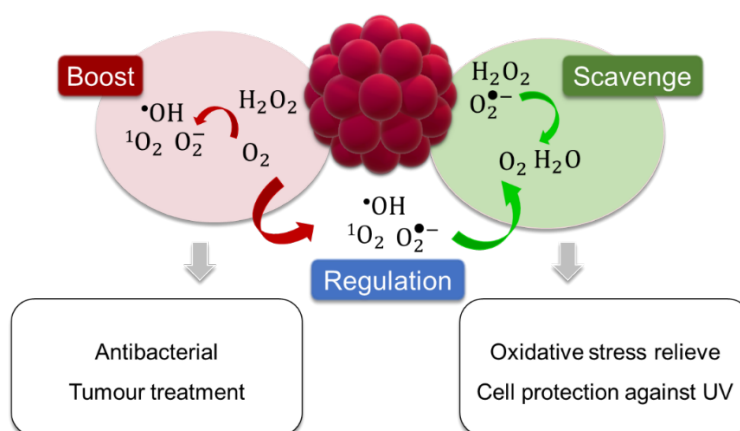


Figure 1.14. Nanozyme mediated ROS reactions examples: production and scavenging.

Although the Nanozyme field is relatively recent, its use in ROS-modulating therapies has already been proven [204]. In the scope of this work, we will focus on metal-based Nanozymes and light-triggered applications. We will discuss some outstanding works focusing on light-enhanced processes and metal-metal oxide combinations, but in **Table 1.3**, we have included more examples.

Table 1.3. Compilation of metal nanoparticles activities towards therapeutics.

| Nanozyme | Activity | Application | Reference |
|---|---|---|------------------|
| MSN-AuNPs | Peroxidase Oxidase | Antibacterial | [205] |
| AuNPs/g-C ₃ N ₄ | Peroxidase | Antibacterial | [206] |
| AuNPs/g-C ₃ N ₄ | Light triggered oxidase | Antibacterial | [207] |
| Pd NCs | Peroxidase Oxidase | Antibacterial | [208] |
| Ag/ Bi ₂ MoO ₆ | Light enhanced peroxidase | Antibacterial/wound healing | [209] |
| Ag/CeO ₂ | Light enhanced SOD | Antibacterial | [137] |
| Porous Pt-Ag NPs | Peroxidase | Antibacterial | [210] |
| PtCo@Graphene | Oxidase | Antibacterial | [211] |
| Au@Co-Fe NPs | Peroxidase | Antibacterial | [212] |
| Au@HCN | Light enhanced peroxidase Oxidase | Cancer cell death | [213] |
| DMSN-Au-Fe ₃ O ₄ - PEG | Glucose Oxidase Peroxidase | Cancer cell death hypoxia relief | [214] |
| Au/Pt Nanostar | Peroxidase | Cancer cell death | [215] |
| PtCO@MnO ₂ NPs | Oxidase and catalase | Cancer cell death and hypoxia relief | [216] |

| | | | | |
|---|----|---|---|-------|
| PtAu@SiO ₂ | | Oxidase and catalase | Cancer cell death and hypoxia relief | [217] |
| PtFe@Fe ₃ O ₄ NPs | | Light-enhanced peroxidase and catalase | Cancer cell death and hypoxia relief | [135] |
| PtNPs-MOF | | Light-enhanced oxidase and catalase | Cancer cell death and hypoxia relief | [218] |
| Pt NPs | | Superoxide dismutase | Cell protection against ageing | [47] |
| AuNPs@POMD-8pep | | Superoxide dismutase | Cell protection in Alzheimer's Disease (AD) | [219] |
| Pt NPs | | Superoxide dismutase Catalase Peroxidase | Cell protection | [220] |
| Mn-modified NPs | Pt | Superoxide dismutase Catalase | Cell protection in Inflammatory Bowel Disease | [221] |
| Au NPs | | Catalase | Cell protection | [222] |
| GO-Se | | Peroxidase | Cell protection | [223] |
| Pt/CeO ₂ | | Catalase Peroxidase Superoxide dismutase Glucose oxidase | Cell protection after traumatic brain injury | [11] |
| Pt NPs | | Catalase Superoxide dismutase | Cell protection after exposure to cigarette smoke | [224] |
| Au-Pt NPs | | Catalase Superoxide dismutase | Cell protection against UV radiation | [225] |

1.2.1. ROS boosted production for oxidant therapeutics

In the literature, ROS production by metal Nanozymes for cell-damaging and killing related to antimicrobial activity and tumour cell-killing applications are the most reported ones.

1.2.1.1. Antimicrobial activity

The antimicrobial activity of Nanozymes has been mainly focused on antibacterial applications. The increasing resistance of bacteria towards antibiotics is one of the century's biggest challenges. Thus, the requirement for alternatives is a hot topic in therapeutic research [226]. Metal Nanozymes possess peroxidase and oxidase activities that can stop bacterial growth and kill them [227]. For instance, Au NPs deposited on mesoporous silica (MSN-AuNPs) favoured the production of $\bullet\text{OH}$ in the presence of H_2O_2 (peroxidase mimics) and $^1\text{O}_2$, $\bullet\text{OH}$ and $\text{O}_2^{\bullet-}$ in the presence of O_2 . Their application with Gram-positive *Staphylococcus aureus* (*S. aureus*) and Gram-negative *Escherichia coli* (*E. coli*) showed growth inhibition compared to the control group, which was enhanced in the presence of H_2O_2 . In addition, they eliminated biofilm successfully [205]. Using Au NPs combined with ultrathin graphitic carbon nitride (AuNPs/g- C_3N_4) produced a similar effect against Gram-positive and Gram-negative bacteria [206]. However, a recent study showed that the same material did not produce ROS in dark conditions. Therefore, the proposed driving mechanism in AuNPs/g- C_3N_4 antibacterial activity in the dark is the loss of electrons in the respiratory chain of the bacteria caused by the Schottky junction between the two materials due to the proximity of the redox potentials of nicotine adenine redox couple (NAD^+/NADH) and flavin adenine dinucleotide redox couple (FAD/FADH_2) and the Fermi Level of Au. Interestingly, the irradiation with light at the band gap energy of g- C_3N_4 enhanced ROS production by electron-hole separation (Figure 1.15) [207].

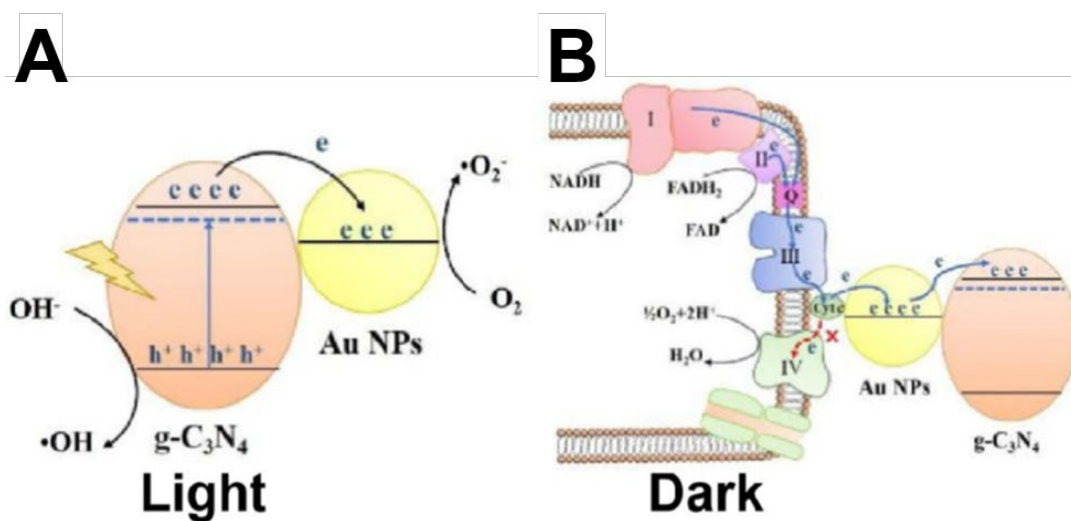


Figure 1.15. Mechanism for Au/g- C_3N_4 NPs for antibacterial activity under (A) light and (B) dark conditions. Extracted from Hongda Zhang *et al.* [207].

Au NPs are not the only ones showing antibacterial activity. Pd nanocrystals (NCs) antibacterial activity was dependent on the nature of their facets. {100}-faceted Pd nano-cubes showed better oxidase and peroxidase activities and increased antibacterial activity towards Gram-positive bacteria (*S. aureus*) than {111}-faceted Pd Nano-octahedra. Interestingly, {111}-faceted Pd Nano-octahedra were more effective against Gram-negative bacteria (*E. coli*). It was shown through molecular dynamics that the nano-cubes internalization by *E. coli* was not as successful as for octahedron-shaped nanoparticles [208]. Ag NPs combined with Bi₂MoO₆, showed a band gap reduction allowing excitation of the nanoparticles with near-infrared light. Ag⁺ release, a known bactericidal, and enhanced ROS production were tested under near-infrared laser irradiation. The results were applied for *in vivo* therapeutic healing of wounds in mice through bacterial killing [209]. Although SOD-mimics mainly reduce oxidative stress, its decomposition produces H₂O₂, which can lead to the production of ROS. On this basis, Ag/CeO₂ SOD-Nanozyme presented antibacterial properties which could be enhanced by visible-light irradiation (**Figure 1.16**) [137].

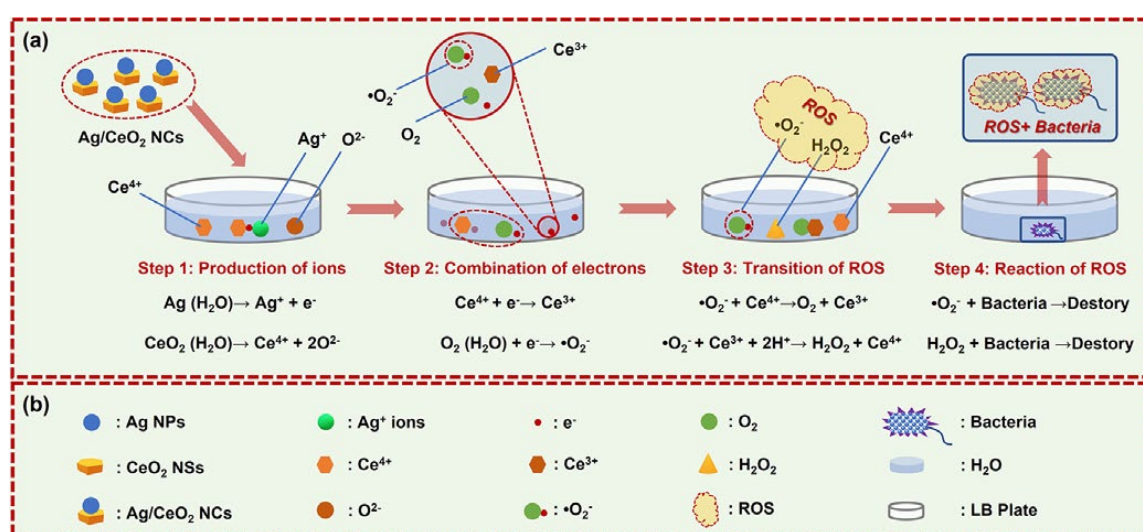


Figure 1.16. Ag/CeO₂ SOD-mimics Nanozyme with antibacterial properties. Extracted from Li *et al.* [137].

1.2.1.2. Tumour-cell therapy

Metal Nanozymes can also promote cancer-cell death by ROS regeneration (**Figure 1.17**). Core-shell Au NPs combined with a porous hollow carbon shell (Au@HCN) with intrinsic oxidase and peroxidase activities were able to cause tumour cell death and *in vivo* experiments showed a significant tumour decrease in mice. This effect was even higher when irradiated

with a near-infrared laser [213]. The tumour microenvironment (TME) demands high concentrations of glucose. However, there is a lack of O₂ (hypoxia) as it is highly consumed by cancer cells; as a consequence, ROS-based drugs and therapies, such as photodynamic therapy (PDT), photothermal therapy (PTT), sonodynamic therapy (SDT) or radiotherapy (RT), loose efficacy (**Figure 1.17**) [30], [228]. Moreover, the lack of O₂ in the TME produces apoptosis of healthy cells [229]. We must point out that even though O₂ is produced through ROS-scavenge activities (catalase and SOD activities), the final application is to amplify apoptosis. That is why we have included them in this section. The combination of dendritic mesoporous SiO₂ with Fe₃O₄ NPs and Au NPs (DMSN-Au-Fe₃O₄-PEG) produced peroxidase and glucose oxidase-active Nanozymes that provoke cancer-cell death due to a cascade effect: Au NPs glucose oxidase activity produced H₂O₂ which was further utilized by Fe₃O₄ NPs peroxidase-mimics to produce •OH, which solves the lack of O₂ to produce ROS [214]. A similar approach was used with PtCo@MnO₂. Their combination synergistically enhanced the H₂O₂ conversion into O₂ through MnO₂ catalase activity, which promoted the oxidase activity of PtCo Nanozyme [216]. PtFe@Fe₃O₄ Nanozymes with peroxidase and catalase activities efficiently kill cancer cells and overcome tumour hypoxia, increasing PTT's effect [135].

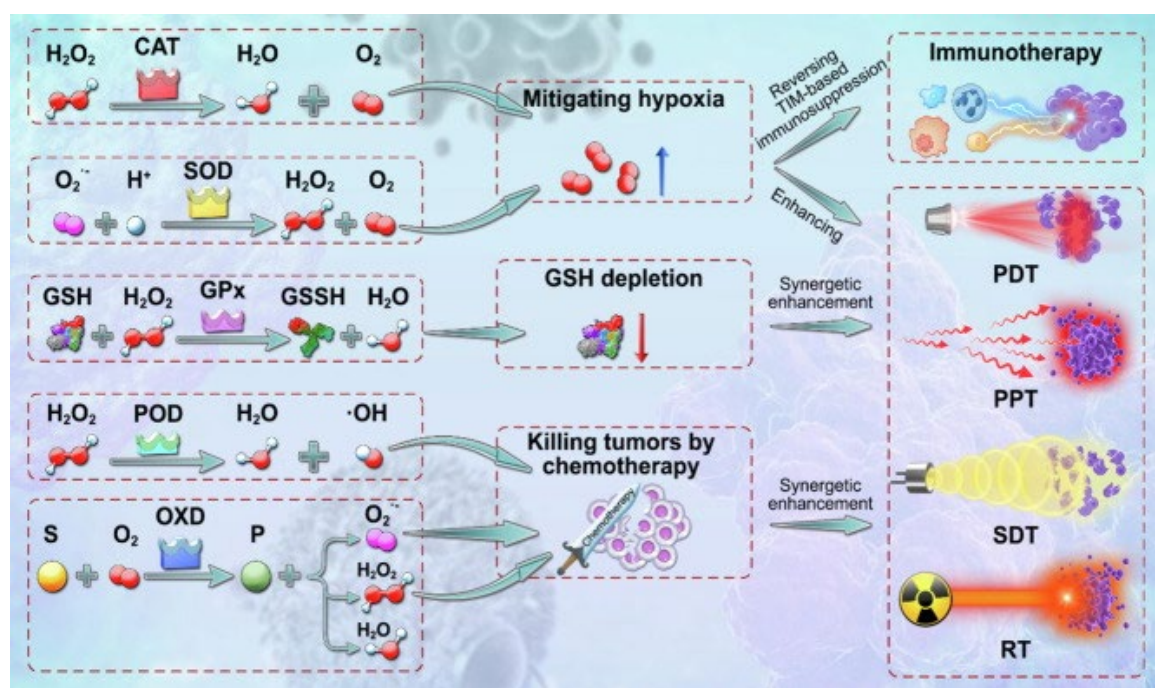


Figure 1.17 Oxidoreductase activities of Nanozymes against cancer cells. S represents a substrate, and P is the oxidized product. CAT is catalase activity, SOD is superoxide dismutase, GSH is glutathione, GPx is glucose peroxidase, POD is peroxidase, OXD is oxidase and SDT is sonodynamic therapy. Extracted from Li *et al.* [228].

In this section, we have reviewed how ROS production by Nanozymes can be advantageously used as anti-microbial agents or for cancer therapy. It was also demonstrated that NIR trigger can be an advantage for such applications as it allows to take advantage of the biological optical transparency window. However, the span of Nanozyme activities also confers ROS scavenging properties which can be also of therapeutic utilities.

1.2.2 ROS scavenging for antioxidant therapeutics

Increased ROS environments produce cell damage which might not be mitigated by cellular protective systems. Nanozymes that possess catalase and SOD activities can relieve oxidative damage. We classify the different ROS-scavenging Nanozymes depending on their ability to protect cells from an internal agent (disease) or an external agent (light, contaminants, drugs).

1.2.2.1. Internal agent protection

Ageing directly correlates to ROS production in organisms; thus, protecting cells from them is a potent tool to extend their viability. Indeed, an early study showed that *Caenorhabditis elegans*, a type of worm treated with Pt NPs showing SOD and catalase activities, extended its life [47]. Oxidative stress related to ageing diseases such as Alzheimer's disease has also been treated with ROS-scavenging Nanozymes. For instance, the combination of Au NPs with polyoxometals and peptides, AuNPs@POMD-8pep, with SOD activity was able to scavenge amyloid β -mediated ROS, which causes apoptosis of neurons in Alzheimer's disease [219]. Genes mutations can cause ROS overexpression. Cerebral Cavernous Malformation is a disease caused by the loss-of-function by mutations in certain genes, directly related to increased levels of intracellular ROS. By treating cells with citrate-capped Pt NPs NPs with catalase, SOD and peroxidase activities, Moglianetti and co-workers were able to recover cellular homeostasis [220].

Another example is alleviating inflammation. Manganese-modified Pt NPs successfully alleviated Inflammatory Bowel Disease (IBD) in mice caused by ulceritis and Crohn's disease. Their SOD and catalase activities acted as protective agents for intestinal cell epithelium [221].

1.2.2.2. External agent protection

External agents cause increased oxidative stress. Injuries, pollutants, or sunlight increase the production of ROS in cells. Nanozymes have proven to protect cells from them. For instance, traumatic brain injury may cause enduring neuronal damage. By depositing Pt onto CeO₂, Ming *et al.* decreased oxidative stress and inflammation responses of neurons in mice [11]. In another work, pulmonary inflammation caused by cigarette smoke was reduced using Pt NPs with SOD and catalase activities [224]. An important external ROS overexpression-driven mechanism is exposure to UV light. An exciting application of Nanozymes is protecting cells from Ultraviolet radiation-related ROS generation [18]. This is the basis of the work of Xiong *et al.* in which Au-Pt nanocomposites with SOD and catalase activities were mixed with cells and exposed to UV radiation. Their results showed that the UV light irradiation for 60 minutes with Nanozyme-containing samples showed no difference in cell growth compared to the non-irradiated control. However, the absence of Nanozymes produced an apparent delay in cell proliferation [225].

To conclude, metal Nanozymes have been reported as potent tools for therapeutics in different areas based on their ability to produce and/or scavenge ROS. Oxidoreductase-mimic metal Nanozymes provide a new approach to various applications, ranging from antibacterial to cancer treatments and light-induced oxidative stress reparation. Moreover, the combination with metal oxides has been investigated and can promote a synergetic effect, but more profound studies are needed.

1.3. Objectives

The state of the art has underlined the outstanding properties of noble metal nanoparticles in combination with metal oxides for Nanozyme mimics. However, the combination of noble metal nanoparticles with LiNbO₃ as a Nanozyme has scarcely been reported despite some advantages of this metal oxide (NLO activity, excitation in the transparent window for biological tissue, band gap in the UV-region or catalytic properties in redox reactions). The possible synergetic effect of combining these two materials as oxidoreductase mimic and ROS active material remains to be studied. Finally, the effect of the ROS activity of these hybrid nanoparticles on bacteria viability has not been explored, yet.

Therefore, in light of the current state of the art, we have set a series of objectives for this work.

- Reproduce and control the synthesis of LiNbO₃/Au hybrid nanoparticles and implement it into the synthesis of new materials.
- Test the ability of the LiNbO₃/metal hybrid nanoparticles as Nanozyme mimics.
- Optimize the conditions of catalytic activity measurement for the Nanozyme mimics.
- Compare the Nanozyme mimics of the LiNbO₃-metal hybrid nanoparticles to the separated counterparts (LiNbO₃, LiNbO₃@BPEI, metal seeds) and a mixture of them to corroborate a synergetic effect.
- Compare the different Nanozyme activities of the different metals deposited on LiNbO₃@BPEI.
- Elucidate the mechanism for enhanced catalytic activity through kinetic studies, band structure studies and reactive oxygen species probes.
- Investigate the interaction of the Nanozymes to the cell growth of *Escherichia Coli*.
- Investigate the interaction of Nanozymes and *Escherichia Coli* under oxidative stress conditions: H₂O₂, UV-irradiation and a combination of them.

Chapter 2: Characterization techniques

This chapter summarizes the characterization techniques used in this work. Nanozyme characterization was achieved through various techniques that provided complementary information. We present here the characterization of nanoparticles structure, their enzyme-mimic properties, and the bacterial growth techniques. In this work, as the final application will concern Nanozymes dispersed in liquid media, colloid characterization techniques are particularly important. As the nanoparticles are composed of several materials, it is also required to precisely know the chemical composition of the nanoparticles.

2.1. Transmission electron microscopy (TEM)

To characterize the shape and size distribution of the nanoparticles, transmission electron microscopy (TEM) was used. TEM principle consists in an accelerated beam of electrons that passes through the specimen. The interaction between the electrons and the sample generates the image. As the *De Broglie* electron wavelength is 1.22 nm for 1 eV, one can visualize specimens with nanometric precision. Moreover, TEM has several operating modes: conventional imaging or scanning TEM imaging (STEM) or diffraction to study crystal structure; Energy dispersive X-Ray spectroscopy (that will be detailed in the next section) or electron energy loss spectroscopy (EELS) to determine the chemical composition may also be performed during image acquisition [230].

The microscope comprises an electron emission source (electron gun) consisting of a tungsten filament or a single-crystal of lanthanum hexaboride (LaB₆). When a high voltage (200 kV for most applications) is applied between the electron source and the grounded anode, it will emit electrons in the vacuum. Following this acceleration, the electrons will travel through a series of aperture and condenser lenses which gather the electrons and focus them onto the sample to illuminate only the area being examined. The projector lenses are used to magnify the beam after the interaction with the sample, and they focus the image onto a phosphorescent screen or imaging device. Additional stigmators are used to correct astigmatism. Moreover, depending on the manufacturers, one can add spherical aberration correction lenses or energy filters to remove chromatic aberration. Inside the TEM, the pressure should reach at least 10⁻⁴ Pa; however, for high-voltage TEM (200 kV), a pressure of 10⁻⁷ to 10⁻⁹ Pa is required (**Figure 2.1**) [230].

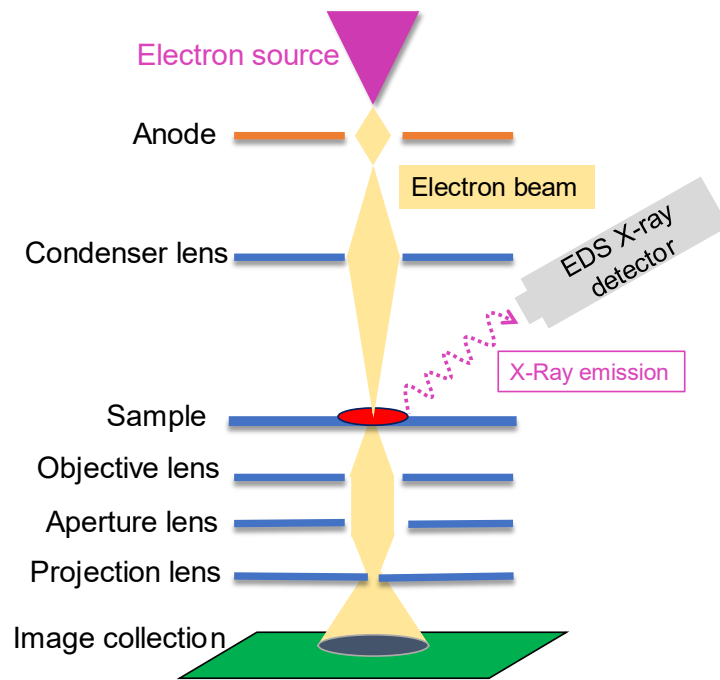


Figure 2.1. TEM coupled to EDS operating display.

For the scope of this work, scanning TEM imaging (STEM) and high-resolution TEM imaging (HRTEM) are discussed. STEM imaging is similar to TEM conventional imaging, but in this case, a system is introduced that rasters a convergent beam across the sample to obtain the image. HRTEM allows the imaging of the crystallographic structure of the sample at the atomic scale, which makes it a potent tool for the nanostructure characterization of semiconductors and metals. In HRTEM, the setting is identical to TEM, but the magnification is sufficiently high to reach a resolution of several Angströms (\AA) [230].

TEM microscope can be equipped with an Energy-dispersive X-ray spectroscopy (EDS, EDX) detector, which allows the detection of the X-rays emitted by the sample under the electron beam. It is a non-destructive technique that gives chemical and elemental information about the sample. The incident electrons excite inner electrons creating a hole which will be filled by an outer electron. During this process, X-rays are emitted, which are detected by an energy-dispersive spectrometer (**Figure 2.2**). For each element the energy difference between the outer and the inner shell electrons is characteristic, allowing the chemical composition elucidation [231].

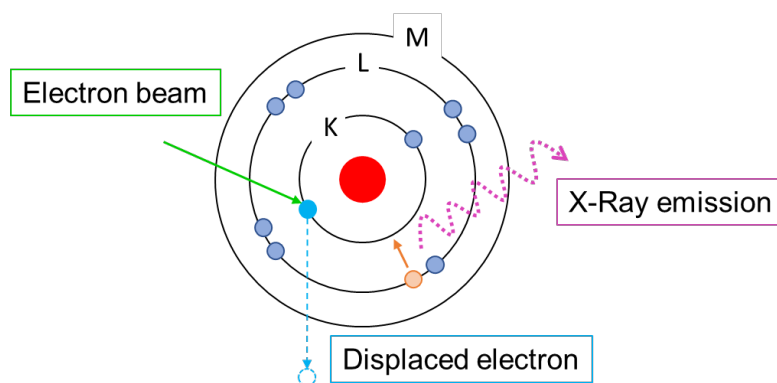


Figure 2.2. EDS principle.

As seen in **Figure 2.1**, EDS is usually coupled to a TEM and STEM to allow chemical mapping of the sample. The EDS detector contains a crystal that captures the X-rays emitted by the sample provoking its ionization. The resulting free electrons of the crystal produce electrical pulses that correspond to the X-rays emission line of each element [231].

In this work, we acquired TEM images before EDS analysis to avoid sample damage due to the electron beam focused on the same specimen region for a long time. EDS analysis was obtained by spotting the beam at three different points of the sample, obtaining three spectra. The atomic percentage of each chemical element was then extracted from curve fitting.

TEM and EDS analysis were performed with a JEOL 2100HT microscope (Tokyo, Japan) equipped with a LaB₆ electron source at a 200 kV operating voltage and an X-Max 80 mm² EDS silicon drift detector (Oxford Instruments, Abingdon-on-Thames, UK). The microscope had incorporated a bottom mount Orius SC1000 CCD camera (Gatan, Pleasanton, CA, USA). EDS spectra were obtained using spot sizes of 35, 25 and 7 nm. An ETEM FEI TITAN microscope, also equipped with an EDX XMAX 80 mm² silicon drift detector, was employed for chemical maps. TEM and STEM images were analysed with ImageJ software (Version 1.50i) and EDS data with Aztec software from Oxford Instruments.

Sample preparation for TEM imaging was done by deposition of 2 μ L of each sample (with concentrations ranging from 0.03 to 0.06 g/L) onto a previously UV-ozone etched (25 °C, 20 min) carbon-coated 400 mesh copper grid from TED PELLA Inc (Redding, CA, USA), followed by oven-drying at 50 °C for 10 min.

2.2. Dynamic Light Scattering (DLS)

Dynamic light scattering (DLS) was used to determine the hydrodynamic diameter of the nanoparticles in suspension and to ensure their colloidal stability. It is a non-destructive technique. The principle relies on Rayleigh scattering: when light hits particles smaller than its wavelength, it is scattered in all directions. In the scope of this work, we will refer to the small particles as nanoparticles, but this technique can be applied to proteins, liposomes, and other small particles. Nanoparticles in colloidal suspension undergo Brownian motion; therefore, the distance between them constantly changes. When incident light hits the nanoparticle suspension, the intensity of the scattered light fluctuates, giving information about the diffusion of the nanoparticles through the solvent, which is directly related to their radii. The smaller the radius of the nanoparticles, the faster they move, causing faster light intensity fluctuations. Therefore, light intensity fluctuations contain information about the diffusion of nanoparticles and the diffusion coefficient, which allows the calculation of the particle size. In the DLS apparatus, the correlation function of the second order, $g^{(2)}(\tau)$, quantifies light fluctuations (**Equation 2.1**). The intensity function is shifted by a time delay (τ), and the correlation function $g(\tau)$ is calculated. Qualitatively, it measures how similar the intensity function is to its self-shifted by time (τ) [232].

Equation 2.1

$$g^{(2)}(\tau) = 1 + \beta \cdot e^{-2D_t q(\tau)}$$

where β is the correlation function amplitude at zero delays, D_t is the translational diffusion coefficient, and q is the scattering vector.

The translational diffusion coefficient, D_t , is inversely related to the hydrodynamic radius, D_h , of a diffusing sphere through the Stokes-Einstein equation (**Equation 2.2**):

Equation 2.2

$$D_h = \frac{kT}{6\pi\eta D_t}$$

where k is Boltzmann's constant, T is the temperature, and η is the liquid viscosity [232].

The apparatus provides hydrodynamic diameter as the harmonic intensity averaged particle diameter. The intensity value can be converted into volume and number distributions thanks to Mie's theory. However, it assumes that the nanoparticles are spherical and homogeneous, and that all-optical parameters are known (the absorption value of the colloidal suspension at the correspondent wavelength of the laser has to be known) [233].

Hydrodynamic diameter of NPs dispersed in water was obtained with a NanoZS zeta sizer (Malvern, UK) apparatus. Measurements were done at a 173° back-scattering angle with DTS1070 disposable folded capillary cells (Malvern, UK). The sample absorbance was measured at 632 nm, corresponding to the laser source's wavelength. All values reported here result from triplicate measurements and 30 counts per measurement at 25 °C.

2.3. Laser Doppler Velocimetry and Electrophoresis

The zeta potential value is an essential parameter in the characterization of nanoparticles in suspension as it provides crucial information about their colloidal stability. Laser Doppler Velocimetry and Electrophoresis were performed to extract the zeta potential value of the synthesized nanoparticles (zetammetry).

Particles dispersed in a liquid media develop a net surface charge due to various factors: adsorption of charged species from the media, presence of ionizable compounds or self-dissociation of the surface molecules. As a result, the particle will be surrounded by a tight-bound layer of species of opposite charges (Stern layer) and a second layer in which the oppositely-charged species are loosely bound (diffuse layer) (**Figure 2.3**). The zeta potential is the electrical potential of the interface (slipping plane) in the diffuse layer that separates the moving liquid region from the static one [234].

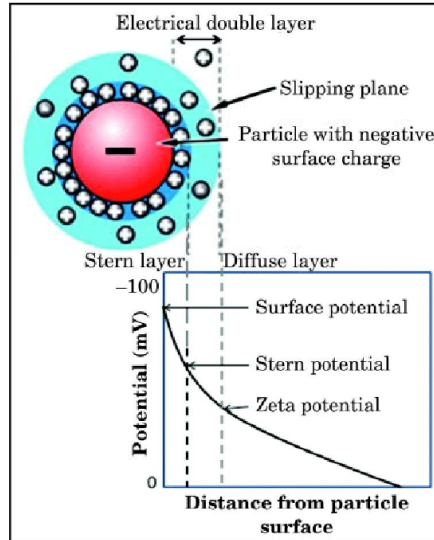


Figure 2.3. Electrical double layer around a negatively-charged particle, surrounded by positively-charged species in the Stern layer and the diffusion layer. Extracted from Tengku Mohd *et al.* [235].

Electrophoresis is used to obtain the zeta potential. The application of an electric field to suspended charged particles causes their migration towards the opposite electrode. This technique is combined with Laser Doppler Velocimetry (LDV) which permits to determine the velocity at which the particles move in a fluid flow and obtain electrophoretic mobility (μ_e) (**Equation 2.3**).

Equation 2.3.

$$\mu_e = \frac{V}{E}$$

where V is the velocity ($\mu\text{m}\cdot\text{s}^{-1}$) and E is the electric field strength ($\text{V}\cdot\text{cm}^{-1}$). From electrophoretic mobility, zeta-potential (ζ) can be determined (**Equation 2.4**).

Equation 2.4.

$$\mu_e = \frac{2\epsilon_r\epsilon_0\zeta}{3\eta}$$

where ϵ_r is the relative permittivity or dielectric constant, ϵ_0 is the permittivity of vacuum, and η is the viscosity of the media at experimental temperature.

Zeta potential values of NPs dispersed in water were obtained with a NanoZS zeta sizer apparatus (Malvern, UK). Measurements were done at a 173° back-scattering angle with DTS1070 disposable folded capillary cells (Malvern, UK). Smoluchowski model was used to fit the zeta potential data. The absorbance of the samples was measured at 632 nm, corresponding to the laser source's wavelength. All values reported here were the average of triplicate measurements at 25 °C.

2.4. Inductively coupled plasma atomic emission spectroscopy (ICP-AES)

Inductively coupled plasma atomic emission spectroscopy (ICP-AES), or inductively coupled plasma optical emission spectroscopy (ICP-OES), is a destructive analytical technique which is used to quantify the chemical elements in samples. The principle is based on the emission of photons following an excitation-relaxation process. The excitation can be achieved using a flame, or in this case, a coupled induced plasma.

Plasma is produced by an ICP torch that ionizes Argon gas (**Figure 2.4**). The sample is nebulized into the plasma, causing the collision with the charged particles of the plasma. Subsequently, the atom electrons are excited, and their return to lower energy levels causes the emission of electromagnetic radiation at a characteristic wavelength detected by the spectrometer. The intensity of the lines is compared to the ones obtained from known concentrations, allowing the composition quantification. This technique allows a limit of quantification in the µg/L range. In the case of nanoparticles, they need to be digested before the analysis.

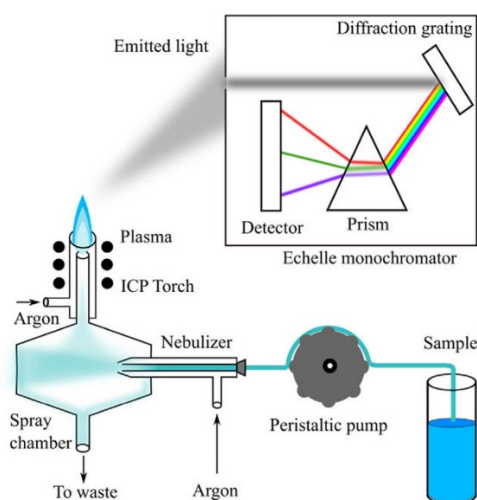


Figure 2.4. ICP-AES scheme. Extracted from Cherevko and Mayrhofer [236].

In this work, the analysed elements were Li, Nb, Au and Pt, as our samples are composed of LiNbO₃, Au and Pt. The technique was carried out in CREALINS laboratory Lyon with ICP-AES ICAP 6300 and an ICP-AES ICAP 6500 analyser from ThermoFisher Scientific. Samples were digested in a 4% H₂SO₄, 4% HNO₃ and 4% HCl in volume solution prior to their analysis.

2.5. UV-Vis spectrophotometry

UV-Visible (UV-Vis) spectrophotometry or spectroscopy is an optical technique based on light absorption of UV and visible electromagnetic radiations by a sample. In this work, UV-Vis absorption spectroscopy was used (**Figure 2.5**):

- to characterize metal nanoparticles' plasmonic properties,
- to study nanoparticles' catalytic activity,
- to determine nanoparticles' optical band gap,
- to measure bacterial density in the growth medium

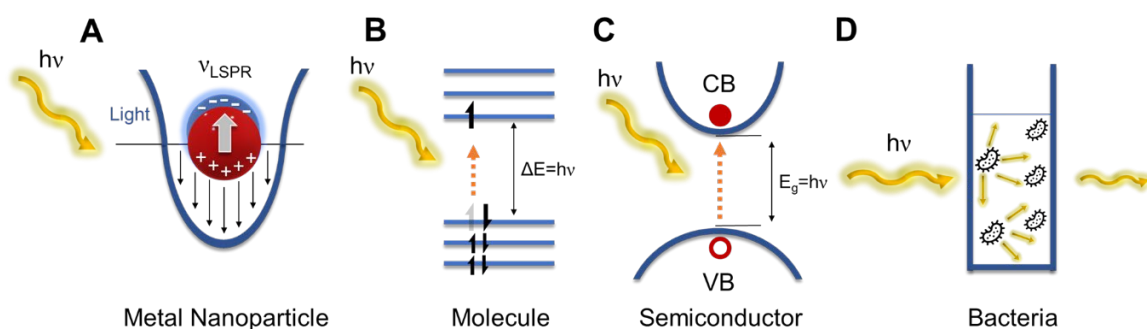


Figure 2.5. Interaction of light with (A) metal nanoparticle, (B) molecule, (C) semiconductor and (D) bacteria.

In the following, a quick overview of light-matter interaction is given. Next, the different instruments used are described.

2.5.1. Light matter-interactions

The principle of UV-Visible absorption spectroscopy lies in light-matter interaction. When an incident beam of light falls on a sample with a certain intensity (I_0), part of it will be absorbed, reflected and/or scattered.

Absorption

In the UV-vis range, the absorption of light by molecules, ions or semiconductors is due to the interaction of the incident photon with the electron of the matter leading to its transition to an unoccupied higher energy level. These transitions are only observed for given wavelengths corresponding to the energy gap between the HOMO and the LUMO for molecules and ions and between the valence band and the conduction band for semiconductors (**Figure 2.5B**).

As presented in **Chapter 1: section 1.1.3.6**, metal nanoparticles generate localized surface plasmons when excited by light, leading to a strong absorbance at a specific wavelength (**Figure 2.5A**). More precisely, the measured signal corresponds to the extinction spectra, *i.e.*, the sum of absorbed and scattered light. The extinction wavelength strongly depends on the metal composition, nanoparticle size, geometry and aggregation level, and the surrounding dielectric environment [237]. These parameters can thus be extracted from the characterization of metal nanoparticles by UV-Vis absorption spectroscopy.

Upon light excitation, semiconductors can promote one electron from the valence band (VB) to the conduction band (CB) if the incident light has the same or higher energy than the band gap (E_g) (**Figure 2.5C**). Having the minimum energy for which the transition is produced, one can obtain the band gap of a material. In semiconductors, there are two types of band gaps: direct and indirect (**Figure 2.6**). In direct band gap transitions, the photon is absorbed, and an electron is promoted to the conduction band, creating a hole in the valence band. In this case, the electrons', and holes' wave vector (k) or momentum is the same in both the VB and the CB. In indirect band gap transitions, the absorbed photon needs to be complemented by a phonon absorption as the wave vectors of the electrons and holes in the VB and CB differ [96].

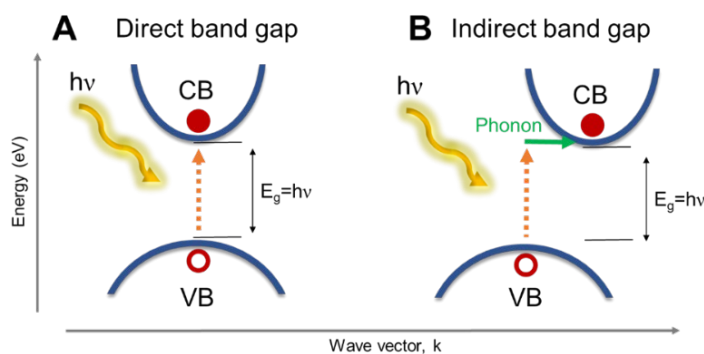


Figure 2.6. Electronic transitions in semiconductors. (A) Direct band gap transition. (B) Indirect band gap transition.

Elastic Scattering

Light scattering is due to the presence of particulate scatterers that have a refraction index different from that of their surrounding medium. When light crosses a suspension with particles' diameter lower than the in-coming light wavelength, a decrease of the transmitted light is observed due to the elastic scattering of the incident light away from the incident beam (Rayleigh scattering process) (**Figure 2.5D**) [238].

2.5.2. UV-Visible spectrophotometric techniques used in this work

From the UV-Vis absorption spectra, one can extract critical information, such as the concentration of optically active species, the frequency of localized surface plasmons or the band gap of a semiconductor.

Determination of catalytic activity

Thanks to the Beer-Lambert law, for a homogeneous solution, *i.e.*, dissolved molecules or ions, the transmitted light is related to the concentration of optically active species (**Equation 2.5**).

Equation 2.5. Beer-Lambert law.

$$A = \varepsilon \cdot l \cdot c$$

where A is absorbance, ε is the extinction molar coefficient for a specific wavelength, l is the path length of the light through the sample, and c is the concentration of the considered species. The absorbance (A) is defined as the negative logarithm of the transmittance (T), which corresponds to the ratio between the incident light's intensity (I_0) and the transmitted light's intensity (I) (**Equation 2.6**).

Equation 2.6.

$$A = \log \frac{I_0}{I} = \log \frac{1}{T} = -\log T = 2 - \log(\%T)$$

For this law to be applicable, the incident light should be at a normal angle from the surface, the solution should be isotropic and not ionizable, not fluorescent, and there should not be complex formation [239]. In addition, absorbance values should be kept between 0 and 1.

By measuring the absorbance of a coloured reactant or product as a function of time, one can follow reaction kinetics [240].

Bacterial density determination

Bacteria in suspension scatter light, producing a reduction of the transmitted light compared to the incident one. This measurement is an important parameter for microbial growth as the amount of scattered light is proportional to the organism in the solution (**Figure 2.5D**). By measuring the difference between incident light intensity and transmitted light intensity with a UV-vis spectrometer, it is possible to quantify bacterial growth by obtaining the optical density (OD). The light that passes through the sample should not harm bacteria; thus, a 600 nm wavelength is chosen to measure OD. This measurement is called OD600 [241].

Determination of semiconductor band gap

In the case of a semiconductor, the band gap can be determined using the Tauc equation (**Equation 2.7**).

Equation 2.7.

$$(\alpha \cdot h\nu)^{1/\gamma} = B(h\nu - E_g)$$

where α is the absorption coefficient, h is Planck's constant, ν is the photon frequency, and B is a constant. The γ factor depends on the type of transition, direct (1/2) and indirect (2) allowed transitions, respectively. It has to be noted that this factor can also be 3 and 3/2 for direct forbidden transition and indirect forbidden transition, respectively, but in the scope of this work, we only focus on the allowed transitions.

Assuming that the scattering of light passing through a sample is negligible, the normal incident light passing through a sample is the sum of the absorbed, transmitted, and reflected light. If the percentage of reflected light is lower than 10%, the reflectance can be neglected to obtain the absorption coefficient. The absorption coefficient is calculated following the Beer-Lambert law (**Equation 2.8**) [242]:

Equation 2.8.

$$\alpha = \frac{2.303 \cdot A}{d} = 2.303 \times \frac{2 - \log(\%T)}{d} = \frac{\ln\left(\frac{100}{\%T}\right)}{d}$$

where d is the pathlength.

By plotting the Tauc plot vs the photon energy ($h\nu$) of semiconductors, a steep linear increase is observed, which implies the energy absorption by the material (**Equation 2.7**). As shown in **Figure 2.7A**, the x-axis intersection point of the linear fit provides the approximate value of the band gap energy [243]. In the case of indirect semiconductors, there may be two linear parts, which allow to calculate the energy of the band gap (E_g) and the energy of the phonon (E_p) as shown in **Figure 2.7B** [244].

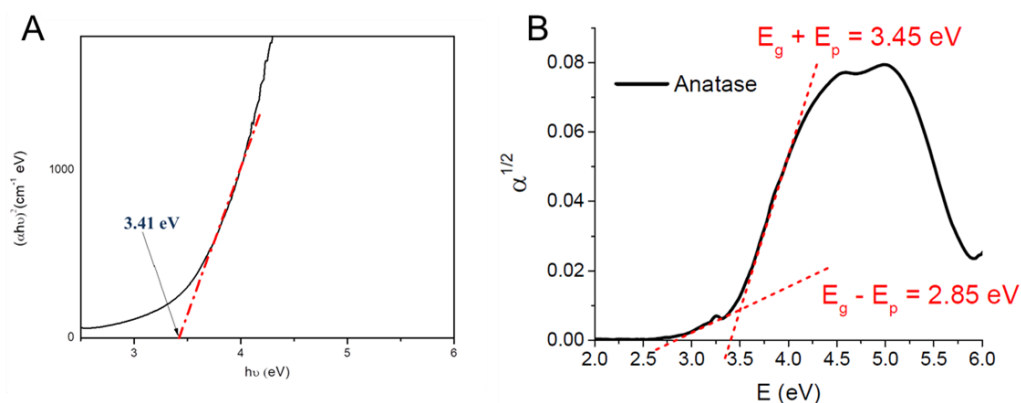


Figure 2.7. (A) Tauc's plot for the direct band gap energy calculation. The linear part extrapolated to the x-axis intersection provides a value of a direct band gap of 3.41 eV. Extracted from Yogamoorthy *et al.* [245]. (B) Tauc plot for the indirect band gap energy calculation. The linear part extrapolated to the x-axis intersection provides a value of indirect band gap of 3.05 eV. Extracted from Maheu *et al.*[246]

2.5.3. UV-Vis instruments used in this work

UV-Vis spectrophotometer is composed of two light sources. The most common light sources are a deuterium lamp, which produces light in the UV region (190-400 nm) and a tungsten filament, which produces light in the visible-IR region (300-2500 nm). Subsequently, the light is filtrated with a monochromator, passing through the sample, and the transmitted light is amplified and then detected.

2.5.3.1. UV-Vis absorption spectroscopy: nanoparticles surface plasmon resonance

The UV-Visible absorption spectroscopy was done with a SAFAS-UV mc2 double-beam spectrometer (Monaco). The spectra acquisition was made by scanning the 400 to 800 nm wavelength range, using a bandwidth of 2 nm, a wavelength step of 1 nm and an optical path of 1 cm.

2.5.3.2. UV-Vis well plate reader: study of nanoparticles catalytic activity, singlet oxygen production and bacterial growth

Study of nanoparticles' catalytic activity

The catalytic activity of nanoparticles as peroxidase mimics was investigated through the oxidation of a substrate, 3,3',5,5'-Tetramethylbenzidine (TMB), in the presence of H₂O₂. The catalysed reaction produces a change of colour (blue, 650 nm) which is measured with a UV-vis spectrometer. A Multiskan Go UV-Visible microplate reader from ThermoFisher Scientific was used to measure catalytic activity. Data were collected using SkanIt software. More details are provided in **Chapter 4: section 4.1.2**.

Study of singlet oxygen production/scavenging

A UV-Vis well plate reader was also used to characterize the qualitative production or scavenging of singlet oxygen by the nanoparticles by measuring the absorbance decay of 9,10-Anthracenediyl-bis(methylene)dimalonic acid (ABDA) upon reaction with singlet oxygen (¹O₂). ABDA is a coloured substrate (absorption maximum at 380 nm), but in the presence of ¹O₂, it is oxidized to an uncoloured product. H₂O₂ and/or O₂ dissolved in water can be transformed into ¹O₂ spontaneously or by external factors such as UV light. Nanoparticles can enhance their production or scavenge the ones produced. The difference between the absorbance decay of ABDA+H₂O₂/O₂ (control) with the one of the ABDA+H₂O₂/O₂+nanoparticles allows knowing if the nanoparticles catalyse the production of ¹O₂ or scavenge the ones produced spontaneously or by external factors [247]. A CLARIOstar plate reader (BMG Labtech) was used for these measurements. More details are provided in **Chapter 4: section 4.1.3.2**.

Study of bacterial growth

The characterization of bacterial growth was followed by a CLARIOstar plate reader (BMG Labtech) used for these measurements at OD600. More details are provided in **Chapter 5: section 5.1.2**.

2.5.3.3. UV-Vis absorbance spectroscopy: optical band gap determination

The band gap (E_g) can be calculated from the absorbance following Tauc model [248]. The sample transmittance and reflectance were performed with a Perkin Elmer Lambda 45 spectrometer equipped with an integrating sphere (RSA-PE-20) at room temperature. The inner wall of the integrating sphere was made of BaSO₄ powder as the reference. BaSO₄ is a white material with high reflectance that causes light to scatter uniformly, enabling a highly accurate detection of transmitted or reflected light from the sample. More details are provided in **Chapter 4: section 4.1.3.1**.

Table 2.1 summarizes the different UV-Vis-based techniques used in this work with their physical principles.

Table 2.1. Summary of UV-Vis spectrophotometric techniques.

| Objectives | Light-matter interaction | Physical law applied | Technique used | Type of instrument |
|------------------------|---------------------------------|-----------------------------|-----------------------|--|
| Catalytic activity | Absorption | Beer-Lambert | Transmission | UV-Vis microplate reader |
| Bacterial density | Scattering | Beer-Lambert | Transmission | UV-Vis microplate reader |
| Plasmonic properties | Absorption, scattering | - | Transmission | UV-Vis standard spectrophotometer |
| Band Gap determination | Absorption | Tauc plot | Transmission | UV-Vis spectrophotometer with integrating sphere |

2.6. X-ray and Ultraviolet photoelectron spectroscopy (XPS/UPS)

In this work, XPS/UPS was used to obtain the work function and the valence band of LiNbO_3 (LN) NPs, LN@BPEI NPs and LN/Au NPs.

Ultraviolet photoelectron spectroscopy (UPS) and X-ray photoelectron spectroscopy (XPS) are techniques that measure the kinetic energy of photoelectrons emitted from a sample in order to gain information on the electronic structure of the valence band, elemental composition of the external surface of a material (few nanometres of depth) as well as its chemical/oxidation state. The underlying mechanism in photoelectron spectroscopy is based on the photoelectric effect: when a photon of energy $h\nu$ hits a surface, it excites one electron of the valence band (UPS) or core electrons (XPS). The resulting kinetic energy (KE) of the photo-emitted electron is specified in **Equation 2.9**.

Equation 2.9

$$KE = h\nu - E_B - \phi$$

where $h\nu$ is the energy of the source, E_B is the binding energy between the electron and its corresponding state and ϕ is the work function.

The main difference between the techniques is the energy of the source and, consequently, the probed electron levels: UPS uses ultraviolet photon energy, and as a result, photoelectrons from the valence band are emitted. In the case of XPS, X-ray photon sources ($\text{AlK}\alpha$ or $\text{MgK}\alpha$ radiations) are used, and core-level electrons are analysed. Depending on the energies, it is possible to obtain different parameters summarized in **Table 2.2**. and **Figure 2.8** [249], [250].

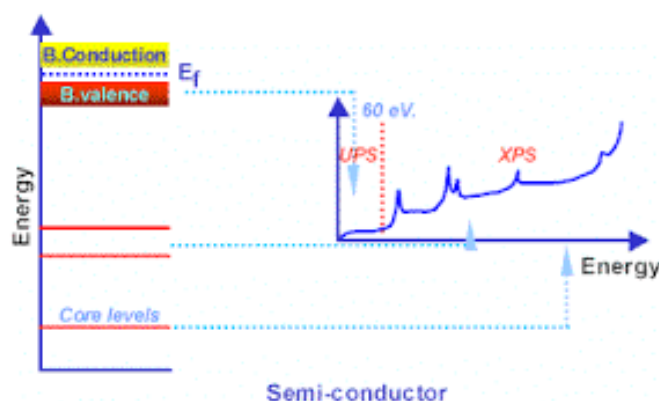


Figure 2.8. UPS and XPS spectra diagram. Extracted from Roland [251].

Table 2.2. Comparative table of UPS and XPS photoelectron spectroscopies.

| Parameter | UPS | XPS |
|-----------------------|---|---|
| Energy source | 10-60 eV | 200-2000 eV |
| Electron's excitation | Valence-level | Core-level |
| Information | Density of states Frontier orbital energies (HOMO) Work function | Elemental composition Electronic structure Chemical/oxidation state |
| Maximum depth | 3 nm | 10 nm |

The instrument is composed of a photon source that strikes the sample in an ultrahigh vacuum chamber (10^{-9} Torr). A collection lens collects the ejected electrons, and the kinetic energy is measured. Each peak energy is specific for each orbital of each element [249].

In this work, each sample was deposited by drop-casting onto an Ag foil previously cleaned by argon sputtering to reduce charge effects and for UPS calibration purposes [246]. Photoemission spectroscopy (PES) analysis was performed at IRCELYON using a commercial Kratos spectrometer. The valence band and core levels were analysed at 21.2 eV (He I) and 1486.6 eV (Al $K\alpha$), respectively, to determine the electronic density of orbitals O 2p, Ti 3d, and Au 4d at the outermost surface and the chemical environment by probing Ti 2p, Li 1s, Nb 3d, and Au 4f. Ag and Au foils were analysed as reference samples to determine the density of excited states around the Fermi level. In this context, the spectral weights of Au and Ag are required to determine their position and shape signal inside the valence band of each hybrid nanoparticle.

2.7. Fluorescence spectroscopy

This technique was used to characterize the generation or scavenging of hydroxyl and superoxide radicals. Certain substrates only react with one type of ROS and produce a change in fluorescence. For instance, the reaction products of terephthalic acid (TA) with hydroxyl

radicals and dihydroethidium (DHE) with superoxide radicals are fluorescent. If the fluorescence is lower in comparison to the control (substrate+H₂O₂/O₂), the nanoparticles scavenge the production of ROS, and if the fluorescent is higher to control, the nanoparticle produces ROS.

Fluorescence spectroscopy is a non-destructive technique which allows one to characterize and quantify species called fluorophores. Fluorophores are molecules which can be excited at a specific wavelength, followed by the emission of a photon with lower energy upon returning to the ground state. In brief, the incident light excites electrons from HOMO to LUMO. Due to collisions and other energy losses, the photon emitted from its relaxation possesses lower energy than the incident one (**Figure 2.9**). Both absorption and emission wavelengths are characteristic of a compound allowing qualitative and quantitative analysis [239].

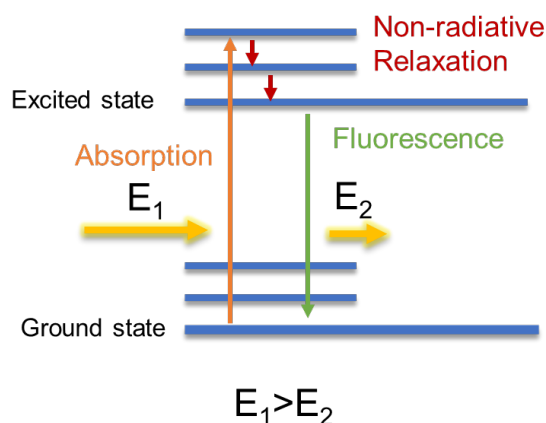


Figure 2.9. Fluorescent electronic transitions scheme.

The instrument that is used is a spectrofluorometer. It consists in a light source that passes through a filter or monochromator and excites the sample at a specific wavelength. The sample absorbs the incident light, and a detector measures the resultant fluorescent emission. Usually, the detector is placed at 90° from the incident beam to minimize the risk of transmitted and reflected light.

The hydroxyl radicals production (OH[•]) in the presence of O₂ or H₂O₂ in a solution can be measured through the hydroxylation of terephthalic acid (TA), which results in a fluorescent specie, 2-hydroxyl terephthalic acid. The fluorophore absorbs at $\lambda_{exc} = 320 \pm 15$ nm and emits at $\lambda_{em} = 420 \pm 10$ nm [252]. Similarly, the oxidation of dihydroethidium with superoxide radicals results in a fluorescent product, which is excited at $\lambda_{exc} = 490 \pm 10$ nm and emits at

$\lambda_{em} = 625 \pm 10$ nm [253]. In the present work, fluorescence spectroscopy measurements were done using a CLARIOstar plate reader (BMG Labtech). More details are provided in **Chapter 4: section 4.1.3.2**.

2.8. Conclusion

In this chapter, we discussed a set of techniques and apparatus that allowed us to characterize the physical and chemical properties of the nanoparticles, the enzyme-mimics of the potential Nanozymes, the elucidation of the mechanism of enzyme-mimics, and cell growth.

Chapter 3: Synthesis and Characterization of Hybrid Nanozymes.

This chapter aims to provide the synthesis and characterization of hybrid nanoparticles composed of LiNbO_3 and AuSeeds (LN/Au) and LiNbO_3 and PtSeeds (LN/Pt). An attempt was also made to produce LiNbO_3/Ag hybrid nanoparticles. The synthesis was implemented in TiO_2/Au and TiO_2/Pt hybrid NPs. As discussed in Chapter 1, seed decoration was selected to elaborate them. Seed decoration provides a large surface-to-volume ratio among the different structures of hybrid nanoparticles, which is ideal for catalysis purposes. In particular, seed decoration using an intermediate link between LN and metal seeds allows fine control of the synthesis of both components prior to their coupling (**Chapter 1: section 1.1.5**), and the possibility of a uniform distribution provides a good template for Nanozyme activity. The driving force in the synthesis is electrostatic interactions, as seen in **Figure 3.1**. The characterization of the as-prepared nanoparticles and the different steps during the synthesis are also shown.

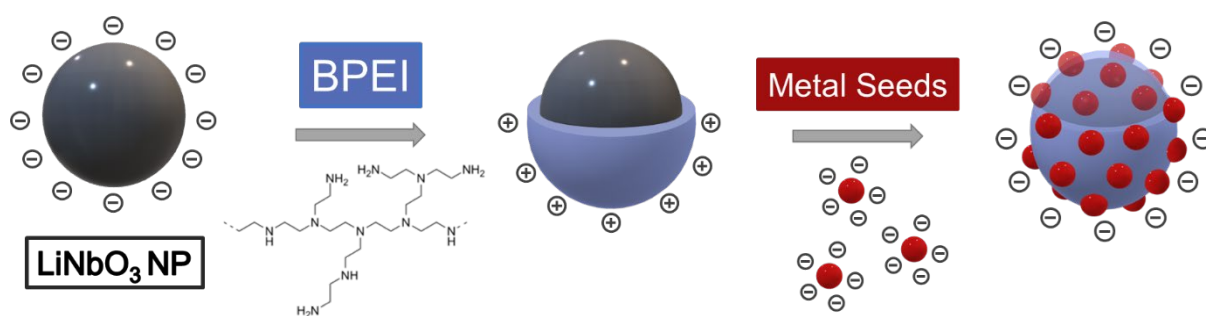


Figure 3.1. Scheme of the layer-by-layer synthesis method for LN/Au and LN/Pt hybrid NPs.

3.1. Materials and methods

3.1.1. Chemicals

Lithium niobium ethoxide ($\text{LiNb}(\text{OEt})_6$), (99+% metal basis, 5% w/v in ethanol) was obtained from Alfa Aesar (Kandel, Germany), Teflon cup (model 4749) was obtained from Parr Instrument (Moline, IL, USA). Butane-1,4-diol (99%), ethanol, gold (III) chloride trihydrate

($\text{HAuCl}_4 \cdot 3\text{H}_2\text{O}$, $\geq 99,9\%$ trace metals basis), chloroplatinic acid solution 8 wt. % in H_2O (H_2PtCl_6), silver nitrate (AgNO_3) ($>99\%$), sodium hydroxide (NaOH) pellets, branched polyethylenimine (BPEI), 25,000 g/mol, tetrakis-(hydroxymethyl)-phosphonium chloride (THPC) solution (80% w/v in water), and hydrogen peroxide (H_2O_2) solution 30 wt. % in H_2O (contains inhibitor) were purchased from Sigma Aldrich and used without modification. Titanium oxide P25 nanoparticles (TiO_2 NPs) were purchased from Degussa.

3.1.2. Synthesis of LiNbO_3 nanoparticles (LN NPs)

LN NPs were synthesized by the SYMME laboratory (Annecy) using a non-aqueous solvothermal alkoxide process, as previously described [188]. Briefly, inside an autoclave equipped with a 23 mL Teflon cup, 2.25 mL of lithium niobium ethoxide and 1.25 mL of butane-1,4-diol were added. The mixture was then heated in an oven (Mettert, Schwabach, Germany), increasing the temperature by 5 °C intervals every ten minutes until the temperature of 230 °C was attained, and this temperature was maintained for three days. After cooling to room temperature, the precipitate was transferred to Nalgene centrifuge tubes. Three centrifugation rounds at 13500 rpm for three minutes were carried out to collect the precipitate, which was washed in ethanol under sonication for ten minutes. The obtained LN NPs were dried at 75 °C and dispersed in water at 1 g/L mass concentration.

3.1.3. Polymer Adsorption onto LN NPs

BPEI polymer was used to coat the LN NPs. First, 50 mg of BPEI was weighed into a glass reactor vessel and dissolved in 40 mL of water while heating at 90 °C. The temperature was maintained at 90 °C with continuous stirring, and 4.9 mL of the 1 g/L LN NP dispersion was added to the reactor and left for 4 h. The mixture was allowed to cool to room temperature, and then the resulting BPEI-coated LN NPs (LN@BPEI NPs) were separated from any BPEI in excess by performing four, 10-minute centrifugation washing steps in water at 10 °C and 9100 g. The LN@BPEI NPs were then re-dispersed in water to obtain a final concentration of 0.35 g/L.

3.1.4. Synthesis of LN Coated with Noble Metal Seeds

As previously reported, the coating of BPEI-modified LN NPs by noble metal seeds was achieved in a two-step process [12]. Gold, platinum and silver seeds (AuSeeds, PtSeeds and AgSeeds) were prepared first. AuSeeds were synthesized using the protocol reported by Duff *et al.* [199]. The protocol for the synthesis of AgSeeds was the same as for AuSeeds, while PtSeeds were prepared using a slightly modified protocol [192].

For AuSeeds and AgSeeds, 540 μL of 0.1 M NaOH were added to 45.5 mL of deionized water, followed by 2.14 mL of a 4.2 mM solution of THPC under stirring and in the dark. For PtSeeds, the same protocol was used except that the reaction media (45.5 mL of deionized water) was pre-heated to 90-95 $^{\circ}\text{C}$. Subsequently, 360 μL of 25 mM HAuCl_4 , H_2PtCl_6 or AgNO_3 solution were added to produce AuSeeds, PtSeeds or AgSeeds, respectively. The final concentrations were 180 μM of HAuCl_4 , H_2PtCl_6 , or AgNO_3 , 180 μM of THPC and 1.08 mM of NaOH. The colour of the solutions quickly changed from transparent to red, dark green or yellow for AuSeeds, PtSeeds, or AgSeeds, respectively. The solutions were kept under stirring for 10 minutes, then for PtSeeds, it was let to cool down, and both solutions were stored at 4 $^{\circ}\text{C}$. The final theoretical concentrations of AuSeeds, PtSeeds, and AgSeeds were 0.037, 0.036 and 0.020 g/L, respectively.

The attachment of the noble metal seeds to LN NPs was done following a layer-by-layer method [12], [254]. The positively-charged LN@BPEI NPs (0.35 g/L) were seeded with negatively-charged THPC-functionalized AuSeeds, AgSeeds and PtSeeds by electrostatic interactions (**Figure 3.1**). The ratios of AuSeeds to LN NPs, PtSeeds to LN NPs and AgSeeds to LN NPs in the 30-200, 10-60, and 1-10 ranges were selected, respectively. Based on the concentrations of LN@BPEI, AuSeeds, PtSeeds and AgSeeds, the volume ratios presented in **Table 3.1** were used to prepare hybrid LN/Au, LN/Pt, and LN/Ag NPs.

Table 3.1. The ratios of noble metal seeds to LN NPs and volumes of AuSeeds, PtSeeds and AgSeeds used to prepare noble metal seeded-LN NPs, starting from a 0.35 g/L LN@BPEI NPs dispersion and 0.037 g/L, 0.036 g/L and 0.020 g/L of AuSeeds, PtSeeds, and AgSeeds, respectively.

| Sample name | Noble metal seeds | Noble metal seeds to LN NPs theoretical ratio | Volume Ratio metal seeds to LN@BPEI |
|-------------|-------------------|---|-------------------------------------|
| LN/Au1 | | 30 | 0.35 |
| LN/Au2 | AuSeeds | 100 | 1.05 |
| LN/Au3 | | 200 | 2.44 |
| LN/Pt1 | | 10 | 0.35 |
| LN/Pt2 | PtSeeds | 60 | 2.44 |
| LN/Ag1 | | 1 | 0.35 |
| LN/Ag2 | AgSeeds | 10 | 2.44 |

Water was added to the mixture of LN@BPEI and noble metal seeds to get an identical total reaction volume for all the samples. Each mixture was stirred for 30 min and aged for 72 h at 4 °C. The non-attached noble metal seeds were removed by two centrifugation steps of 10 min, 20 °C and 8603 g. Finally, deionized water was added to get a final theoretical LN concentration of 0.35 g/L in all samples. Samples nomenclature is specified in the first column of **Table 3.1**.

3.1.5. Synthesis of TiO₂ NPs Coated with Noble Metal Seeds

As for LN NPs, we synthesized TiO₂/metal hybrid nanoparticles through electrostatic interactions. Metal Seeds were synthesized as in the previous section (3.1.4), and TiO₂ NPs were purchased from Degussa, P25 type. TiO₂ NPs commercial powder was dispersed in water to a final concentration of 0.35 g/L. The solutions were stored at 4 °C.

The attachment of the noble metal seeds to TiO₂ NPs was done following a layer-by-layer method [12], [254]. The positively-charged TiO₂ NPs (0.35 g/L) were seeded with negatively-charged THPC-functionalized AuSeeds and PtSeeds by electrostatic interactions. The ratios of AuSeeds to TiO₂ NPs and PtSeeds to TiO₂ NPs in the 30-200 and 10-60 ranges were selected, respectively. Based on the concentrations of TiO₂ NPs, AuSeeds and PtSeeds, the volume ratios presented in **Table 3.2** were used to prepare hybrid TiO₂/Au and TiO₂/Pt NPs.

Table 3.2. The ratios of noble metal seeds to TiO₂ NPs and volumes of AuSeeds and PtSeeds used to prepare noble metal seeded-TiO₂ NPs, starting from a 0.35 g/L LN@BPEI NPs dispersion and 0.037 g/L and 0.036 g/L of AuSeeds and PtSeeds, respectively.

| Sample name | Noble metal seeds | Noble metal seeds to TiO ₂ NPs theoretical ratio | Volume Ratio metal seeds to TiO ₂ |
|----------------------|-------------------|---|--|
| TiO ₂ /Au | AuSeeds | 30 | 1 |
| TiO ₂ /Pt | PtSeeds | 10 | 1 |

Water was added to the mixture of TiO₂ NPs and noble metal seeds to get an identical total reaction volume for all the samples. Each mixture was stirred for 30 min and aged for 72 h at 4 °C. The non-attached noble metal seeds were removed by two centrifugation steps of 10 min, 20 °C and 8603 g. Finally, deionized water was added to get a final theoretical TiO₂ concentration of 0.35 g/L in all samples. Samples nomenclature is specified in the first column of **Table 3.2**.

3.1.6. Structural Characterization of NPs

The techniques used to characterize the structure of NPs are TEM, EDS, DLS, zetammetry and UV-Vis absorption spectroscopy. Their principle and operating conditions are detailed in **Chapter 2**.

3.2. Results and Discussion

3.2.1. Characterization of the starting building blocks of LN/Au and LN/Pt hybrid NPs (LN NPs, LN@BPEI, AuSeeds, PtSeeds)

The characterization of the building blocks forming the hybrid nanoparticles is shown in **Figure 3.2** and **Table 3.3**.

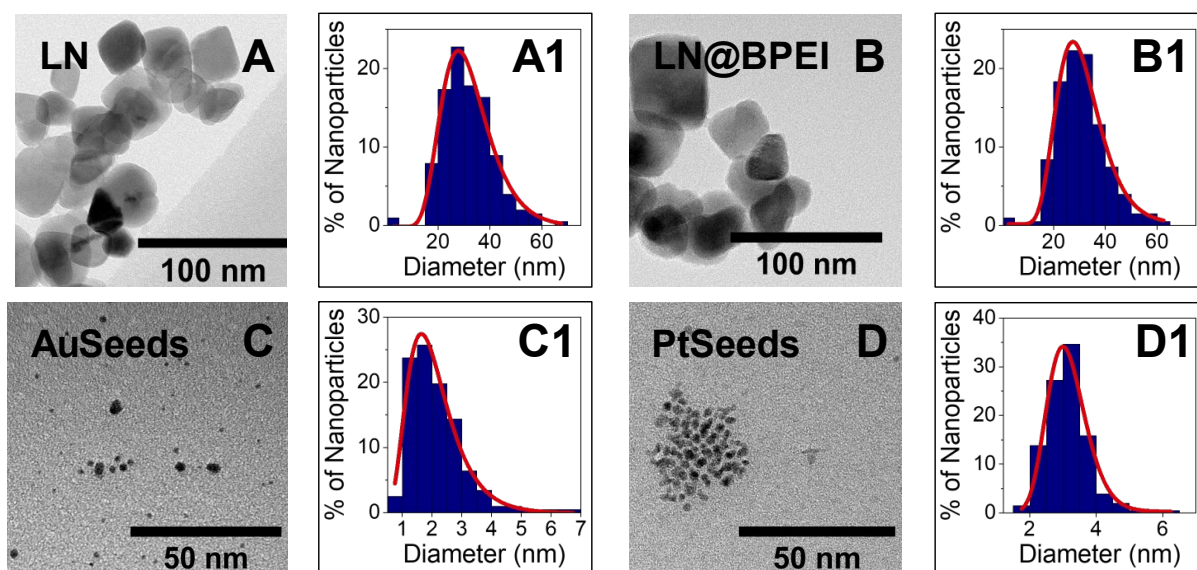


Figure 3.2. TEM image and TEM diameter lognormal distribution of (A, A1) LN NPs, (B, B1) LN@BPEI, (C, C1) AuSeeds and (D, D1) PtSeeds.

Table 3.3. TEM diameter, hydrodynamic diameter, and zeta potential values of LN NPs, LN@BPEI NPs, AuSeeds and PtSeeds.

| Sample name | TEM diameter (nm) \pm SD | Hydrodynamic diameter (nm) \pm SD | Zeta potential (mV) \pm SD |
|-------------|----------------------------|-------------------------------------|------------------------------|
| LN | 30.4 \pm 8.6 | 114.2 \pm 1.7 | -42.5 \pm 0.8 |
| LN@BPEI | 29.6 \pm 8.4 | 147.6 \pm 2.8 | +39.4 \pm 3.6 |
| AuSeeds | 2.0 \pm 0.8 | 36.0 \pm 8.5 | -12.1 \pm 6.0 |
| PtSeeds | 3.1 \pm 0.6 | 135.7 \pm 6.6 | -14.7 \pm 2.4 |

The average TEM diameter calculated from 200 LN NPs was 30.4 \pm 8.6 nm (**Figure 3.2A-A1**), and the corresponding hydrodynamic diameter from DLS measurements was 114.2 \pm 1.7 nm (**Table 3.3**). This latter value is significantly larger than the average diameter determined by TEM as it considers the entire solvation sphere consisting of the ions in the Stern and diffuse layers around the LN NPs. The zeta potential was around -40 mV in water leading to a stable LN NPs dispersion. This negative zeta potential can be attributed to uncoordinated -OH groups on the LN surface, which are commonly observed on the surface of oxide nanoparticles [12]. The Li/Nb atomic ratio was determined by ICP-AES, leading to a ratio of 1.02, which is close

to the theoretical expected value in LiNbO_3 [255]. Following BPEI adsorption onto LN NPs, LN@BPEI NPs showed blurred edges and difficulty in focussing particles during TEM, which may be attributed to the presence of BPEI polymer on their surface, as marked in **Figure 3.2B-B1**. The hydrodynamic diameter of LN@BPEI NPs was 147.6 ± 2.8 nm (**Table 3.3**), an increase of around 30% compared to the native LN NPs suggesting the presence of an additional hydrodynamic layer on the NPs. Additionally, the zeta potential was found to be 39.4 ± 3.6 mV and was reversed from negative to positive, which supports the presence of protonated $-\text{NH}_2$ groups on the surface of LN@BPEI NPs [256].

AuSeeds and PtSeeds were synthesized by the salt reduction method using THPC as a reducer (**Figure 3.2C** and **Figure 3.2D**). AuSeeds' average diameter calculated from 200 NPs observed by TEM was 2.0 ± 0.8 nm (**Table 3.3**). PtSeeds diameter was slightly higher, with an average value of 3.1 ± 0.6 nm. UV-Vis absorption spectroscopy reveals a slight plasmon band around 504 nm for AuSeeds and no plasmon band in the visible region for PtSeeds (**Figure 3.3**). The hydrodynamic diameters for AuSeeds and PtSeeds were 36.0 ± 8.5 nm and 135.7 ± 6.6 nm (**Table 3.3**). The THPC coating and the solvating layer of nanoparticles associated with the presence of some aggregates may explain AuSeeds difference in TEM-determined diameter and DLS hydrodynamic diameter. Similarly, for PtSeeds, the presence of aggregates is more significant (as seen in the TEM image, **Figure 3.2D**), leading to a considerable increase in the hydrodynamic diameter measured by DLS [257]. Both noble metal seeds' zeta potential values in water were negative due to the presence of THPC's product on their surface [192], [258].

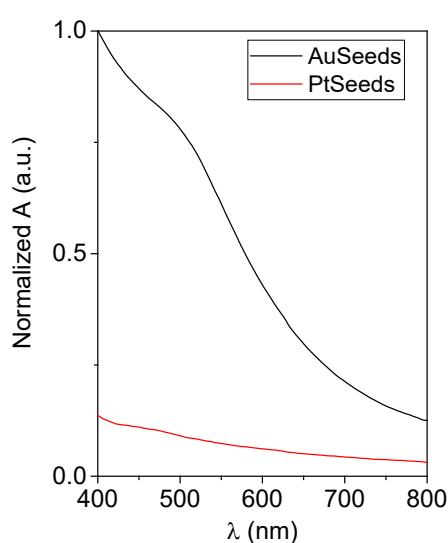


Figure 3.3. UV-Vis absorption spectra of AuSeeds (black) and PtSeeds (red).

3.2.2. Characterization of LN/Au and LN/Pt Hybrid Nanoparticles

Gold or platinum-coated LN NPs were then prepared by electrostatic assembly of the individual building blocks while employing the opposite surface charges of LN@BPEI particles and noble metal seeds. TEM images of LN/Au and LN/Pt NPs prepared with different noble metal seeds to LN ratios are shown in **Figure 3.4**, and the corresponding hydrodynamic diameters and zeta potential values are presented in **Table 3.4**.

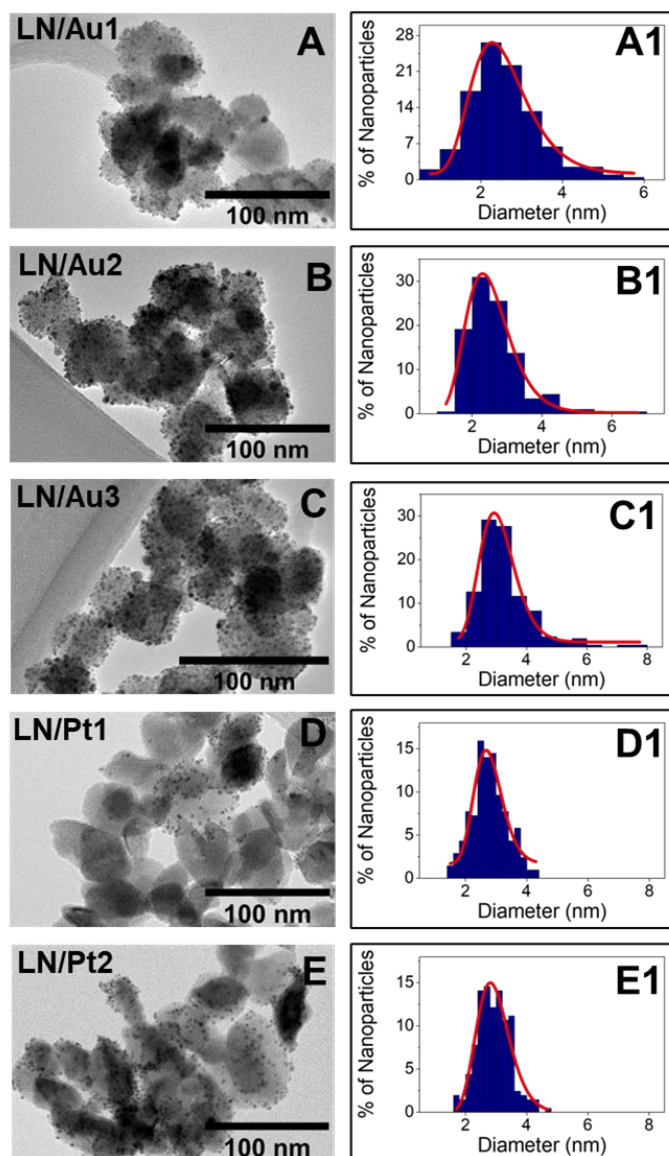


Figure 3.4. TEM images and corresponding diameter of noble metal seeds deposited onto LN fitted to a lognormal distribution for LN/Au (A-A1, B-B1, C-C1) and LN/Pt (D-D1, E-E1) NPs. LN/Au NPs and LN/Pt NPs were prepared with the following metal seeds to LN ratios: 30 for LN/Au1 (A, A1), 100 for LN/Au2 (B, B1), 200 for LN/Au3 (C, C1), 10 for LN/Pt1 (D, D1) and 60 for LN/Pt2 (E, E1).

Table 3.4 TEM diameter of metal seeds onto LN@BPEI, hydrodynamic diameter, zeta potential values of LN/Au and LN/Pt NPs measured in water, and molar percentage of noble metal content in LN/Au and LN/Pt determined by EDS.

| Sample name | TEM diameter of metal seeds onto the LN@BPEI (nm) \pm SD | Hydrodynamic diameter of hybrid NPs (nm) \pm SD | Zeta potential of hybrid NPs (mV) \pm SD | Molar percentage of noble metal determined by EDS (%) |
|-------------|--|---|--|---|
| LN/Au1 | 2.4 \pm 0.8 | 233.7 \pm 8.6 | +24.6 \pm 1.0 | 5.7 (Au) |
| LN/Au2 | 2.5 \pm 0.7 | 164.2 \pm 0.5 | -28.7 \pm 0.3 | 11.2 (Au) |
| LN/Au3 | 3.1 \pm 0.8 | 160.5 \pm 2.1 | -32.1 \pm 0.4 | 16.2 (Au) |
| LN/Pt1 | 2.5 \pm 0.6 | 176.4 \pm 3.3 | +23.2 \pm 1.5 | 3.9 (Pt) |
| LN/Pt2 | 2.5 \pm 0.5 | 366.9 \pm 2.1 | -12.6 \pm 0.5 | 6.8 (Pt) |

A brownish supernatant, corresponding to free AuSeeds, was observed for LN/Au3 after the first centrifugation step, indicating the saturation of LN@BPEI surface with the AuSeeds. As shown in **Table 3.4**, when deposited onto LN@BPEI NPs, for LN/Au1 and LN/Au2, AuSeeds TEM diameter seems to not significantly increase compared to the initial AuSeeds (see **Table 3.3**). In the case of LN/Au3, a slight increase in the TEM diameter is observed. This slight diameter increase may come from the reduction and coalescence of the AuSeeds on the surface of LN@BPEI. Indeed, the NH_3^+ groups of the BPEI polymer can also act as a reducing agent [254], which may reduce any previously unreduced chloroaurate ions present in the gold seed solution, especially when an excess of this solution is added to LN@BPEI such as for LN/Au3. The hydrodynamic diameter of LN/Au NPs tends to decrease with the increasing amount of gold on the surface of LN, which is consistent with the increase in the absolute value of their zeta potential from positive in the case of LN@BPEI to highly negative for LN/Au3. This could be attributed to a higher degree of surface coverage by Au Seeds for LN/Au3 compared to LN/Au1 and LN/Au2. In fact, the zeta potential value of the least gold-coated LN/Au1 nanoparticles is still positive, perhaps due to the predominance of positive charges from BPEI, which negative AuSeeds are unable to screen. As reflected from **Figure 3.4A**, the coating of LN@BPEI NPs with AuSeeds at the lowest concentration is uneven. However, when the

AuSeeds surface density increases, zeta potential becomes negative; thus, it could be supposed that, in this case, most of the amine groups of BPEI have been utilised to immobilize AuSeeds. The gold loading determined by EDS confirms the gold deposition control by varying the volume of AuSeeds suspension added to LN@BPEI. We further confirmed the presence of AuSeeds onto LN@BPEI NPs by STEM and EDS chemical mappings (**Figure 3.5A-A3**). The surface density of LN/Pt was monitored by varying the PtSeeds to LN NPs ratio, as for LN/Au. As shown in **Figure 3.4**, the increasing PtSeeds to LN ratio leads to a higher surface density associated with a more homogeneous spatial distribution of PtSeeds onto LN. As for LN/Au NPs, the zeta potential of LN/Pt NPs decreases with the Pt coverage, starting from a positive value for the lowest Pt amount. For the highest Pt loading, the zeta potential around -12 mV can be associated with low repulsive electrical charges between NPs, which can explain the increased hydrodynamic diameter. Concerning the molar percentage of Pt, as for LN/Au, the EDS results show an increasing content of Pt as the ratio of PtSeeds volume to LN@BPEI volume is increased. We further confirmed the presence of PtSeeds onto LN@BPEI by STEM and EDS chemical mappings (**Figure 3.5B-B3**).

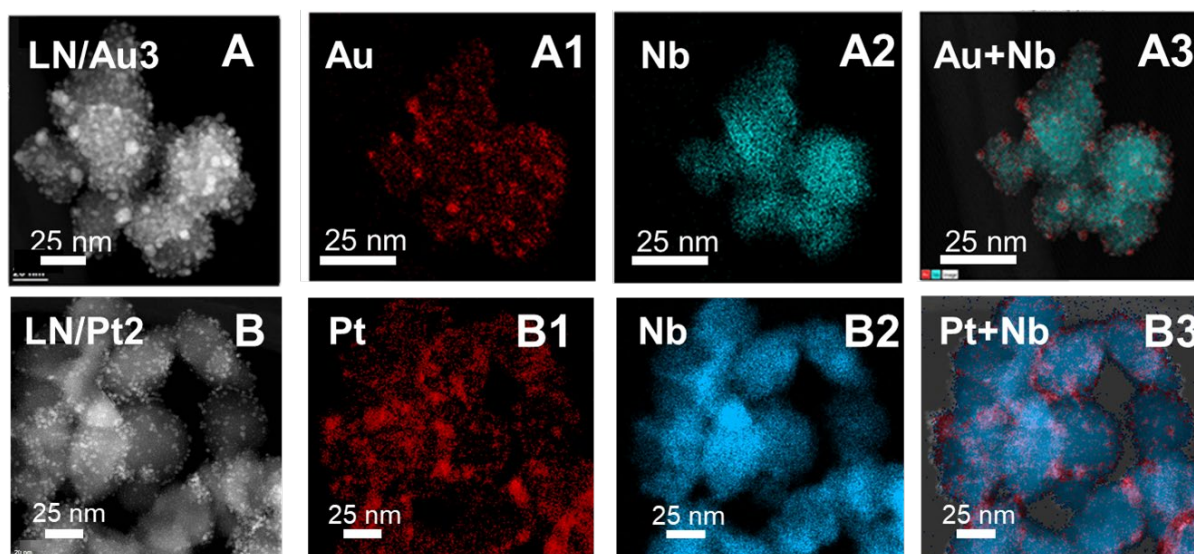


Figure 3.5. (A) STEM image of LN/Au₃ with corresponding EDS chemical maps of (A1) Au, (A2) Nb and (A3) Au and Nb merged on the same image. (B) STEM image of LN/Pt₂ with corresponding EDS chemical maps of (B1) Pt, (B2) Nb and (B3) Pt and Nb merged on the same image.

Furthermore, the characterization of the crystalline facets by HRTEM of AuSeeds in LN/Au₃ (**Figure 3.6A**) and PtSeeds in LN/Pt₂ (**Figure 3.6B**) leads to the conclusion that the same facets

of Au and Pt are present on the LN surface, which suggests that similar mode of interactions are likely to be involved during the construction of LN/Au and LN/Pt hybrid materials. It has been shown that Au (111) facet, which is equivalent to (1-11) or (11-1) facets (**Figure 3.6A**), is less catalytically active than other facets (110) or (211) [54]. The presence of (200) facets in PtSeeds may confer a higher catalytic activity.

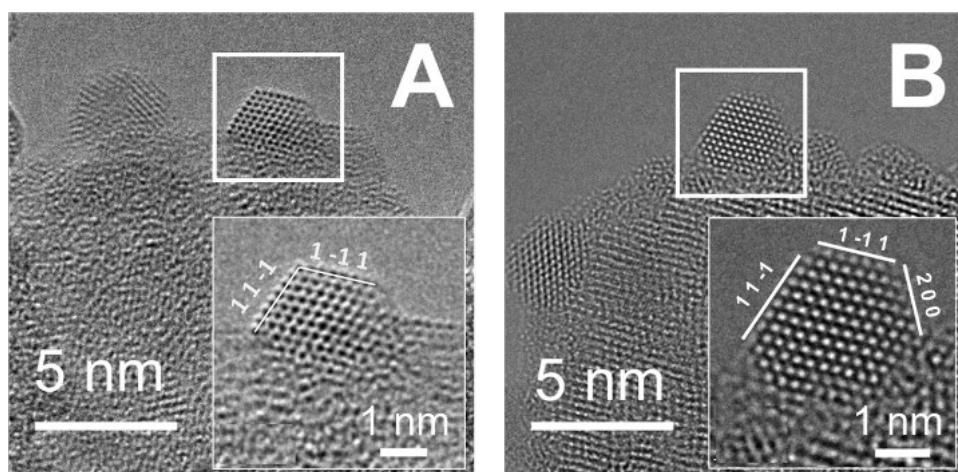


Figure 3.6. HRTEM image and facets characterization of metal seeds: (A) AuSeeds on LN/Au3 and (B) PtSeeds on LN/Pt2. In both cases, LN-bound Au and Pt have an expected well-defined face centred cubic (fcc) structure.

3.2.3. Attempt to produce LN/Ag hybrid NPs

We further extend the method for synthesising AgSeeds and LN/Ag hybrid NPs. We prepared them according to the same protocol used for LN/Au and LN/Pt (**section 3.1.4**) but using AgNO₃ as a silver precursor. Then we deposit them onto LN@BPEI with two AgSeeds to LN@BPEI volume ratios: 0.35 (LN/Ag1) and 2.44 (LN/Ag2). Their characterization is presented in **Figure 3.7** and **Table 3.5**.

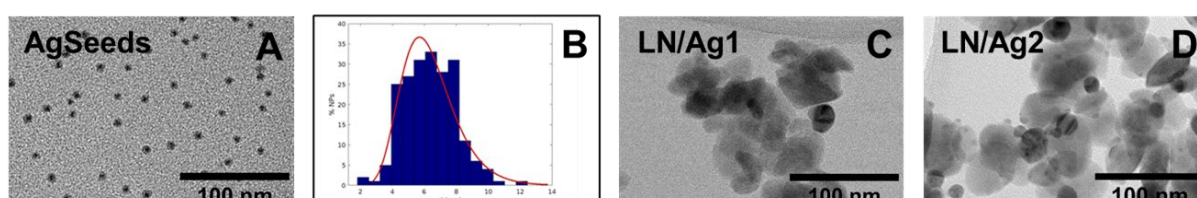


Figure 3.7. TEM images of AgSeeds (A), log normal fitted diameter distribution of AgSeeds (B), LN/Ag1 hybrid nanoparticles (C) and LN/Ag2 hybrid nanoparticles (D).

Table 3.5. TEM diameter of AgSeeds and AgSeeds onto LN@BPEI, hydrodynamic diameter and zeta potential values of AgSeeds and LN/Ag measured in water, and molar percentage of noble Ag content in LN/Ag determined EDS.

| Sample name | TEM diameter of metal seeds onto the LN@BPEI | Hydrodynamic diameter of NPs (nm) | Zeta potential of NPs (mV) | Molar percentage of noble metal determined by EDS (%) |
|-------------|--|-----------------------------------|----------------------------|---|
| AgSeeds | 6.1 ± 1.7 | 17.0 ± 0.1 | -43.6 ± 1.4 | - |
| LN/Ag1 | 14.2 ± 5.7 | 224.1 ± 5.2 | $+18.5 \pm 0.2$ | 10.3 (Ag) |
| LN/Ag2 | 14.4 ± 5.6 | 263.7 ± 5.6 | $+10.2 \pm 0.2$ | 31.6 (Ag) |

AgSeeds TEM diameter is of 6.1 ± 1.7 nm. This value is significantly higher than the values obtained for AuSeeds (2.0 ± 0.8) and PtSeeds (3.1 ± 0.6) (**Table 3.3**). Similarly, for LN/Ag1 and LN/Ag2, the TEM diameter of the AgSeeds onto LN@BPEI (~ 14 nm) is much higher than the ones measured for AuSeeds and PtSeeds on LN@BPEI, which remain under 4 nm (**Table 3.4**). BPEI is a reducing agent which can produce the coalescence of the already-formed AgSeeds [259]. Additionally, their distribution over LN@BPEI was inhomogeneous. Ag NPs' bigger size and poorer distribution than for Au or Pt hybrid nanoparticles have already been reported in Fe₂O₃/metal hybrid nanoparticles [53]. AgSeeds zeta potential value (-43.6 ± 1.4 mV) is much more negative than for AuSeeds or PtSeeds (**Table 3.3**). Surprisingly, LN/Ag2 does not overcome the LN@BPEI positive zeta potential as in LN/Au3 and LN/Pt2. LN/Ag1 (**Figure 3.7C**) and LN/Ag2 (**Figure 3.7D**) TEM images show LN NPs in pale grey and AgSeeds in dark grey due to the higher electron density in AgSeeds [230]. LN/Ag1 present less amount of AgSeeds than LN/Ag2, which confirms the control of the synthesis for LN/Au nanohybrids and LN/Pt nanohybrids. However, their structure cannot be related to a seed-decorated one (**Chapter 1: Figure 1.9**). Moreover, AgSeeds diameter is closer to LN NPs. Therefore, the marked differences in the diameter, the surface charge, and the disposition of the seeds in the LN NPs do not allow us to compare LN/Ag with LN/Au and LN/Pt in catalysis.

3.2.4. Reproducibility and ageing

We also assessed the impacts of batch-to-batch variability in the synthesis and the influence of long-term storage stability of these hybrid nanoparticles. For this study, we produced two independent batches of these hybrids (**Table 3.6, Figure 3.8, Appendix: Figure A1**) and re-characterised one after more than one year of storage under ambient conditions (**Figure 3.8**).

Table 3.6. Data was collected from multiple samples for LN/Au and LN/Pt, including samples aged more than 1 year (old). TEM diameter of metal seeds onto LN@BPEI, zeta potential values of LN/Au and LN/Pt NPs measured in water, and molar percentage of noble metal content in LN/Au and LN/Pt determined by EDS. In parenthesis, it is included the average of the same parameters of the sample presented before (**Table 3.3, Table 3.4**).

| Sample name | TEM diameter of metal seeds and metal seeds onto the LN@BPEI (nm) | Zeta potential of metal seeds and hybrid NPs (mV) | Molar percentage of noble metal in the hybrid NPs determined by EDS (%) |
|-------------|---|---|---|
| AuSeeds-2 | 2.0 ± 0.5 (2.0) | -24.4 ± 3.3 (-12.1) | - |
| AuSeeds-old | 3.8 ± 1.0 (2.0) | -14.7 ± 4.6 (-12.1) | - |
| LN/Au1-2 | 2.6 ± 0.7 (2.4) | +31.6 ± 0.2 (+24.6) | 3.6 (Au) (5.7) |
| LN/Au2-2 | 3.2 ± 0.8 (2.5) | -24.7 ± 0.5 (-28.7) | 11.0 (Au) (11.2) |
| LN/Au3-2 | 3.3 ± 0.6 (3.1) | -34.4 ± 0.3 (-32.1) | 17.4 (Au) (16.2) |
| LN/Au3 old | 4.8 ± 1.6 (3.1) | -31.8 ± 0.7 (-32.1) | - |
| PtSeeds-2 | 2.8 ± 0.9 (3.1) | -31.6 ± 2.1 (-14.7) | - |
| PtSeeds-old | 2.9 ± 0.6 (3.1) | -13.9 ± 3.2 (-14.7) | - |
| LN/Pt1-2 | 2.9 ± 0.7 (2.5) | -0.6 ± 0.1 (+23.2) | 3.7 (Pt) (3.9) |
| LN/Pt2-2 | 2.9 ± 0.6 (2.5) | -22.8 ± 1.1 (-12.6) | 10.8 (Pt) (6.8) |
| LN/Pt2 old | 2.5 ± 0.3 (2.5) | -24.6 ± 3.7 (-12.6) | - |

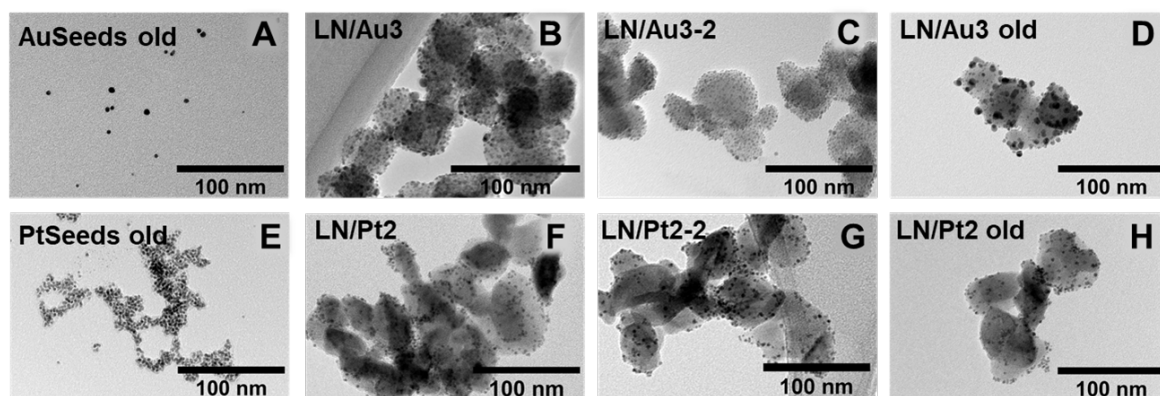


Figure 3.8. (A) TEM images of AuSeeds aged for more than one year. (B and C) TEM images of two independent batches of LN/Au3 and (D) LN/Au3 aged for more than one year. (E) TEM images of PtSeeds aged for more than one year. (F and G) TEM images of two independent batches of LN/Pt2 and (H) LN/Pt2 aged for more than one year.

The outcomes reveal that the synthesis method is reproducible with an acceptable level of variability between the batches in regard to the size of the metal seeds and their loading on LN (Table 3.6, Figure 3.8, Appendix: Figure A1). For instance, synthesis control on the deposition seems to be reproducible for both LN/Au and LN/Pt hybrids, as seen in the TEM images (Figure 3.8B and C, Appendix: Figure A1B and C) and (Figure 3.8F and G, Appendix: Figure A1E) and the EDS molar percentage (Table 3.6). The most remarkable changes are the ageing of AuSeeds (AuSeeds old), which produces a 90% increase in TEM size, and zeta potential substantially decreases (becomes more negative) (Table 3.6, Figure 3.8A). Long-term storage may cause the coalescence between the seeds to reduce surface energy [260]. This is also observed in AuSeeds' apparent increased size (+55%) in LN/Au3 old after long-term storage. It may come from the coalescence of the seeds due to the presence of BPEI, which, as mentioned before, is a reducer (Figure 3.8D). In any case, the deposition of the AuSeeds onto LN@BPEI reduces this ageing effect. The PtSeeds and LN/Pt hybrid nanoparticles appear to be reasonably stable during long-term storage (Figure 3.8E and H). In this case, the coalescence of the PtSeeds alone and deposited on LN@BPEI is not produced due to the better inertness of Pt compared to Au, and the nanoparticles are more stable [261].

3.2.5. TiO₂/metal Hybrid Nanoparticles

We studied the possibility of implementing the synthesis method to hybrid metal-metal oxide nanoparticles with different oxides. For this, we chose TiO₂ (Appendix: Figure A2) to obtain

TiO₂/Au, and TiO₂/Pt as Au and Pt deposition on TiO₂ have been widely studied in classical catalysts [93], [246], [262], [263].

The synthesis of TiO₂ hybrid nanoparticles was similar to the LN/Au and LN/Pt, but the polymer addition step was not necessary as TiO₂ possess positive zeta potential (**Table 3.7**).

Table 3.7. TEM diameter of metal seeds onto TiO₂, hydrodynamic diameter and zeta potential values of TiO₂/Au and TiO₂/Pt NPs measured in water.

| Nanoparticles | TEM diameter of metal seeds onto the TiO ₂ (nm) | Hydrodynamic diameter (nm) | Zeta potential (mV) |
|----------------------|--|----------------------------|---------------------|
| TiO ₂ | 20.8 ± 6.4 | 292.8 ± 20.0 | +20.2 ± 0.2 |
| TiO ₂ /Au | 3.3 ± 0.3 | 184.9 ± 2.1 | -21.5 ± 0.1 |
| TiO ₂ /Pt | 2.7 ± 0.2 | 261.7 ± 10.8 | -4.97 ± 0.6 |

We deposited the preformed AuSeeds and PtSeeds directly by mixing them. As seen in **Figure 3.9A and B**, the surface density of AuSeeds and PtSeeds on TiO₂ was much lower than for LN/Au and LN/Pt.

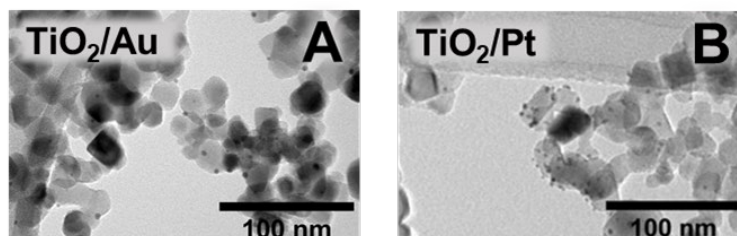


Figure 3.9. (A) TiO₂/Au Nanoparticles TEM image. (B) TiO₂/Pt Nanoparticles TEM image.

From **Table 3.7** and **Figure 3.9**, although the attachment of AuSeeds and PtSeeds onto TiO₂ positive nanoparticles is lower than for LN/Au and LN/Pt, we can state that the layer-by-layer synthesis based on electrostatic forces is transferable with other oxides. The seeds' negative charge for LN/Au and LN/Pt surmounts the positive one of TiO₂ (**Table 3.7**). However, the volume variation does not differ depending on the volume added to the solution (**Appendix: Figure A3**). We can hypothesize that the polymer helps to control the seeds surface density, which makes the LN@BPEI more attractive than TiO₂.

3.3. Conclusion

Seeded hybrid NPs with different noble metal (Au, Pt or Ag) loadings were prepared through electrostatic assembling using branched polyethyleneimine as a linker. The Au-seeded LN synthesis protocol was successfully implemented to LiNbO₃ and PtSeeds hybrid nanoparticles (LN/Pt) and LiNbO₃ and AgSeeds hybrid nanoparticles (LN/Ag) with different loadings. Moreover, the synthesis protocol allowed us to obtain comparable LN/Au and LN/Pt hybrid nanoparticles with similar diameter, surface charge and crystalline structure, as confirmed by the different characterization techniques. The Au and Pt seeds' diameter remained under 5 nm, which is ideal for catalytic purposes. However, for silver, the properties observed upon characterization strongly differ from the ones of AuSeeds, PtSeeds, LN/Au and LN/Pt hybrid nanoparticles, and further investigations would be needed to prepare comparable nanoparticles. The synthesis of LN/Au and LN/Pt hybrid NPs is reproducible across batches. The effect of ageing is negligible for both PtSeeds alone and deposited onto LN@BPEI. In the case of AuSeeds, their deposition onto LN@BPEI decreases the effect of ageing, especially in the size change. Finally, the protocol was successfully implemented to synthesise TiO₂ hybrid Au and Pt NPs. However, controlling the seed coating was not possible in this case, validating LN/Au and LN/Pt as more promising hybrid NPs for Nanozyme applications.

Chapter 4: Nanozyme activity of LN/Au and LN/Pt hybrid nanoparticles as peroxidase mimics. Optimization and elucidation of their catalytic mechanism.

In this chapter, the previously synthesized nanoparticles are tested as peroxidase mimics. The hybrid nanoparticles composed of LN/Au and LN/Pt catalyse the reaction between redox substrates and H_2O_2 as natural peroxidases to produce an oxidized coloured product. We optimized the reaction conditions, colourimetric substrate, pH, temperature, and quantity of hybrid Nanozymes of LN/Au₃ (from now this sample will be named LN/Au); subsequently, we proceeded with LN/Pt₂ (from now this sample will be named LN/Pt) peroxidase mimic optimization. We compared its ability to act as peroxidase mimics against its separated counterparts or a simple mixture of them. We studied the effect of ageing and batch-to-batch activity reproducibility. We also compared LN/Au and LN/Pt peroxidase mimics with TiO_2/Au and TiO_2/Pt . We have ensured that Nanozymes, LN/Au and LN/Pt also follow the Michaelis-Menten kinetic model as natural enzymes do and calculated the quantitative parameters of this kinetic model for the hybrid nanoparticles.

On the one hand, the enhanced catalytic activity of the hybrid nanoparticles compared to the separated counterparts can result from the synergetic effect between the LN NPs and metal Seeds, *i.e.*, Fermi level stabilization and oxygen vacancies creation. On the other hand, the enhancement could be produced from a cascade effect in redox reactions. We did UPS and UV-Vis spectroscopic characterization of the hybrid nanoparticles to elucidate the mechanism of enhanced catalytic activity. In addition, catalase and oxidase activities were evaluated, and ROS production was assessed.

4.1. Materials and Methods for Peroxidase Mimics Characterization

4.1.1. Chemicals

The following materials were used to characterize the peroxidase activity of the nanoparticles: 2,2'-Azino-bis(3-ethylbenzthiazoline-6-sulfonic acid) (ABTS), o-phenylenediamine dihydrochloride (OPD), sodium acetate trihydrate, glycine (99+%), citric acid anhydrous (fine-granular, extra pure), sodium dihydrogen phosphate monohydrate, sodium citrate dihydrate, sodium phosphate monobasic dihydrate, potassium chloride (99%+), hydrochloric acid (37%), hydrogen peroxide (H₂O₂) solution 30 wt. % in H₂O (for enzyme mimics experiments), sodium hydroxide (NaOH) in pellets, dimethyl sulfoxide (DMSO), terephthalic acid (TA) (98%), dihydroethidium (DHE) ($\geq 95\%$), 9,10-anthracenediyl-bis(methylene)dimalonic acid (ABDA) ($\geq 90\%$) were purchased from Sigma Aldrich and used without modification. Hydrogen peroxide (30% w/w) was purchased from Chem-Supply Pty Ltd (for ROS characterization) and used without modification. Acetic acid (glacial, 100%) was purchased from EMPARTA and used without modification. 3,3',5,5'-tetramethylbenzidine (TMB) substrate reagent kit was obtained from BD Biosciences and used without modification. Unless otherwise stated, any water used was deionized water (18.2 M Ω ·cm). The following nanoparticles (see **Chapter 3: section 3.2**) were used: LN NPs, LN@BPEI, AuSeeds, PtSeeds, LN/Au₃ (LN/Au), LN/Pt₂ (LN/Pt), TiO₂/Au, and TiO₂/Pt.

4.1.2. Peroxidase-Mimics of LN/Au and LN/Pt Optimization and Characterization

The Nanozymes with peroxidase-mimicking activities can oxidize different peroxidase substrates (TMB, ABTS or OPD) in the presence of H₂O₂. As their oxidation produces a colour change, the kinetics of the catalytic reaction can be followed by UV-Vis absorption spectroscopy. A Multiskan Go UV-Visible microplate reader from ThermoFisher Scientific was used to measure the absorbance in each well of a 96-well polystyrene microplate (FisherBrand) at wavelengths of 405 nm, 450 nm, and 650 nm for ABTS, OPD and TMB, respectively. Data were collected using SkanIt software. Catalytic reactions were performed using a constant total volume of 150 μ L. The reaction temperature was varied from 20 to 45 °C, and the influence of pH was studied from 2 to 7 (**Table 4.1**). Enzyme kinetic parameters

were studied by varying the concentrations of TMB from 0 to 0.2 mM and H₂O₂ from 0 to 29.7 mM and applying the Michaelis-Menten enzyme kinetic model. Data were treated using the nonlinear curve fitting algorithm from OriginPro 2016 software.

Table 4.1. Buffer preparation table showing the expected pH, final measured pH and the type of buffer used.

| Expected buffer pH | Final pH | Buffer |
|--------------------|-----------|-------------|
| 2 | 1.87-1.93 | KCl-HCl |
| 3 | 2.97-3.14 | Glycine-HCl |
| 3.5 | 3.43-3.50 | Acetate |
| 4 | 4.00-4.13 | Acetate |
| 4.5 | 4.57 | Acetate |
| 5 | 4.94-4.98 | Acetate |
| 5.5 | 5.46-5.50 | Acetate |
| 6 | 5.96-6.09 | Citrate |
| 7 | 6.98-7.06 | Phosphate |

4.1.3. Mechanism elucidation

4.1.3.1. Optical Band Gap

UV-vis optical band gap determination was performed using UV-vis spectroscopy (**Chapter 2: section 2.5.3.2**). The lamp was turned on, and the stability of the light over time was measured until it was stable (between 2 h to 3 h). Subsequently, the percentage of transmittance (%T) of the samples in three different quartz cuvettes (10 mm, 5 mm, and 1 mm) was measured by triplicates from 1100 nm to 200 nm. It allowed us to find the samples dilution factor for which the minimum value of the %T was higher than 50%. We diluted the nanoparticles, followed by the measurement of %T. We finally measured the samples' reflectance percentage, which has to be lower than 10%, to be in the conditions of application of Beer-Lambert for colloids.

4.1.3.2. ROS characterization

The qualitative characterization of the ROS was performed using two fluorescent and one colourimetric probes: terephthalic acid (TA) for $\bullet\text{OH}$ with fluorescence, dihydroethidium (DHE) for $\text{O}_2^{\bullet-}$ with fluorescence and 9,10-anthracenediyl-bis(methylene)dimalonic acid (ABDA) for $^1\text{O}_2$ with absorbance. The experiments were performed in a CLARIOstar plate reader (BMG Labtech). Stock solutions of the three reactants were prepared as follows. TA was dissolved in H_2O , and NaOH was added to ensure solubility to a final concentration of 10 mM. DHE was dissolved in DMSO to a final concentration of 0.1 mM. ABDA was dissolved in DMSO to a final concentration of 2 mM. The fluorescent experiments were carried out in Greiner black 96-well plates in polystyrene to minimize background fluorescence using a total volume of 100 μL . The absorbance measurements were done with transparent 96 well-plate COSTAR[®] flat bottom in a total volume of 100 μL . The H_2O_2 concentration was 29.7 mM in the well for all the experiments, and acetate buffer at pH 4 was used. All measurements were performed at room temperature. We added 10 μL of each ROS probe to the well.

4.2. Optimization of the peroxidase mimics of LN/Au NPs and LN/Pt NPs

For the characterization of the peroxidase mimics, LN/Au3 will be LN/Au, and LN/Pt2 will be LN/Pt. They were selected as they show similar characteristics in terms of metal surface coverage (number of metal Seeds per LN NP) and an even distribution of the metal Seeds on the surface of LN@BPEI (**Chapter 3: section 3.2.2**). The absolute metal seed and hybrid NP concentrations were measured by ICP-AES to obtain the exact amount of Au, Pt and Nb in each sample. Obtaining the values of these absolute concentrations was compulsory to compare the catalytic properties of metal Seeds and hybrid NPs at equal metal concentrations. For LN/Au, the Au content was 12.9 %, corresponding to 40 AuSeeds per LN NP. For LN/Pt, the Pt content was 16.1 %, corresponding to 73 PtSeeds per LN NP. The comparison between the samples was made based on noble metal concentration.

Catalytic activity optimization was then carried out. First, the intrinsic peroxidase-mimic of the LN/Au Nanozyme was confirmed, followed by substrate optimization, pH and temperature, and quantity optimization. Subsequently, we proceeded similarly with LN/Pt. Finally, the different materials were compared, and the Michaelis-Menten kinetic parameters of the LN/Au and LN/Pt Nanozymes were calculated.

4.2.1. LN/Au and LN/Pt Peroxidase-Mimics Optimization.

The first step was establishing the inherent peroxidase mimic catalytic activity of LN/Au Nanozymes. For this, we carried out a time-dependent kinetic study with a fixed amount of LN/Au ($[Au] = 27 \mu\text{M}$; $[\text{LiNbO}_3] = 182 \mu\text{M}$ in the well) (**Figure 4.1**).

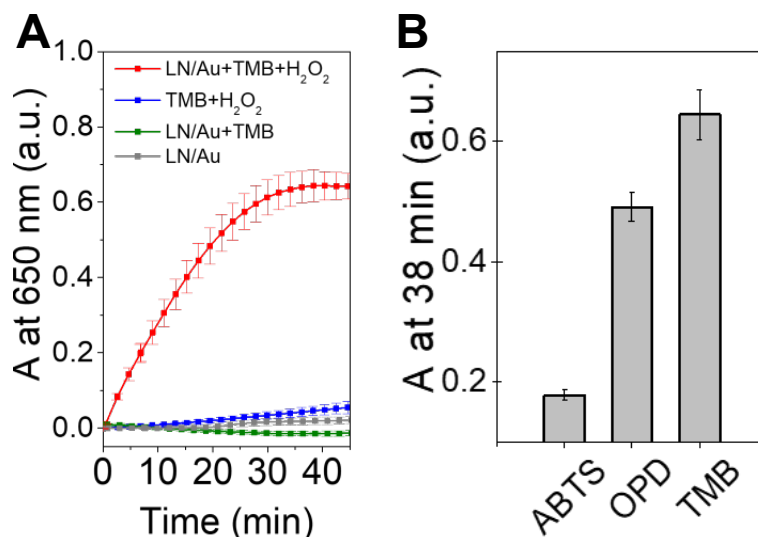


Figure 4.1. (A) Time-dependent kinetics of the LN/Au Nanozyme mediated oxidation of TMB. TMB + LN/Au allowed to test the oxidase activity, TMB + H₂O₂ and LN/Au were negative controls, (B) measurement of the absorbance maximum at an incubation time of 38 min for LN/Au peroxidase reaction using different substrates (ABTS, OPD and TMB). All the experiments were carried out at 37 °C and pH 4 (acetate buffer).

As seen in **Figure 4.1A**, for the reaction to proceed, the presence of TMB (167 μM) and H₂O₂ (29.7 mM) is critical to confirm the peroxidase mimics of LN/Au. The reaction proceeds almost linearly until the saturation point of absorbance, which is obtained after a reaction duration of 38 min. However, the absence of H₂O₂ hindered the reaction from proceeding, excluding the Nanozymes as a potential oxidase-mimic, similar to other nanomaterials [5], [37], [50], [264]. In contrast, the control experiment in the absence of Nanozymes showed insignificant oxidation. LN/Au alone did not lead to any significant change. However, in the presence of H₂O₂, catalase-like activity was demonstrated by the presence of bubbles (**Figure 4.2**) [42].

Nanozyme catalytic activity was optimized regarding substrate nature (**Figure 4.1B**). A fixed amount of the LN/Au Nanozyme ($[Au] = 27 \mu\text{M}$; $[\text{LiNbO}_3] = 182 \mu\text{M}$ from LN/Au in the well) was exposed to different substrates (ABTS, OPD and TMB). Typically, 167 μM of each

substrate was exposed to the concentration mentioned above of LN/Au and 29.7 mM of H₂O₂. The ability of the Nanozymes to oxidize the colourless substrates, ABTS, OPD and TMB, to produce green ($\lambda_{\max} = 415$ nm), yellow ($\lambda_{\max} = 450$ nm) and blue ($\lambda_{\max} = 650$ nm) products, respectively, was proven. The best performance was achieved with TMB, followed by OPD and ABTS, as shown in **Figure 4.1B**. The better activity towards the TMB substrate may come from the better interaction between the negatively-charged Nanozymes and the positively-charged TMB [265] and/or the better capability of the Nanozymes to detach the oxidized product [266]. Due to its better activity, the optimization continued with TMB as the colourimetric substrate.



Figure 4.2. Catalase mimics of Au-based Nanozymes after 38 minutes. Control experiment, H₂O₂+Buffer (A). AuSeeds catalase mimics, H₂O₂+AuSeeds+Buffer; [Au] = 27 μ M (B). LN/Au catalase mimics, H₂O₂+LN/Au; [Au] = 27 μ M; [LiNbO₃] = 182 μ M (C). For all the samples, the measurements were performed in the presence of H₂O₂ (29.7 mM) at pH 4 (acetate buffer) and 37°C. All the concentrations are in the reaction well.

During the oxidation of TMB, two coloured products can be produced: a blue charge transfer complex that results from the combination of TMB and a radical cation initially produced from TMB oxidation and a yellow diimine that results from subsequent oxidation of radical cation, which gives an absorbance maximum at 450 nm (**Figure 4.3**) [267]. Both absorbances were measured after reaction completion at 38 min, as shown in **Figure 4.4**. The absorbance corresponding to diimine group is less than 10% compared to the one corresponding to the blue complex, which is in agreement with previous works [64], [88].

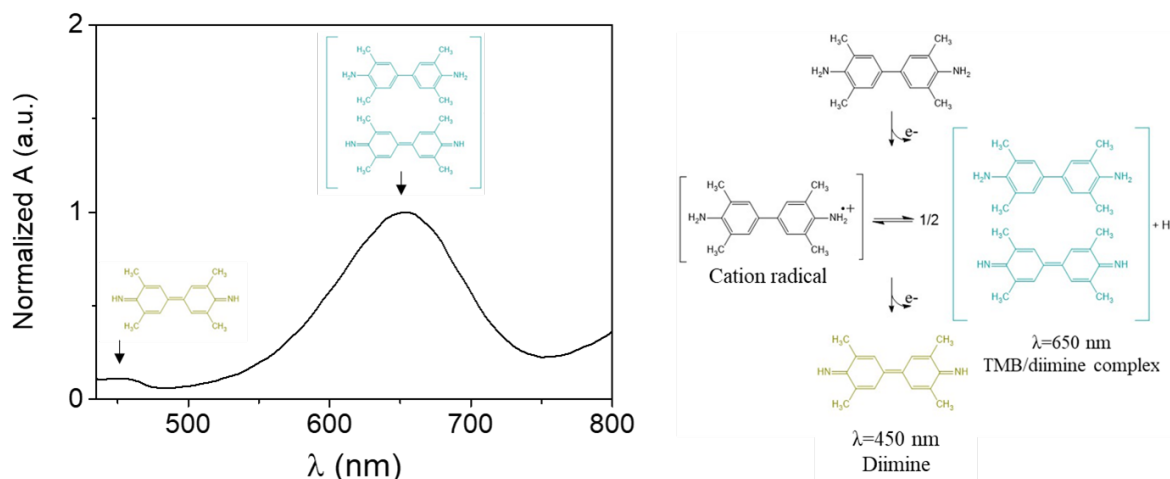


Figure 4.3. The absorbance spectrum after the completion of TMB oxidation shows peaks at 450 nm and 650 nm due to the formation of yellow and blue products, respectively. The schematic of the TMB oxidation reaction is also provided.

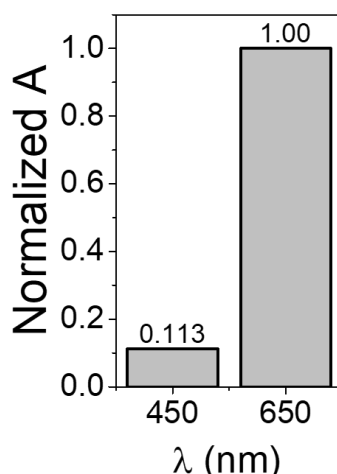


Figure 4.4. Normalized absorbance at 450 nm and 650 nm at 37 °C and pH 4 (acetate buffer) for the completed reaction with TMB, the absorbance corresponds to the maximum reached after 38 minutes of reaction time.

The peroxidase-mimic activity was also studied as a function of pH and temperature (**Figure 4.5**).

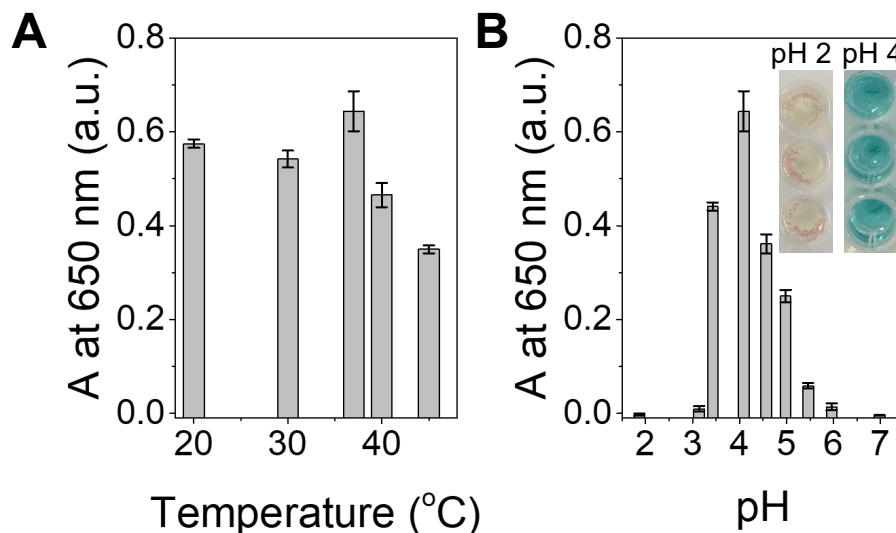


Figure 4.5. Measurement of the absorbance maximum (reaction time 38 min) for LN/Au peroxidase reaction using TMB substrate, (A) at pH 4 as a function of temperature, (B) at 37°C as a function of pH. (B, insert) The colour difference between the reaction at pH 2 and pH 4.

The NPs' optimum peroxidase activity was obtained at 37 °C and pH 4, which is in corroboration with other studies (**Figure 4.5**) [41], [122], [268]. As for natural enzymes, 37 °C is the optimum working temperature which makes LN/Au Nanozyme an excellent candidate to potentially substitute them. Moreover, it shows nearly similar performance at 20 °C, diversifying its application. The best performance was at pH 4, as at this pH, one of the amine groups of TMB is protonated, favouring the electrostatic interaction between the positively-charged TMB and the negatively-charged nanoparticles [269]. It is also notable that at further lower pH 3 and 2, while the absorbance at 650 nm appears to reduce (**Figure 4.5B**), this may not necessarily reflect the poor catalytic performance of LN/Au Nanozyme at lower pH. At highly acidic pH, the blue product tends to rapidly convert to a yellow product which should not be neglected [268], as reflected from the photos of the reaction products at different pHs provided in **Figure 4.5B, insert**. These findings make the Nanozymes more suitable to work in harsher conditions than the Horseradish peroxidase (HRP) enzyme, as HRP's optimal activity for TMB oxidation is typically obtained at pH 5.6 [270].

The kinetic curves at different nanoparticle concentrations are presented in **Figure 4.6A**.

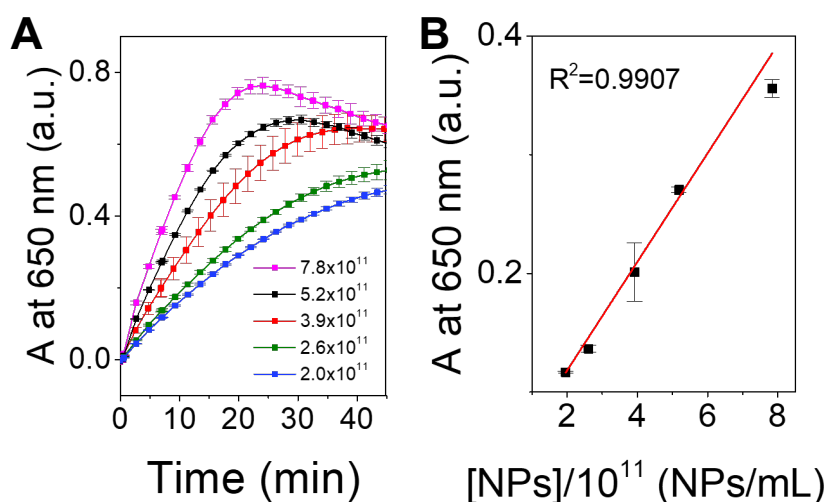


Figure 4.6. Optimization of the quantity of LN/Au Nanozyme. (A) Peroxidase activity kinetics at different concentrations of Nanozymes (concentrations are given in number of NPs/mL) and (B) plot of the absorbance at 650 nm of oxidized TMB as a function of NPs concentration after 7 min of reaction. All reactions were carried out at $[\text{H}_2\text{O}_2] = 29.7 \text{ mM}$, $[\text{TMB}] = 167 \text{ }\mu\text{M}$, $37 \text{ }^\circ\text{C}$ and pH 4 (acetate buffer).

We varied the concentration of hybrid nanoparticles from 2.0×10^{11} to 7.8×10^{11} hybrid NPs/mL, corresponding to $13.5 \text{ }\mu\text{M}$ of Au and $91 \text{ }\mu\text{M}$ of LN for the lowest concentration and of $54 \text{ }\mu\text{M}$ of Au and $364 \text{ }\mu\text{M}$ of LN for the highest concentration in the wells. As seen in **Figure 4.6A**, the increasing NPs concentration variation enhances the oxidation of TMB. When the concentration of nanoparticles is higher than 3.9×10^{11} NPs/mL, the concentration of oxidized TMB, as evaluated from the blue product, reaches a maximum, and then it decreases rapidly, meaning that the diimine yellow product starts forming more rapidly with an increase in the nanoparticle concentration (**Figure 4.3**). We chose 7 min reaction time, as it is in the linear range of the kinetic curve, and plotted the absorbance obtained against the number of nanoparticles (**Figure 4.6B**). This data supports a linear dependence of catalytic efficiency as a function of nanoparticle concentration.

We followed the same optimization process for LN/Pt. In order to compare the two materials, we chose TMB as the substrate. Initially, we optimized the quantity of LN/Pt to adapt the protocol to its higher activity over LN/Au towards TMB oxidation. Subsequently, we confirmed the intrinsic peroxidase-mimic activity of the LN/Pt Nanozyme and finally, we optimized the reaction's pH and temperature.

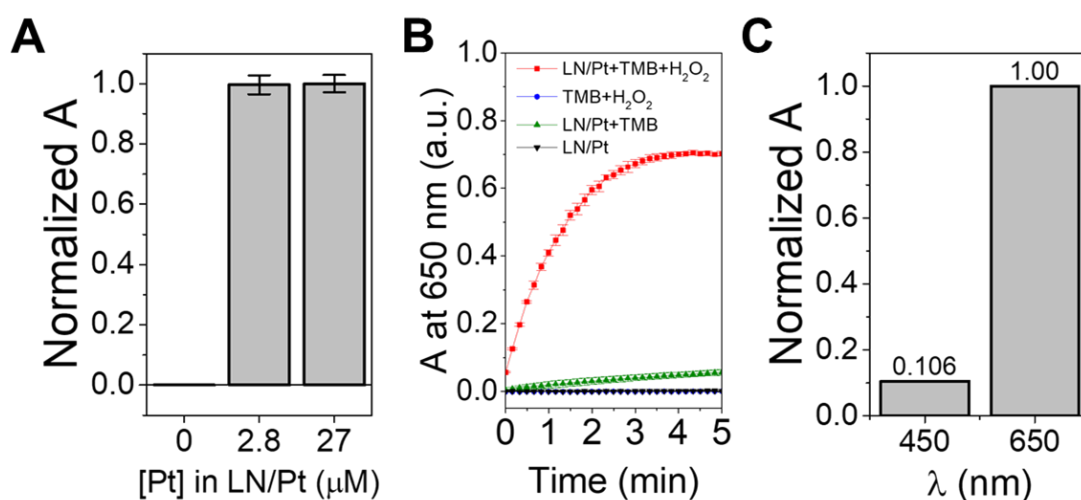


Figure 4.7. (A) Normalized absorbance at 650 nm after 5 min of reaction for two different concentrations of Pt in LN/Pt. (B) Time-dependent kinetics of the LN/Pt Nanozyme mediated oxidation of TMB under different conditions. TMB + LN/Pt allowed to test the oxidase activity, TMB + H₂O₂ and LN/Pt were negative controls. (C) Normalized absorbance at 450 nm and 650 nm at 37 °C and pH 4 for the completed reaction with TMB; the absorbance corresponds to the maximum reached at 5 minutes.

As seen in **Figure 4.7A**, the catalytic activity of the LN/Pt peroxidase activity was measured at two different concentrations. The same conditions as for LN/Au ([TMB] = 167 μM, [H₂O₂] = 29.7 μM, pH 4 and 37 °C) were used. The highest concentration of LN/Pt has the same performance as the lowest after 5 min. Thus, for the optimization experiments, we chose the lowest concentration of Nanozymes, which corresponds to 2.8 μM of Pt and 14.5 μM of LN (2.8 × 10¹⁰ hybrid NPs/mL). Compared to LN/Au (27 μM of Au and 182 μM of LN, 3.9 × 10¹¹ NPs/mL), LN/Pt can complete the reaction 8 times faster using 10 times less metal concentration. These results agree with previous catalysis works in which the authors used non-supported Au NPs and Pt NPs [54] but also supported NPs on bulk oxides [271] and found that Pt is catalytically more active than Au for TMB oxidation. The inherent catalytic Nanozyme activity of LN/Pt was then further evaluated. For this, a time-dependent kinetic study with a fixed amount of LN/Pt ([Pt] = 2.8 μM; [LiNbO₃] = 14.5 μM) was carried out (**Figure 4.7B**). For the reaction to proceed, like for LN/Au, the presence of TMB (167 μM) and H₂O₂ (29.7 mM) is critical to confirm the peroxidase mimics of LN/Pt. The reaction proceeded almost linearly until the saturation point was attained in less than 5 min (4 min 20s). In the absence of H₂O₂, the absorbance increased more slowly than in the presence of it. However, this change indicates that LN/Pt Nanozyme is able to oxidize TMB by itself [272], so LN/Pt also has some

level of oxidase activity, contrary to LN/Au. Similarly to LN/Au control experiment, in the absence of Nanozymes, TMB oxidation was not possible. As for LN/Au, the production of the yellow product (diimine) is not significant at pH 4 (**Figure 4.7C**). We also performed the experiment with H₂O₂ and Nanozymes, observing the appearance of bubbles, which suggest catalase-mimics activity (**Figure 4.8**) [220] of LN/Pt, similar to LN/Au. Moreover, LN/Pt bubble generation is more evident than for PtSeeds, suggesting a synergetic effect. These results proved that LN/Pt is a faster, more powerful, and more versatile Nanozyme than LN/Au. Finally, we observed some level of subsequent oxidation of TMB to yellow diimine (**Figure 4.7C**).



Figure 4.8. Catalase mimics of Pt-based NanoZymes after 5 minutes. Control experiment, H₂O₂+Buffer (A). PtSeeds catalase-mimics, H₂O₂+PtSeeds+Buffer; [Pt] = 2.8 μ M (B). LN/Pt catalase-mimics, H₂O₂+LN/Pt+Buffer; [Pt] = 2.8 μ M; [LiNbO₃] = 14.5 μ M (C). For all the samples, the measurements were performed in the presence of H₂O₂ (29.7 mM) at pH 4 (acetate buffer) and 37°C. All the concentrations are in the reaction well.

LN/Pt's temperature and pH optimization are shown in **Figure 4.9**.

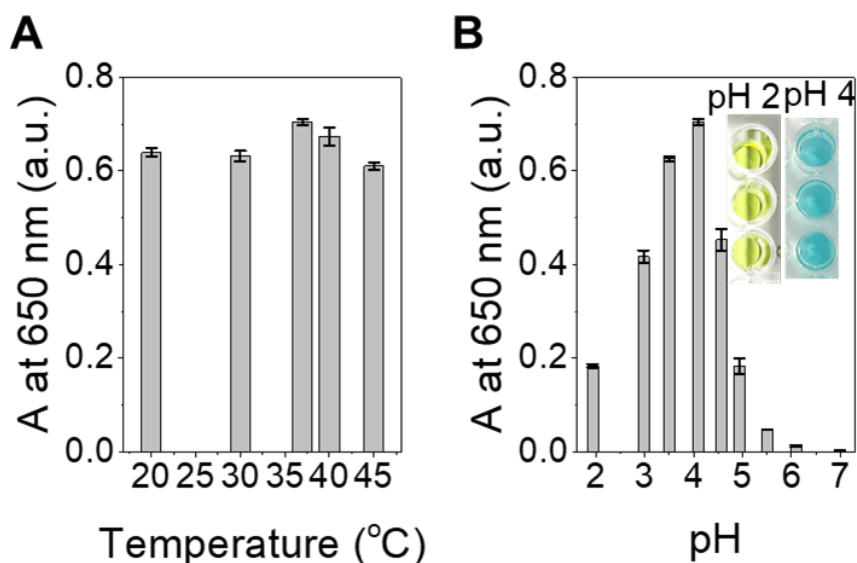


Figure 4.9. Measurement of the absorbance maximum at a duration of 4 min 20 s for LN/Pt peroxidase reaction using TMB substrate, (A) at pH 4 as a function of temperature, and (B) at 37 °C as a function of pH. (C, insert) The colour difference between the reaction at pH 2 and pH 4.

The pH optimization shows that although the activity at 37 °C is the highest, the difference between temperatures is negligible (**Figure 4.9A**). Even at 45 °C, which caused a substantial decrease in activity for LN/Au (~ 45%) (**Figure 4.5A**), for LN/Pt, the decrease was only 13%. This suggests that LN/Pt is more resistant than LN/Au to harsh environments. For LN/Pt, the optimum pH is 4, which is similar to that observed for LN/Au, and a similar explanation based on the protonated form of TMB's first oxidation product and negative surface charge of LN/Pt, as provided previously for LN/Au, can explain the optimum activity of LN/Pt at this pH [269]. Further, at lower pH of 3 and 2, the activity of LN/Pt, as evaluated from the blue TMB product, while appears to decline from that at pH 4, it seems to be relatively better than that observed for LN/Au. This suggests that LN/Au can drive a higher conversion of blue TMB product to the yellow product at lower pH compared to that driven by LN/Pt.

Finally, the potential leaching of gold and platinum ions from LN/Au and LN/Pt, respectively, and their role in catalysing the reaction was studied by incubating the Nanozymes for one hour in the pH 4 buffer and exposing the supernatant of the reaction after centrifugation to H₂O₂ (29.7 μM) and TMB (167 μM), while keeping all the other parameters constant (Au, Pt, LN, H₂O₂ and TMB concentrations, pH 4 and 37 °C). The results in **Figure 4.10**. provide evidence

of minimal catalytic activity of potentially leached metal ions and confirm that the presence of the nanoparticles is crucial for the reaction to proceed in both systems.

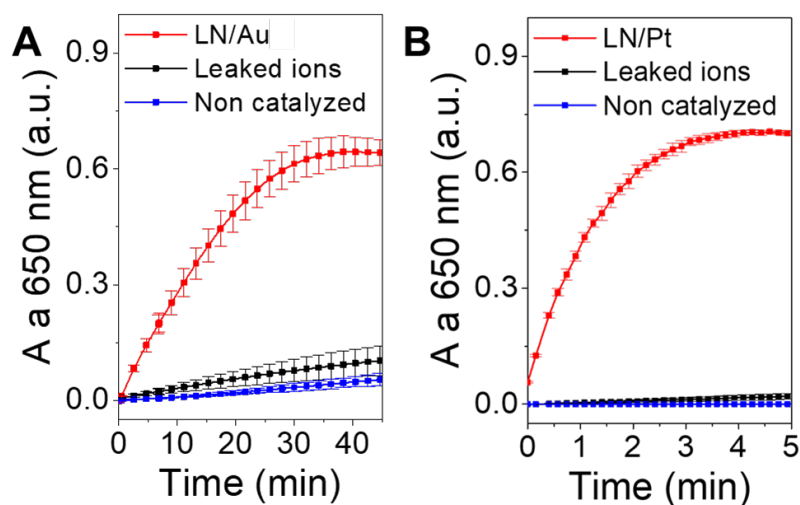


Figure 4.10. Comparison of the peroxidase-mimic activity of (A) LN/Au (red) and (B) LN/Pt (red) with potentially leached ions from these hybrid nanoparticles (black) and the non-catalysed reaction (blue) measured with TMB at pH 4 and 37 °C.

From these studies, we can conclude that LN/Au and LN/Pt have peroxidase-mimicking activity, and they can readily catalyse the reaction between TMB and H₂O₂ to produce a predominantly blue product ($\lambda_{\text{max}}=650$ nm, one electron complex diimine-diamine [267]). Although both Nanozymes show catalase-like activity and LN/Pt shows some degree of oxidase-like activity, we will focus the discussion on peroxidase activity to compare these materials. Both systems produce residual oxidation to diimine ($\lambda_{\text{max}}=450$ nm), which can be neglected when the pH is higher than 3. The optimum conditions are found at pH 4, 37 °C for LN/Au and LN/Pt. For LN/Au, we chose a concentration of 27 μM of Au and 182 μM of LiNbO₃, corresponding to 3.9×10^{11} hybrid NPs/mL (40 AuSeeds per hybrid NP). Due to the higher catalytic activity of the LN/Pt hybrid, by reducing 10 times the metal concentration, we chose 2.8 μM of Pt and 14.5 μM of LiNbO₃, corresponding to 2.8×10^{10} hybrid NPs/mL (73 NPs of PtSeeds per hybrid NP).

4.2.2. Synergetic effect of AuSeeds and PtSeeds on the surface of LN.

To understand the potential synergetic effect created by the interface of LN with the catalytic metal Seeds in hybrid nanoparticles, we compared the ability of LN/Au and LN/Pt to oxidize TMB in the presence of H₂O₂ with the individual components of these hybrids (LN, LN@BPEI, AuSeeds and PtSeeds) and a simple physical mixture of them without BPEI (LN+AuSeeds and LN+PtSeeds) (**Figure 4.11**). Here, for a more meaningful comparison, the results are presented as a function of the concentration of the TMB oxidized to the blue product (TMB^{Ox}), whose extinction coefficient at 650 nm is 39000 L·mol⁻¹·cm⁻¹ [126].

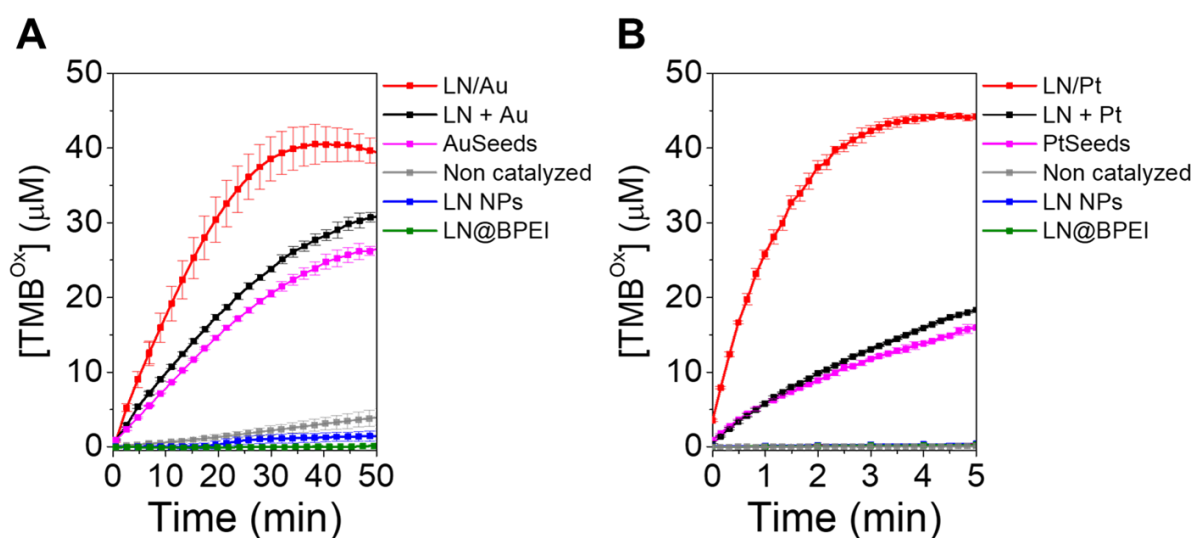


Figure 4.11. (A) The peroxidase-mimic activity of LN/Au (red) compared to its individual constituents. The concentration of the Nanozymes is: [Au] = 27 μM; [LiNbO₃] = 182 μM, corresponding to 3.9×10^{11} NPs/mL and 40 AuSeeds per LN. (B) The peroxidase-mimic activity of LN/Pt (red) compared to its individual constituents. The concentration of the Nanozymes is: [Pt] = 2.8 μM; [LiNbO₃] = 14.5 μM, corresponding to 2.8×10^{10} hybrid NPs/mL and 73 PtSeeds per LN in the reaction well. For both LN/Au and LN/Pt, the measurements were performed in the presence of TMB (167 μM) and H₂O₂ (29.7 mM) at pH 4 and 37°C.

Clearly, the activities of LN/Au and LN/Pt are significantly higher than any other tested component. LN NPs alone do not present any catalytic activity, and it may even be the case that they perhaps inhibit the spontaneous basal level oxidation of TMB in the presence of H₂O₂. This observation is even more pronounced for LN@BPEI NPs. As expected, AuSeeds and PtSeeds have peroxidase-mimicking activities, but only a slight increase in their activity is observed when LN NPs are also present in the reaction as a physical mixture. But the overall

activity of these physical mixtures remains significantly lower in comparison to LN/Au and LN/Pt hybrid NPs. This suggests that close proximity of LN and metal Seeds provided by the chemical link created by BPEI between LN NPs and AuSeeds or PtSeeds is necessary to increase the catalytic activity. It has already been observed that the deposition of metal NPs onto oxides can enhance their catalytic activity [31], [93], [263], [273]. The combination of a semiconductor and a metal may provoke a charge transfer between the oxide and the metal, increasing the electron density around the junction and thus favouring the electron transfer in redox-type reactions [274], [275]. Moreover, the inclusion of the metal onto the oxide surface causes the partial reduction of the latter at the interface, which may potentially create oxygen vacancies (**Chapter 1: section 1.1.4**). These oxygen-deficient locations within the semiconductor can help oxygen-containing species (like H₂O₂) to bind and cleave more efficiently and thus enhance the catalytic activity of the hybrid systems [94], [276]. Finally, the distribution of metal Seeds onto the LN@BPEI surface can also hinder their aggregation during catalysis compared to the pristine form of metal Seeds, enhancing the accessibility to the catalytically-active metal surface, which is a key to obtaining better catalytic performance [277]. The combination of these processes is expected to lead to the observed synergetic effect of the enhanced peroxidase-mimic activity of LN/Au and LN/Pt hybrid nanoparticles.

4.2.3. Ageing and reproducibility across batches

Having observed this remarkable synergetic effect from the LN/metal interface, we also assessed the impacts of potential batch-to-batch variability and the influence of long-term storage stability on their peroxidase-mimic activity. Comparing the peroxidase-mimic activity of these batches shows a reasonably similar high catalytic activity across batches (**Figure 4.12**). During long-term storage, although both materials undergo slight deterioration in the activity after one year, the amount of oxidized TMB remains high, making the Nanozyme activity reasonably stable over time.

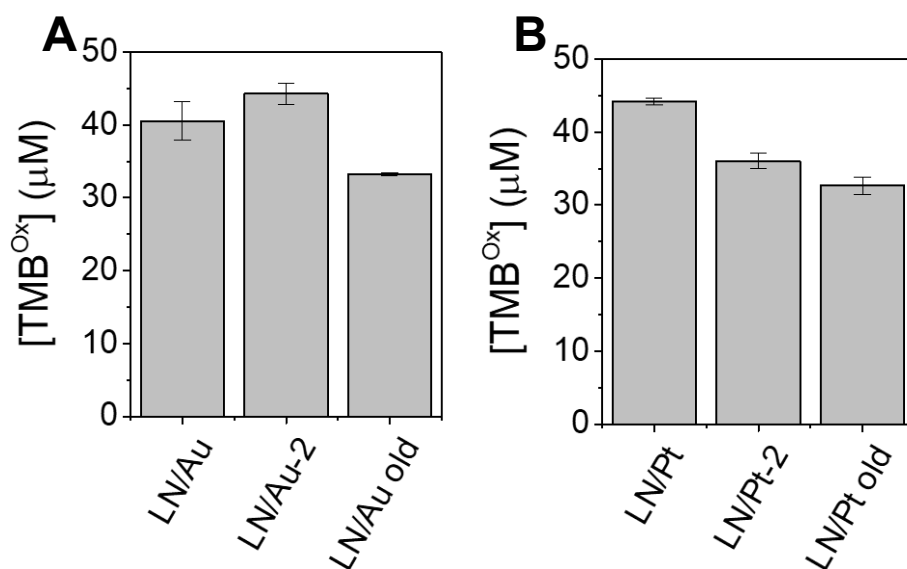


Figure 4.12. (A) Comparison of the peroxidase-mimicking activity of LN/Au synthesised in two independent batches and one aged for more than one year, as evaluated after 38 min of reaction while employing TMB (167 μM) and H₂O₂ (29.7 mM) at pH 4 and 37°C. The concentration of the Au is constant across the batches (27 μM). For LN/Au, [LiNbO₃] = 182 μM; for LN/Au-2, [LiNbO₃] = 184 μM and for LN/Au old, [LiNbO₃] = 163 μM based on the independent ICP-MS measurements. (B) Comparison of the peroxidase-mimicking activity of LN/Pt synthesised in two independent batches and one aged for more than one year, as evaluated after 5 min of reaction while employing TMB (167 μM) and H₂O₂ (29.7 mM) at pH 4 and 37°C. The concentration of Pt is constant across the batches (2.8 μM). For LN/Pt, [LiNbO₃] = 14.5 μM; for LN/Pt-2, [LiNbO₃] = 19.2 μM and for LN/Pt old; [LiNbO₃] = 14.5 μM.

4.2.4. TiO₂/Au and TiO₂/Pt hybrid NPs as peroxidase-mimics

TiO₂/Au Nanozyme and TiO₂/Pt Nanozymes have shown increased peroxidase and catalase mimics, respectively, compared to TiO₂ alone [150], [278]. Therefore, we have prepared TiO₂/Au and TiO₂/Pt hybrid nanoparticles and compared their activity to LN/Au and LN/Pt.

We performed ICP-AES on both samples and TiO₂ to obtain the exact concentrations. As for TiO₂/Au, Au concentration was extremely low in the prepared samples. To be able to compare them, we reduced 10 times the concentration of Au in LN/Au, in this case, 2.7 μM. We used the same Au concentration for TiO₂ (**Figure 4.13A**). As seen in **Figure 4.13A**, LN/Au possess higher activity than TiO₂/Au, and after 35 minutes of reaction, TiO₂/Au aggregates lead to a

noisy curve. For TiO₂/Pt, **Figure 4.13B**, the peroxidase mimics activity is slightly lower than for LN/Pt. We can conclude that LiNbO₃ remains a good candidate for peroxidase mimics, which avoids aggregation and possess higher peroxidase mimics than TiO₂ hybrids.

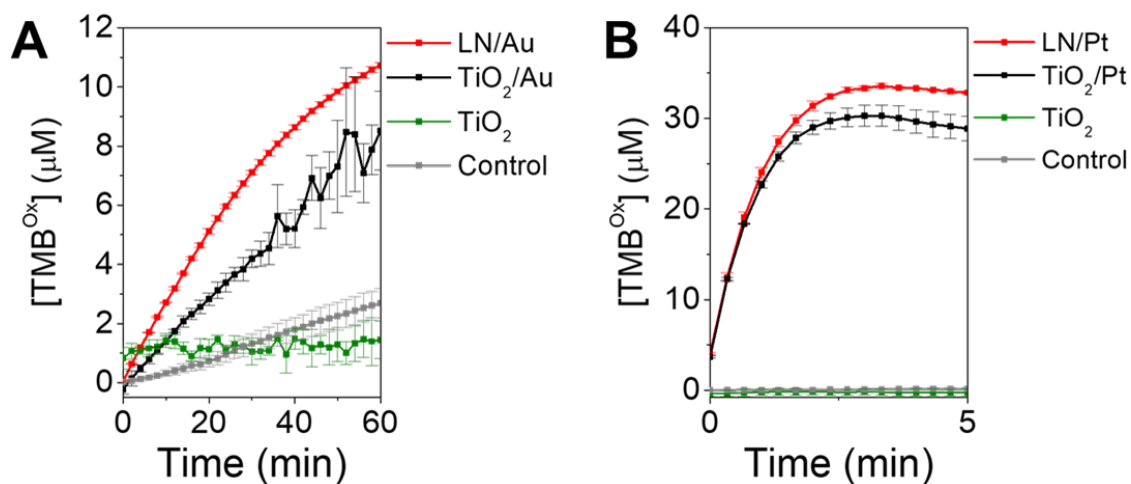


Figure 4.13. (A) Peroxidase mimics TiO₂/Au hybrids compared to LN/Au, TiO₂ and the non-catalysed reaction. The concentrations are: [Au] = 2.7 μM, [TiO₂] = 498 μM in TiO₂/Au and TiO₂ and [Au] = 2.7 μM, [LiNbO₃] = 16.6 μM in LN/Au. (B) Peroxidase mimics TiO₂/Pt hybrids compared to LN/Pt, TiO₂ and the non-catalysed reaction. The concentrations are: [Pt] = 2.8 μM, [TiO₂] = 279 μM in TiO₂/Pt and TiO₂ and [Pt]=2.8 μM, [LiNbO₃]=14.5 μM in LN/Pt. For A and B, control experiments were TMB+H₂O₂+Buffer. For all the reactions, substrate concentrations were [TMB] = 167 μM and [H₂O₂] = 29.7 mM, and it was performed at pH 4 and 37 °C.

4.3. Calculation of the enzymatic kinetic parameters

As nanoparticles mimic enzyme activity, the catalytic parameters of Nanozymes can be calculated using the Michaelis-Menten model proposed for natural enzymes (**Chapter 1: Equation 1.2**) [24], [129]. This model allows us to obtain important data related to steady-state kinetics such as maximum initial velocity (V_{max}), Michaelis constant (K_m), catalytic constant or turnover number (K_{cat}) and catalytic efficiency (K_{eff}). V_{max} is the maximum speed of catalysis achieved by the system at saturated substrate concentration, and it is directly proportional to the reaction speed. Substrate concentration ($[S]$) at which the reaction speed is half of the V_{max} is defined by K_m and is inversely proportional to the affinity of the Nanozyme surface towards the substrate (TMB or H₂O₂), *i.e.*, the lower the K_m , the higher the affinity of

the substrate to the Nanozyme. K_{cat} indicates the number of molecules converted per unit of time per unit of the enzyme, which can be calculated by dividing V_{max} by the enzyme concentration (**Chapter 1: section 1.1.2.2**). Although this value permits us to address many mechanism questions, we need to calculate the K_{eff} , which results from the ratio K_{cat}/K_m , to standardise our data. To calculate these parameters, we varied the concentration of one substrate while keeping the concentration of the other constant [152]. The rest of the parameters were kept constant (pH 4, 37 °C), and Nanozyme concentration was fixed for LN/Au ([Au]=27 μ M, [LiNbO₃]=182 μ M) and LN/Pt ([Pt]=2.8 μ M, [LiNbO₃]=182 μ M) (**Figure 4.14**). We also calculated the steady-state kinetic parameters for AuSeeds and PtSeeds and compared them to the ones of hybrid Nanozymes (**Table 4.2**). It has to be pointed out that to calculate K_{cat} , V_{max} is divided by the concentration of enzyme, which in this case is Nanozyme. We considered that AuSeeds and PtSeeds were the catalytic hot points in LN/Au and LN/Pt and that each surface metal atom works as a single enzyme. This calculation did not consider LN NPs as they did not show any peroxidase mimics (**Figure 4.11**).

We note that the calculated values of kinetic parameters, in particular, K_{cat} , depend upon the consideration of whether a single atom, single surface metal atom or a single metal nanoparticle is considered equivalent to a single Nanozyme. Since the surface atoms of metal NPs are expected to predominantly participate in the catalysis reaction, it can be safely presumed that a single metal NP will offer more than one catalytic site, while at the same time, all atoms (particularly those not on the NP surface) will not participate in catalysis. Moreover, not all the surface atoms are active sites, nor all core atoms are inactive. Since it is highly challenging to determine the absolute number of catalytic sites on a particle, especially in hybrid nanoparticles, we employed the number of surface metal atoms available during the reaction, as this will underestimate the catalytic efficiency rather than reporting an overestimated efficiency. Detailed calculation is provided in **Appendix** [279]. Overall, irrespective of the absolute values, the obtained kinetic parameters among different samples are still valid and can be confidently compared.

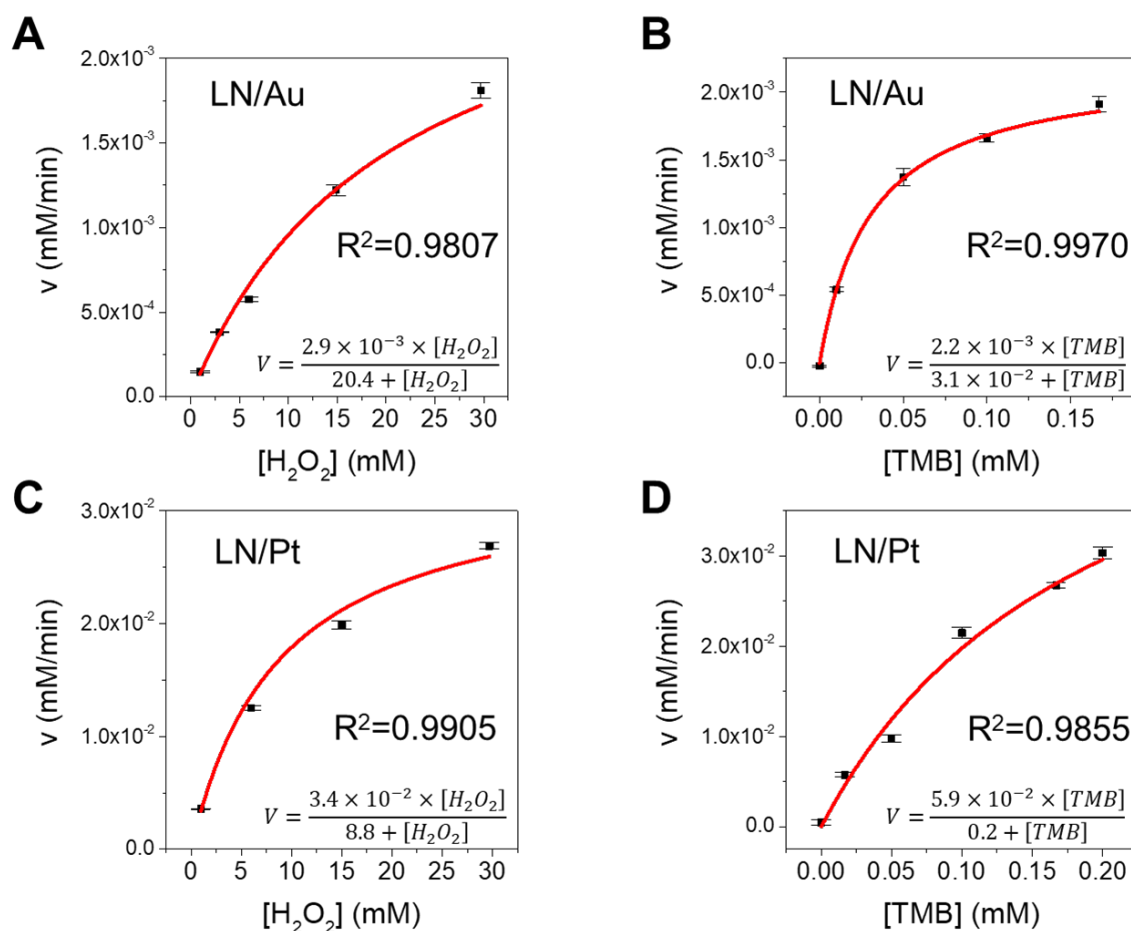


Figure 4.14. Michaelis-Menten plots and equations for the best fit for the LN/Au and LN/Pt Nanozymes. LN/Au curve fitting at different (A) H_2O_2 (0-29.7 mM) and (B) TMB (0-200 μ M) concentrations. LN/Pt curve fitting at different (C) H_2O_2 and (D) TMB concentrations. To obtain the curves, the velocity of each reaction was calculated by converting the absorbance values at 650 nm into concentration values using Beer-Lambert law (molar extinction coefficient of TMB at 650 nm is $39000 \text{ L} \cdot \text{mol}^{-1} \cdot \text{cm}^{-1}$) and then plotting the first derivative at the beginning of the reaction (linear part of the reaction). The fittings were obtained using the Michaelis-Menten enzyme kinetic model with a Levenberg Marquardt iteration algorithm in OriginPro 2016 software.

Table 4.2. Apparent steady-state kinetic parameters for LN/Au, AuSeeds, LN/Pt and PtSeeds for driving a peroxidase-mimic reaction.

| Nanozyme | Substrate | K_m (10^{-3} M) | V_{max} (10^{-8} M·s ⁻¹) | K_{cat} (s ⁻¹) | K_{eff} (M ⁻¹ ·s ⁻¹) |
|----------|-------------------------------|-----------------------|---|------------------------------|---|
| LN/Au | H ₂ O ₂ | 20.43 | 4.9 | 5.2×10^{-3} | 26×10^{-2} |
| | TMB | 3.08×10^{-2} | 3.7 | 3.9×10^{-3} | 128.8 |
| AuSeeds | H ₂ O ₂ | 44.26 | 2.8 | 2.1×10^{-3} | 4.7×10^{-2} |
| | TMB | 1.34×10^{-2} | 3.1 | 2.3×10^{-3} | 173.6 |
| LN/Pt | H ₂ O ₂ | 8.81 | 56.1 | 55.9×10^{-2} | 63.5 |
| | TMB | 20×10^{-2} | 97.9 | 97.6×10^{-2} | 5.0×10^4 |
| PtSeeds | H ₂ O ₂ | 12.31 | 3.6 | 3.1×10^{-2} | 2.5 |
| | TMB | 3.82×10^{-2} | 5.9 | 5.1×10^{-2} | 1.3×10^3 |

From the data presented in **Table 4.2**, it is clear that all the Nanozymes present higher affinity towards TMB over H₂O₂ as K_m is lower for all of them compared to those for H₂O₂. This suggests a preference of these Nanozymes towards TMB adsorption over H₂O₂, *i.e.* peroxidase activity may be predominant over catalase activity at pH 4 in these Nanozymes [54]. As we discussed above, the affinity towards H₂O₂ increases in the hybrid nanoparticles compared to the Seeds, which may be attributed to the creation of oxygen vacancies at the LN/metal interface [129], [280]. On the other hand, the affinity of TMB decreases in the corresponding hybrids. TMB's bigger size is held up from entering in contact with the hybrid nanoparticles because of a steric hindrance as they may possess BPEI on their surface [269]. Further, while Au-containing Nanozymes have a higher affinity to TMB, the Pt-containing samples have a higher affinity towards H₂O₂. This is consistent with previous observations in the literature,

where Au-based Nanozymes are typically good peroxidase-mimic catalysts, while Pt-based catalysts show more promising catalase-mimicking activity [24], [54]. According to V_{\max} , the LN/metal hybrid nanoparticles can drive the reaction faster than their corresponding metal Seeds, and particularly in the case of the Pt system, a nearly 15-20 times increase in the reaction maximum velocity is observed for the hybrid LN/Pt over PtSeeds Nanozymes (**Table 4.2**). A combination of favourable K_m and V_{\max} values of hybrid Nanozymes is translated into higher K_{cat} over pristine metal Seeds as seen in **Figure 4.15**. [281]. This is not surprising, considering that this parameter depends on the number of surface atoms. In particular, the Pt-based hybrid nanoparticles show remarkable K_{cat} and K_{eff} enhancement, supporting the extraordinary synergetic effect of these hybrid nanoparticles over their individual components. However, the deposition of the AuSeeds onto LN@BPEI NPs, provokes a decrease in the K_{eff} (**Figure 4.15B**). This is because this value depends on the affinity of the nanozyme towards the substrate. AuSeeds possess better affinity for TMB than LN/Au, as reflected in K_m values (**Table 4.2**), provoking this decrease in K_{eff} .

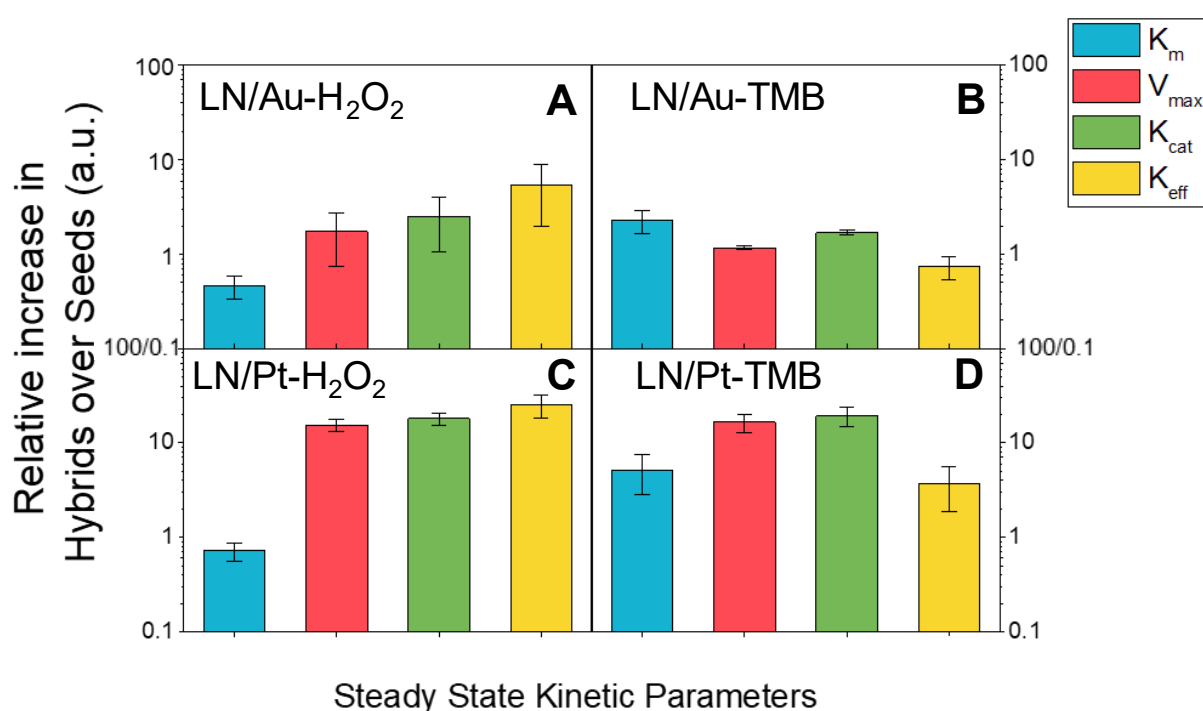


Figure 4.15. Relative increase of steady kinetic parameters of hybrids over Seeds. LN/Au increase over AuSeeds with H_2O_2 as a substrate (A). LN/Au increase over AuSeeds with TMB as a substrate (B). LN/Pt increase over PtSeeds with H_2O_2 as a substrate (C). LN/Pt increase over PtSeeds with TMB as a substrate (D).

We can theorize that H₂O₂ cleavage is more efficient on the surface of Pt than Au, and as TMB is not strongly linked to the surface, the produced OH• radicals cause the TMB^{Ox} to detach faster [128]. Nevertheless, when depositing AuSeeds onto LN NPs, the values are similar to the ones of PtSeeds, demonstrating the enhancement upon deposition of the Seeds.

4.4. Mechanistic elucidation

4.4.1. Synergetic effect in the band structure

As presented in **Chapter 1: section 1.1.4**, forming a metal/semiconductor (metal oxide) junction led to a re-equilibration of metal and metal oxide energy levels at their interface. Therefore, to understand better the phenomena that lead to a higher catalytic activity of the hybrid Nanozymes, we characterized their semiconducting properties, in particular their optical band gap, for the different materials: LN NPs, LN@BPEI NPs, AuSeeds, LN/Au, PtSeeds and LN/Pt with UV-Vis spectroscopy (Coll. IRCE Lyon). In addition, we resolved the work function and the valence band maximum relative to the Fermi level ($V_{B_{max}}$) with XPS/UPS spectroscopy for LN NPs, LN@BPEI and LN/Au (Coll. IRCE Lyon).

The optical band gap characterization with UV-Vis was done using an apparatus with an integrating sphere of BaSO₄. The principle was detailed in **Chapter 2 section 2.5.3.3**. We measured the percentage of transmittance (%T) of the samples and diluted them until less than 50% of the light was transmitted in 200-1100 nm range spectra. The percentage of absorbance (%A) was obtained, and the absorptivity (α) resulted from dividing the %A by the length of the cuvette (0.01 m). By plotting the Tauc function for direct (**Figure 4.16B and D**) and indirect band gap (**Appendix: Figure A4**) against the photon energy and extrapolating the linear part to $y=0$, we obtain the band gap energy (**Figure 4.16, Table 4.3, Appendix: Figure A4, Table A1**).

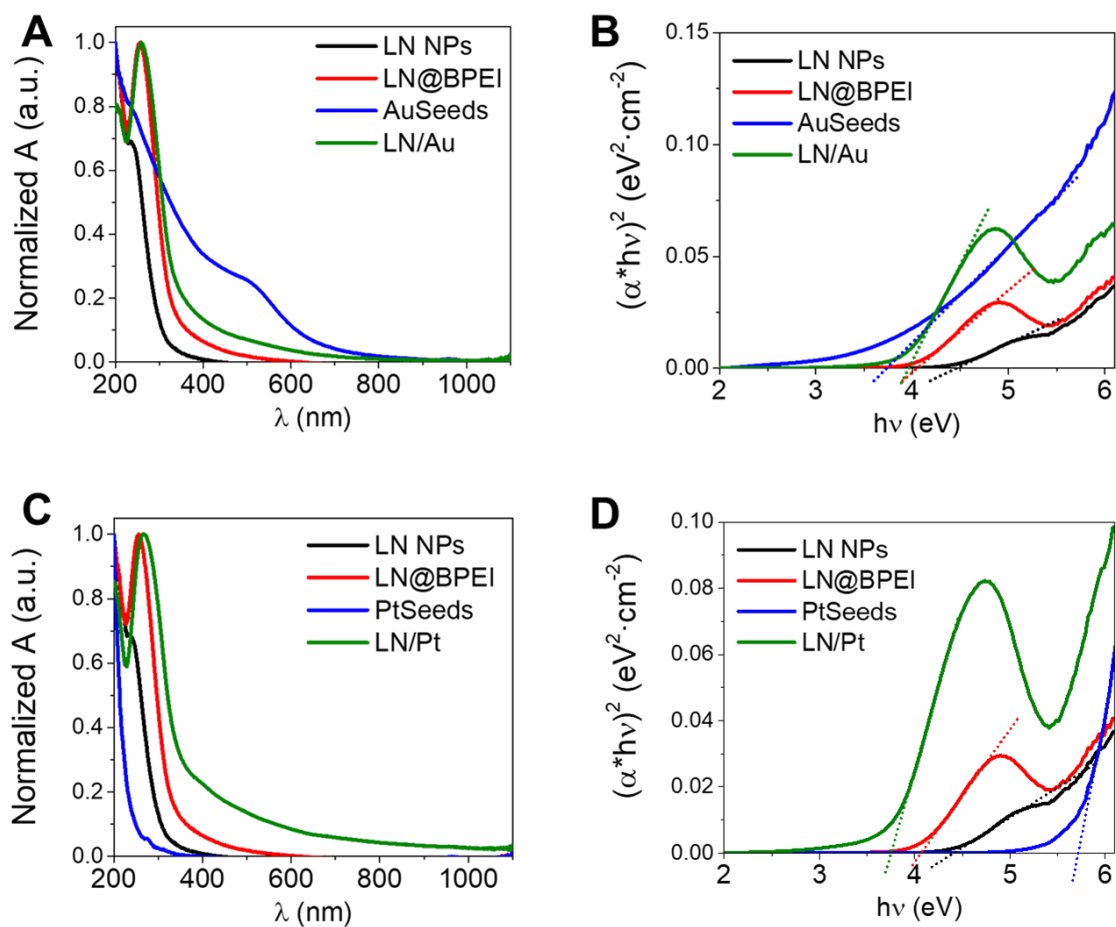


Figure 4.16. Normalized absorbance spectra (A) and Tauc plot for direct band gap (B) were obtained from the percentage of transmittance of LN (black), LN@BPEI (red), AuSeeds (blue) and LN/Au (green). Normalized absorbance spectra (C) and Tauc plot for direct band gap (D) obtained from the percentage of transmittance of LN (black), LN@BPEI (red), PtSeeds (blue) and LN/Pt (green).

Table 4.3. Direct band gap energies of the different materials obtained from extrapolation in the Tauc plot.

| Sample | Direct band gap (eV) |
|-------------|----------------------|
| LN NPs | 4.40 |
| LN@BPEI NPs | 4.08 |
| AuSeeds | 3.75 |
| LN/Au | 3.89 |
| PtSeeds | 5.78 |
| LN/Pt | 3.78 |

From the results presented in **Figure 4.16** and **Table 4.3**, we can see that the LN NPs band gap is placed at 4.40 eV. In the literature, the LN direct band gap values are reported between 3.5-4.7 eV depending on the grain size, composition, and defects [282]. The deposition of BPEI produces an energy decrease of the direct band gap of 9%. This effect may be caused by the tendency of -NH₂ groups, abundant in BPEI, to donate electrons, causing a shift of the LN NPs' valence band [283]. AuSeeds and PtSeeds present direct band gaps at 3.75 eV and 5.78 eV, respectively. This suggests that AuSeeds and PtSeeds are not in metallic state. This could be explained by the incomplete reduction of the metal ions during the synthesis. Thus, the presence of ionic species of Au and Pt in AuSeeds and PtSeeds, respectively, may cause the presence of the band gap [12], [192]. Another possibility that explains the presence of a band gap would be the complexation of Au or Pt with other species, for example, THPC or Cl⁻ ions [12], [192]. Finally, nanosized related effect could also play a role [284]. Further experiments could confirm these hypotheses.

LN/Au, direct band gap, is reduced by 12% with respect to LN NPs. In the case of the LN/Pt, the reduction is 14% (**Table 4.3**). The electron transfer and the possible vacancies creation in LN NPs upon metal deposition may explain these results [285].

We also obtained the optical band gap of TiO₂, TiO₂/Au and TiO₂/Pt, previously presented (Chapter 3: section 3.2.5). The results are shown in Figure 4.17 and Table 4.4. Indirect band gap calculation is provided in the appendix (Appendix: Figure A4C).

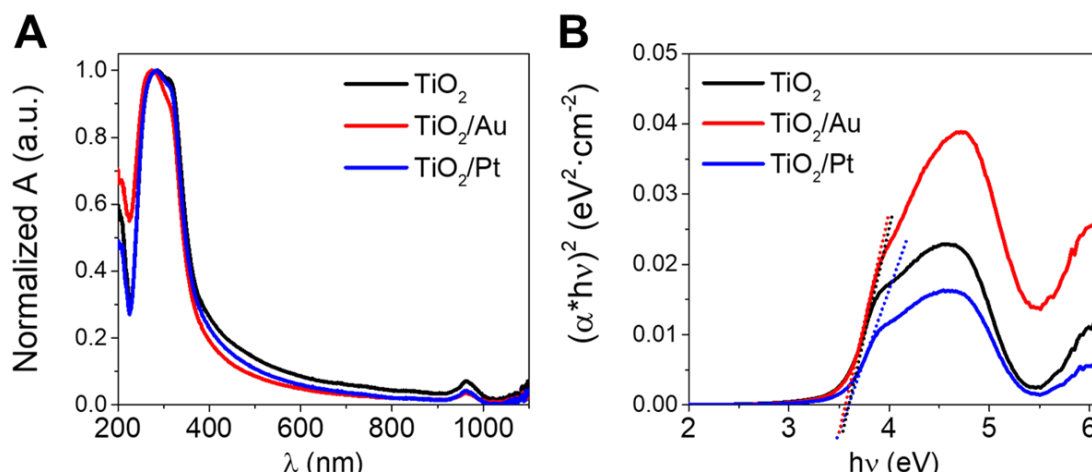


Figure 4.17. Normalized absorbance spectra (A) and Tauc plot for direct band gap (B) were obtained from the percentage of transmittance of TiO₂ (black), TiO₂/Au (red) and TiO₂/Pt (blue).

Table 4.4. Direct band gap energies of the different materials obtained from extrapolation in the Tauc plot.

| Sample | Direct band gap (eV) |
|----------------------|----------------------|
| TiO ₂ | 3.51 |
| TiO ₂ /Au | 3.55 |
| TiO ₂ /Pt | 3.53 |

TiO₂ NPs band gap at 3.51 eV (Figure 4.17 and Table 4.4) has been previously reported as a direct band gap in the anatase phase [286]. Interestingly, the deposition of Au or Pt does not produce any significant change in the direct band gap. The difference from LN hybrids is the absence of BPEI as LN/Au, and LN/Pt presented a band gap decrease compared to LN NPs, which was also shown in LN@BPEI. We thus made the hypothesis that BPEI may play a key role. This is also supported by the previous observation in which LN@BPEI, quenched the basal oxidation of TMB by H₂O₂ (Figure 4.11). Its role was investigated by complementary experiments that will be presented in the next section (4.4.2).

To understand the band structure, we performed XPS/UPS measurements in LN NPs, LN@BPEI and LN/Au. Indeed, a combined UPS and XPS analysis will allow obtaining the valence band maxima and the work function of each sample to determine the electron density close to the Fermi level and propose thus a diagram of their electronic structure. As mentioned in **Chapter 2: section 2.6**, NPs were deposited by drop-casting onto an Ag foil to reduce charge effects and UPS calibration purposes. Thus, Ag and Au foils alone were analysed as reference samples to determine the density of excited states around the Fermi level (**Figure 4.18**).

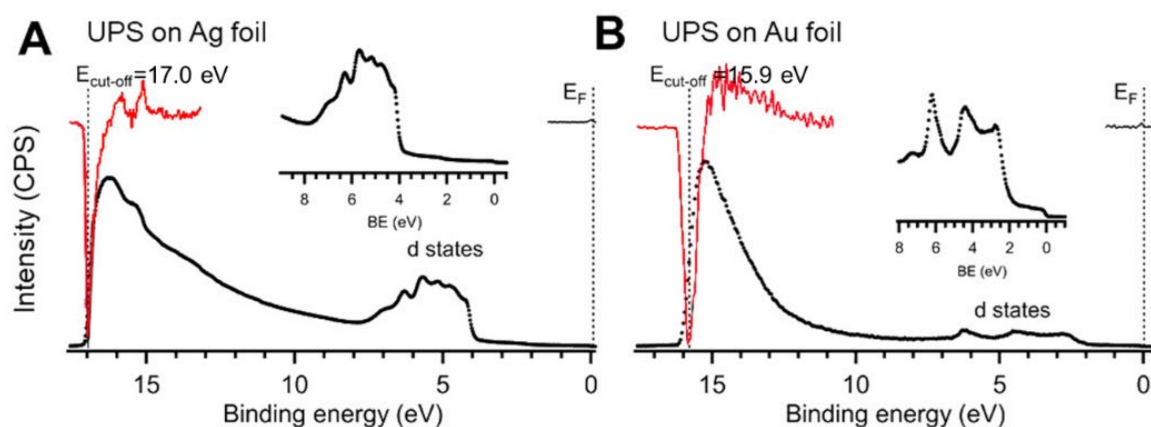


Figure 4.18. UPS analysis of Ag (A) and Au (B) foils. Insert: zoom on Ag (A) and Au (B) electron density. The UPS spectra (black) and their first derivatives (red) are represented.

Figure 4.18 shows the UPS spectra of Ag (A) and Au (B) foils with their classical *d* states and Fermi level. They provide the appropriate references for the Ag support used for UPS analysis purposes and Au to identify the electron density on hybrid nanoparticles. Both spectra indicate two apparent features: energy cut-off or photoionization edge ($E_{\text{cut-off}}$) and work function (Φ) values. Electrons provoking a sharp cut-off are the ones with just sufficient kinetic energy to leave the surface ($KE = 0$, $E_B = E_{\text{cut-off}}$). The $E_{\text{cut-off}}$ corresponds to the minimum of the first derivative. The work function was calculated using **Equation 4.1**, in which $h\nu$ is the energy of the source (21.2 eV).

Equation 4.1.

$$\phi = h\nu - E_{\text{cut-off}}$$

Ag and Au foils exhibits ϕ values of 4.2 eV and 5.3 eV, respectively, in good agreement with literature values [287], [288].

XPS/UPS analysis on LN NPs is presented in **Figure 4.19**.

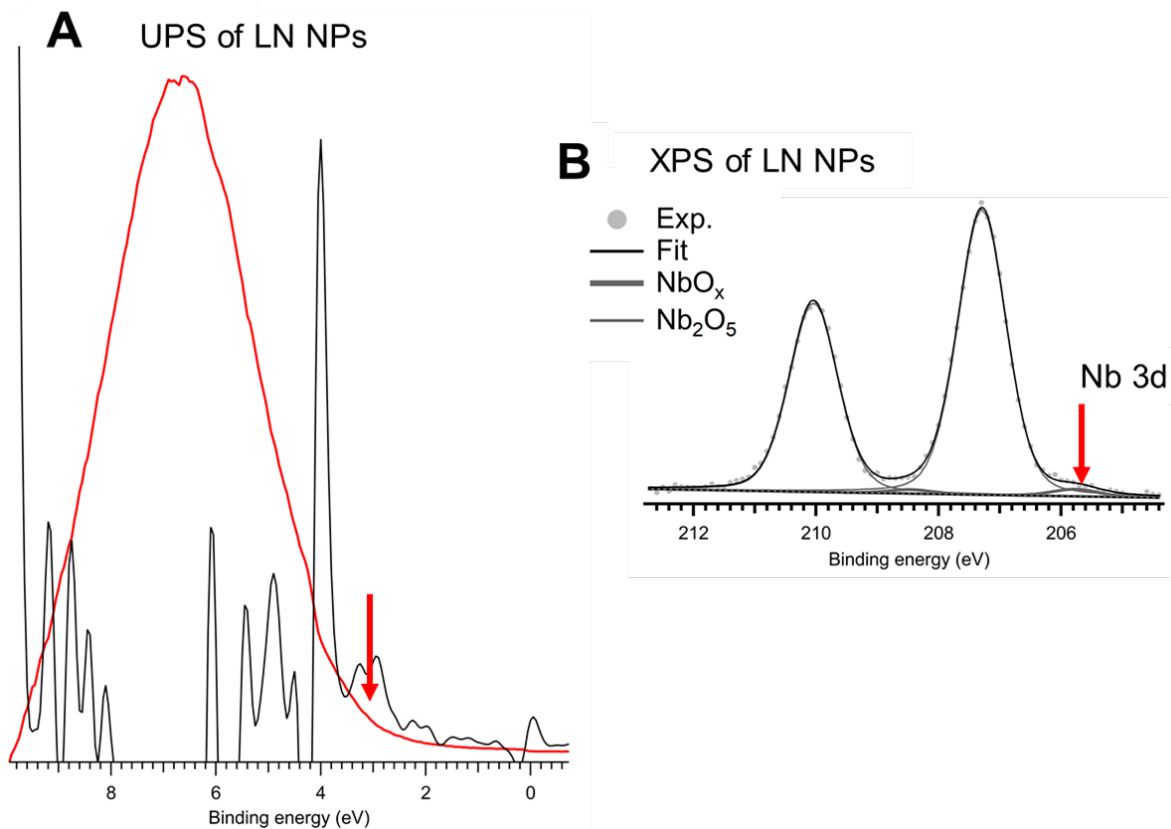


Figure 4.19. (A) UPS spectrum of LN NPs (red curve). The black curve is the 2nd derivative of the red curve used to identify the inflection points (arrow, 3 eV). (B) XPS spectrum of LN NPs focused on the region of Nb 3d peak at 205.8 eV (arrow).

UPS reveals a maximum of the valence band for LN NPs at around 3 eV, determined using the 2nd derivative of the UPS spectra to obtain the inflection point, concomitant with a work function (ϕ) of 3.8 eV (**Figure 4.19A**). **Figure 4.19B** highlighted the presence of a NbO_x oxide layer on the Nb 3d core level, reaching 2% at 205.8 eV in good agreement with previous literature [289]. The LN NPs UPS spectrum was then compared to the UPS spectra of LN/Au, LN@BPEI and Au foil. The spectra are shown in **Figure 4.20**.

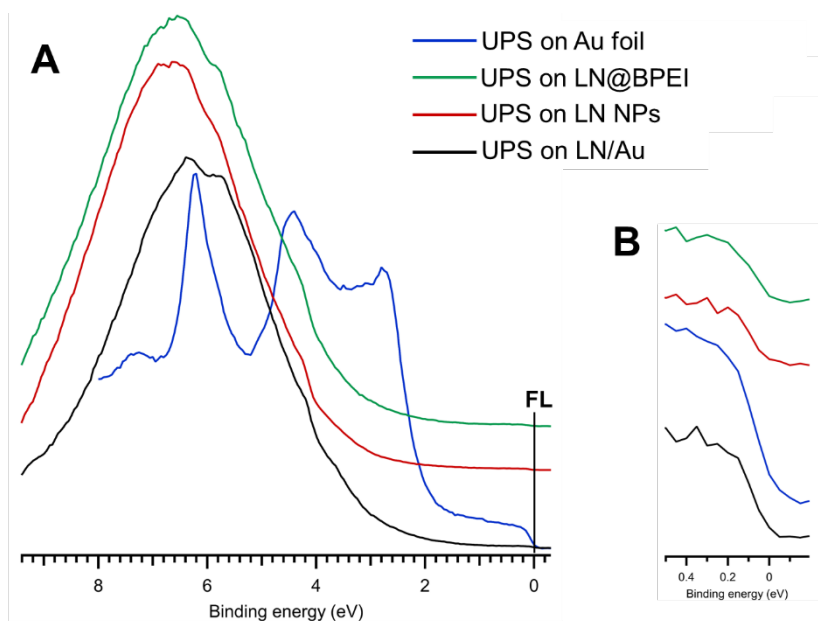


Figure 4.20. (A) UPS analysis and (B) zoom in the Fermi Level (FL) of LN NPs (red curve), LN@BPEI NPs (green curve), LN/Au NPs (black curve) and Au foil (blue curve).

Figure 4.20A shows that the states correspond to the LiNbO_3 for the LN@BPEI, LN NPs and LN/Au. However, it highlights a marked evolution with the presence of gold on the surface, notably demonstrated by the band narrowing of the states and a shift towards lower binding energies around 6.2 eV. As previously reported, this may demonstrate an electronic exchange between LiNbO_3 and Au in the interface, thanks to the hybridisation of states [246]. This preliminary conclusion should be corroborated through DFT calculations. In addition, in the zoom in **Figure 4.20B**, we observe that the LN/Au has a sharpened FL, similar to the Au foil. This indicates that the LN/Au possess a more metallic character than the LN NPs or LN@BPEI.

We obtained the values of the Fermi level (FL) and the work function from the second derivative at low binding energies, summarized in **Table 4.5**.

Table 4.5. Work function ϕ and valence band maximum (VB_{\max}) values for the samples determined by XPS/UPS analysis.

| Sample | Work function (eV) | VB_{\max} (eV) relative to the Fermi level of Ag |
|-------------|--------------------|--|
| Ag foil | 4.2 | / |
| Au foil | 5.3 | / |
| LN NPs | 3.8 | 3 |
| LN@BPEI NPs | 3.6 | 3.2 |
| LN/Au | 3.7 | 3.1 |

Au foil work function is in agreement with the one reported in the literature [290]. However, gold nanoparticles' work function has been reported to be much lower. For instance, 10 nm gold nanoparticles presented a work function of 3.6 eV and continues decreasing with the decreasing size. Indeed, when the diameter reaches 3 nm, the metallic properties start to fade [284]. From the data presented in **Table 4.5**, we see that LN NPs, LN@BPEI and LN/Au work function is similar. As mentioned, the peak shift to lower binding energies obtained for LN/Au (**Table 4.5**) suggests a charge transfer. However, regarding the work function of the different materials (**Table 4.5**), the deposition of AuSeeds does not cause a significant effect on the stabilization of bands compared to the LN NPs and LN@BPEI NPs.

The determination of the VB_{\max} with respect to the Fermi level of Ag foil (4.2 eV) by UPS and the band gap energy by UV-Vis, allowed us to propose a preliminary band structure position for LN NPs, LN@BPEI NPs, LN/Au, TiO_2 and TiO_2/Au (**Figure 4.21**). To obtain the absolute position of the VB_{\max} , we added the Fermi level position of Ag foil (reference) to the position of the maximum of the valence with respect to it. The band gap calculations obtained through Tauc plot (**Table 4.3**, **Table 4.4**) allowed us to obtain the minimum position of the conduction band (CB_{\min}).

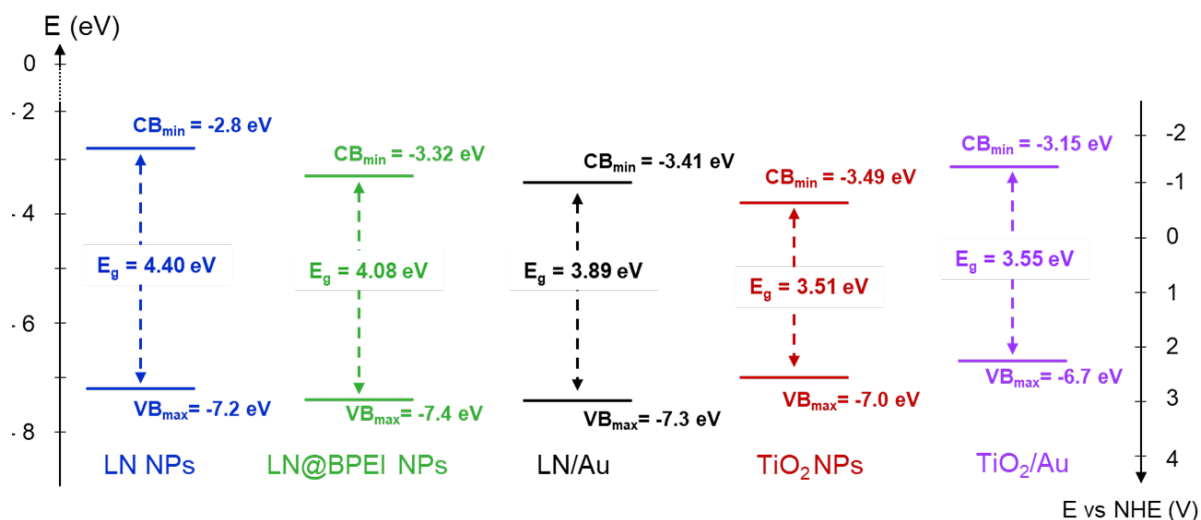


Figure 4.21. Absolute band structure position for LN NPs (blue), LN@BPEI (green), LN/Au (black), TiO₂ NPs (red) and TiO₂/Au (purple). Absolute VB_{max} positions were obtained by UPS and E_g (band gap) was obtained by UV-Vis.

To summarize, **Figure 4.21** probes that the charge transfer between the different materials might be negligible. However, as mentioned before, AuSeeds provoke some electronic exchanges (**Figure 4.20**), and interestingly the band gap in LN/Au is considerably reduced and so is the CB_{min}. Thus, electron transfers are favoured, and we can state that the increased peroxidase mimics might come from this effect. More experiments are being done to obtain the band structure for LN/Pt. Moreover, the band gap reduction in LN/Au and LN/Pt opens a wide range of applications for photocatalysis and it will be explored in the next chapter (**Chapter 5: section 5.4**).

4.4.2. Metal Seeds and BPEI effect

The decrease in the LN@BPEI band gap compared to LN NPs (**Table 4.3**) implies that BPEI influences the band structure. Thus, we decided to test the effect of BPEI on AuSeeds and PtSeeds in the absence of LN NPs in the peroxidase mimics. We used old samples (> 1 year) of AuSeeds and PtSeeds, and we recharacterized their TEM diameter to check their stability over long-time storage. Then we repeated the synthesis protocol of the hybrids, as described in the previous chapter (**Chapter 3: section 3.1.4**), but we did not add LN. We dissolve 50 mg of BPEI in 40 mL water for 4h at 90 °C. We add the correspondent volumes of BPEI solution (1.25 g/L) to the Seeds solution, considering that each LN NP is coated with 1210 molecules of BPEI [174] and that in the hybrid nanoparticles, there are 40 and 73 Seeds of AuSeeds and

PtSeeds, respectively. After cooling it down, we mixed it with AuSeeds and PtSeeds, respectively, for 30 minutes. No washing steps were carried out as the Seeds' diameter was so small that centrifugation did not precipitate them. The samples were stored at 4 °C.

The samples were characterised by TEM (Figure 4.22, Table 4.6). In Table 4.6, we have included the values of the fresh samples (Chapter 3: Table 3.3) for better comparison.

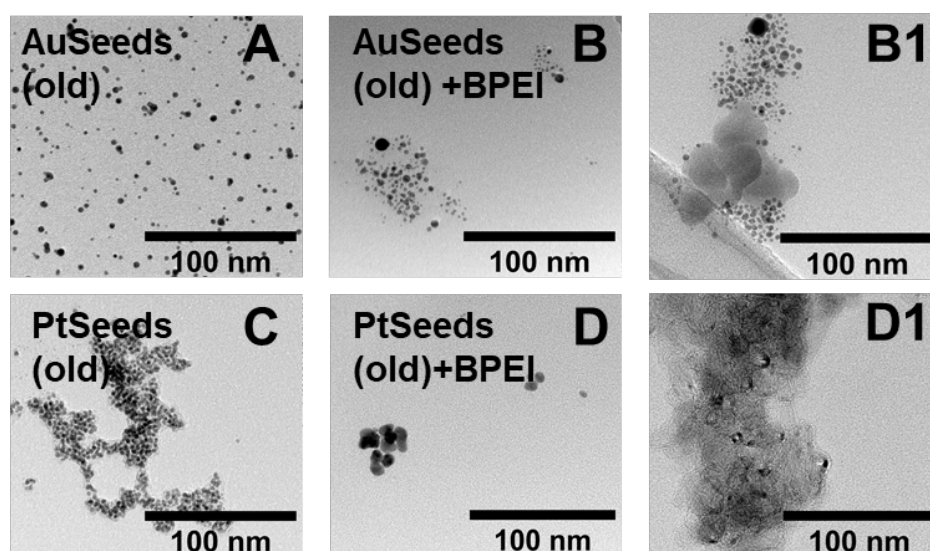


Figure 4.22. TEM images of AuSeeds (old) (A), AuSeeds (old)+BPEI (B, B1), PtSeeds (old) (C) and PtSeeds (old)+BPEI (D, D1).

Table 4.6. TEM diameters obtained for fresh and old samples of AuSeeds and PtSeeds, and for old samples of AuSeeds and PtSeeds after BPEI addition.

| Sample name | TEM diameter (nm) \pm SD |
|---------------------|----------------------------|
| AuSeeds (fresh) | 2.0 \pm 0.8 |
| AuSeeds (old) | 3.1 \pm 1.0 |
| AuSeeds (old) +BPEI | 2.8 \pm 1.0 |
| PtSeeds (fresh) | 3.1 \pm 0.6 |
| PtSeeds (old) | 2.9 \pm 0.6 |
| PtSeeds (old) +BPEI | 5.2 \pm 0.5 |

The results of TEM diameter (**Figure 4.22A and B, B1 and Table 4.6**) indicate an increase in size for AuSeeds over time. The addition of BPEI does not show any significant difference compared to AuSeeds (old). However, TEM images indicate the formation of aggregates and the apparition of grey blurred areas, which may be due to the excess of BPEI (**Figure 4.22B1**). The TEM diameter of PtSeeds is not affected by time, but the addition of BPEI produces a large increase in the diameter (5.2 nm) (**Figure 4.22 and Table 4.6**). Moreover, like for AuSeeds, grey blurred areas are visible, as seen in **Figure 4.22D1**. The presence of this supposed excess of BPEI made useless the measurement of hydrodynamic diameters and zeta potential values to characterize the properties of single metal seeds.

Following the characterization, we conducted the peroxidase mimics experiment with the conditions optimized in the previous section (**4.1.2**), *i.e.* $[\text{H}_2\text{O}_2] = 29.7 \text{ mM}$, $[\text{TMB}] = 167 \text{ }\mu\text{M}$, $[\text{Au}] = 27 \text{ }\mu\text{M}$, $[\text{Pt}] = 2.8 \text{ }\mu\text{M}$, pH 4 and $37 \text{ }^\circ\text{C}$ (**Figure 4.23**).

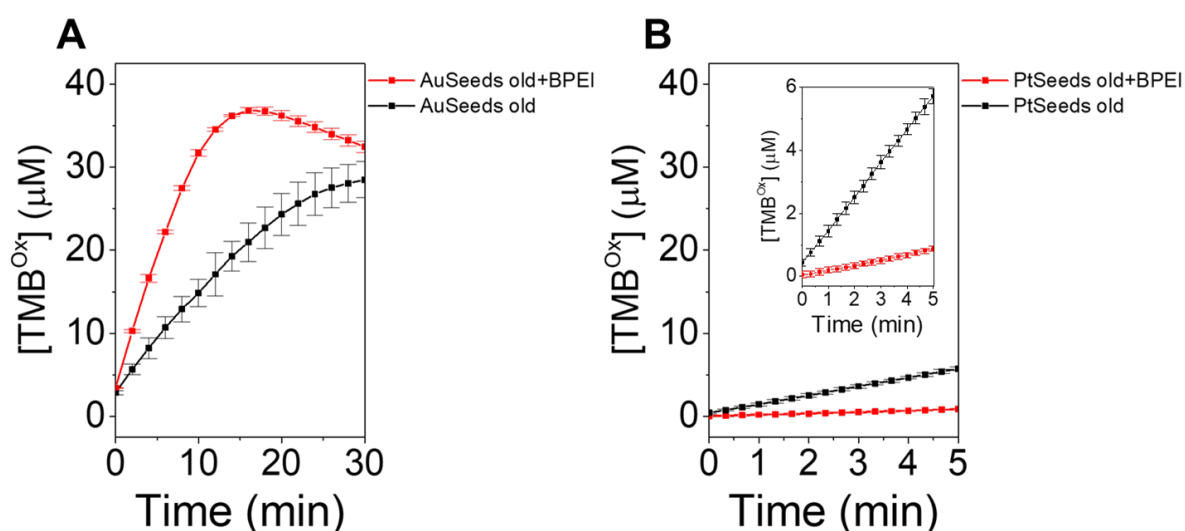


Figure 4.23. (A) Peroxidase-mimics of AuSeeds old+BPEI (red) and AuSeeds old (black) (B) Peroxidase-mimics of PtSeeds old+BPEI (red) and PtSeeds old (black). (B, insert) Zoom on the activity of PtSeeds old+BPEI and PtSeeds. Experiment conditions: $[\text{H}_2\text{O}_2] = 29.7 \text{ mM}$, $[\text{TMB}] = 167 \text{ }\mu\text{M}$, $[\text{Au}] = 27 \text{ }\mu\text{M}$, $[\text{Pt}] = 2.8 \text{ }\mu\text{M}$, pH 4 and $37 \text{ }^\circ\text{C}$.

In **Figure 4.23A**, we observe that BPEI plays a significant role combined with the metal Seeds. AuSeeds+BPEI presents a slightly higher activity than AuSeeds while on the contrary, PtSeeds+BPEI presents a significantly lower activity than PtSeeds.

Therefore, several hypotheses can be discussed. First, for PtSeeds+BPEI, the TEM diameter significantly increases compared to PtSeeds, and this diameter is higher than 5 nm (see **Table 4.6**), which has been proven to be a threshold in catalysis above which activity is not ensured [93]. For AuSeeds+BPEI, as the diameter remained almost unchanged compared to AuSeeds (see **Table 4.6**), the activity is not significantly modified. Second, the difference between Au-BPEI and Pt-BPEI chemical affinities due to the complexation of Au and Pt by nitrogen could contribute to the observed changes in catalytic activities. However, the excess of BPEI may also affect the catalytic activity, because of its reducing properties [254]. Thus the production of oxidized TMB may be hindered by free BPEI molecules in the Seeds dispersions. To conclude, it would be worth characterizing the catalytic activity of BPEI alone to get more insights into its effect on catalytic properties.

4.4.3. ROS characterization

The results presented in **Figure 4.11** showed that LN/Au and LN/Pt improve AuSeeds and PtSeeds peroxidase-mimics. ROS generation is one of the most accepted mechanisms that cause the substrate's oxidation (**Chapter 1: section 1.1.4.6**) [126]. To elucidate the reactive species generated, we decided to qualitatively measure the ROS production of the systems at pH 4. For this, we used three chemical traps for the three most common ROS generated from H₂O₂ and O₂: terephthalic acid (TA) for •OH, dihydroethidium (DHE) for O₂•⁻ and 9,10-anthracenediyl-bis(methylene)dimalonic acid (ABDA) for ¹O₂. As mentioned in **Chapter 2: section 2.7**, TA, upon reaction with •OH, produces a fluorescent product whose excitation wavelength is at $\lambda_{exc} = 320 \pm 15$ nm and emission is at $\lambda_{em} = 420 \pm 10$ nm (**Figure 4.24A**) [252]. DHE reaction with O₂•⁻ produces a fluorescent product that can be excited at $\lambda_{exc} = 490 \pm 10$ nm and that emits at $\lambda_{em} = 625 \pm 10$ nm (**Figure 4.24B**) [253]. Finally, ABDA presents an absorption maximum at 380 nm, but its reaction with singlet oxygen provokes an endoperoxide which does not absorb in the UV-vis region, resulting in a decrease in absorbance when the reaction progresses (**Figure 4.24C**) (**Chapter 2: section 2.5.3.2**) [247].

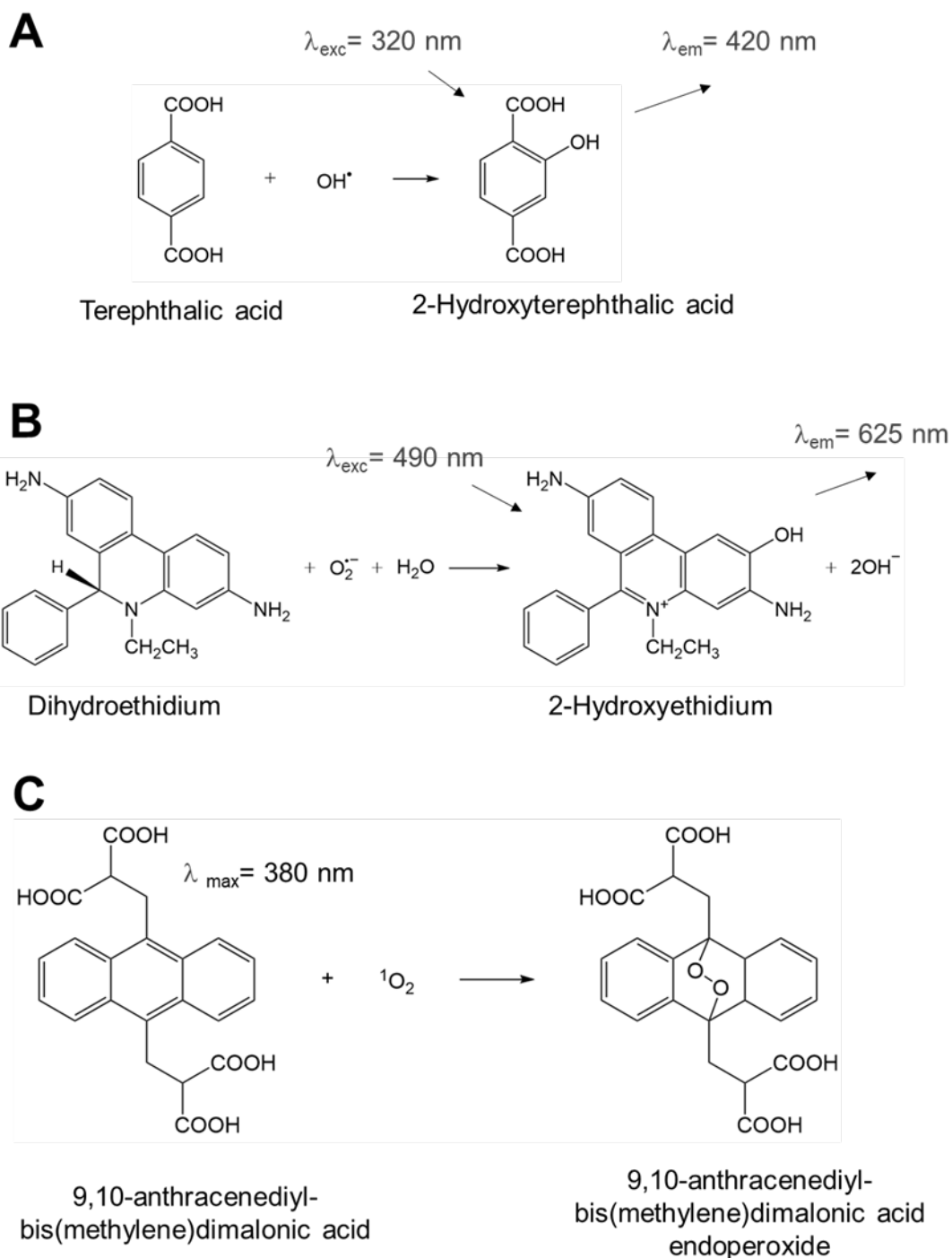


Figure 4.24. (A) The reaction of terephthalic acid (TA) with OH[•] producing 2-hydroxyterephthalic acid. (B) The reaction of dihydroethidium (DHE) with O₂^{•-} producing 2-hydroxyethidium. (C) The reaction of 9,10-Anthracenediyl-bis(methylene)dimalonic acid (ABDA) with ¹O₂ producing the correspondent endoperoxide. λ_{exc} is excitation wavelength, λ_{em} is fluorescent emission wavelength, λ_{max} is the absorption maximum.

As this was a qualitative measurement, we reduced the total reaction volume and the concentration of Nanozyme. The volume was fixed at 100 μL , the H_2O_2 concentration was kept at 29.7 mM, and the pH was fixed at 4. For the Nanozymes, LN/Au and LN/Pt, we selected batches 2 (LN/Au-2 and LN/Pt-2), whose peroxidase activities are presented in **Figure 4.12**. The concentration of Au was fixed to 11 μM in AuSeeds and LN/Au (with a correspondent concentration of LN of 78.1 μM). The concentration of Pt in PtSeeds and LN/Pt was reduced to 1.1 μM (with a correspondent concentration of LN of 7.6 μM) to keep consistent the previous 10 times reduction of concentration in the catalytic experiments. The concentrations of the ROS traps in the wells were selected according to previous literature, $[\text{TA}] = 1 \text{ mM}$ [126], $[\text{DHE}] = 0.01 \text{ mM}$ [291] and $[\text{ABDA}] = 0.2 \text{ mM}$ [292]. The results are shown in **Figure 4.25**.

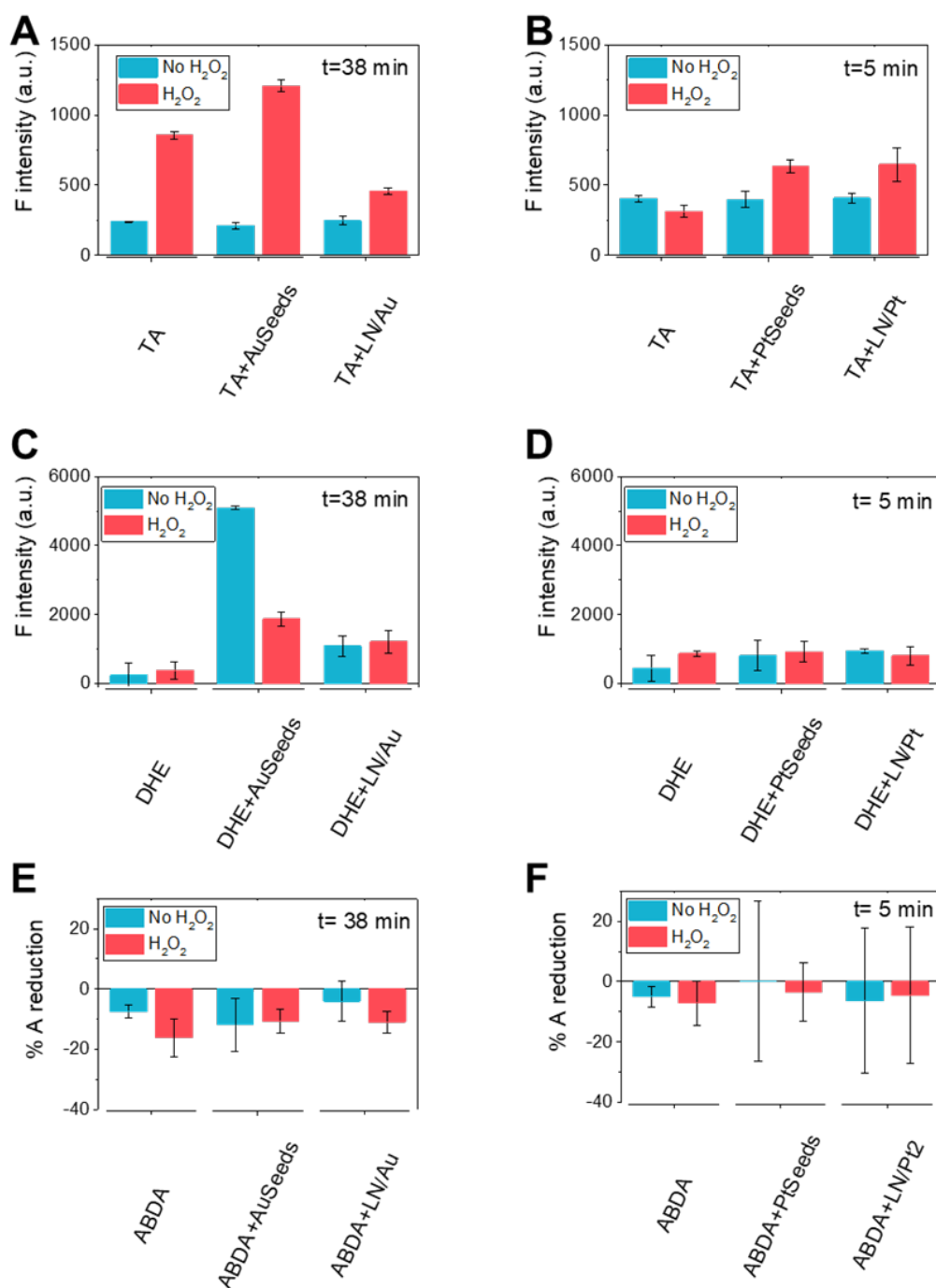


Figure 4.25. (A, B) Fluorescent (F) intensity of the reaction of TA and the possible OH[•] generated by the Nanozymes at different times using [TA] = 1 mM. (C, D) Fluorescent (F) intensity of the reaction of DHE and the possible O₂^{•-} generated by the Nanozymes at different times using [DHE] = 0.01 mM. (E, F) % Absorbance (A) reduction of the reaction of ABDA and the possible ¹O₂ generated by the Nanozymes at different times using [ABDA] = 0.2 mM. (A, C, E) [Au] = 11 μM; [LN] = 78.1 μM. (B, D, F) [Pt] = 1.1 μM; [LN] = 7.6 μM. For all the systems, the reactions were done at pH 4 with acetate buffer and [H₂O₂] = 29.7 mM.

As seen in **Figure 4.25A and B**, the fluorescent intensity after 38 and 5 min, respectively, without H₂O₂, does not produce any significant change when the Nanozymes are present, which means that they do not generate OH• from the dissolved O₂. In the presence of H₂O₂, the fluorescent intensity in the presence of AuSeeds increases by 50% compared to the TA+H₂O₂ system, favouring the production of OH• [54]. Interestingly, in TA+H₂O₂+LN/Au system, the fluorescent intensity remains much lower than for the TA+H₂O₂ and TA+H₂O₂+AuSeeds with H₂O₂. In the presence of H₂O₂, PtSeeds and LN/Pt Nanozymes generate OH•, which remains low compared to the TA+H₂O₂+AuSeeds system. This contrasts with the higher activity towards TMB oxidation as peroxidase mimics of LN/Au and, especially, for LN/Pt as one of the most accepted mechanisms for TMB oxidation with metal Nanozymes is the OH• production [80], [130]. Nevertheless, it has been shown that OH• is not the only ROS that can oxidize TMB, and O₂•⁻ and ¹O₂ can also be generated [131]. Thus, we characterized their production. The only system that produces a significant change is DHE+AuSeeds (**Figure 4.25C**), which means that AuSeeds produce O₂•⁻ from the dissolved O₂. ABDA reduction of absorbance means it reacts with ¹O₂. The system that generates the most ¹O₂ is ABDA+H₂O₂ after 38 min (**Figure 4.25E**). AuSeeds and LN/Au may even be quenching their production. From these experiments, we can conclude that the enhanced generation of ROS by LN/Au and LN/Pt Nanozymes remains negligible in comparison to the systems without Nanozymes.

The mechanistic explanation could be that both TMB and H₂O₂ are adsorbed at the surface of the Nanozyme thanks to the interface between the metal and metal oxide using BPEI as a linker and the reaction occurs *in situ*, which is a mechanism similar to the one of natural enzymes.

4.5. Conclusion

LN/Au and LN/Pt Nanozyme activities were characterized. LN/Au and LN/Pt present peroxidase mimic as they oxidise TMB in the presence of H₂O₂. They may also present catalase activity, especially LN/Pt, as they show bubble production in the presence of only H₂O₂. In addition, LN/Pt presents oxidase mimics as it is able to oxidise TMB in the absence of H₂O₂. For the sake of comparison, we chose to study peroxidase-mimics. We initially optimized the conditions for LN/Au (substrate, pH and temperature), resulting in TMB, pH 4 (acetate buffer) and 37 °C as the best ones. In the case of LN/Pt, we optimize pH and temperature, resulting in the same conditions. We compared the peroxidase mimics of LN/Au and LN/Pt to their counterparts (Seeds, LN NPs, LN@BPEI) and a simple mixture of them (*i.e.*, without the BPEI), which resulted in increased activity as a result of the combination of materials. We validated the batch-to-batch reproducibility and long-term activity of the hybrid Nanozymes, which offers an improvement over natural enzymes. We further probed them as better peroxidase mimics than TiO₂/Au and TiO₂/Pt, respectively. We obtained the Michaelis-Menten parameters (K_m , V_{max} , K_{cat} and K_{eff}) for the AuSeeds, LN/Au, PtSeeds and LN/Pt for the two substrates, TMB and H₂O₂, and we observed the effect of deposition of the Seeds on the LN@BPEI. Except for the K_m of TMB (an indicator of the affinity towards the substrate), the rest of the parameters were improved, especially in LN/Pt. Observing this improvement, we tried to elucidate the band structure of the materials. However, the most remarkable was a band gap reduction for both hybrid nanoparticles compared to the LN NPs and LN@BPEI NPs. We also coated the AuSeeds and PtSeeds with BPEI. However, the absence of cleaning steps led to the presence of artefacts in both samples, which makes comparison not possible, and more experiments are being conducted to elucidate the role of BPEI. Finally, we studied the ROS generation by the Seeds and the hybrid nanoparticles, but no significant change was observed.

To summarize, LN/Au and LN/Pt improve peroxidase mimics compared to the separated counterparts and a simple mixture of the LN NPs and the Seeds. The mechanistic study suggests a band gap reduction, but no significant difference was observed in the position of the bands. BPEI play a significant role, but the comparison is difficult. Finally, the peroxidase-mimics does not seem to be mediated by ROS production, suggesting that both reactants approach the surface of the Nanozyme and react *in situ* to proceed to the detachment, which is closer to the mechanism of natural enzymes.

Chapter 5: Nanozyme ROS production/ scavenging and their interaction with bacteria

The last chapter of this thesis focuses on the influence of the LN/Au and LN/Pt Nanozymes to the bacterial culture under oxidative stress. The sources of oxidative stress are H₂O₂ and UV-radiation (302 nm) and their combination. Initially, we investigated the interaction between bacteria and the different components of the Nanozymes (LN NPs, LN@BPEI, AuSeeds, PtSeeds) and the hybrid Nanozymes LN/Au and LN/Pt. We continued to explore how adding H₂O₂ and the exposition to UV light (302 nm) induced oxidative stress and if the Nanozymes and the different components contributed to enhancing or scavenging it. Finally, we induced oxidative stress through H₂O₂ and UV light radiation simultaneously. We also did complementary studies with ROS probes used in **Chapter 4: section 4.4.3**, to validate the results.

5.1. Materials and Methods for Bacterial culture and ROS characterization

5.1.1. Chemicals

The following materials were used in this chapter: sodium hydroxide (NaOH) in pellets, dimethyl sulfoxide (DMSO), terephthalic acid (TA) (98%), dihydroethidium (DHE) ($\geq 95\%$), 9,10-anthracenyl-bis-(methylene)dimalonic acid (ABDA) ($\geq 90\%$) were purchased from Sigma Aldrich and used without modification. Hydrogen peroxide (30% w/w) was purchased from Chem-Supply Pty Ltd. Nutrient Broth (NB) was purchased from Amyl Media and used without modification, and *Escherichia Coli* (*E. coli*) (DH5 α) bacterial strain was purchased from ATCC and frozen at -80 °C. Unless otherwise said, any water used was deionized (18.2 M Ω ·cm) decanted from a Millipore unit.

5.1.2. Microbial Culture of *E. coli*. and Nanozymes under Oxidative Stress

All materials and chemicals were sterilized in an autoclave at 120 °C for 30 min. Each experiment of microbial culture was prepared as follows (**Figure 5.1**). Monocolony of *E. coli* pure culture stored at -80 °C was unfrozen, spread on a Nutrient Agar plate, and a single colony was inoculated into 1x Nutrient Broth (1.30 g of NB in 100 mL of H₂O, as indicated by the manufacturer) media and incubated overnight at 37 °C and 100 rpm. Control samples were also prepared during the experiments to ensure sterilization. The cell density of the overnight growth was measured and adjusted to 0.5 optical density (OD) with a UV-Vis spectrophotometer at 600 nm, OD₆₀₀. Subsequently, 1 mL of the bacterial solution was inoculated into 80 mL of fresh media and incubated at 37 °C and 250 rpm for 3 h. Finally, the bacterial density was adjusted, so the OD₆₀₀ in the well plate was 0.05, corresponding to 4×10^7 CFU/mL (CFU: colony forming units). The final volume of all the experiments was fixed at 150 μ L. This procedure ensures the bacteria's quality and starts the experiments in the exponential growth phase.

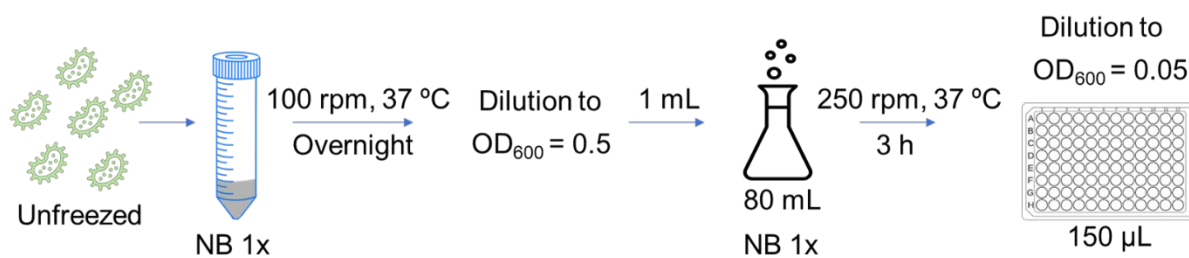


Figure 5.1. *E. coli* colony incubation and preparation process.

We cultured the as-prepared *E. coli* in the well plate with hybrid Nanozymes and the separated counterparts: LN NPs, LN@BPEI, AuSeeds, PtSeeds, LN/Au and LN/Pt. Throughout this chapter, we have referred LN and LN@BPEI as NPs, and those containing Au and Pt-based materials as Nanozymes. The concentrations were chosen as follows: [LN]= 7µM, [Au]= 1 µM, [Pt]= 1µM. To assess ROS production or scavenging, we determined the minimum cytotoxicity of H₂O₂ by varying its concentration from 0-100 mM. Similarly, we determined the cytotoxicity of UV irradiation using UVB-lamp 8-Watt halogen tubes with λ_{max}= 302 nm at different exposure times: 30 s, 1 min and 2 min. The working distance between the sample and the light source was optimised to obtain the needed photo intensity/dose at the sample surface using a Thorlabs PM 200 optical power and energy meter with a S302C sensor. The quantitative assessment of the experiments was done using **Equations 5.1, 5.2 and 5.3**:

Equation 5.1

$$\% \text{ cell death} = \left(1 - \frac{\text{Normalized \# Treated bacteria}}{\text{Normalized \# Control bacteria}} \right) \times 100$$

Equation 5.2

$$\text{Relative increase to control} = \frac{\text{Normalized \# Treated bacteria}}{\text{Normalized \# Control bacteria}}$$

Equation 5.3.

$$\% \text{ induced relative cell growth} = \left(\frac{\text{Normalized \# Treated bacteria}}{\text{Normalized \# Control bacteria}} - 1 \right) \times 100$$

Each experiment was carried out for 3 h at 37 °C and without agitation.

ROS complementary studies with the different probes were done as in **Chapter 4: section 4.4.3**. In the case of UV-related oxidative stress, the total time of irradiation was 2 min at the same wavelength (302 nm).

5.2. *E. coli* growth interaction with Nanozymes and nanoparticles.

We first measured the interaction of *E. coli* and the different nanoparticles and Nanozymes over time by UV-Vis absorbance spectroscopy (**Figure 5.2**) and normalized the OD values to the number of bacteria. We then compared each sample growth to the control and compared the effect of the deposition of the metal seeds effect onto LN@BPEI (**Figure 5.3**).

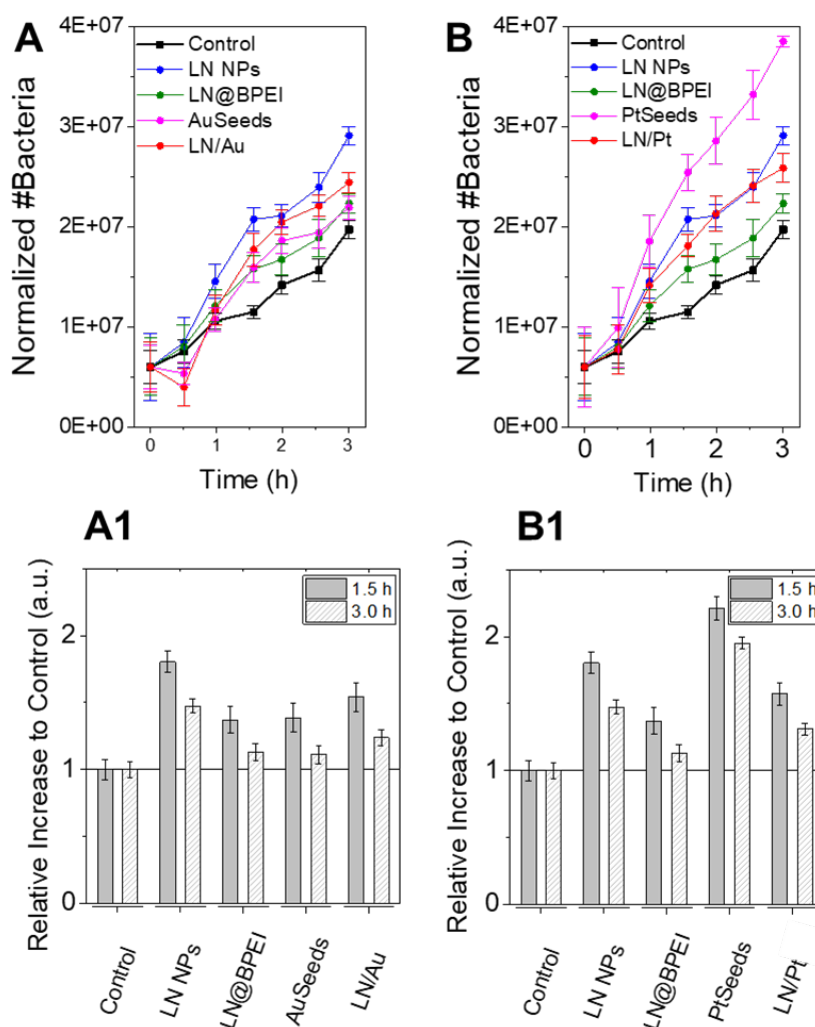


Figure 5.2. Bacterial growth over time and relative increase to control in the Au (A, A1) and the Pt system (B, B1). Control, *i.e.*, bacteria without any treatment (black), LN NPs (blue), LN@BPEI (green), metal Seeds (pink), and hybrid Nanozymes (red) are shown. Concentrations are [Au] = 1 μ M, [Pt] = 1 μ M and [LiNbO₃] = 7 μ M.

As seen in **Figure 5.2**, all the nanoparticles present a probiotic effect by enhancing bacterial growth over control which is more prominent in the first 1.5 h. Bacteria commonly generate ROS due to their routine metabolism, and the potential ability of Nanoparticles and Nanozymes to scavenge them may cause a probiotic effect thanks to the production of additional O₂ during scavenging activity, for instance through peroxidase and catalase-mimicking pathways [132]. LN NPs present a good probiotic effect, but the functionalization with BPEI, a cationic polymer, decreases this effect. Cationic polymers are known to react with the cytoplasmic membrane producing cell death, and are widely used antibacterial agents [293]. Moreover, the surface charge on nanoparticles (zeta potential) can play a crucial role in Nanoparticle-bacteria interaction. It has been shown that positively-charged nanoparticles are prone to be absorbed by bacteria as the latter possess a negative surface charge [294]. On the other hand, negatively-charged nanoparticles at low concentrations were observed to possess low antimicrobial activity [295]. AuSeeds probiotic effect is lower than the one of PtSeeds, which can be explained by the catalase-mimics activities presented in **Chapter 4: Figure 4.8B**. PtSeeds generated O₂ (bubbles) through catalase-mimic activity, which was not appreciable in the case of AuSeeds (**Chapter 4: Figure 4.2B**). Oxygen is critical for the growth of aerobic bacteria such as *E. coli*, and local access to this molecular oxygen via PtSeeds Nanozyme to bacteria can enhance their growth. Besides, PtSeeds have already been reported as probiotic agents [87]. Although LN/Au and LN/Pt present similar behaviour in bacteria growth, the effects produced upon the deposition of metal seeds onto LN@BPEI NPs, *i.e.*, effects of LN/Au and LN/Pt relative to their metal seed precursors, are different. AuSeeds deposition causes a slight increase in bacterial growth, which is statistically insignificant. However, LN/Pt produces an apparent decrease in bacterial growth compared to PtSeeds (**Figure 5.3**).

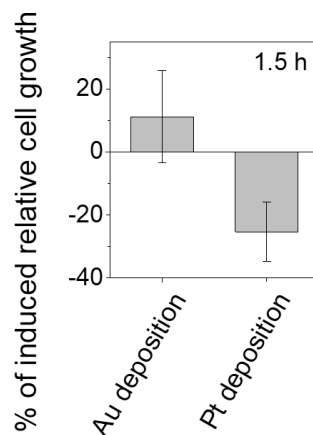


Figure 5.3. Induced relative bacterial growth upon deposition of the metal seeds onto LN@BPEI measured after 1.5 h of incubation. The data represents relative change in the bacterial populations upon deposition of either Au or Pt Seeds on LN@BPEI compared to the respective AuSeeds and PtSeeds.

5.3. *E. coli* growth interaction with Nanozymes and H₂O₂

After observing the effect provoked by Nanozyme in bacterial growth, we studied their effect with an externally added H₂O₂ during their growth. The aim of this study was to understand whether these Nanozymes are able to overcome the oxidative stress caused by H₂O₂ or make its effect more pronounced.

5.3.1. *E. coli* growth response to increasing concentration of H₂O₂

We studied the oxidative stress induced by H₂O₂ combined with the nanoparticles. Initially, we measured the cytotoxicity of various concentrations of H₂O₂, followed by calculating the percentage of cell death after 3 h (Figure 5.4) using Equation 5.1.

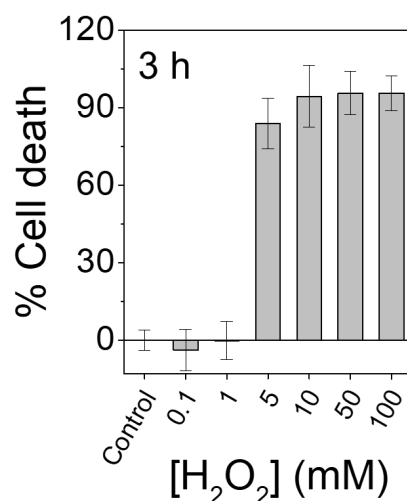


Figure 5.4. H₂O₂ cytotoxicity at different concentrations after 3 h, from 0 mM (control) to 100 mM.

As seen in **Figure 5.4**, H₂O₂ concentrations alone, when higher than 1 mM, drastically induce bacterial death. This is in agreement with other studies [296], [297]. H₂O₂ is a potent antimicrobial agent that produces oxidative stress. However, it is also a by-product of bacterial metabolism, and small quantities can be harmless as the protective mechanisms of bacteria are able to handle them [298]. We chose 1 mM as the concentration of H₂O₂ to combine with the Nanozymes as it is the highest tested dose that does not provoke cell death.

5.3.2. *E. coli* growth response to H₂O₂ and Nanoparticles

We combined LN NPs and LN@BPEI at [LiNbO₃]= 7 μM with 1 mM of H₂O₂ and measured OD₆₀₀ of bacteria after 3 h. The results are shown in **Figure 5.5**.

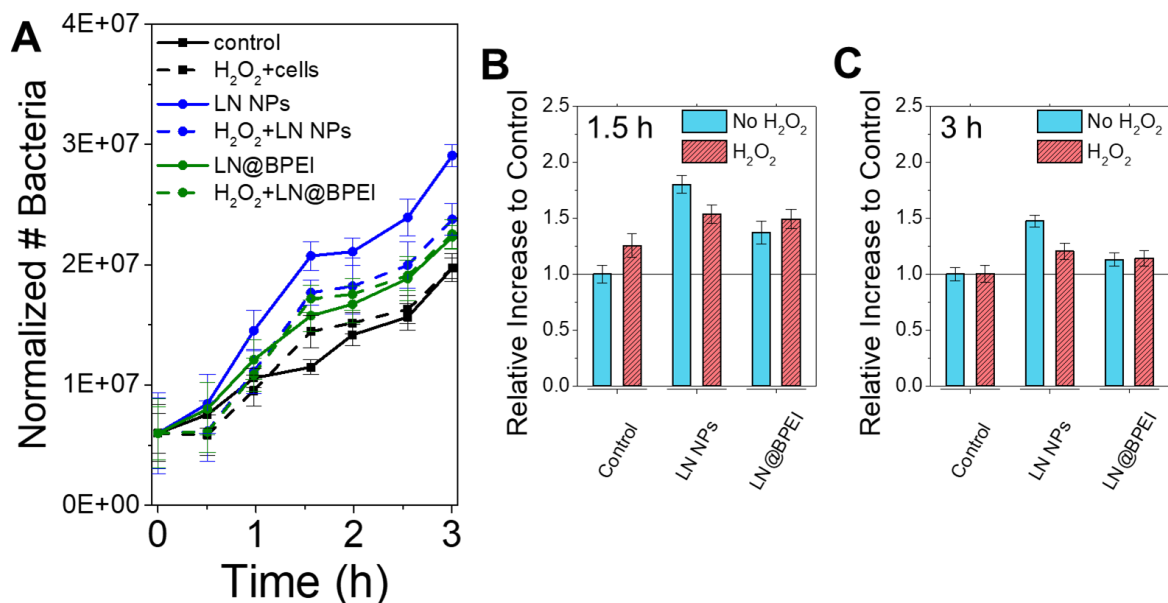


Figure 5.5. Normalized number of bacteria without Nanoparticles (black), with LN NPs (blue), or LN@BPEI (green) grown over time in the absence (solid line) and presence of H₂O₂ (dashed line) (A). Relative change in the bacterial population for different treatment groups on exposure to H₂O₂ after 1.5 h (B) and 3 h (C). Concentrations were: [LiNbO₃] = 7 μM; [H₂O₂] = 1 mM.

As seen in **Figure 5.5A**, bacterial growth suffers an initial shock when H₂O₂ is added (dashed lines) in the first 30 minutes, but it is substantially recovered after 1 h. The growth is even slightly enhanced after 1.5 h for the untreated bacteria and those treated with LN@BPEI (**Figure 5.5B**), but this effect stabilises after 3 h (**Figure 5.5C**). These effects are better seen in **Figure 5.6**. It is noteworthy that although the growth with LN NPs and H₂O₂ is high (**Figure 5.5**), H₂O₂ induces a relative growth decrease in this case (**Figure 5.6**). LN NPs in the presence of H₂O₂ could favour some ROS production which could counteract the effect observed in its absence. Interestingly, LN@BPEI do not show a similar effect, and adding H₂O₂ does not seem to affect cell growth. Overall, these results suggest that both LN and LN@BPEI promote bacterial growth relative to their respective controls, both in the absence and presence of H₂O₂.

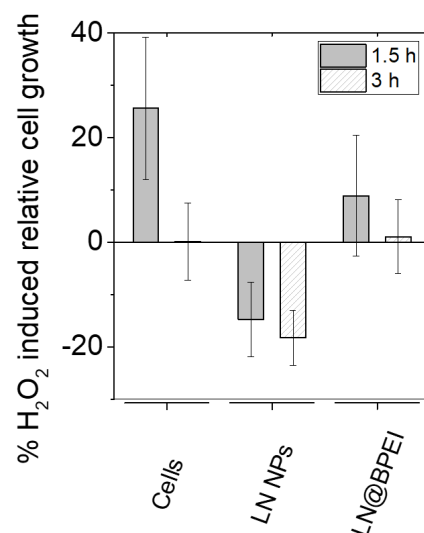


Figure 5.6. H₂O₂ induced relative cell growth in bacteria untreated and treated with LN NPs and LN@BPEI. The data represents relative change in the bacterial populations with reference to each of the specific treatment group upon treatment with H₂O₂ compared to non-H₂O₂ treated controls.

5.3.3. *E. coli* growth response to H₂O₂ and Nanozyme

Next, we also introduced the Nanozyme in combination with H₂O₂ to assess their combined effect on bacterial growth. In this case, a combined effect of AuSeeds, LN/Au, PtSeeds or LN/Pt along with H₂O₂ are shown in **Figure 5.7**.

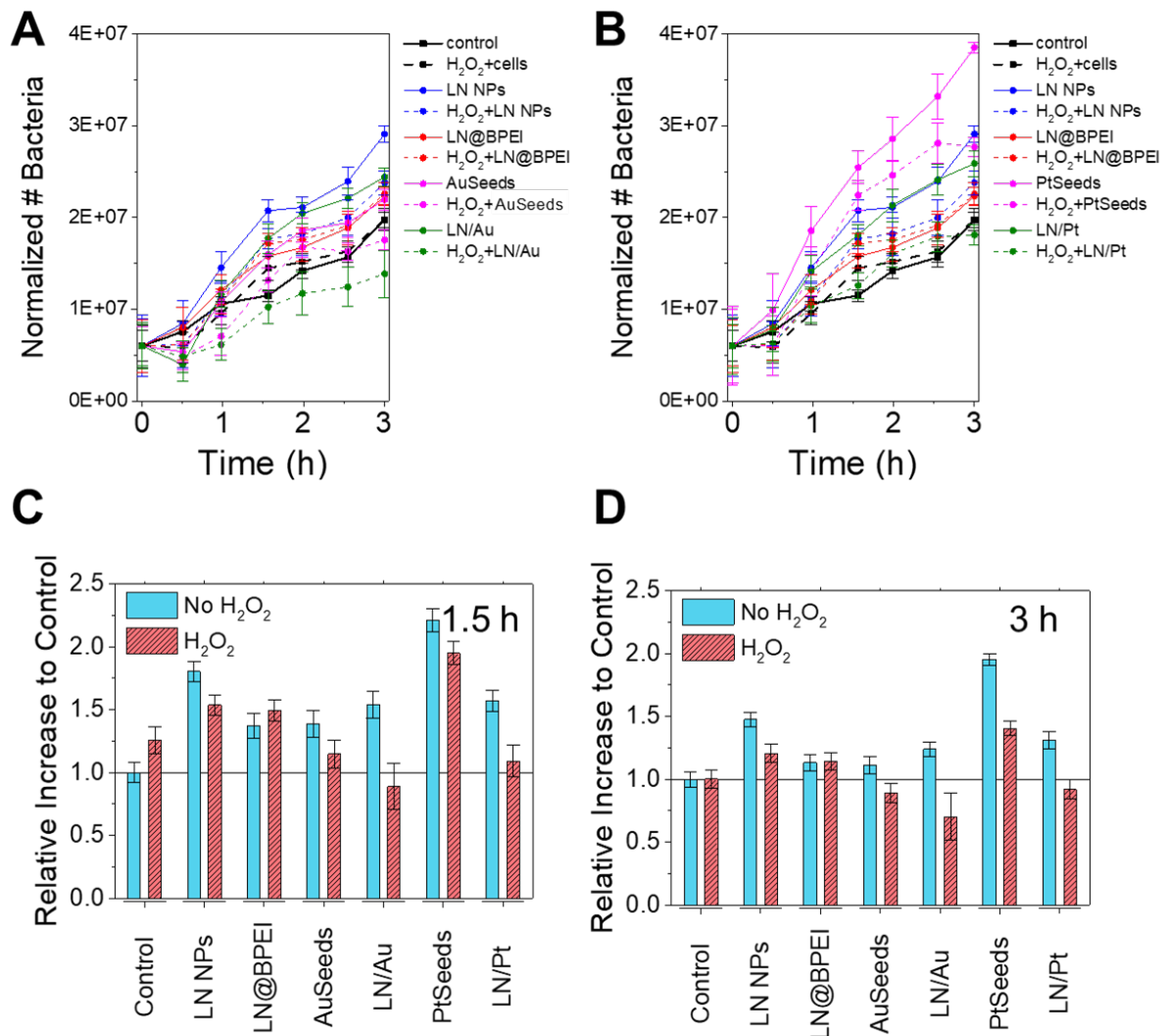


Figure 5.7. Bacterial growth over time without Nanoparticles (black), with LN NPs (blue), LN@BPEI (green), AuSeeds (pink), LN/Au (red), either non-treated (solid line) or treated with H₂O₂ (dashed line) (A). Bacterial growth over time without Nanoparticles (black), with LN NPs (blue), LN@BPEI (green), PtSeeds (pink), LN/Pt (red), either non-treated (solid line) or treated with H₂O₂ (dashed line) (B). Relative increase in the treatment groups to control (non-treated) after 1.5 h (C) and 3 h (D). Concentrations were: [LiNbO₃] = 7 μM; [Au] = 1 μM; [Pt] = 1 μM; [H₂O₂] = 1 mM.

From **Figure 5.7**, the most remarkable effect is observed to be provided by LN/Au in the presence of H₂O₂, which causes a decrease in growth compared to the control. AuSeeds and LN/Pt also show a similar effect after 3 h, but it is less prominent. Considering that in the absence of H₂O₂ these nanozyme systems promoted bacterial growth, it appears that adding H₂O₂ to the culture media may promote the production of ROS in the presence of those

Nanozymes. Surprisingly, PtSeeds do not cause an overall lower growth compared to control with the addition of H_2O_2 , although we observed its peroxidase mimic activity in the previous chapter, which should have resulted in the production of hydroxy radicals that are harmful for bacteria (**Chapter 4: section 4.1.2**). The observed effect on the bacterial system may be due to the fact that the peroxidase mimics activity alone does not counteract the probiotic effect of PtSeeds. However, PtSeeds do have growth inhibitory properties. This effect becomes obvious for LN/Pt in the presence of H_2O_2 . As seen in **Figure 5.7B**, the growth stagnates during the last 30 minutes (from 2.5 h to 3 h), which is not the case for the other Nanozymes and nanoparticles. These effects are well reflected in **Figure 5.8**.

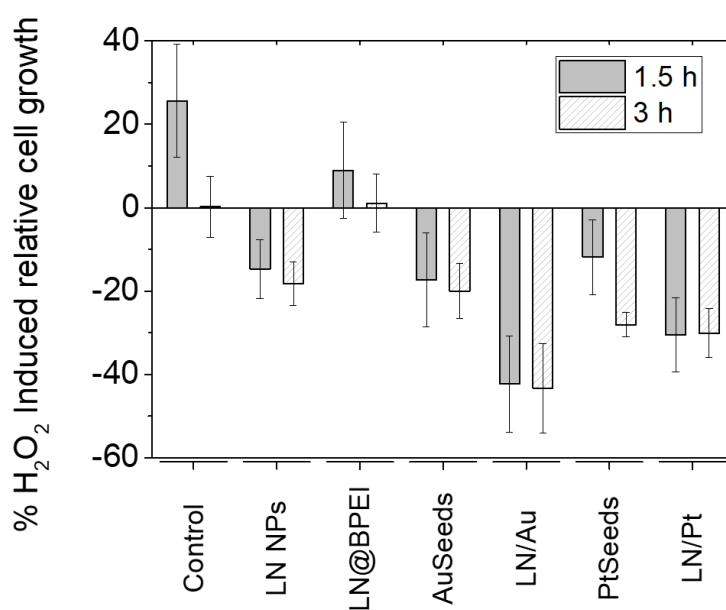


Figure 5.8. H_2O_2 induced relative cell growth in bacteria untreated and treated with LN NPs, LN@BPEI, AuSeeds, LN/Au, PtSeeds and LN/Pt. The data represents relative change in the bacterial populations with reference to each of the specific treatment group upon treatment with H_2O_2 compared to non- H_2O_2 treated controls.

LN NPs and AuSeeds present a similar behaviour upon treatment with H_2O_2 (**Figure 5.8**). This contrasts with the fact that LN NPs did not show peroxidase mimics. AuSeeds and PtSeeds deposition onto LN/Au and LN/Pt, respectively, causes a decrease in bacteria growth induced by H_2O_2 ; after 3 h, there is no significant difference.

5.4. *E. coli* interaction with Nanozymes and UV

In the previous chapter (**Chapter 4: section 4.4.1**), we elucidated the band gap of the different Nanozymes and nanoparticles. We will focus on direct band gaps as indirect band gap excitation requires phonon coupling, making them less statistically significant [299]. To better understand, we translated the band gap edges into light wavelength (**Table 5.1**) and carefully chose the photoexcitation wavelength during bacterial studies. We chose a UVB lamp with 302 nm irradiance to photoexcite the materials whose direct band gap absorption edge wavelength is above that of the lamp one (**Figure 5.9**). It has to be considered that the lamp is not monochromatic and exhibits some range of wavelengths.

Table 5.1. Direct band gap energies and corresponding wavelengths of the different materials.

| Sample | Direct band gap (eV) | Direct band gap (nm) |
|-------------|----------------------|----------------------|
| LN NPs | 4.40 | 282 |
| LN@BPEI NPs | 4.08 | 304 |
| AuSeeds | 3.75 | 331 |
| LN/Au | 3.89 | 319 |
| PtSeeds | 5.78 | 215 |
| LN/Pt | 3.78 | 328 |

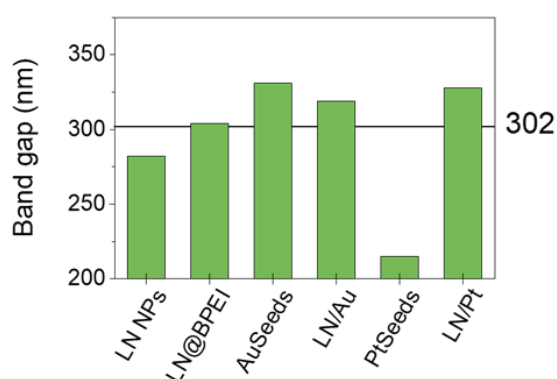


Figure 5.9. Band gap edge wavelengths of the different materials compared to UV-irradiation lamp (302 nm).

We also selected the lamp height from the sample to modulate light intensity (**Figure 5.10**). Overall, we chose $1 \text{ mW}\cdot\text{cm}^{-2}$ to avoid heating the samples and keeping photointensity consistent during our experiments.

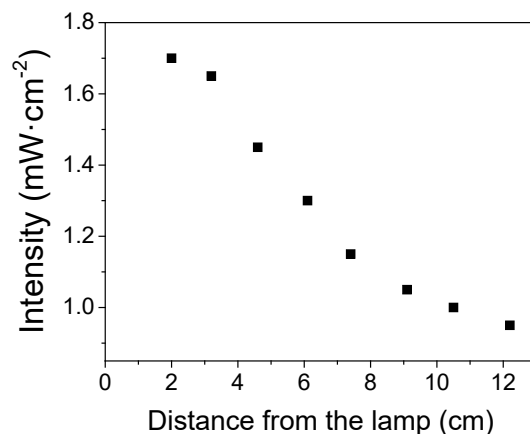


Figure 5.10. Intensity of light as a function of distance from the lamp.

5.4.1. Optimization of the UV exposure time

We determined the maximum exposure time to UVB-light (302 nm) to which *E. coli* growth was possible without causing significant UV-induced death to the bacterial controls. We chose 30 s, 1 min and 2 min of UV exposure times and calculated the percentage of cell death after 3 h of subsequent bacterial growth using **Equation 5.1** (**Figure 5.11**).

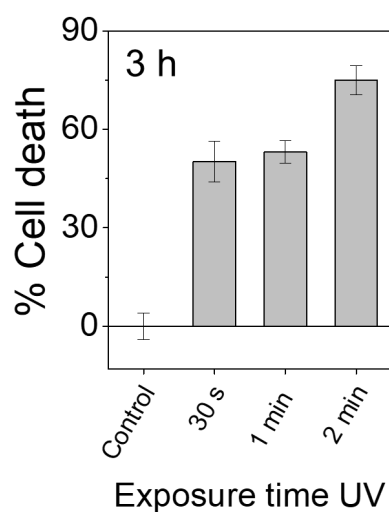


Figure 5.11. Percentage of cell death as a function of exposure time to UV light ($\lambda_{\text{max}} = 302 \text{ nm}$, $1 \text{ mW}/\text{cm}^2$).

From the results presented in **Figure 5.11**, the effect on cell death upon UV light exposure between 30 s and 1 min is $\sim 50\%$, but 2 minutes produces almost 75% of cell death. To sufficiently excite the Nanozymes and the nanoparticles while not causing major cell death, we chose 1 min to proceed with the incubation of Nanozymes and nanoparticles. This 50% baseline cell count in the controls provides a reasonable opportunity to assess how in the presence of Nanoparticles, photoexcitation of Nanozymes influences cell growth.

5.4.2. *E. coli* growth interaction with Nanoparticles and UV light

We incubated *E. coli* with the LN NPs and LN@BPEI NPs after exposure to 1 min of UV light ($\lambda_{\max} = 302$ nm, 1 mW/cm²) (**Figure 5.12**).

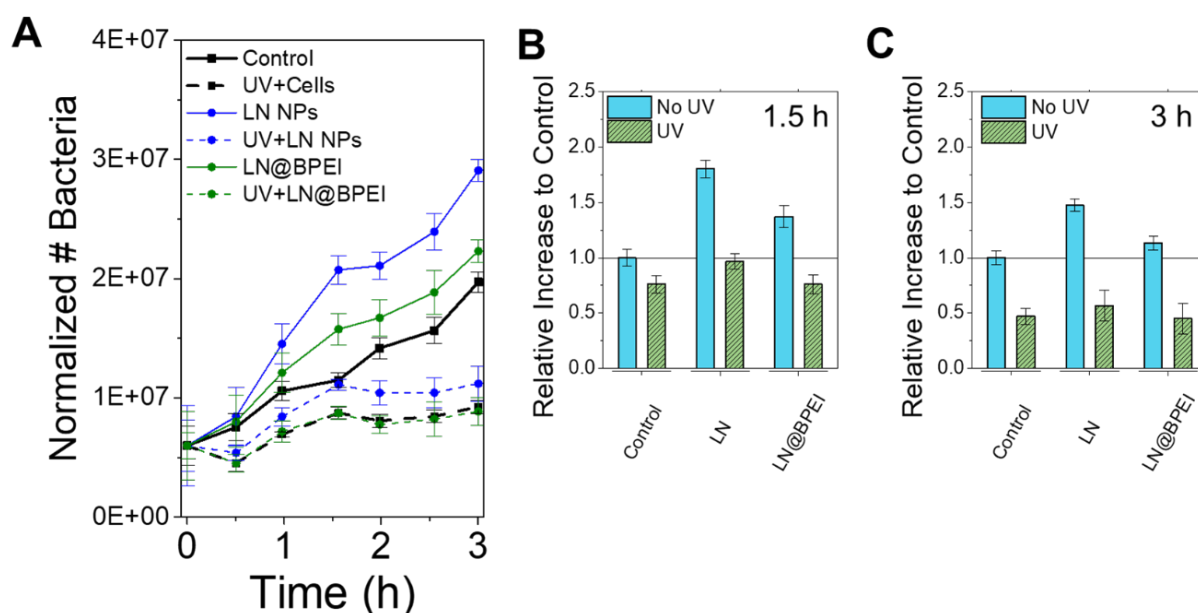


Figure 5.12. Bacterial growth over time without Nanoparticles (black), with LN NPs (blue), LN@BPEI (green) either in the absence (solid line) or presence of UV (dashed line) (A). Relative increase to control (non-treated) after 1.5 h (B) and 3 h (C). Concentration was: $[\text{LiNbO}_3] = 7 \mu\text{M}$.

Irradiation with UV light for 1 minute produces an apparent decrease in growth for the untreated control, as well as for the LN and LN@BPEI NPs treated bacteria (**Figure 5.12A**). However, this effect is more pronounced for both NPs, especially in the first 1.5 h (**Figure 5.12B**) compared to 3 h (**Figure 5.12C**). Although at 1.5 h, LN NPs overall protect the bacteria from UV light radiation (**Figure 5.12B**), the UV-induced relative growth is practically the same

for LN and LN@BPEI NPs at both time points (**Figure 5.13**). In the fundamental context, it is also notable that compared to UV exposure effects on bacteria not treated with NPs, the relative bacterial cell death tends to increase when LN and LN@BPEI treated bacteria are exposed to UV. The band gap edge for LN is 282 nm, which means that it cannot be excited with a 302 nm UV source. While the band gap edge for LN@BPEI NPs is 304 nm, which should allow a 302 nm source to photoexcite these particles, photo-degradation of BPEI by UV light should also be considered, which could potentially reduce the band gap wavelength edge of LN@BPEI towards that of LN NPs. For instance, C-H, C-C, and C-N bonds are known to break upon exposure to UV light [300], [301]. This could also make LN@BPEI NPs non-excitable by the employed UV source. However, complementary stability studies should be done to confirm this aspect. Irrespective of the mechanism, it is overall apparent that the use of either LN or LN@BPEI in the presence of UV light masks the original probiotic effects of these NPs and does not provide any advantage in protecting bacteria from the UVB radiation.

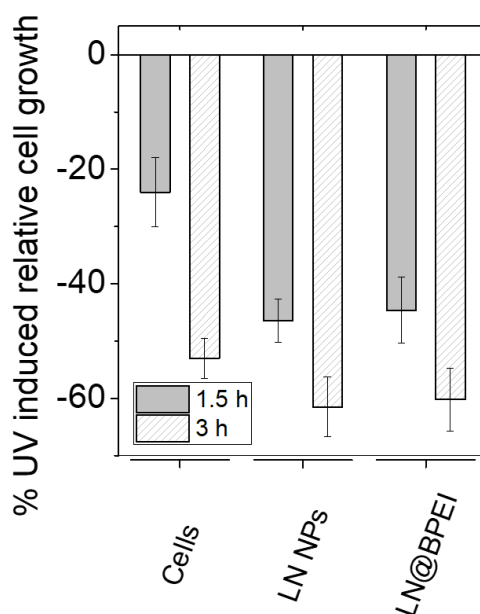


Figure 5.13. The percentage of UV-induced relative cell growth for the non-treated bacteria and those treated with LN and LN@BPEI NPs at 1.5 h and 3 h. The data represents relative change in the bacterial populations with reference to each of the specific treatment group upon their UV exposure.

5.4.3. *E. coli* growth interaction with Nanozymes and UV light

In **Figure 5.14**, the potential effect of UV light on cell growth is studied in the presence of Nanozymes, AuSeeds, LN/Au, PtSeeds and LN/Pt.

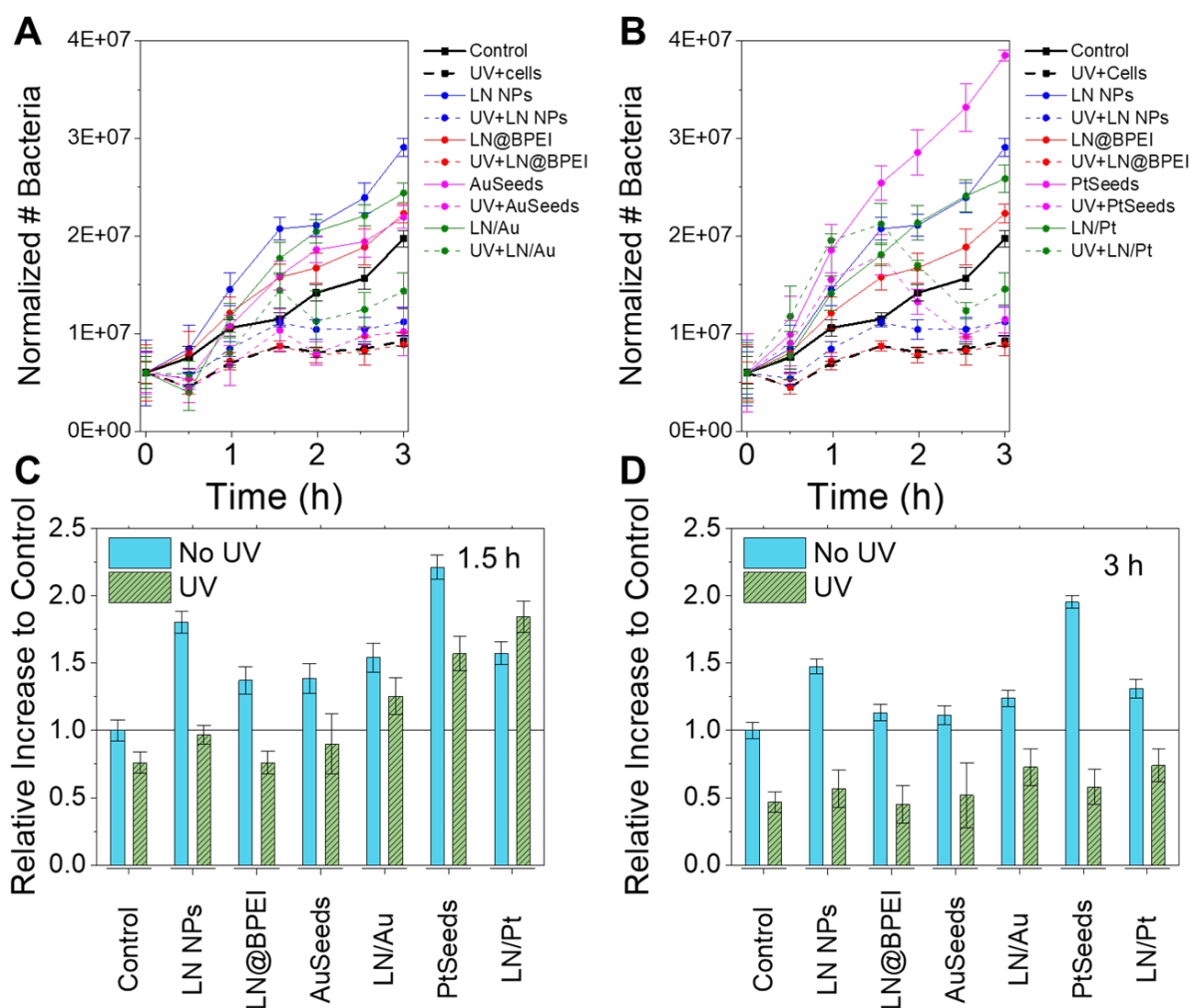


Figure 5.14. Bacterial growth over time without Nanoparticles (black), with LN NPs (blue), LN@BPEI (green), AuSeeds (pink), LN/Au (red) either non-treated (solid line) or treated with UV (dashed line) (A). Bacterial growth over time without Nanoparticles (black), with LN NPs (blue), LN@BPEI (green), PtSeeds (pink), LN/Pt (red) either non-treated (solid line) or treated with UV (dashed line) (B). Relative increase to control (non-treated) after 1.5 h (C) and 3 h (D). Concentrations were: $[\text{LiNbO}_3] = 7 \mu\text{M}$; $[\text{Au}] = 1 \mu\text{M}$; $[\text{Pt}] = 1 \mu\text{M}$.

In **Figure 5.14A and B**, we observe a clear effect in cell growth during the first 1.5 h. This effect is even more evidenced in **Figure 5.14C**. In contrast to all other Nanozyme systems that show increased growth over control even after UV irradiation, AuSeeds exposure to UV light

causes a decrease in cell growth compared to the control. However, the relative growth of bacteria in the presence of LN/Au, PtSeeds and LN/Pt Nanozymes remains higher than control. **Figure 5.15** shows that when the relative change in activity between each of the UV-exposed and non-exposed Nanozymes is compared, the damage to the bacterial cells in the presence of Nanozymes is more in most cases compared to bacteria not exposed to the Nanozyme. This is however not the case with LN/Au and LN/Pt both at 1.5 h and 3 h of treatments. In particular, at 1.5 h, LN/Pt is the only Nanozyme system that promotes bacterial growth in the presence of UVB light. Conversely, the probiotic effect of PtSeeds is most severely affected upon UV treatment. This is interesting, especially considering the absorption edge of PtSeeds at 215 nm, implying that it should not get excited by the light source, whereas all other Nanozyme systems should be photoexcitable. Conversely, LN/Pt shows the lowest bandgap, suggesting that it should be more easily excited by the UVB lamp. There are different possible mechanisms that can be considered for LN/Pt induced bacterial growth upon UVB excitation. LN/Pt possesses strong catalase activity (**Chapter 4: Figure 4.8**) and exciting its band gap edge with UV light may boost the quenching of the ROS produced by cells and transform them into O₂. This could have two parallel effects, *viz.* reduction of ROS that will promote bacterial growth, and also availability of extra localized molecular oxygen to bacteria that is critical for the growth of an aerobic bacteria such as *E. coli*. Another possibility may be a photolyase activity in LN/Pt Nanozyme. Photolyases are natural enzymes in certain organisms (algae and planktons) that repair DNA upon light excitation. A recent study has shown how TiO₂ Nanozymes have photolyase properties, which protect cells from UV light induced damage and reverse it. The UV light excites electron-hole pairs, and the excited electrons promote the bond reconstruction of DNA [302]. Although this effect is reversed after 3 h in both LN/Au and LN/Pt, the growth is higher than in the experiment in the absence of Nanozymes (**Figure 5.14D**). In summary, UV light is a potent tool to modulate Nanozyme activity in cell growth, where both LN/metal Nanozymes appear to show probiotic effect for the bacterial growth.

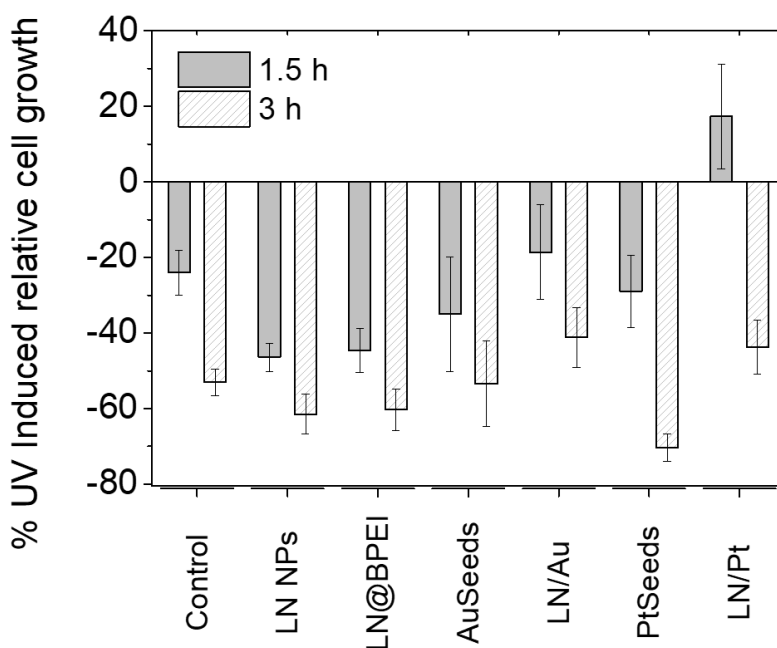


Figure 5.15. Percentage of induced relative cell growth for the non-treated bacteria and those treated with LN and LN@BPEI NPs, AuSeeds, LN/Au, PtSeeds and LN/Pt at 1.5 h and 3 h. The data represents relative change in the bacterial populations with reference to each of the specific treatment group upon their UV exposure.

To support these results, we decided to carry out a complementary experiment with the ROS probes we used already in **Chapter 4: section 4.4.3**. As this was a qualitative study, we kept the same conditions as before: [TA] = 1 mM, [DHE] = 0.01 mM, [ABDA] = 0.2 mM. The concentrations of the Nanozymes were: [Au] = 11 μ M, [Pt] = 1.1 μ M and the correspondent [LiNbO₃] for the hybrids, [LN] = 78.1 μ M for LN/Au and [LN] = 7.6 μ M for LN/Pt. The final reaction volume was 100 μ L. In this case, we substituted the acetate buffer at pH 4 for MilliQ water, which is closer to physiological pH. To verify the effect, we used an irradiation time of 2 min. Although UV light source was situated at a sufficient distance from the sample, photothermal (heating) effects could also potentially influence the reaction. Thus, we divided the well plate into 2 sides, one part was covered with aluminium foil, and the other was uncovered. The foil covered part of the plate acted as photothermal controls (No UV in **Figure 5.16**). Both parts were exposed to the same UV irradiation, and the fluorescence or absorbance was measured and compared in **Figure 5.16**.

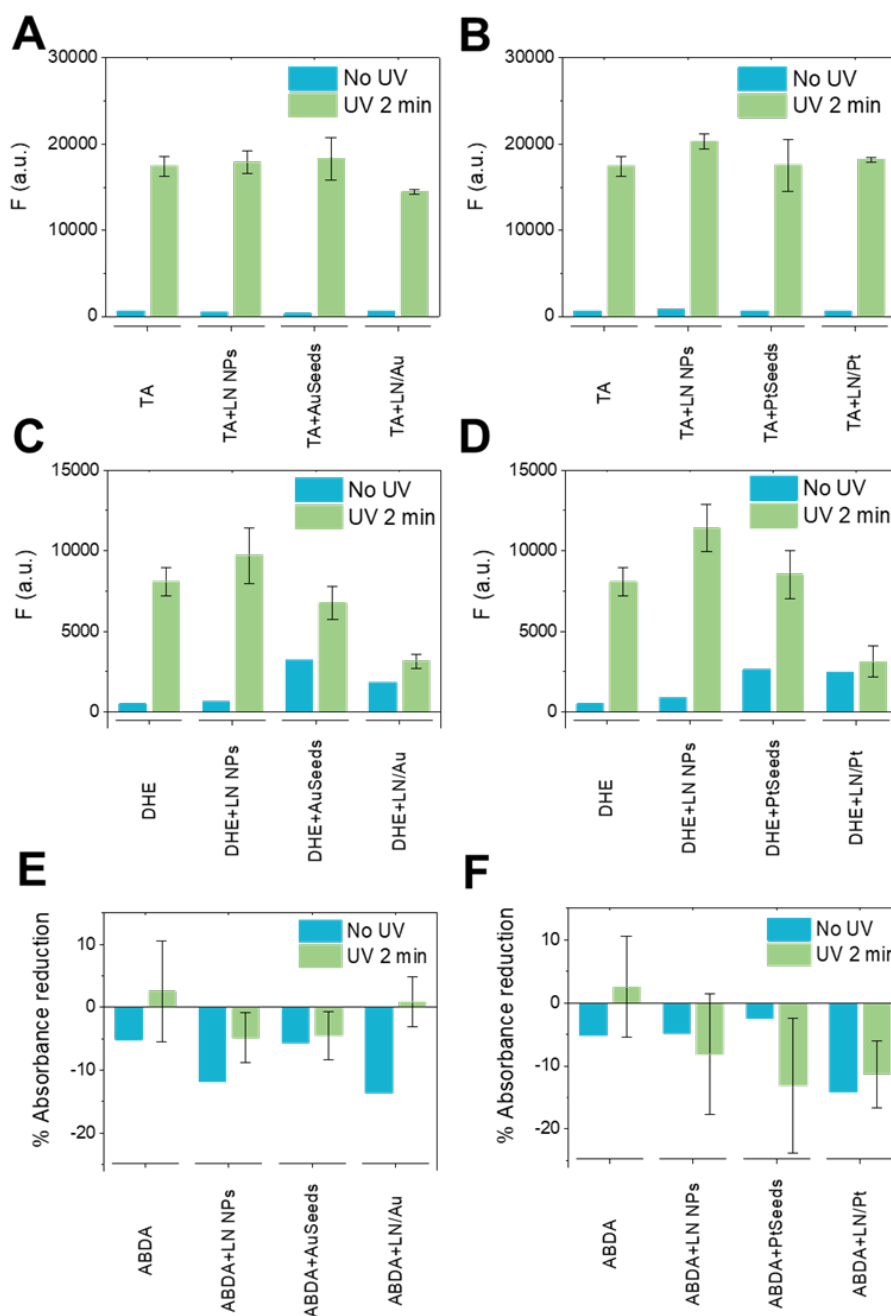


Figure 5.16. (A, B) Fluorescent (F) intensity of the reaction of terephthalic acid and the possible OH^\bullet generated by the Nanozymes, $[\text{TA}] = 1 \text{ mM}$. (C, D) Fluorescent (F) intensity of the reaction of dihydroethidium (DHE) and the possible $\text{O}_2^{\bullet-}$ generated by the Nanozymes, $[\text{DHE}] = 0.01 \text{ mM}$. (E, F) % Absorbance (A) reduction of the reaction of ABDA and the possible $^1\text{O}_2$ generated by the Nanozymes, $[\text{ABDA}] = 0.2 \text{ mM}$. (A, C, E) $[\text{Au}] = 11 \text{ }\mu\text{M}$; $[\text{LN}] = 78.1 \text{ }\mu\text{M}$. (B, D, F) $[\text{Pt}] = 1.1 \text{ }\mu\text{M}$; $[\text{LN}] = 7.6 \text{ }\mu\text{M}$. For all the systems, the reactions were done in MilliQ. UV light irradiation $\lambda_{\text{max}} = 302 \text{ nm}$, 1 mW/cm^2 . Panels A, C, and E correspond to Au-based Nanozymes, while panels B, D and F correspond to Pt-based Nanozymes.

From the graphs presented above, we observed that UV irradiation oxidises the fluorescent ROS probes, TA and DHE. However, LN/Au seems to avoid both degradations, indicating that it has the potential to quench both OH^\bullet and $\text{O}_2^{\bullet-}$ (Figure 5.16A and C), especially $\text{O}_2^{\bullet-}$ radicals. DHE oxidation by UV light is also avoided by AuSeeds but to a lesser extent. It is also interesting to observe that while in the absence of UV light, both AuSeeds and LN/Au produce some $\text{O}_2^{\bullet-}$ radicals relative to control, this production is significantly reversed upon UV excitation to an extent that the DHE fluorescence upon UV excitation on AuSeeds and LN/Au is lower than that of pure DHE without Nanozymes. In case of ABDA, which is a probe for $^1\text{O}_2$ (Figure 5.16E), while AuSeeds do not show a remarkable effect, LN/Au is once again able to sequester $^1\text{O}_2$ upon UV irradiation, while it promoted production of this ROS without UV irradiation. These observations support that the metal oxide/metal hybrid interface does play an active role in sequestering $\text{O}_2^{\bullet-}$ radicals during exposure to UV irradiation. In the case of LN/Pt, there is no significant change in TA and ABDA degradation compared to the controls (Figure 5.16B and F). However, DHE showed a similar trend, as that for LN/Au, *i.e.*, the ability of this Nanozyme to quench $\text{O}_2^{\bullet-}$ radicals upon UV irradiation (Figure 5.16). From these experiments, we might infer that both LN/metal hybrids, and especially LN/Pt Nanozyme, seem to have a good protective effect against UVB radiation.

5.5. *E. coli* interaction with Nanozymes, UV light and H_2O_2

After studying the different sources of oxidative stresses separately, we combined them (UV light and H_2O_2) to see if any overall effect on bacterial growth is observed. We theorize that UV light irradiation during 1 min may also catalyse the cleavage of H_2O_2 (1 mM) into ROS species such as $^1\text{O}_2$, $\text{O}_2^{\bullet-}$ or OH^\bullet . The nanoparticles' or Nanozymes' behaviour may promote the production or may scavenge them, either decreasing cell growth or increasing it, respectively.

5.5.1. *E. coli* growth interaction with Nanoparticles, H_2O_2 and UV light

We first investigated the interaction between LN and LN@BPEI NPs with H_2O_2 and UV light simultaneously. The parameters were chosen as optimised before, $[\text{H}_2\text{O}_2]=1$ mM and 1 min of UV light exposure $\lambda_{\text{max}}=302$ nm, 1 mW/cm² (Figure 5.17).

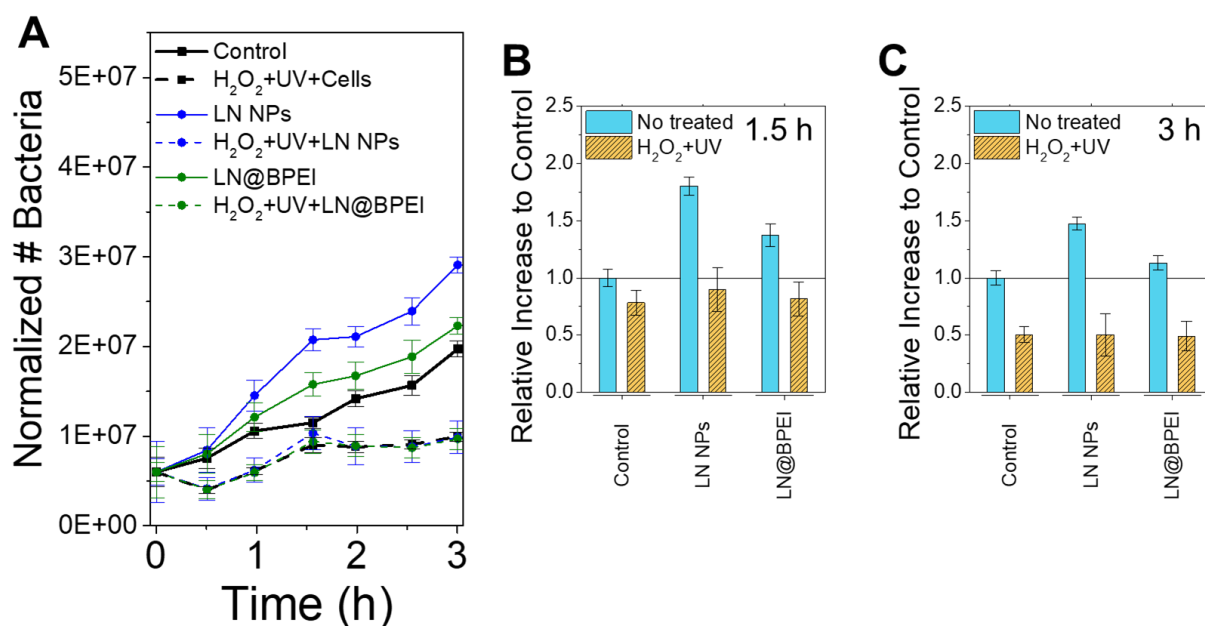


Figure 5.17. Bacterial growth over time without Nanoparticles (black), with LN NPs (blue), LN@BPEI (green) either non-treated (solid line) or treated with H₂O₂ and UV (dashed line) (A). Relative increase to control (non-treated) after 1.5 h (B) and 3 h (C). Concentration were: [LiNbO₃] = 7 μM; [H₂O₂] = 1 mM.

While LN and LN@BPEI NPs without H₂O₂+UV treatment promoted bacterial growth over control, the combination of H₂O₂ and UV irradiation produced similar growth curves in the three samples (**Figure 5.17A**). This is also evidenced in **Figure 5.17B and C**, where there is no significant difference between the treated samples. However, the behaviour induced by the treatment differs. LN NPs highly promoted the cells' viability; however, when treated with both oxidative-stress-causing factors, the number of cells decreased much more than for the sample without nanoparticles, as seen in (**Figure 5.18**). This suggests that LN NPs may promote the production of ROS species more efficiently from H₂O₂ when also simultaneously irradiated with UV light, causing a higher decrease in cell growth. LN@BPEI presents a similar scenario, however with lesser decrease in cell growth induced by H₂O₂ and UV light compared to LN NPs.

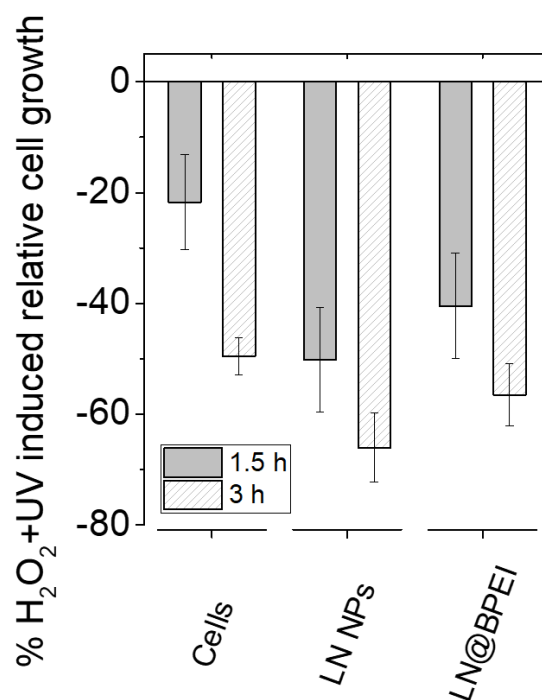


Figure 5.18. Percentage of induced relative cell growth for the non-treated bacteria and those treated with LN and LN@BPEI NPs at 1.5 h and 3 h. The data represents relative change in the bacterial populations with reference to each of the specific treatment group upon their simultaneous exposure to UV+H₂O₂.

5.5.2. *E. coli* growth response to H₂O₂ and UV with Nanozymes

We further investigated the action of the Nanozymes, AuSeeds, LN/Au, PtSeeds and LN/Pt combined with H₂O₂ and UV light irradiation. The parameters were chosen as before, [H₂O₂]= 1 mM and 1 min of UV light exposure $\lambda_{\text{max}}= 302 \text{ nm}$, 1 mW/cm² (**Figure 5.19**).

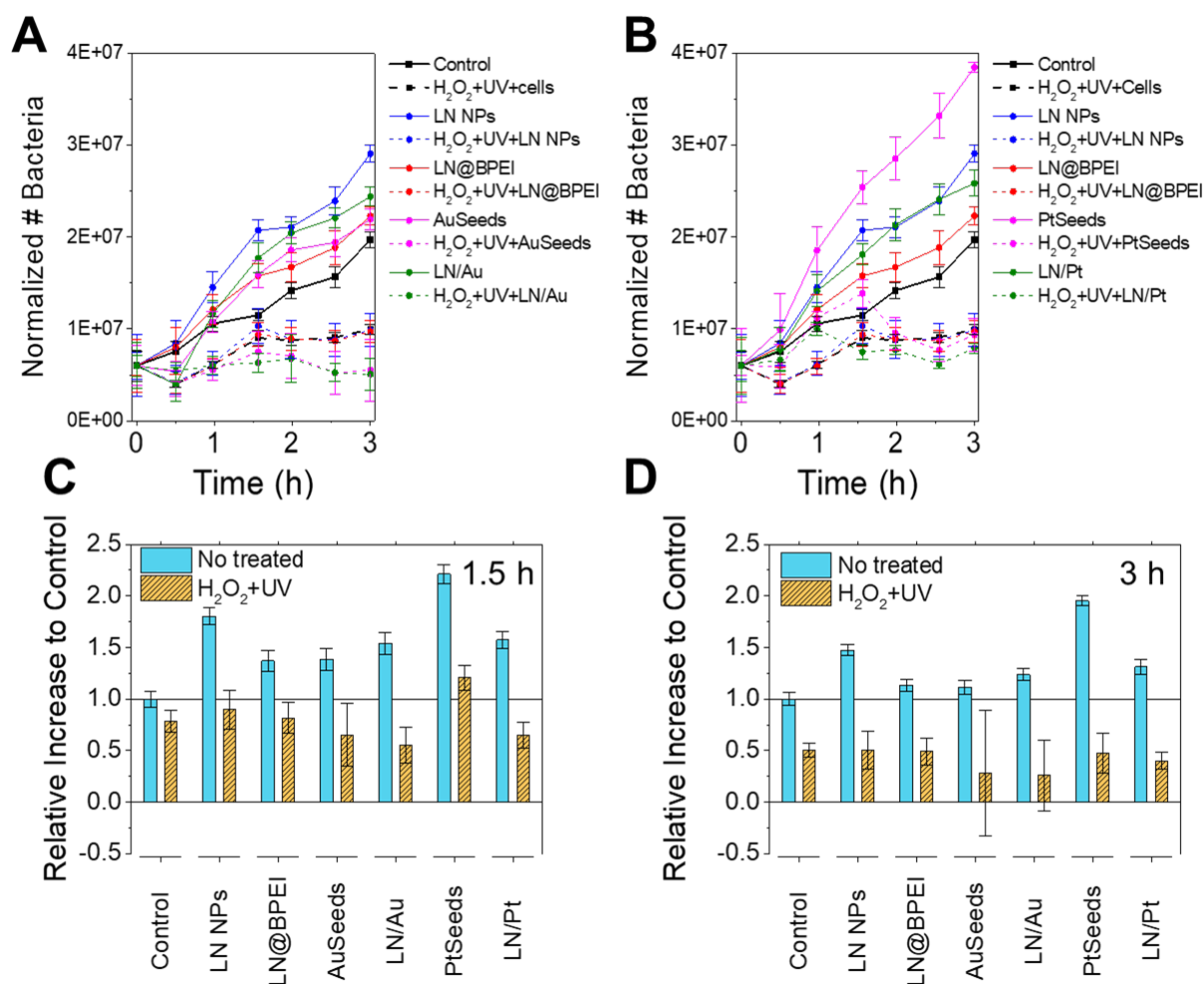


Figure 5.19. Bacterial growth over time without Nanoparticles (black), with LN NPs (blue), LN@BPEI (green), AuSeeds (pink), LN/Au (red) either non-treated (solid line) or treated with H₂O₂ and UV (dashed line) (A). Bacterial growth over time without Nanoparticles (black), with LN NPs (blue), LN@BPEI (green), PtSeeds (pink), LN/Pt (red) either non-treated (solid line) or treated with H₂O₂ and UV (dashed line) (B). Relative increase to control (non-treated) after 1.5 h (C) and 3 h (D). Concentrations were: [LiNbO₃] = 7 μM; [Au] = 1 μM; [Pt] = 1 μM; [H₂O₂] = 1 mM.

As seen in **Figure 5.19A and C**, AuSeeds and LN/Au combined with H₂O₂, and UV light irradiation produce a decrease in cell growth both after 1.5 h and 3 h of growth kinetics. The ROS production from H₂O₂ may be enhanced after UV light irradiation, especially for LN/Au. Band gap excitation in LN/Au can promote electron separation in the Nanozymes, which can increase the degradation of H₂O₂ into ROS. In the case of PtSeeds, their strong ability to increase bacteria viability is overcome after 3 h but not in the first 1.5 h (**Figure 5.19B, C and D**). In the case of LN/Pt, we have a similar image as for LN/Au; however, the decrease in

relative growth is not that marked, probably because it has better properties as catalase-mimics (Chapter 4: Figure 4.2), and there is some ROS scavenging (Figure 5.19D). This is also evidenced in Figure 5.20. H₂O₂ and UV light irradiation cause a significant decrease in AuSeeds and LN/Au relative cell growth. In the case of Pt, the decrease seems to overcome that of LN/Pt after 3h.

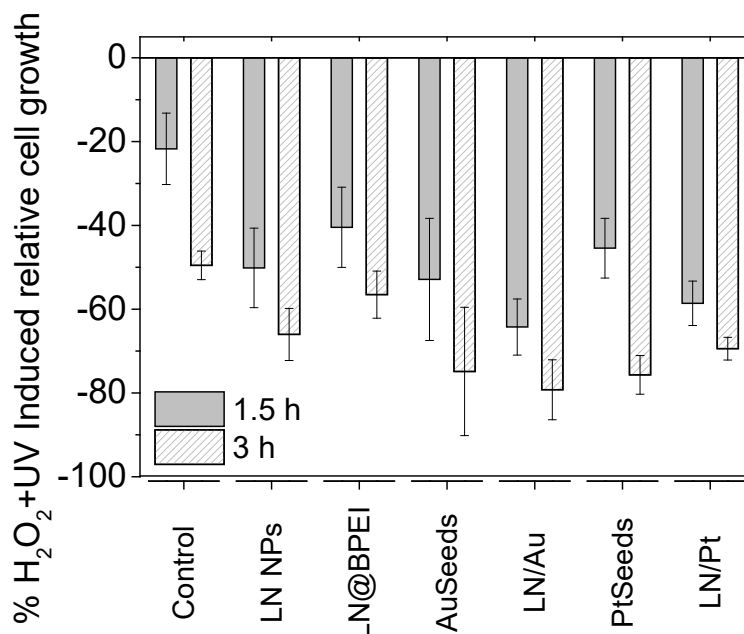


Figure 5.20. H₂O₂ and UV induced relative cell growth in bacteria untreated and treated with LN NPs, LN@BPEI, AuSeeds, LN/Au, PtSeeds and LN/Pt. The data represents relative change in the bacterial populations with reference to each of the specific treatment group upon their simultaneous exposure to UV+H₂O₂.

5.6. Effect of oxidative-stress treatments as a function of material

We have seen how the different treatments affect the ability of nanoparticles and Nanozymes to influence bacterial growth. Now the discussion will focus on how each treatment affects each material. For all the treatments, we have chosen 1.5 h for comparison, as there seems to be more differences between the materials, and as such, over longer periods, the materials' effects may be masked and tend to become less prominent. We have also selected a colour code from red to green, indicating how much the viability of the bacteria is enhanced compared to the control. Green indicates enhanced viability compared to control, red means worsened

viability and yellow means that the viability is similar to the control, *i.e.*, the cells without any treatment.

In **Figure 5.21**, we have plotted the response of bacteria to the treatment of LN and LN@BPEI NPs in the presence of various external oxidative stress stimuli.

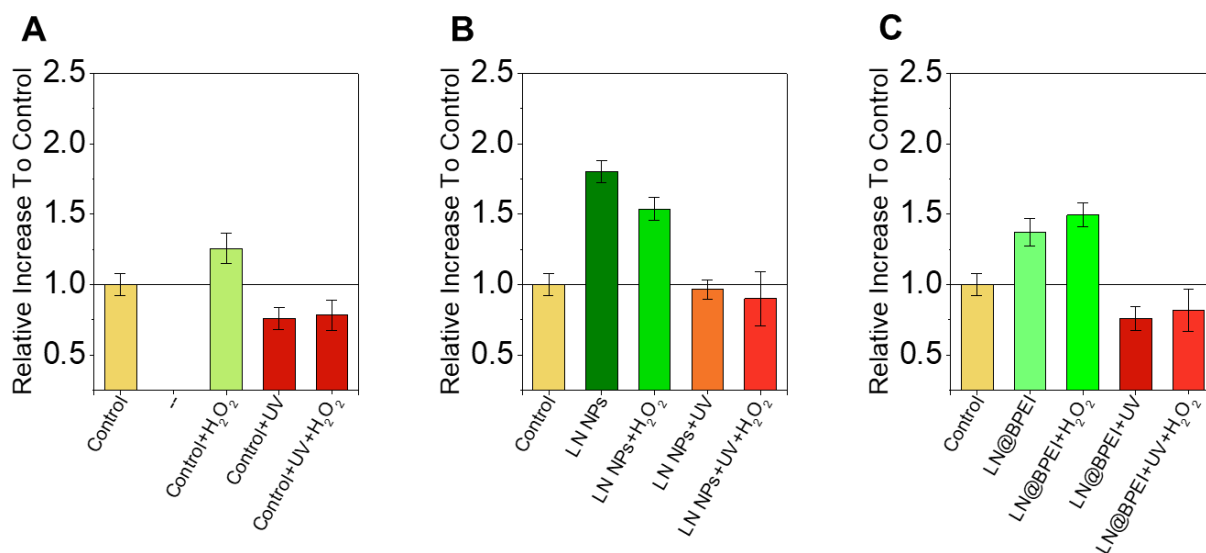


Figure 5.21. Response to NPs treatment of the bacteria relative to control at 1.5 h in the presence of various external oxidative stress stimuli. No treatment (A), treated with LN NPs (B), treated with LN@BPEI NPs (C).

In **Figure 5.21A**, we see how the cells behave with the treatments of H₂O₂, UV and H₂O₂+UV. As already commented, H₂O₂, at low concentrations, can be scavenged by cells, and we observe an increase in viability in the first 1.5 h. Either the decomposition of H₂O₂ into O₂ can enhance growth, or H₂O₂ can also act as a signalling molecule, and a small amount of H₂O₂ can therefore promote bacterial metabolism to enhance growth [296]. The effect of UV reduces viability. The treatment with both H₂O₂ and UV does not show a significant difference compared to the treatment with UV alone. Treatment of bacteria with LN NPs enhances viability (**Figure 5.21B**). However, when either H₂O₂ or UV are also present, the viability is decreased. The effect of UV is more pronounced. The combination of H₂O₂ and UV does not show a significant difference over that of UV alone. Coating LN with BPEI decreases viability as cationic polymers are known to have antibacterial activities, but it does not completely overcome the growth promoting effect of LN NPs (**Figure 5.21C**). In this case, the treatment with H₂O₂ increases the viability of cells, which is similar to that in the control when NPs were not present, but contrary to LN NPs (**Figure 5.21B**). BPEI possess reductant properties which may favour

the scavenging of H₂O₂. The effects of UV and H₂O₂+UV in case of LN@BPEI are similar to that observed for LN NPs.

AuSeeds and LN/Au treated bacterial response to oxidative stress treatments are shown in **Figure 5.22**. We have included the bacteria without the Nanozymes for better comparisons.

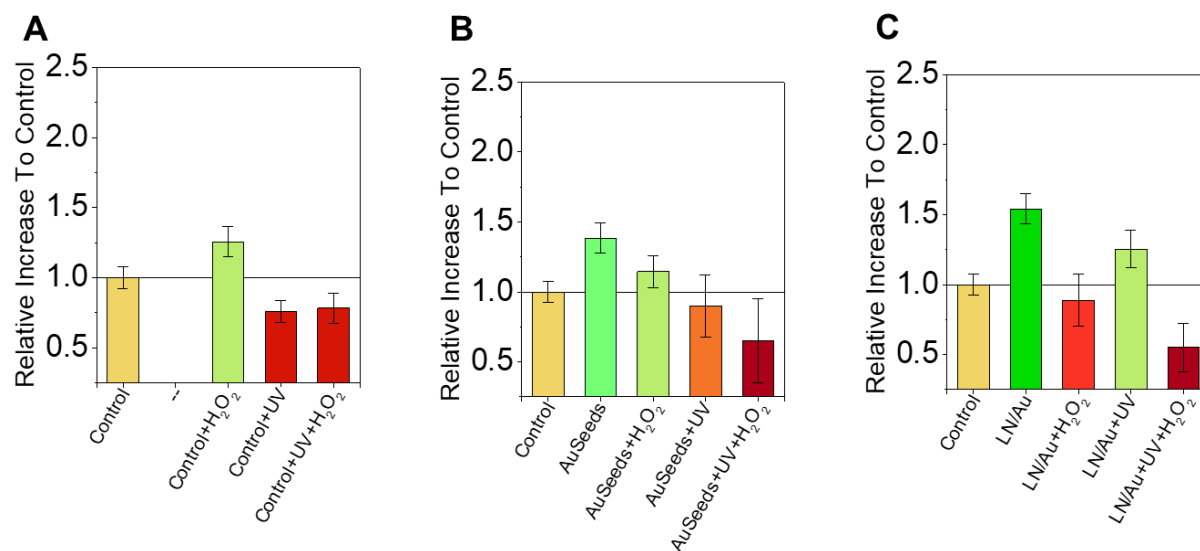


Figure 5.22. Response to Au-based Nanozymes treatment of the bacteria relative to control at 1.5 h in the presence of various external oxidative stress stimuli. No treatment (A), treated with AuSeeds (B), treated with LN/Au (C).

As seen in **Figure 5.22B**, treating bacteria with AuSeeds increases their viability, while the presence of oxidative stress decreases this effect. AuSeeds seem to produce ROS irrespective of the treatment, with effects more pronounced upon UV treatment. Compared to LN and LN@BPEI that showed nearly similar effects of UV and H₂O₂+UV, when both oxidative stresses were combined, the effects were more pronounced for AuSeeds. In the case of LN/Au (**Figure 5.22C**), H₂O₂ caused a decreased viability compared to the untreated bacteria. In contrast to other cases, in the case of only UV light irradiation, LN/Au seems to not only protect the bacteria from it, but also cause a growth promoting effect. This could be attributed to band gap induced scavenging of ROS by LN/Au Nanozyme. However, when both H₂O₂ and UV light are present, LN/Au possess more damaging effect, likely due to faster conversion of additional H₂O₂ to ROS than its quenching ability.

PtSeeds and LN/Pt treated bacterial response to different oxidative treatments is shown in **Figure 5.23**. As for AuSeeds and LN/Au, we have included the bacteria without the Nanozymes for better comparisons.

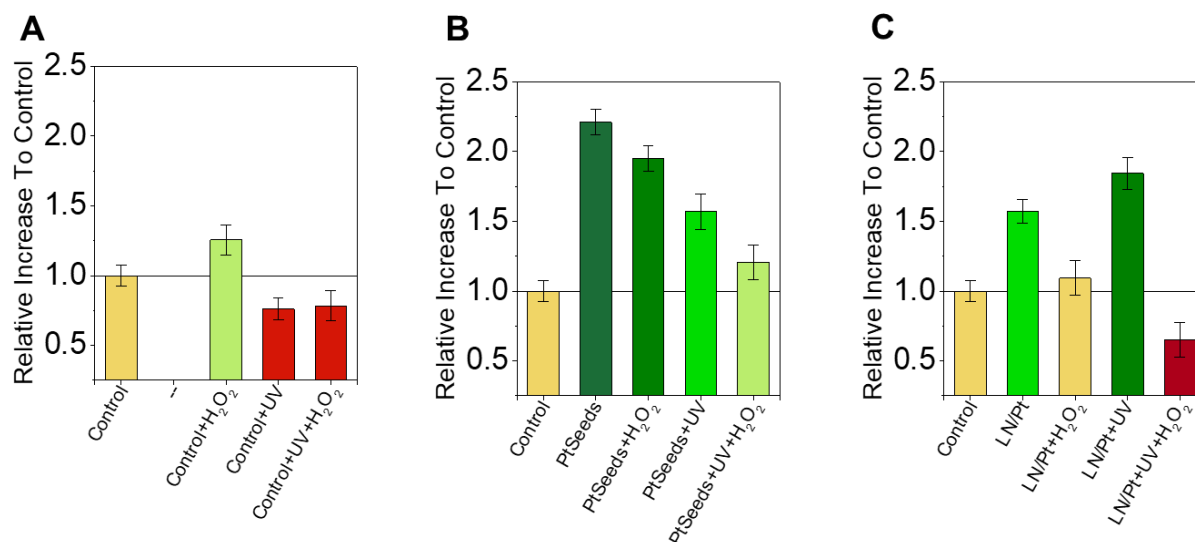


Figure 5.23. Response to Pt-based Nanozymes treatment of the bacteria relative to control at 1.5 h in the presence of various external oxidative stress stimuli. No treatment (A), treated with AuSeeds (B), treated with LN/Au (C).

PtSeeds follow a similar trend as AuSeeds, but due to the increased growth promoting ability of the PtSeeds, any subsequent treatments allow overcoming it in the first 1.5 h (**Figure 5.23B**). This allows PtSeeds to promote better bacterial growth than control even when they are simultaneously exposed to H₂O₂ and UV radiation. A different picture is observed for LN/Pt Nanozyme, as seen in **Figure 5.23C**. The behaviour in this case is more similar to the LN/Au Nanozyme. While the UV light in the absence of H₂O₂ significantly promotes bacterial growth, both treatments involving H₂O₂ cause a decrease in bacterial viability. As already discussed in **section 5.4.3.**, one of the most remarkable results from this study is increased viability of bacteria under UV irradiation, which is not observed in LN/Au. This implies that UV light boosts the viability of cells in the presence of LN/Pt.

5.7. Conclusion

The results presented in this chapter provide evidence for the versatility of the different materials to promote and impede *E. coli* viability depending on the different oxidative stress treatments. Through the synthesis stages of the LN/Au and LN/Pt Nanozymes, the constituting materials LN, LN@BPEI, AuSeeds, and PtSeeds modulate the response of the bacteria depending on the addition of H₂O₂ or UV light or both (**Table 5.2**). Moreover, LN/Au presents a protective effect against UV light irradiation, and LN/Pt not only protects the bacteria, but also boost their viability. We have also corroborated these results with ROS probes, and although further experiments, such as electron spin resonance (ESR) spectroscopy may be required to confirm the status of different ROS (as the probes were sensitive to light), the preliminary experiments with appropriate controls do suggest the ability of these hybrid Nanozymes to effectively sequester different ROS. These results agree with the reduced band gap of the hybrids, which may be able to absorb the UVB light. Although more experiments would add further value to the underlying mechanisms, the applications are promising.

Table 5.2. Summarization of the percentage of induced relative bacterial growth upon treatment with different sources of oxidative stress (H₂O₂, UVB, H₂O₂+UVB). The data represents relative change in the bacterial populations with reference to each of the specific treatment group upon their exposure to sources of oxidative stress. All numbers are expressed in percentage. Green indicates enhanced viability compared to control, red means worsened viability and yellow means that the viability is similar to the control.

| NPs or Nanozymes | Induced oxidative stress source | | |
|------------------|---------------------------------|-----|------------------------------------|
| | H ₂ O ₂ | UVB | H ₂ O ₂ +UVB |
| No | +26 | -24 | -22 |
| LN NPs | -15 | -46 | -50 |
| LN@BPEI | +9 | -45 | -40 |
| AuSeeds | -17 | -35 | -53 |
| LN/Au | -42 | -19 | -64 |
| PtSeeds | -12 | -29 | -45 |
| LN/Pt | -31 | +17 | -59 |

Conclusion and prospects

Metal Nanozymes have been reported to mimic different enzymes in particular oxidoreductase. As such, they are foreseen as potent tools for future therapeutics. Furthermore, the literature reports on their combination with metal oxide nanoparticles in order to enhance their catalytic effect. The mechanisms underlying this synergetic effect seem to involve charge transfer and defect accumulation among others.

Different metal/metal oxide nanohybrids have been described. However, despite the many features of LiNbO₃, its combination with metal nanoparticles has not been reported in the field of Nanozymes. Therefore, our aims were:

- To synthesize LiNbO₃/Au, LiNbO₃/Pt and LiNbO₃/Ag hybrid nanoparticles,
- To test the ability of the LiNbO₃/metal hybrid nanoparticles as Nanozyme mimics,
- To optimize the conditions of catalytic activity measurement for the Nanozyme mimics,
- To compare the Nanozyme mimics of the LiNbO₃-metal hybrid nanoparticles to the separated counterparts (LiNbO₃, LiNbO₃@BPEI, metal seeds) and a mixture of them to corroborate a synergetic effect,
- To compare the different Nanozyme activities of the different metals deposited on LiNbO₃@BPEI,
- To elucidate the mechanism for enhanced catalytic activity through kinetic studies, band structure studies and reactive oxygen species probes,
- To investigate the interaction of the Nanozymes to the cell growth of *Escherichia Coli*,
- To investigate the interaction of Nanozymes and *Escherichia Coli* under oxidative stress conditions: H₂O₂ and UV-irradiation.

We synthesized LiNbO₃/Au, LiNbO₃/Pt and LiNbO₃/Ag hybrid NPs through a layer-by-layer method based on electrostatic interactions. LN NPs of 30.4 ± 8.6 nm diameter were synthesized through a solvothermal method (SYMME). Their surface charge in water was of -42.5 ± 0.8 mV. By adding branched polyethyleneimine (BPEI), we reversed the surface charge to $+39.4 \pm 3.6$ mV. AuSeeds, PtSeeds and AgSeeds were also synthesized through a salt reduction method and a negative surface charge. Their diameters were 2.0 ± 0.8 nm, 3.1 ± 0.6 nm and 6.1 ± 1.7 .

We successfully attached the metal seeds to the LN@BPEI NPs, and we demonstrated the synthesis control by varying the volume ratios of the added seeds. LN/Au and LN/Pt hybrid nanoparticles possessed similar metal seeds sizes under 5 nm which makes them ideal for catalysis purposes and comparable surface charge in water. We further characterized the most coated hybrid LN/Au and LN/Pt with STEM and HRTEM confirming a similar structure.

We also implemented the synthesis into TiO₂/Au and TiO₂/Pt hybrid nanoparticles. In this case, the introduction of the intermediate polymer layer was not required due to the positive charge of TiO₂ in water.

We established the peroxidase mimics of LN/Au, confirming the necessity of H₂O₂ and TMB for the reaction to proceed. We optimized the coloured peroxidase substrate and we selected TMB as it possesses the highest performance. The exposition of LN/Au to H₂O₂ presented some bubble formation indicating a potential catalase mimic. Then we optimized the pH and the temperature, leading to a maximum activity at pH 4 and 37 °C. The quantity of Nanozymes was also optimized and the amount corresponding to 27 μM of Au and 182 μM of LN was selected.

Likewise, LN/Pt peroxidase was more potent; thus, we reduced the amount of metal 10 times (2.8 μM of Pt) compared to Au. This provided high efficiency in the first 5 min of reaction. The oxidation of TMB by LN/Pt was also possible in the absence of H₂O₂ which confirms oxidase activity. H₂O₂ in the presence of LN/Pt generated numerous bubbles, which indicates catalase activity. Thus, LN/Pt is a more versatile and effective Nanozyme than LN/Au. As for LN/Au, the highest catalytic activity was obtained at pH 4 and 37 °C. We also ruled out the possibility of the leaked ions to be responsible of the catalytic activity.

We finally compared the peroxidase mimics of LN/Au and LN/Pt to the separated counterparts and a simple mixture of them (in the absence of BPEI) under the previously optimized parameters. Both LN/Au and LN/Pt present a synergetic effect. LN and LN@BPEI did not show peroxidase mimics. AuSeeds and PtSeeds present peroxidase mimics, but their activity was lower than for the hybrids. The simple mixture of LN with the metal seeds showed higher activity than the metal seeds, but it was lower than the one of the hybrid Nanozymes.

We investigated the mechanism of this synergetic effect through XPS/UPS and optical band gap measurements. LN/Au and LN/Pt presented a reduced optical band gap compared to LN NPs and LN@BPEI. Moreover, LN/Au showed a sharpening of the states and a slight shift

towards lower binding energies and a more sharpened FL compared to LN, which may imply a charge transfer from LN to Au.

BPEI deposition onto LN NPs produced a band gap decrease, thus we investigated if BPEI played a role in the enhanced peroxidase mimics. Peroxidase mimics of AuSeeds and PtSeeds combination with BPEI was tested. However, the absence of cleaning steps led to the presence of artefacts in both samples, which makes comparison not possible, and more experiments are being conducted to elucidate the role of BPEI.

We also investigated if peroxidase-mimics was mediated through ROS generation. The tested ROS traps did not show significant change in the presence of the hybrids and the ROS-mediated mechanism was outruled.

The Michaelis-Menten parameters were obtained for the AuSeeds, LN/Au, PtSeeds and LN/Pt. We demonstrated that H₂O₂ present higher affinity towards the hybrid Nanozymes, possibly because of its stabilization resulting from oxygen vacancies. The catalytic performance of LN/Au towards H₂O₂ improved with the deposition. In the case of LN/Pt the catalytic performance was improved for both H₂O₂ and TMB. Overall, the deposition of AuSeeds and PtSeeds onto LN@BPEI, provoked a synergetic effect in Nanozyme activity.

The reproducibility and the durability of the Nanozyme properties were also validated with old samples and new batches.

We finally investigated the effect of the Nanozymes in bacterial growth and induced oxidative stress. Bacterial growth was promoted when Nanozymes were present specially for LN NPs and PtSeeds. The deposition of AuSeeds onto LN@BPEI did not produce a significant effect whereas the deposition of PtSeeds induced growth decrease.

The maximum non cytotoxic concentration of H₂O₂ was 1 mM. The decrease in induced H₂O₂ cell growth with the LN/Au was considerable.

The exposure to UVB-light (λ_{\max} = 302 nm) for 1 minute caused a 50% cell death. Surprisingly, LN/Au protected the cells from it and in the presence of LN/Pt the UV induced cell growth was boosted during the first 1.5 h. This was corroborated by the study of ROS, in which the hybrid Nanozymes quenched the UV-light and the reaction was not produced.

The synergetic effect of H₂O₂ and UV-light in increasing oxidative stress was studied. In this case the oxidative stress sources induced a marked decrease in cell growth for LN/Au and LN/Pt.

We concluded with the comparative study of how each Nanozyme, and bacteria treated affected to the cell growth. As a general conclusion, the Nanozymes are a potent tool to modify oxidative stress in cells.

The future outcomes of this work have been organised as a timeline: ongoing, attainable in the short-term, and long-term.

We are currently studying the band structure of LN/Pt and more band structure experiments will be needed also on LN/Au to confirm the results showed in **Chapter 4**.

In addition, there is some conflict regarding the term of Nanozyme. The main discrepancy is found about the quantification of the active sites, thus active surface related experiments should be carried out. Finally, simulations and theoretical studies could support the experiment-based mechanisms

It would be interesting to test new metals. In particular, we are targeting to use palladium. Indeed, it has been shown (see **Chapter 1**) that palladium NPs present outstanding Nanozyme-mimics. We would also like to improve the synthesis of silver nanohybrids and test them for nanozymes mimics. Moreover, in this work, gold and platinum seeds facets on LN were (111). However, according to the literature (**Chapter 1**), the (211) facet is more active. Therefore, it would be interesting to synthesize LN/Au and LN/Pt with (211) facets and compare the mimic activity with the one of this work.

Also, it would be interesting to test other oxide. In particular, Fe₃O₄ NPs will bring additional properties and facilitate their separation thanks to the magnetic properties, which may allow to reutilize them. The hybrid nanoparticles composed of Fe₃O₄ NPs and Au, Pt and Pd seeds could be tested for their peroxidase properties as we did for LN/Au and LN/Pt, optimization of parameters and establishment of the peroxidase mimics (Coll. SON SAS). .

Apart from therapeutics, the synthesized Nanozymes could be used as sensors in combination with aptamers. This will offer an affordable and easy testing platform. Our group in RMIT has already proven this with metal nanoparticles. We have already tried to use our hybrid

nanoparticles in a similar manner, but the complexity of the system led to unresolved problems. More mechanistic and kinetic studies should be carried out to optimize the use of the hybrid Nanozymes for these applications in particular understanding the effect of surface chemistry on the catalysis. Indeed, for example, some papers report on the quenching of the catalytic activity by aptamers while other reports on the enhancement of it.

In the short term, the optimization of other potential enzyme-mimics is envisioned. Both, LN/Au, and LN/Pt catalase activity was observed through bubble generation. In addition, LN/Pt showed oxidase mimics. Moreover, the ROS-traps and the bacteria-growth experiments suggest catalase and superoxide dismutase activity. We also plan in performing other experiments to detect the ROS generated or scavenged by the Nanozymes.

We decided to study how the excitation with the band gap energy can affect the cell-growth. But, as mentioned, excitation of the plasmon band of the metal nanoparticles can also cause the production of hot electrons and modulate the Nanozyme activity. Wavelengths in the near-infra-red are also appealing approaches, especially, for a potential long-term in vivo application in wound healing or tumour treatment. LN/Au and LN/Pt may also present surface-enhanced Raman spectroscopy (SERS), which is a potent tool for the characterization of biomarkers. Moreover, the combination of LN NPs with metal has been already proposed in our group as a theragnostic tool in combining imaging and photothermal therapeutic properties. This could be a future application. Moreover, the catalase mimics of the hybrid Nanozymes could even boost the latter by the production of O₂ in the tumour microenvironment.

Bibliography

- [1] F. Gomollón-Bel, “IUPAC Top Ten Emerging Technologies in Chemistry 2022,” *Discov. Innov. that will Transform energy, Heal. Mater. Sci. to Tack. Most Urgent Soc. challenges Catal. Sustain. Dev.*, vol. 44, no. 4, pp. 4–13, 2022, doi: 10.1515/ci-2022-0402.
- [2] D. Jiang, D. Ni, Z. T. Rosenkrans, P. Huang, X. Yan, and W. Cai, “Nanozyme: New horizons for responsive biomedical applications,” *Chem. Soc. Rev.*, vol. 48, no. 14, pp. 3683–3704, 2019, doi: 10.1039/c8cs00718g.
- [3] A. Mohamad, H. Teo, N. A. Keasberry, and M. U. Ahmed, “Recent developments in colorimetric immunoassays using nanozymes and plasmonic nanoparticles,” *Crit. Rev. Biotechnol.*, vol. 39, no. 1, pp. 50–66, 2019, doi: 10.1080/07388551.2018.1496063.
- [4] T. Kumar Sharma *et al.*, “Aptamer-mediated ‘turn-off/turn-on’ nanozyme activity of gold nanoparticles for kanamycin detection,” *Chem. Commun.*, vol. 50, no. 100, pp. 15856–15859, 2014, doi: 10.1039/c4cc07275h.
- [5] P. Weerathunge *et al.*, “Dynamic interactions between peroxidase-mimic silver NanoZymes and chlorpyrifos-specific aptamers enable highly-specific pesticide sensing in river water,” *Anal. Chim. Acta*, vol. 1083, pp. 157–165, 2019, doi: 10.1016/j.aca.2019.07.066.
- [6] B. Das, J. Lou Franco, N. Logan, P. Balasubramanian, M. Il Kim, and C. Cao, “Nanozymes in Point-of-Care Diagnosis: An Emerging Futuristic Approach for Biosensing,” *Nano-Micro Lett.*, vol. 13, no. 1, pp. 1–51, 2021, doi: 10.1007/s40820-021-00717-0.
- [7] Q. Wang, J. Jiang, and L. Gao, “Nanozyme-based medicine for enzymatic therapy: Progress and challenges,” *Biomed. Mater.*, vol. 16, no. 4, p. 42002, 2021, doi: 10.1088/1748-605X/abe7b4.
- [8] H. Wei and E. Wang, “Nanomaterials with enzyme-like characteristics (nanozymes): next-generation artificial enzymes,” *Chem. Soc. Rev.*, vol. 42, no. 14, p. 6060, 2013, doi: 10.1039/c3cs35486e.
- [9] B. Hvolbæk, T. V. W. Janssens, B. S. Clausen, H. Falsig, C. H. Christensen, and J. K. Nørskov, “Catalytic activity of Au nanoparticles,” *Nano Today*, vol. 2, no. 4, pp. 14–18, 2007, doi: 10.1016/S1748-0132(07)70113-5.
- [10] M. Haruta, “Novel catalysis of gold deposited on metal oxides,” *Catal. Surv. from Japan*, vol. 1, no. 1, pp. 61–73, 1997, doi: 10.1023/A:1019068728295.
- [11] R. Yan *et al.*, “Nanozyme-Based Bandage with Single-Atom Catalysis for Brain Trauma,” *ACS Nano*, vol. 13, no. 10, pp. 11552–11560, 2019, doi: 10.1021/acsnano.9b05075.
- [12] R. Taitt *et al.*, “Gold-seeded lithium niobate nanoparticles: Influence of gold surface coverage on second harmonic properties,” *Nanomaterials*, vol. 11, no. 4, 2021, doi: 10.3390/nano11040950.
- [13] A. D. McNaught and A. Wilkinson, “Compendium of chemical terminology. IUPAC recommendations,” 1997.

- [14] J. M. Berg, J. L. Tymoczko, and L. Stryer, *Biochemistry*, 5th ed. Basingstoke: W. H. Freeman and Company, 2006.
- [15] E. Kuah, S. Toh, J. Yee, Q. Ma, and Z. Gao, “Enzyme Mimics: Advances and Applications,” *Chem. - A Eur. J.*, vol. 22, no. 25, pp. 8404–8430, 2016, doi: 10.1002/chem.201504394.
- [16] J. Chapman, A. E. Ismail, and C. Z. Dinu, “Industrial applications of enzymes: Recent advances, techniques, and outlooks,” *Catalysts*, vol. 8, no. 6, pp. 20–29, 2018, doi: 10.3390/catal8060238.
- [17] X. Wang, Y. Hu, and H. Wei, “Nanozymes in bionanotechnology: From sensing to therapeutics and beyond,” *Inorg. Chem. Front.*, vol. 3, no. 1, pp. 41–60, 2016, doi: 10.1039/c5qi00240k.
- [18] Y. Huang, J. Ren, and X. Qu, “Nanozymes: Classification, Catalytic Mechanisms, Activity Regulation, and Applications,” *Chem. Rev.*, vol. 119, no. 6, pp. 4357–4412, 2019, doi: 10.1021/acs.chemrev.8b00672.
- [19] T. R. Cech, A. J. Zaugg, and P. J. Grabowski, “In vitro splicing of the ribosomal RNA precursor of tetrahymena: Involvement of a guanosine nucleotide in the excision of the intervening sequence,” *Cell*, vol. 27, no. 3, pp. 487–496, 1981, doi: 10.1016/0092-8674(81)90390-1.
- [20] L. Stefan, T. Lavergne, N. Spinelli, E. Defrancq, and D. Monchaud, “Surface-immobilized DNAzyme-type biocatalysis,” *Nanoscale*, vol. 6, no. 5, pp. 2693–2701, 2014, doi: 10.1039/c3nr05954e.
- [21] D. S. Tawfik, Z. Eshhar, and B. S. Green, “Catalytic antibodies: A critical assessment,” *Mol. Biotechnol.*, vol. 1, no. 1, pp. 87–103, 1994, doi: 10.1007/BF02821512.
- [22] L. Marchetti and M. Levine, “Biomimetic catalysis,” *ACS Catal.*, vol. 1, no. 9, pp. 1090–1118, 2011, doi: 10.1021/cs200171u.
- [23] M. Raynal, P. Ballester, A. Vidal-Ferran, and P. W. N. M. Van Leeuwen, “Supramolecular catalysis. Part 2: Artificial enzyme mimics,” *Chem. Soc. Rev.*, vol. 43, no. 5, pp. 1734–1787, 2014, doi: 10.1039/c3cs60037h.
- [24] X. Yan and L. Gao, *Nanozymology*. Singapore: Springer, 2020. doi: 10.1007/978-981-15-1490-6.
- [25] A. W. Jensen, S. R. Wilson, and D. I. Schuster, “Biological applications of fullerenes,” *Bioorganic Med. Chem.*, vol. 4, no. 6, pp. 767–779, 1996, doi: 10.1016/0968-0896(96)00081-8.
- [26] M. Comotti, C. Della Pina, R. Matarrese, and M. Rossi, “The catalytic activity of ‘naked’ gold particles,” *Angew. Chemie Int. Ed.*, vol. 43, no. 43, pp. 5812–5815, 2004, doi: <https://doi.org/10.1002/anie.200460446>.
- [27] F. Manea, F. B. Houillon, L. Pasquato, and P. Scrimin, “Nanozymes: Gold-nanoparticle-based transphosphorylation catalysts,” *Angew. Chemie - Int. Ed.*, vol. 43, no. 45, pp. 6165–6169, 2004, doi: 10.1002/anie.200460649.
- [28] R. W. Tarnuzzer, J. Colon, S. Patil, and S. Seal, “Vacancy engineered ceria nanostructures for protection from radiation-induced cellular damage,” *Nano Lett.*, vol. 5, no. 12, pp. 2573–2577, 2005, doi: 10.1021/nl052024f.
- [29] L. Gao *et al.*, “Intrinsic peroxidase-like activity of ferromagnetic nanoparticles,” *Nat. Nanotechnol.*, vol. 2, no. 9, pp. 577–583, 2007, doi: 10.1038/nnano.2007.260.
- [30] J. Wu *et al.*, “Nanomaterials with enzyme-like characteristics (nanozymes): Next-

- generation artificial enzymes (II),” *Chem. Soc. Rev.*, vol. 48, no. 4, pp. 1004–1076, 2019, doi: 10.1039/c8cs00457a.
- [31] X. Sun, S. Guo, Y. Liu, and S. Sun, “Dumbbell-like PtPd–Fe₃O₄ Nanoparticles for Enhanced Electrochemical Detection of H₂O₂,” *Nano Lett.*, vol. 12, no. 9, pp. 4859–4863, 2012, doi: 10.1021/nl302358e.
- [32] N. S. Punekar, *Enzyme Kinetic Data: Collection and Analysis*. Singapore: Springer, 2018. doi: 10.1007/978-981-13-0785-0_17.
- [33] N. Gao, H. Sun, K. Dong, J. Ren, and X. Qu, “Gold-nanoparticle-based multifunctional amyloid- β inhibitor against Alzheimer’s disease,” *Chem. - A Eur. J.*, vol. 21, no. 2, pp. 829–835, 2015, doi: 10.1002/chem.201404562.
- [34] Z. Chen, H. Ji, C. Liu, W. Bing, Z. Wang, and X. Qu, “A Multinuclear Metal Complex Based DNase-Mimetic Artificial Enzyme: Matrix Cleavage for Combating Bacterial Biofilms,” *Angew. Chemie*, vol. 128, no. 36, pp. 10890–10894, 2016, doi: 10.1002/ange.201605296.
- [35] D. L. Nelson and M. M. Cox, *Lehninger principles of biochemistry*, 5th ed. New York: W. H. Freeman and Company, 2009.
- [36] S. Li *et al.*, “Fe₃O₄ Nanozymes with Aptamer-Tuned Catalysis for Selective Colorimetric Analysis of ATP in Blood,” *Anal. Chem.*, vol. 91, no. 22, pp. 14737–14742, 2019, doi: 10.1021/acs.analchem.9b04116.
- [37] Z. Gao, M. Xu, L. Hou, G. Chen, and D. Tang, “Irregular-shaped platinum nanoparticles as peroxidase mimics for highly efficient colorimetric immunoassay,” *Anal. Chim. Acta*, vol. 776, pp. 79–86, 2013, doi: 10.1016/j.aca.2013.03.034.
- [38] H. Jia, D. Yang, X. Han, J. Cai, H. Liu, and W. He, “Peroxidase-like activity of the Co₃O₄ nanoparticles used for biodetection and evaluation of antioxidant behavior,” *Nanoscale*, vol. 8, no. 11, pp. 5938–5945, 2016, doi: 10.1039/c6nr00860g.
- [39] V. Patel *et al.*, “Ligand-mediated reversal of the oxidation state dependent ROS scavenging and enzyme mimicking activity of ceria nanoparticles,” *Chem. Commun.*, vol. 54, no. 99, pp. 13973–13976, 2018, doi: 10.1039/c8cc08355j.
- [40] H. Zhang, X. Liang, L. Han, and F. Li, “‘Non-Naked’ Gold with Glucose Oxidase-Like Activity: A Nanozyme for Tandem Catalysis,” *Small*, vol. 14, no. 44, pp. 1–8, 2018, doi: 10.1002/smll.201803256.
- [41] B. Jiang *et al.*, “Standardized assays for determining the catalytic activity and kinetics of peroxidase-like nanozymes,” *Nat. Protoc.*, vol. 13, no. 7, pp. 1506–1520, 2018, doi: 10.1038/s41596-018-0001-1.
- [42] Z. Chen *et al.*, “Dual enzyme-like activities of iron oxide nanoparticles and their implication for diminishing cytotoxicity,” *ACS Nano*, vol. 6, no. 5, pp. 4001–4012, 2012, doi: 10.1021/nn300291r.
- [43] X. Wang, Y. Zhang, T. Li, W. Tian, Q. Zhang, and Y. Cheng, “Generation 9 polyamidoamine dendrimer encapsulated platinum nanoparticle mimics catalase size, shape, and catalytic activity,” *Langmuir*, vol. 29, no. 17, pp. 5262–5270, 2013, doi: 10.1021/la3046077.
- [44] J. Mu, L. Zhang, M. Zhao, and Y. Wang, “Co₃O₄ nanoparticles as an efficient catalase mimic: Properties, mechanism and its electrocatalytic sensing application for hydrogen peroxide,” *J. Mol. Catal. A Chem.*, vol. 378, pp. 30–37, 2013, doi: 10.1016/j.molcata.2013.05.016.
- [45] W. Yang, J. Hao, Z. Zhang, and B. Zhang, “PB@Co₃O₄ nanoparticles as both oxidase

- and peroxidase mimics and their application for colorimetric detection of glutathione,” *New J. Chem.*, vol. 39, no. 11, pp. 8802–8806, 2015, doi: 10.1039/c5nj01744k.
- [46] C. Korsvik, S. Patil, S. Seal, and W. T. Self, “Superoxide dismutase mimetic properties exhibited by vacancy engineered ceria nanoparticles,” *Chem. Commun.*, no. 10, pp. 1056–1058, 2007, doi: 10.1039/b615134e.
- [47] J. Kim *et al.*, “Effects of a potent antioxidant, platinum nanoparticle, on the lifespan of *Caenorhabditis elegans*,” *Mech. Ageing Dev.*, vol. 129, no. 6, pp. 322–331, 2008, doi: 10.1016/j.mad.2008.02.011.
- [48] H. Zhao, R. Zhang, X. Yan, and K. Fan, “Superoxide dismutase nanozymes: an emerging star for anti-oxidation,” *J. Mater. Chem. B*, vol. 9, no. 35, pp. 6939–6957, 2021, doi: 10.1039/d1tb00720c.
- [49] R. Ragg *et al.*, “Molybdenum trioxide nanoparticles with intrinsic sulfite oxidase activity,” *ACS Nano*, vol. 8, no. 5, pp. 5182–5189, 2014, doi: 10.1021/nn501235j.
- [50] L. Gao, K. Fan, and X. Yan, “Iron oxide nanozyme: A multifunctional enzyme mimetic for biomedical applications,” *Theranostics*, vol. 7, no. 13, pp. 3207–3227, 2017, doi: 10.7150/thno.19738.
- [51] I. Celardo, J. Z. Pedersen, E. Traversa, and L. Ghibelli, “Pharmacological potential of cerium oxide nanoparticles,” *Nanoscale*, vol. 3, no. 4, pp. 1411–1420, 2011, doi: 10.1039/c0nr00875c.
- [52] H. Dong, Y. Fan, W. Zhang, N. Gu, and Y. Zhang, “Catalytic mechanisms of nanozymes and their applications in biomedicine,” *Bioconjug. Chem.*, vol. 30, no. 5, pp. 1273–1296, 2019, doi: 10.1021/acs.bioconjchem.9b00171.
- [53] J. Zhang, X. Liu, X. Guo, S. Wu, and S. Wang, “A general approach to fabricate diverse noble-metal (Au, Pt, Ag, Pt/Au)/Fe₂O₃ hybrid nanomaterials,” *Chem. - A Eur. J.*, vol. 16, no. 27, pp. 8108–8116, 2010, doi: 10.1002/chem.201000096.
- [54] J. Li, W. Liu, X. Wu, and X. Gao, “Mechanism of pH-switchable peroxidase and catalase-like activities of gold, silver, platinum and palladium,” *Biomaterials*, vol. 48, pp. 37–44, 2015, doi: 10.1016/j.biomaterials.2015.01.012.
- [55] C. Ge *et al.*, “Facet Energy versus Enzyme-like Activities: The Unexpected Protection of Palladium Nanocrystals against Oxidative Damage,” *ACS Nano*, vol. 10, no. 11, pp. 10436–10445, 2016, doi: 10.1021/acsnano.6b06297.
- [56] B. Klębowski, J. Depciuch, M. Parlińska-Wojtan, and J. Baran, “Applications of Noble Metal-Based Nanoparticles in Medicine,” *Int. J. Mol. Sci.*, vol. 19, no. 12, p. 4031, Dec. 2018, doi: 10.3390/ijms19124031.
- [57] W. Luo *et al.*, “Self-catalyzed, self-limiting growth of glucose oxidase-mimicking gold nanoparticles,” *ACS Nano*, vol. 4, no. 12, pp. 7451–7458, 2010, doi: 10.1021/nn102592h.
- [58] X. Jiang, C. Sun, Y. Guo, G. Nie, and L. Xu, “Peroxidase-like activity of apoferritin paired gold clusters for glucose detection,” *Biosens. Bioelectron.*, vol. 64, pp. 165–170, 2015, doi: 10.1016/j.bios.2014.08.078.
- [59] C. J. Yu, T. H. Chen, J. Y. Jiang, and W. L. Tseng, “Lysozyme-directed synthesis of platinum nanoclusters as a mimic oxidase,” *Nanoscale*, vol. 6, no. 16, pp. 9618–9624, 2014, doi: 10.1039/c3nr06896j.
- [60] Y. Fu, X. Zhao, J. Zhang, and W. Li, “DNA-based platinum nanozymes for peroxidase mimetics,” *J. Phys. Chem. C*, vol. 118, no. 31, pp. 18116–18125, 2014, doi: 10.1021/jp503242e.

- [61] J. Yang *et al.*, “Mechanistic and kinetic insights into size-dependent activity in ultra-small Pt/CNTs nanozymes during antibacterial process,” *Arab. J. Chem.*, vol. 15, no. 11, p. 104238, 2022, doi: 10.1016/j.arabjc.2022.104238.
- [62] X. Shen, W. Liu, X. X. Gao, Z. Lu, X. Wu, and X. X. Gao, “Mechanisms of Oxidase and Superoxide Dismutation-like Activities of Gold, Silver, Platinum, and Palladium, and Their Alloys: A General Way to the Activation of Molecular Oxygen,” *J. Am. Chem. Soc.*, vol. 137, no. 50, pp. 15882–15891, 2015, doi: 10.1021/jacs.5b10346.
- [63] Y. Liu, H. Wu, M. Li, J. J. Yin, and Z. Nie, “pH dependent catalytic activities of platinum nanoparticles with respect to the decomposition of hydrogen peroxide and scavenging of superoxide and singlet oxygen,” *Nanoscale*, vol. 6, no. 20, pp. 11904–11910, 2014, doi: 10.1039/c4nr03848g.
- [64] Y. Jv, B. Li, and R. Cao, “Positively-charged gold nanoparticles as peroxidase mimic and their application in hydrogen peroxide and glucose detection,” *Chem. Commun.*, vol. 46, no. 42, pp. 8017–8019, 2010, doi: 10.1039/c0cc02698k.
- [65] W. Li *et al.*, “BSA-stabilized Pt nanozyme for peroxidase mimetics and its application on colorimetric detection of mercury(II) ions,” *Biosens. Bioelectron.*, vol. 66, pp. 251–258, 2015, doi: 10.1016/j.bios.2014.11.032.
- [66] R. Zhu *et al.*, “Detection of Hg²⁺ based on the selective inhibition of peroxidase mimetic activity of BSA-Au clusters,” *Talanta*, vol. 117, pp. 127–132, 2013, doi: 10.1016/j.talanta.2013.08.053.
- [67] Y. Chang, Z. Zhang, J. Hao, W. Yang, and J. Tang, “BSA-stabilized Au clusters as peroxidase mimetic for colorimetric detection of Ag⁺,” *Sens. Act. B Chem.*, vol. 232, pp. 692–697, 2016, doi: 10.1016/j.snb.2016.04.039.
- [68] Y. Fu, H. Zhang, S. Dai, X. Zhi, J. Zhang, and W. Li, “Glutathione-stabilized palladium nanozyme for colorimetric assay of silver (I) ions,” *Analyst*, vol. 140, no. 19, pp. 6676–6683, 2015, doi: 10.1039/c5an01103e.
- [69] C. W. Lien, Y. C. Chen, H. T. Chang, and C. C. Huang, “Logical regulation of the enzyme-like activity of gold nanoparticles by using heavy metal ions,” *Nanoscale*, vol. 5, no. 17, pp. 8227–8234, 2013, doi: 10.1039/c3nr01836a.
- [70] J. Shah, R. Purohit, R. Singh, A. S. Karakoti, and S. Singh, “ATP-enhanced peroxidase-like activity of gold nanoparticles,” *J. Colloid Interface Sci.*, vol. 456, pp. 100–107, 2015, doi: 10.1016/j.jcis.2015.06.015.
- [71] P. Béteky *et al.*, “Are smaller nanoparticles always better? Understanding the biological effect of size-dependent silver nanoparticle aggregation under biorelevant conditions,” *Int. J. Nanomedicine*, vol. 16, pp. 3021–3040, 2021, doi: 10.2147/IJN.S304138.
- [72] Z. Wang, R. Zhang, X. Yan, and K. Fan, “Structure and activity of nanozymes: Inspirations for de novo design of nanozymes,” *Mater. Today*, vol. 41, no. December, pp. 81–119, 2020, doi: 10.1016/j.mattod.2020.08.020.
- [73] H. H. Deng *et al.*, “Chitosan-stabilized platinum nanoparticles as effective oxidase mimics for colorimetric detection of acid phosphatase,” *Nanoscale*, vol. 9, no. 29, pp. 10292–10300, 2017, doi: 10.1039/c7nr03399k.
- [74] S. R. Ahmed, J. Kim, T. Suzuki, J. Lee, and E. Y. Park, “Detection of influenza virus using peroxidase-mimic of gold nanoparticles,” *Biotechnol. Bioeng.*, vol. 113, no. 10, pp. 2298–2303, 2016, doi: 10.1002/bit.25982.
- [75] Y. Lu, Y. Mei, M. Drechsler, and M. Ballauff, “Thermosensitive core-shell particles as carriers for Ag nanoparticles: Modulating the catalytic activity by a phase transition in

- networks,” *Angew. Chemie - Int. Ed.*, vol. 45, no. 5, pp. 813–816, 2006, doi: 10.1002/anie.200502731.
- [76] Y. Sun *et al.*, “Gold nanoparticle-protein conjugate dually-responsive to pH and temperature for modulation of enzyme activity,” *J. Mater. Chem. B*, vol. 7, no. 20, pp. 3260–3267, 2019, doi: 10.1039/c9tb00325h.
- [77] V. Amendola, R. Pilot, M. Frascioni, O. M. Maragò, and M. A. Iatì, “Surface plasmon resonance in gold nanoparticles: A review,” *J. Phys. Condens. Matter*, vol. 29, no. 20, 2017, doi: 10.1088/1361-648X/aa60f3.
- [78] K. L. Kelly, E. Coronado, L. L. Zhao, and G. C. Schatz, “The Optical Properties of Metal Nanoparticles: The Influence of Size, Shape, and Dielectric Environment,” *J. Phys. Chem. B*, vol. 107, no. 3, pp. 668–677, 2003, doi: 10.1021/jp026731y.
- [79] P. K. Jain and M. A. El-Sayed, “Plasmonic coupling in noble metal nanostructures,” *Chem. Phys. Lett.*, vol. 487, no. 4–6, pp. 153–164, 2010, doi: 10.1016/j.cplett.2010.01.062.
- [80] C. Wang, Y. Shi, Y. Y. Dan, X. G. Nie, J. Li, and X. H. Xia, “Enhanced Peroxidase-Like Performance of Gold Nanoparticles by Hot Electrons,” *Chem. - A Eur. J.*, vol. 23, no. 28, pp. 6717–6723, 2017, doi: 10.1002/chem.201605380.
- [81] F. Wang, E. Ju, Y. Guan, J. Ren, and X. Qu, “Light-Mediated Reversible Modulation of ROS Level in Living Cells by Using an Activity-Controllable Nanozyme,” *Small*, vol. 13, no. 25, 2017, doi: 10.1002/sml.201603051.
- [82] F. Wang, Y. Zhang, Z. Du, J. Ren, and X. Qu, “Designed heterogeneous palladium catalysts for reversible light-controlled bioorthogonal catalysis in living cells,” *Nat. Commun.*, vol. 9, no. 1, 2018, doi: 10.1038/s41467-018-03617-x.
- [83] S. Xu *et al.*, “The preparation of high-index facet Au/Cu NRs and their application for colorimetric determination ascorbic acid,” *Sens. Act. B Chem.*, vol. 281, pp. 375–382, 2019, doi: 10.1016/j.snb.2018.10.114.
- [84] L. Li *et al.*, “Ag/Pd bimetal nanozyme with enhanced catalytic and photothermal effects for ROS/hyperthermia/chemotherapy triple-modality antitumor therapy,” *Chem. Eng. J.*, vol. 397, p. 125438, 2020, doi: 10.1016/j.cej.2020.125438.
- [85] W. He, X. Han, H. Jia, J. Cai, Y. Zhou, and Z. Zheng, “AuPt alloy nanostructures with tunable composition and enzyme-like activities for colorimetric detection of bisulfide,” *Sci. Rep.*, vol. 7, pp. 1–10, 2017, doi: 10.1038/srep40103.
- [86] S. R. Ahmed, J. Kim, T. Suzuki, J. Lee, and E. Y. Park, “Enhanced catalytic activity of gold nanoparticle-carbon nanotube hybrids for influenza virus detection,” *Biosens. Bioelectron.*, vol. 85, pp. 503–508, 2016, doi: 10.1016/j.bios.2016.05.050.
- [87] J. Li *et al.*, “Synergistic effect enhances the peroxidase-like activity in platinum nanoparticle-supported metal–organic framework hybrid nanozymes for ultrasensitive detection of glucose,” *Nano Res.*, vol. 14, no. 12, pp. 4689–4695, 2021, doi: 10.1007/s12274-021-3406-z.
- [88] X. Sun, S. Guo, C.-S. S. Chung, W. Zhu, and S. Sun, “A sensitive H₂O₂ assay based on dumbbell-like PtPd-Fe₃O₄ nanoparticles,” *Adv. Mater.*, vol. 25, no. 1, pp. 132–136, Jan. 2013, doi: 10.1002/adma.201203218.
- [89] L. Qin *et al.*, “Synthetic strategies and application of gold-based nanocatalysts for nitroaromatics reduction,” *Sci. Total Environ.*, vol. 652, pp. 93–116, 2019, doi: 10.1016/j.scitotenv.2018.10.215.
- [90] M. Haruta, N. Yamada, T. Kobayashi, and S. Iijima, “Gold catalysts prepared by

- coprecipitation for low-temperature oxidation of hydrogen and of carbon monoxide,” *J. Catal.*, vol. 115, no. 2, pp. 301–309, 1989, doi: 10.1016/0021-9517(89)90034-1.
- [91] M. Schmal, D. A. G. Aranda, R. R. Soares, F. B. Noronha, and A. Frydman, “A study of the promoting effect of noble metal addition on niobia and niobia alumina catalysts,” *Catal. Today*, vol. 57, no. 3–4, pp. 169–176, 2000, doi: 10.1016/S0920-5861(99)00323-5.
- [92] D. Chen *et al.*, “Comparative studies of silver based catalysts supported on different supports for the oxidation of formaldehyde,” *Catal. Today*, vol. 175, no. 1, pp. 338–345, 2011, doi: 10.1016/j.cattod.2011.03.059.
- [93] J. Jońca *et al.*, “Au/MO_x (M = Zn, Ti) nanocomposites as highly efficient catalytic filters for chemical gas sensing at room temperature and in humid atmosphere,” *Sens. Act. B Chem.*, vol. 249, pp. 357–363, 2017, doi: 10.1016/j.snb.2017.04.061.
- [94] L. Delannoy, K. Fajerweg, P. Lakshmanan, C. Potvin, C. Méthivier, and C. Louis, “Supported gold catalysts for the decomposition of VOC: Total oxidation of propene in low concentration as model reaction,” *Appl. Catal. B Environ.*, vol. 94, no. 1–2, pp. 117–124, 2010, doi: 10.1016/j.apcatb.2009.10.028.
- [95] H. Chen *et al.*, “Hydrogen production via autothermal reforming of ethanol over noble metal catalysts supported on oxides,” *J. Nat. Gas Chem.*, vol. 18, no. 2, pp. 191–198, 2009, doi: 10.1016/S1003-9953(08)60106-1.
- [96] S. M. Sze and K. K. Ng, *Physics of semiconductor devices*, 3rd ed. New York: John Wiley & sons, 2006.
- [97] Z. Zhang and J. T. Yates, “Band bending in semiconductors: Chemical and physical consequences at surfaces and interfaces,” *Chem. Rev.*, vol. 112, no. 10, pp. 5520–5551, 2012, doi: 10.1021/cr3000626.
- [98] J. C. Frost, “Junction effect interactions in methanol synthesis catalysts,” *Nature*, vol. 334, no. 6183, pp. 577–580, Aug. 1988, doi: 10.1038/334577a0.
- [99] Z. P. Liu, X. Q. Gong, J. Kohanoff, C. Sanchez, and P. Hu, “Catalytic role of metal oxides in gold-based catalysts: A first principles study of CO oxidation on TiO₂ supported Au,” *Phys. Rev. Lett.*, vol. 91, no. 26, pp. 1–4, 2003, doi: 10.1103/PhysRevLett.91.266102.
- [100] L. M. Molina and B. Hammer, “Some recent theoretical advances in the understanding of the catalytic activity of Au,” *Appl. Catal. A Gen.*, vol. 291, no. 1–2, pp. 21–31, 2005, doi: 10.1016/j.apcata.2005.01.050.
- [101] H. Huang, X. Ye, H. Huang, L. Zhang, and D. Y. C. Leung, “Mechanistic study on formaldehyde removal over Pd/TiO₂ catalysts: Oxygen transfer and role of water vapor,” *Chem. Eng. J.*, vol. 230, pp. 73–79, 2013, doi: 10.1016/j.cej.2013.06.035.
- [102] M. S. Chen and D. W. Goodman, “The structure of catalytically active gold on titania,” *Science*, vol. 306, no. 5694, pp. 252–255, 2004, doi: 10.1126/science.1102420.
- [103] A. A. Herzing, C. J. Kiely, A. F. Carley, P. Landon, and G. J. Hutchings, “Identification of active gold nanoclusters on iron oxide supports for CO oxidation,” *Science*, vol. 321, no. 5894, pp. 1331–1335, 2008, doi: 10.1126/science.1159639.
- [104] C. J. Pan *et al.*, “Tuning/exploiting Strong Metal-Support Interaction (SMSI) in Heterogeneous Catalysis,” *J. Taiwan Inst. Chem. Eng.*, vol. 74, pp. 154–186, 2017, doi: 10.1016/j.jtice.2017.02.012.
- [105] A. Ruiz Puigdollers, P. Schlexer, S. Tosoni, and G. Pacchioni, “Increasing Oxide Reducibility: The Role of Metal/Oxide Interfaces in the Formation of Oxygen

- Vacancies,” *ACS Catal.*, vol. 7, no. 10, pp. 6493–6513, 2017, doi: 10.1021/acscatal.7b01913.
- [106] J. Liu, Z. Zhao, Z. Ding, Z. Fang, and F. Cui, “Degradation of 4-chlorophenol in a Fenton-like system using Au–Fe₃O₄ magnetic nanocomposites as the heterogeneous catalyst at near neutral conditions,” *RSC Adv.*, vol. 6, no. 58, pp. 53080–53088, 2016, doi: 10.1039/C6RA10929B.
- [107] Y. Lee, M. A. Garcia, N. A. Frey Huls, and S. Sun, “Synthetic Tuning of the Catalytic Properties of Au-Fe₃O₄ Nanoparticles,” *Angew. Chemie Int. Ed.*, vol. 49, no. 7, pp. 1271–1274, 2010, doi: 10.1002/anie.200906130.
- [108] C. Wang, H. Yin, S. Dai, and S. Sun, “A general approach to noble metal-metal oxide dumbbell nanoparticles and their catalytic application for CO oxidation,” *Chem. Mater.*, vol. 22, no. 10, pp. 3277–3282, 2010, doi: 10.1021/cm100603r.
- [109] J. Goniakowski and C. Noguera, “Electronic States and Schottky Barrier Height at Metal/MgO(100) Interfaces,” *Interface Sci.*, vol. 12, no. 1, pp. 93–103, 2004, doi: 10.1023/B:INTS.0000012298.34540.50.
- [110] X. Lin *et al.*, “Quantum well states in two-dimensional gold clusters on MgO thin films,” *Phys. Rev. Lett.*, vol. 102, no. 20, pp. 1–4, 2009, doi: 10.1103/PhysRevLett.102.206801.
- [111] I. Marri and S. Ossicini, “Oxygen vacancy effects on the Schottky barrier height at the Au/TiO₂(110) interface: A first principle study,” *Solid State Commun.*, vol. 147, no. 5–6, pp. 205–207, 2008, doi: 10.1016/j.ssc.2008.05.018.
- [112] Y. Liu *et al.*, “Rational synthesis and tailored optical and magnetic characteristics of Fe₃O₄–Au composite nanoparticles,” *J. Mater. Sci.*, vol. 52, no. 17, pp. 10163–10174, 2017, doi: 10.1007/s10853-017-1200-9.
- [113] H. Yu, M. Chen, P. M. Rice, S. X. Wang, R. L. White, and S. Sun, “Dumbbell-like Bifunctional Au–Fe₃O₄ Nanoparticles,” *Nano Lett.*, vol. 5, no. 2, pp. 379–382, 2005, doi: 10.1021/nl047955q.
- [114] D. A. M.C. Daniel, “Gold nanoparticles: assembly, supramolecular chemistry, quantum-size-related properties, and applications toward,” *Chem. Rev.*, vol. 104, pp. 293–346, 2004.
- [115] I. Schick *et al.*, “Effect of Charge Transfer in Magnetic-Plasmonic Au@MO_x (M = Mn, Fe) Heterodimers on the Kinetics of Nanocrystal Formation,” *Chem. Mater.*, vol. 27, no. 13, pp. 4877–4884, 2015, doi: 10.1021/acs.chemmater.5b01968.
- [116] M. R. Buck, J. F. Bondi, and R. E. Schaak, “A total-synthesis framework for the construction of high-order colloidal hybrid nanoparticles,” *Nat. Chem.*, vol. 4, no. 1, pp. 37–44, 2012, doi: 10.1038/nchem.1195.
- [117] C. Wang, H. Daimon, and S. Sun, “Dumbbell-like Pt–Fe₃O₄ Nanoparticles and Their Enhanced Catalysis for Oxygen Reduction Reaction,” *Nano Lett.*, vol. 9, no. 4, pp. 1493–1496, 2009, doi: 10.1021/nl8034724.
- [118] W. Song and E. J. M. Hensen, “Structure sensitivity in CO oxidation by a single Au atom supported on ceria,” *J. Phys. Chem. C*, vol. 117, no. 15, pp. 7721–7726, 2013, doi: 10.1021/jp400977m.
- [119] N. Serpone and A. V. Emeline, “Semiconductor photocatalysis - Past, present, and future outlook,” *J. Phys. Chem. Lett.*, vol. 3, no. 5, pp. 673–677, 2012, doi: 10.1021/jz300071j.
- [120] X. Kang, S. Liu, Z. Dai, Y. He, X. Song, and Z. Tan, “Titanium dioxide: From engineering to applications,” *Catalysts*, vol. 9, no. 2, p. 191, 2019, doi: 10.3390/catal9020191.

- [121] L. Jing, W. Zhou, G. Tian, and H. Fu, "Surface tuning for oxide-based nanomaterials as efficient photocatalysts," *Chem. Soc. Rev.*, vol. 42, no. 24, pp. 9509–9549, 2013, doi: 10.1039/c3cs60176e.
- [122] H. Sun, X. Jiao, Y. Han, Z. Jiang, and D. Chen, "Synthesis of Fe₃O₄-Au Nanocomposites with Enhanced Peroxidase-Like Activity," *Eur. J. Inorg. Chem.*, vol. 2013, no. 1, pp. 109–114, 2013, doi: 10.1002/ejic.201201159.
- [123] X. Li *et al.*, "Synergistically enhanced peroxidase-like activity of Pd nanoparticles dispersed on CeO₂ nanotubes and their application in colorimetric sensing of sulfhydryl compounds," *J. Mater. Sci.*, vol. 53, no. 19, pp. 13912–13923, 2018, doi: 10.1007/s10853-018-2657-x.
- [124] M. S. Kim *et al.*, "Pt-Decorated Magnetic Nanozymes for Facile and Sensitive Point-of-Care Bioassay," *ACS Appl. Mater. Interfaces*, vol. 9, no. 40, pp. 35133–35140, 2017, doi: 10.1021/acsami.7b12326.
- [125] A. Robert and B. Meunier, "How to Define a Nanozyme," *ACS Nano*, vol. 16, no. 5, pp. 6956–6959, 2022, doi: 10.1021/acsnano.2c02966.
- [126] S. Naveen Prasad *et al.*, "Non-invasive detection of glucose in human urine using a color-generating copper NanoZyme," *Anal. Bioanal. Chem.*, vol. 413, no. 5, pp. 1279–1291, 2021, doi: 10.1007/s00216-020-03090-w.
- [127] J. Liu, L. Meng, Z. Fei, P. J. Dyson, and L. Zhang, "On the origin of the synergy between the Pt nanoparticles and MnO₂ nanosheets in Wonton-like 3D nanozyme oxidase mimics," *Biosens. Bioelectron.*, vol. 121, pp. 159–165, 2018, doi: 10.1016/j.bios.2018.08.004.
- [128] H. Liu, Y. Ding, B. Yang, Z. Liu, Q. Liu, and X. Zhang, "Colorimetric and ultrasensitive detection of H₂O₂ based on Au/Co₃O₄-CeO_x nanocomposites with enhanced peroxidase-like performance," *Sens. Act. B Chem.*, vol. 271, pp. 336–345, 2018, doi: 10.1016/j.snb.2018.05.108.
- [129] J. Lu *et al.*, "Oxygen-Vacancy-Enhanced Peroxidase-like Activity of Reduced Co₃O₄ Nanocomposites for the Colorimetric Detection of H₂O₂ and Glucose," *Inorg. Chem.*, vol. 59, no. 5, pp. 3152–3159, 2020, doi: 10.1021/acs.inorgchem.9b03512.
- [130] Q. Gao *et al.*, "Enhancement of Fe₃O₄/Au Composite Nanoparticles Catalyst in Oxidative Degradation of Methyl Orange Based on Synergistic Effect," *Chinese J. Chem.*, vol. 35, no. 9, pp. 1431–1436, 2017, doi: 10.1002/cjoc.201700032.
- [131] M. Sun *et al.*, "Synthesis of pH-switchable Pt/Co₃O₄ nanoflowers: Catalytic mechanism, four-enzyme activity and smartphone biosensing applications," *Chem. Eng. J.*, vol. 437, p. 134414, 2022, doi: 10.1016/j.cej.2021.134414.
- [132] W. Zhang *et al.*, "Prussian Blue Nanoparticles as Multienzyme Mimetics and Reactive Oxygen Species Scavengers," *J. Am. Chem. Soc.*, vol. 138, no. 18, pp. 5860–5865, 2016, doi: 10.1021/jacs.5b12070.
- [133] S. Bhagat, N. V. Srikanth Vallabani, V. Shutthanandan, M. Bowden, A. S. Karakoti, and S. Singh, "Gold core/ceria shell-based redox active nanozyme mimicking the biological multienzyme complex phenomenon," *J. Colloid Interface Sci.*, vol. 513, pp. 831–842, 2018, doi: 10.1016/j.jcis.2017.11.064.
- [134] C. Wang, Y. Li, W. Yang, L. Zhou, and S. Wei, "Nanozyme with Robust Catalase Activity by Multiple Mechanisms and Its Application for Hypoxic Tumor Treatment," *Adv. Healthc. Mater.*, vol. 10, no. 19, pp. 1–12, 2021, doi: 10.1002/adhm.202100601.
- [135] S. Li *et al.*, "A Nanozyme with Photo-Enhanced Dual Enzyme-Like Activities for Deep

- Pancreatic Cancer Therapy,” *Angew. Chemie - Int. Ed.*, vol. 58, no. 36, pp. 12624–12631, 2019, doi: 10.1002/anie.201904751.
- [136] D. Xu, L. Wu, H. Yao, and L. Zhao, “Catalase-Like Nanozymes: Classification, Catalytic Mechanisms, and Their Applications,” *Small*, vol. 18, no. 37, 2022, doi: 10.1002/smll.202203400.
- [137] Y. Li, S. Li, R. Zhou, G. Li, and X. Li, “Selective laser welding in liquid: A strategy for preparation of high-antibacterial activity nanozyme against *Staphylococcus aureus*,” *J. Adv. Res.*, vol. In press, 2022, doi: 10.1016/j.jare.2022.03.015.
- [138] A. Clark, A. Zhu, K. Sun, and H. R. Petty, “Cerium oxide and platinum nanoparticles protect cells from oxidant-mediated apoptosis,” *J. Nanoparticle Res.*, vol. 13, no. 10, pp. 5547–5555, 2011, doi: 10.1007/s11051-011-0544-3.
- [139] L. Zhang *et al.*, “Reducing stress on cells with apoferritin-encapsulated platinum nanoparticles,” *Nano Lett.*, vol. 10, no. 1, pp. 219–223, 2010, doi: 10.1021/nl903313r.
- [140] Z. Wang *et al.*, “Accelerated discovery of superoxide-dismutase nanozymes via high-throughput computational screening,” *Nat. Commun.*, vol. 12, no. 1, p. 6866, 2021, doi: 10.1038/s41467-021-27194-8.
- [141] C. Liu *et al.*, “NIR enhanced peroxidase-like activity of Au@CeO₂ hybrid nanozyme by plasmon-induced hot electrons and photothermal effect for bacteria killing,” *Appl. Catal. B Environ.*, vol. 295, p. 120317, 2021, doi: 10.1016/j.apcatb.2021.120317.
- [142] K. W. Kwon and M. Shim, “ γ -Fe₂O₃/II-VI sulfide nanocrystal heterojunctions,” *J. Am. Chem. Soc.*, vol. 127, no. 29, pp. 10269–10275, 2005, doi: 10.1021/ja051713q.
- [143] C. Wang, C. Xu, H. Zeng, and S. Sun, “Recent progress in syntheses and applications of dumbbell-like nanoparticles,” *Adv. Mater.*, vol. 21, no. 30, pp. 3045–3052, 2009, doi: 10.1002/adma.200900320.
- [144] M. Kluncker *et al.*, “Pd@Fe₂O₃ Superparticles with Enhanced Peroxidase Activity by Solution Phase Epitaxial Growth,” *Chem. Mater.*, vol. 29, no. 3, pp. 1134–1146, 2017, doi: 10.1021/acs.chemmater.6b04283.
- [145] J. Hu, S. Zhou, Y. Sun, X. Fang, and L. Wu, “Fabrication, properties and applications of Janus particles,” *Chem. Soc. Rev.*, vol. 41, no. 11, pp. 4356–4378, 2012, doi: 10.1039/c2cs35032g.
- [146] S. Campuzano, M. Gamella, V. Serafín, M. Pedrero, P. Yáñez-Sedeño, and J. M. Pingarrón, “Magnetic Janus Particles for Static and Dynamic (Bio)Sensing,” *Magnetochemistry*, vol. 5, no. 3, p. 47, 2019, doi: 10.3390/magnetochemistry5030047.
- [147] H. Su, C. A. Hurd Price, L. Jing, Q. Tian, J. Liu, and K. Qian, “Janus particles: design, preparation, and biomedical applications,” *Mater. Today Bio*, vol. 4, p. 100033, 2019, doi: 10.1016/j.mtbio.2019.100033.
- [148] T. Chen, G. Chen, S. Xing, T. Wu, and H. Chen, “Scalable routes to janus Au-SiO₂ and ternary Ag-Au-SiO₂ nanoparticles,” *Chem. Mater.*, vol. 22, no. 13, pp. 3826–3828, 2010, doi: 10.1021/cm101155v.
- [149] L. Zhang, L. Li, and C. Wang, “Janus nanozyme–drug nanosystems for synergistic anti-inflammatory treatment of nasal polyps,” vol. 22, no. 45, pp. 7800–7807, 2020, doi: 10.1039/d0ce00450b.
- [150] S. Liang *et al.*, “A Novel Pt–TiO₂ Heterostructure with Oxygen-Deficient Layer as Bilaterally Enhanced Sonosensitizer for Synergistic Chemo-Sonodynamic Cancer Therapy,” *Adv. Funct. Mater.*, vol. 30, no. 13, 2020, doi: 10.1002/adfm.201908598.

- [151] L. Long, R. Cai, J. Liu, and X. Wu, "A Novel Nanoprobe Based on Core-Shell Au@Pt@Mesoporous SiO₂ Nanozyme With Enhanced Activity and Stability for Mumps Virus Diagnosis," *Front. Chem.*, vol. 8, pp. 1–9, 2020, doi: 10.3389/fchem.2020.00463.
- [152] M. Ma, J. Xie, Y. Zhang, Z. Chen, and N. Gu, "Fe₃O₄@Pt nanoparticles with enhanced peroxidase-like catalytic activity," *Mater. Lett.*, vol. 105, pp. 36–39, 2013, doi: 10.1016/j.matlet.2013.04.020.
- [153] J. Lian *et al.*, "Core-shell structured Ag-CoO nanoparticles with superior peroxidase-like activity for colorimetric sensing hydrogen peroxide and o-phenylenediamine," *Colloids Surf. A*, vol. 603, p. 125283, 2020, doi: 10.1016/j.colsurfa.2020.125283.
- [154] I. Y. Goon, L. M. H. Lai, M. Lim, P. Munroe, J. J. Gooding, and R. Amal, "Fabrication and dispersion of gold-shell-protected magnetite nanoparticles: Systematic control using polyethyleneimine," *Chem. Mater.*, vol. 21, no. 4, pp. 673–681, 2009, doi: 10.1021/cm8025329.
- [155] Q. L. Zhu and Q. Xu, "Immobilization of Ultrafine Metal Nanoparticles to High-Surface-Area Materials and Their Catalytic Applications," *Chem*, vol. 1, no. 2, pp. 220–245, 2016, doi: 10.1016/j.chempr.2016.07.005.
- [156] S. Fedorenko *et al.*, "Surface decoration of silica nanoparticles by Pd(0) deposition for catalytic application in aqueous solutions," *Colloids Surf. A*, vol. 486, pp. 185–191, 2015, doi: 10.1016/j.colsurfa.2015.09.044.
- [157] J. M. Walker and J. M. Zaleski, "A simple route to diverse noble metal-decorated iron oxide nanoparticles for catalysis," *Nanoscale*, vol. 8, no. 3, pp. 1535–1544, 2016, doi: 10.1039/c5nr06700f.
- [158] J. Bao *et al.*, "Bifunctional Au-Fe₃O₄ nanoparticles for protein separation," *ACS Nano*, vol. 1, no. 4, pp. 293–298, 2007, doi: 10.1021/nn700189h.
- [159] W. Guo, Q. Wang, G. Wang, M. Yang, W. Dong, and J. Yu, "Facile hydrogen-bond-assisted polymerization and immobilization method to synthesize hierarchical Fe₃O₄@Poly(4-vinylpyridine-co-divinylbenzene)@Au nanostructures and their catalytic applications," *Chem. - An Asian J.*, vol. 8, no. 6, pp. 1160–1167, 2013, doi: 10.1002/asia.201201186.
- [160] L. Zhou, C. Gao, and W. Xu, "Robust Fe₃O₄/SiO₂-Pt/Au/Pd magnetic nanocatalysts with multifunctional hyperbranched polyglycerol amplifiers," *Langmuir*, vol. 26, no. 13, pp. 11217–11225, 2010, doi: 10.1021/la100556p.
- [161] F. Yan and R. Sun, "Facile synthesis of bifunctional Fe₃O₄/Au nanocomposite and their application in catalytic reduction of 4-nitrophenol," *Mater. Res. Bull.*, vol. 57, pp. 293–299, 2014, doi: 10.1016/j.materresbull.2014.06.012.
- [162] R. Huang and R. Liu, "Efficient in situ growth of platinum nanoclusters on the surface of Fe₃O₄ for the detection of latent fingerprints," *J. Mater. Sci.*, vol. 52, no. 23, pp. 13455–13465, 2017, doi: 10.1007/s10853-017-1475-x.
- [163] A. Pearson, S. K. Bhargava, and V. Bansal, "UV-switchable polyoxometalate sandwiched between TiO₂ and metal nanoparticles for enhanced visible and solar light photocatalysis," *Langmuir*, vol. 27, no. 15, pp. 9245–9252, 2011, doi: 10.1021/la201655n.
- [164] K. Zheng, C. Shen, J. Qiao, J. Tong, J. Jin, and P. Zhang, "Novel Magnetically-Recyclable, Nitrogen-Doped Fe₃O₄@Pd NPs for Suzuki–Miyaura Coupling and Their Application in the Synthesis of Crizotinib," *Catalysts*, vol. 8, no. 10, p. 443, Oct. 2018,

- doi: 10.3390/catal8100443.
- [165] J. Liu, W. Wang, T. Shen, Z. Zhao, H. Feng, and F. Cui, "One-step synthesis of noble metal/oxide nanocomposites with tunable size of noble metal particles and their size-dependent catalytic activity," *RSC Adv.*, vol. 4, no. 58, pp. 30624–30629, 2014, doi: 10.1039/c4ra04504a.
- [166] D. Andreeva, P. Petrova, J. W. Sobczak, L. Ilieva, and M. Abrashev, "Gold supported on ceria and ceria-alumina promoted by molybdena for complete benzene oxidation," *Appl. Catal. B Environ.*, vol. 67, no. 3–4, pp. 237–245, 2006, doi: 10.1016/j.apcatb.2006.05.004.
- [167] S. Podder, C. K. Ghosh, A. Das, and J. G. Hardy, "Light-responsive nanomaterials with pro-oxidant and anti-oxidant activity," *Emergent Mater.*, vol. 5, no. 2, pp. 455–475, 2022, doi: 10.1007/s42247-022-00361-3.
- [168] D. Mohanty, G. S. Chaubey, A. Yourdkhani, S. Adireddy, G. Caruntu, and J. B. Wiley, "Synthesis and piezoelectric response of cubic and spherical LiNbO₃ nanocrystals," *RSC Adv.*, vol. 2, no. 5, p. 1913, 2012, doi: 10.1039/c2ra00628f.
- [169] R. S. Weis and T. K. Gaylord, "Lithium niobate: Summary of physical properties and crystal structure," *Appl. Phys. A Solids Surfaces*, vol. 37, no. 4, pp. 191–203, 1985, doi: 10.1007/BF00614817.
- [170] M. Niederberger, N. Pinna, J. Polleux, and M. Antonietti, "A general soft-chemistry route to perovskites and related materials: Synthesis of BaTiO₃, BaZrO₃, and LiNbO₃ nanoparticles," *Angew. Chemie - Int. Ed.*, vol. 43, no. 17, pp. 2270–2273, 2004, doi: 10.1002/anie.200353300.
- [171] J. Vuilleumier *et al.*, "Photocontrolled Release of the Anticancer Drug Chlorambucil with Caged Harmonic Nanoparticles," *Helv. Chim. Acta*, vol. 103, no. 1, p. e1900251, 2020, doi: 10.1002/hlca.201900251.
- [172] D. Staedler *et al.*, "Harmonic nanocrystals for biolabeling: A survey of optical properties and biocompatibility," *ACS Nano*, vol. 6, no. 3, pp. 2542–2549, 2012, doi: 10.1021/nn204990n.
- [173] J. Li *et al.*, "Cellular internalization of LiNbO₃ nanocrystals for second harmonic imaging and the effects on stem cell differentiation," *Nanoscale*, vol. 8, no. 14, pp. 7416–7422, 2016, doi: 10.1039/c6nr00785f.
- [174] R. Taitt, "Core-shell nanoparticles active in non-linear optics for the imagery and phototherapy of cancer," PhD Dissertation, École Centrale de Lyon, 2021.
- [175] N. Hoshyar, S. Gray, H. Han, and G. Bao, "The effect of nanoparticle size on in vivo pharmacokinetics and cellular interaction," *Nanomedicine*, vol. 11, no. 6, pp. 673–692, 2016. doi: 10.2217/nnm.16.5.
- [176] J. Richter, A. Steinbrück, T. Pertsch, A. Tünnermann, and R. Grange, "Plasmonic Core-Shell Nanowires for Enhanced Second-Harmonic Generation," *Plasmonics*, vol. 8, no. 1, pp. 115–120, 2013, doi: 10.1007/s11468-012-9429-2.
- [177] M. Bokseveld *et al.*, "Nonlinear plasmonic nanohybrids as probes for multimodal cell imaging and potential phototherapeutic agents," *Biomed. Phys. Eng. Express*, vol. 5, no. 2, p. 25039, 2019, doi: 10.1088/2057-1976/ab0232.
- [178] M. A. Khan, M. A. Nadeem, and H. Idriss, "Ferroelectric polarization effect on surface chemistry and photo-catalytic activity: A review," *Surf. Sci. Rep.*, vol. 71, no. 1, pp. 1–31, 2016, doi: 10.1016/j.surfrep.2016.01.001.
- [179] R. K. Nath, M. F. M. Zain, A. A. H. Kadhum, and A. B. M. A. Kaish, "An investigation

- of LiNbO₃ photocatalyst coating on concrete surface for improving indoor air quality,” *Constr. Build. Mater.*, vol. 54, pp. 348–353, 2014, doi: 10.1016/j.conbuildmat.2013.12.072.
- [180] Y. Yun, L. Kampschulte, M. Li, D. Liao, and E. I. Altman, “Effect of Ferroelectric Poling on the Adsorption of 2-Propanol on LiNbO₃ (0001),” *J. Phys. Chem. C*, vol. 111, no. 37, pp. 13951–13956, 2007, doi: 10.1021/jp074214f.
- [181] O. Sánchez-Dena, S. D. Villalobos-Mendoza, R. Farías, and C. D. Fierro-Ruiz, “Lithium niobate single crystals and powders reviewed—part II,” *Crystals*, vol. 10, no. 11, pp. 1–33, 2020, doi: 10.3390/cryst10110990.
- [182] B. Cai, M. Zhao, Y. Ma, Z. Ye, and J. Huang, “Bio-inspired formation of mesoporous LiNbO₃ nanotubes and application for glucose biosensor,” *Electrochim. Acta*, vol. 147, pp. 176–182, 2014, doi: 10.1016/j.electacta.2014.09.054.
- [183] Y. Inoue, I. Yoshioka, and K. Sato, “Polarization effects upon adsorptive and catalytic properties. 1. Carbon monoxide oxidation over palladium deposited on lithium niobate (LiNbO₃) ferroelectrics,” *J. Phys. Chem.*, vol. 88, no. 6, pp. 1148–1151, 1984, doi: 10.1021/j150650a025.
- [184] I. C. Amaechi, A. Hadj Youssef, A. Dörfler, Y. González, R. Katoch, and A. Ruediger, “Catalytic Applications of Non-Centrosymmetric Oxide Nanomaterials,” *Angew. Chemie*, vol. 134, no. 43, p. e202207975, 2022, doi: 10.1002/ange.202207975.
- [185] A. Raturi, P. Mittal, and S. Choudhary, “Electronic and optical properties of lithium niobate (LiNbO₃) under tensile and compressive strain for optoelectronic applications: Insights from DFT,” *Mater. Sci. Semicond. Process.*, vol. 144, p. 106606, 2022, doi: 10.1016/j.mssp.2022.106606.
- [186] V. T. Kalinnikov, O. G. Gromov, G. B. Kunshina, A. P. Kuz’min, E. P. Lokshin, and V. I. Ivanenko, “Preparation of LiTaO₃, LiNbO₃, and NaNbO₃ from peroxide solutions,” *Inorg. Mater.*, vol. 40, no. 4, pp. 411–414, 2004, doi: 10.1023/B:INMA.0000023967.76203.61.
- [187] C. Debnath, S. Kar, S. Verma, and K. S. Bartwal, “Synthesis of LiNbO₃ Nanoparticles by Citrate Gel Method,” *J. Nanosci. Nanotechnol.*, vol. 15, no. 5, pp. 3757–3763, 2015, doi: 10.1166/jnn.2015.9769.
- [188] M. Urbain *et al.*, “On the reaction pathways and growth mechanisms of LiNbO₃ nanocrystals from the non-aqueous solvothermal alkoxide route,” *Nanomaterials*, vol. 11, no. 1, pp. 1–18, 2021, doi: 10.3390/nano11010154.
- [189] H. Kominami, M. Inoue, and T. Inui, “Formation of niobium double oxides by the glycothermal method,” *Catal. Today*, vol. 16, no. 3–4, pp. 309–317, 1993, doi: 10.1016/0920-5861(93)80070-H.
- [190] R. F. Ali and B. D. Gates, “Synthesis of Lithium Niobate Nanocrystals with Size Focusing through an Ostwald Ripening Process,” *Chem. Mater.*, vol. 30, no. 6, pp. 2028–2035, 2018, doi: 10.1021/acs.chemmater.7b05282.
- [191] B. H. Kim, M. J. Hackett, J. Park, and T. Hyeon, “Synthesis, Characterization, and Application of Ultrasmall Nanoparticles,” *Chem. Mater.*, vol. 26, no. 1, pp. 59–71, 2014, doi: 10.1021/cm402225z.
- [192] W. W. Bryan, A. C. Jamison, P. Chinwangso, S. Rittikulsittichai, T. R. C. Lee, and T. R. C. Lee, “Preparation of THPC-generated silver, platinum, and palladium nanoparticles and their use in the synthesis of Ag, Pt, Pd, and Pt/Ag nanoshells,” *RSC Adv.*, vol. 6, no. 72, pp. 68150–68159, 2016, doi: 10.1039/c6ra10717f.

- [193] Y. Xia, K. D. Gilroy, H. C. Peng, and X. Xia, "Seed-Mediated Growth of Colloidal Metal Nanocrystals," *Angew. Chemie - Int. Ed.*, vol. 56, no. 1, pp. 60–95, 2017, doi: 10.1002/anie.201604731.
- [194] Z. Liu, Z. Wu, Q. Yao, Y. Cao, O. J. H. Chai, and J. Xie, "Correlations between the fundamentals and applications of ultrasmall metal nanoclusters: Recent advances in catalysis and biomedical applications," *Nano Today*, vol. 36, p. 101053, 2021, doi: 10.1016/j.nantod.2020.101053.
- [195] G. Habibullah, J. Viktorova, and T. Ruml, "Current Strategies for Noble Metal Nanoparticle Synthesis," *Nanoscale Res. Lett.*, vol. 16, no. 1, p. 47, 2021, doi: 10.1186/s11671-021-03480-8.
- [196] V. K. LaMer and R. H. Dinegar, "Theory, Production and Mechanism of Formation of Monodispersed Hydrosols," *J. Am. Chem. Soc.*, vol. 72, no. 11, pp. 4847–4854, 1950, doi: 10.1021/ja01167a001.
- [197] R. Khan, A. Rehman, A. Hayat, and S. Andreescu, "Magnetic particles-based analytical platforms for food safety monitoring," *Magnetochemistry*, vol. 5, no. 4, pp. 1–20, 2019, doi: 10.3390/magnetochemistry5040063.
- [198] V. Pareek, A. Bhargava, R. Gupta, N. Jain, and J. Panwar, "Synthesis and Applications of Noble Metal Nanoparticles: A Review," *Adv. Sci. Eng. Med.*, vol. 9, no. 7, pp. 527–544, 2017, doi: 10.1166/ asem.2017.2027.
- [199] D. G. Duff, A. Baiker, and P. P. Edwards, "A new hydrosol of gold clusters. 1. Formation and particle size variation," *Langmuir*, vol. 9, no. 9, pp. 2301–2309, 1993, doi: 10.1021/la00033a010.
- [200] J. L. Hueso, V. Sebastián, Á. Mayoral, L. Usón, M. Arruebo, and J. Santamaría, "Beyond gold: Rediscovering tetrakis-(hydroxymethyl)-phosphonium chloride (THPC) as an effective agent for the synthesis of ultra-small noble metal nanoparticles and Pt-containing nanoalloys," *RSC Adv.*, vol. 3, no. 26, pp. 10427–10433, 2013, doi: 10.1039/c3ra40774h.
- [201] J. Zhang *et al.*, "ROS and ROS-Mediated Cellular Signaling," *Oxid. Med. Cell. Longev.*, p. 4350965, 2016, doi: 10.1155/2016/4350965.
- [202] A. A. Dayem *et al.*, "The role of reactive oxygen species (ROS) in the biological activities of metallic nanoparticles," *Int. J. Mol. Sci.*, vol. 18, no. 1, pp. 1–21, 2017, doi: 10.3390/ijms18010120.
- [203] S. Jia, S. Ge, X. Fan, K. W. Leong, and J. Ruan, "Promoting reactive oxygen species generation: A key strategy in nanosensitizer-mediated radiotherapy," *Nanomedicine*, vol. 16, no. 9, pp. 759–778, 2021, doi: 10.2217/nmm-2020-0448.
- [204] C. Zhang, X. Wang, J. Du, Z. Gu, and Y. Zhao, "Reactive Oxygen Species-Regulating Strategies Based on Nanomaterials for Disease Treatment," *Adv. Sci.*, vol. 8, no. 3, pp. 1–34, 2021, doi: 10.1002/advs.202002797.
- [205] Y. Tao, E. Ju, J. Ren, and X. Qu, "Bifunctionalized mesoporous silica-supported gold nanoparticles: Intrinsic oxidase and peroxidase catalytic activities for antibacterial applications," *Adv. Mater.*, vol. 27, no. 6, pp. 1097–1104, 2015, doi: 10.1002/adma.201405105.
- [206] Z. Wang *et al.*, "Activation of biologically relevant levels of reactive oxygen species by Au/g-C₃N₄ hybrid nanozyme for bacteria killing and wound disinfection," *Biomaterials*, vol. 113, pp. 145–157, 2017, doi: 10.1016/j.biomaterials.2016.10.041.
- [207] H. Zhang *et al.*, "Antibacterial Performance of a Gold-Loaded g-C₃N₄ Nanocomposite

- System in Visible Light-Dark Dual Mode,” *Chempluschem*, vol. 85, no. 12, pp. 2722–2730, 2020, doi: 10.1002/cplu.202000676.
- [208] G. Fang *et al.*, “Differential Pd-nanocrystal facets demonstrate distinct antibacterial activity against Gram-positive and Gram-negative bacteria,” *Nat. Commun.*, vol. 9, no. 1, pp. 1–9, 2018, doi: 10.1038/s41467-017-02502-3.
- [209] C. Cao *et al.*, “POD Nanozyme optimized by charge separation engineering for light/pH activated bacteria catalytic/photodynamic therapy,” *Signal Transduct. Target. Ther.*, vol. 7, no. 1, p. 86, 2022, doi: 10.1038/s41392-022-00900-8.
- [210] S. Cai, X. Jia, Q. Han, X. Yan, R. Yang, and C. Wang, “Porous Pt/Ag nanoparticles with excellent multifunctional enzyme mimic activities and antibacterial effects,” *Nano Res.*, vol. 10, no. 6, pp. 2056–2069, 2017, doi: 10.1007/s12274-016-1395-0.
- [211] L. Zhang *et al.*, “In vivo activation of pH-responsive oxidase-like graphitic nanozymes for selective killing of *Helicobacter pylori*,” *Nat. Commun.*, vol. 12, no. 1, pp. 1–10, 2021, doi: 10.1038/s41467-021-22286-x.
- [212] M. Mirhosseini, A. Shekari-Far, F. Hakimian, B. F. Haghirsadat, S. K. Fatemi, and F. Dashtestani, “Core-shell Au@Co-Fe hybrid nanoparticles as peroxidase mimetic nanozyme for antibacterial application,” *Process Biochem.*, vol. 95, pp. 131–138, 2020, doi: 10.1016/j.procbio.2020.05.003.
- [213] L. Fan *et al.*, “Tumor Catalytic-Photothermal Therapy with Yolk-Shell Gold@Carbon Nanozymes,” *ACS Appl. Mater. Interfaces*, vol. 10, no. 5, pp. 4502–4511, 2018, doi: 10.1021/acsami.7b17916.
- [214] S. Gao, H. Lin, H. Zhang, H. Yao, Y. Chen, and J. Shi, “Nanocatalytic Tumor Therapy by Biomimetic Dual Inorganic Nanozyme-Catalyzed Cascade Reaction,” *Adv. Sci.*, vol. 6, no. 3, p. 1801733, 2019, doi: 10.1002/advs.201801733.
- [215] A. Zhang *et al.*, “GSH-triggered sequential catalysis for tumor imaging and eradication based on star-like Au/Pt enzyme carrier system,” *Nano Res.*, vol. 13, no. 1, pp. 160–172, 2020, doi: 10.1007/s12274-019-2591-5.
- [216] Z. Wang *et al.*, “Biomimetic nanoflowers by self-assembly of nanozymes to induce intracellular oxidative damage against hypoxic tumors,” *Nat. Commun.*, vol. 9, no. 1, p. 3334, 2018, doi: 10.1038/s41467-018-05798-x.
- [217] Z. Ma, L. Wu, K. Han, and H. Han, “Pt nanozyme for O₂ self-sufficient, tumor-specific oxidative damage and drug resistance reversal,” *Nanoscale Horizons*, vol. 4, no. 5, pp. 1124–1131, 2019, doi: 10.1039/c9nh00088g.
- [218] Y. Zhang *et al.*, “Nanozyme Decorated Metal-Organic Frameworks for Enhanced Photodynamic Therapy,” *ACS Nano*, vol. 12, no. 1, pp. 651–661, 2018, doi: 10.1021/acs.nano.7b07746.
- [219] N. Gao *et al.*, “Polyoxometalate-based nanozyme: Design of a multifunctional enzyme for multi-faceted treatment of Alzheimer’s disease,” *Nano Res.*, vol. 9, no. 4, pp. 1079–1090, 2016, doi: 10.1007/s12274-016-1000-6.
- [220] M. Moglianetti *et al.*, “Platinum nanozymes recover cellular ROS homeostasis in an oxidative stress-mediated disease model,” *Nanoscale*, vol. 8, no. 6, pp. 3739–3752, 2016, doi: 10.1039/c5nr08358c.
- [221] Y. Liu *et al.*, “Integrated cascade nanozyme catalyzes in vivo ROS scavenging for anti-inflammatory therapy,” *Sci. Adv.*, vol. 6, no. 29, p. eabb2695, 2020, doi: 10.1126/sciadv.abb2695.
- [222] C. P. Liu, T. H. Wu, Y. L. Lin, C. Y. Liu, S. Wang, and S. Y. Lin, “Tailoring Enzyme-

- Like Activities of Gold Nanoclusters by Polymeric Tertiary Amines for Protecting Neurons Against Oxidative Stress,” *Small*, vol. 12, no. 30, pp. 4127–4135, 2016, doi: 10.1002/smll.201503919.
- [223] Y. Huang, C. Liu, F. Pu, Z. Liu, J. Ren, and X. Qu, “A GO-Se nanocomposite as an antioxidant nanozyme for cytoprotection,” *Chem. Commun.*, vol. 53, no. 21, pp. 3082–3085, 2017, doi: 10.1039/c7cc00045f.
- [224] S. Onizawa, K. Aoshiba, M. Kajita, Y. Miyamoto, and A. Nagai, “Platinum nanoparticle antioxidants inhibit pulmonary inflammation in mice exposed to cigarette smoke,” *Pulm. Pharmacol. Ther.*, vol. 22, no. 4, pp. 340–349, 2009, doi: 10.1016/j.pupt.2008.12.015.
- [225] B. Xiong, R. Xu, R. Zhou, Y. He, and E. S. Yeung, “Preventing UV induced cell damage by scavenging reactive oxygen species with enzyme-mimic Au-Pt nanocomposites,” *Talanta*, vol. 120, pp. 262–267, 2014, doi: 10.1016/j.talanta.2013.12.020.
- [226] D. Yang, Z. Chen, Z. Gao, S. K. Tammina, and Y. Yang, “Nanozymes used for antimicrobials and their applications,” *Colloids Surf. B*, vol. 195, p. 111252, 2020, doi: 10.1016/j.colsurfb.2020.111252.
- [227] Y. Zhou, B. Liu, R. Yang, and J. Liu, “Filling in the Gaps between Nanozymes and Enzymes: Challenges and Opportunities,” *Bioconjug. Chem.*, vol. 28, no. 12, pp. 2903–2909, 2017, doi: 10.1021/acs.bioconjchem.7b00673.
- [228] Q. Li, T. Wu, X. Fan, X. Guo, W. Jiang, and K. Fan, “Materials & Design Multifaceted nanozymes for synergistic antitumor therapy: A review,” *Mater. Des.*, vol. 224, p. 111430, 2022, doi: 10.1016/j.matdes.2022.111430.
- [229] N. Chakraborty, S. Gandhi, R. Verma, and I. Roy, “Emerging Prospects of Nanozymes for Antibacterial and Anticancer Applications,” *Biomedicines*, vol. 10, no. 6, pp. 1–24, 2022, doi: 10.3390/biomedicines10061378.
- [230] D. B. Williams, C. B. Carter, and D. B. Williams, *Transmission Electron Microscopy*. Boston, MA: Springer, 2016. doi: 10.1007/978-0-387-76501-3.
- [231] J. I. Goldstein, D. E. Newbury, J. R. Michael, N. W. M. Ritchie, J. H. J. Scott, and D. C. Joy, *Scanning Electron Microscopy and X-Ray Microanalysis*, 3rd ed. New York, NY: Springer, 2018. doi: 10.1007/978-1-4939-6676-9.
- [232] B. J. Berne and R. Pecora, *Dynamic Light Scattering with Applications to Chemistry, Biology, and Physics*. New York, NY: Dover Publications, 2000.
- [233] H. C. van de Hulst, *Light Scattering by Small Particles*. New York, NY: Dover Publications, 1981.
- [234] I. D. Morrison and S. Ross, *Colloidal dispersions: suspensions, emulsions, and foams*. New York, NY: Wiley-Interscience, 2002.
- [235] T. A. Tengku Mohd, M. Z. Jaafar, A. A. Ali Rasol, and M. F. Hamid, “Measurement of Streaming Potential in Downhole Application: An Insight for Enhanced Oil Recovery Monitoring,” *MATEC Web Conf.*, vol. 87, p. 3002, 2016, doi: 10.1051/mateconf/20178703002.
- [236] S. Cherevko and K. J. J. Mayrhofer, “On-Line Inductively Coupled Plasma Spectrometry in Electrochemistry: Basic Principles and Applications,” in *Encyclopedia of Interfacial Chemistry*, Elsevier, 2018, pp. 326–335. doi: 10.1016/B978-0-12-409547-2.13292-5.
- [237] E. Petryayeva and U. J. Krull, “Localized surface plasmon resonance: Nanostructures, bioassays and biosensing-A review,” *Anal. Chim. Acta*, vol. 706, no. 1, pp. 8–24, 2011,

- doi: 10.1016/j.aca.2011.08.020.
- [238] P. Anzini, D. Redoglio, M. Rocco, N. Masciocchi, and F. Ferri, “Light Scattering and Turbidimetry Techniques for the Characterization of Nanoparticles and Nanostructured Networks,” *Nanomaterials*, vol. 12, no. 13, p. 2214, 2022, doi: 10.3390/nano12132214.
- [239] D. A. Skoog, F. J. Holler, and S. R. Crouch, *Principles of instrumental analysis*, 7th ed. Boston, MA: Cengage learning, 2017.
- [240] M. Valcárcel Cases, Á. I. López-Lorente, and M. Á. López-Jiménez, *Foundations of Analytical Chemistry*. Cham: Springer International Publishing, 2018. doi: 10.1007/978-3-319-62872-1.
- [241] A. L. Koch, “Turbidity measurements of bacterial cultures in some available commercial instruments,” *Anal. Biochem.*, vol. 38, no. 1, pp. 252–259, 1970, doi: 10.1016/0003-2697(70)90174-0.
- [242] K. Nama Manjunatha and S. Paul, “Investigation of optical properties of nickel oxide thin films deposited on different substrates,” *Appl. Surf. Sci.*, vol. 352, pp. 10–15, 2015, doi: 10.1016/j.apsusc.2015.03.092.
- [243] P. Makuła, M. Pacia, and W. Macyk, “How To Correctly Determine the Band Gap Energy of Modified Semiconductor Photocatalysts Based on UV-Vis Spectra,” *J. Phys. Chem. Lett.*, vol. 9, no. 23, pp. 6814–6817, 2018, doi: 10.1021/acs.jpcclett.8b02892.
- [244] C. Maheu, “Study of Titania supported transition metal sulfides for the photocatalytic production of hydrogen,” PhD Dissertation, Claude Bernard University - Lyon 1, 2019.
- [245] A. Yogamoorthy and S. M. Sundarapandian, “Green synthesis of gold nanoparticles and evaluation of its cytotoxic property against colon cancer cell line,” *Res. J. Life Sci. Bioinformatics, Pharm. Chem. Sci.*, vol. 4, no. 1, pp. 1–17, 2018, doi: 10.26479/2018.0406.01.
- [246] C. Maheu, L. Cardenas, E. Puzenat, P. Afanasiev, and C. Geantet, “UPS and UV spectroscopies combined to position the energy levels of TiO₂ anatase and rutile nanopowders,” *Phys. Chem. Chem. Phys.*, vol. 20, no. 40, pp. 25629–25637, 2018, doi: 10.1039/c8cp04614j.
- [247] Z. Zheng *et al.*, “Highly efficient singlet oxygen generation, two-photon photodynamic therapy and melanoma ablation by rationally designed mitochondria-specific near-infrared AIEgens,” *Chem. Sci.*, vol. 11, no. 9, pp. 2494–2503, 2020, doi: 10.1039/c9sc06441a.
- [248] J. Tauc, R. Grigorovici, and A. Vancu, “Optical Properties and Electronic Structure of Amorphous Germanium,” *Phys. status solidi*, vol. 15, no. 2, pp. 627–637, 1966, doi: 10.1002/pssb.19660150224.
- [249] S. Hüfner, *Photoelectron Spectroscopy*. Berlin, Heidelberg: Springer, 2003. doi: 10.1007/978-3-662-09280-4.
- [250] A. Theodosiou, B. F. Spencer, J. Counsell, and A. N. Jones, “An XPS/UPS study of the surface/near-surface bonding in nuclear grade graphites: A comparison of monatomic and cluster depth-profiling techniques,” *Appl. Surf. Sci.*, vol. 508, p. 144764, 2020, doi: 10.1016/j.apsusc.2019.144764.
- [251] B. Roland, “Comparison UPS and XPS.” <http://www.lasurface.com/ups/comparaison.php> (accessed Dec. 13, 2022).
- [252] X. M. Kuang *et al.*, “Hydroxyl radical formation and soluble trace metal content in particulate matter from renewable diesel and ultra low sulfur diesel in at-sea operations of a research vessel,” *Aerosol Sci. Technol.*, vol. 51, no. 2, pp. 147–158, 2017, doi:

- 10.1080/02786826.2016.1271938.
- [253] H. Zhao *et al.*, “Superoxide reacts with hydroethidine but forms a fluorescent product that is distinctly different from ethidium: Potential implications in intracellular fluorescence detection of superoxide,” *Free Radic. Biol. Med.*, vol. 34, no. 11, pp. 1359–1368, 2003, doi: 10.1016/S0891-5849(03)00142-4.
- [254] D. K. Lee, Y. Song, V. T. Tran, J. Kim, E. Y. Park, and J. Lee, “Preparation of concave magnetoplasmonic core-shell supraparticles of gold-coated iron oxide via ion-reducible layer-by-layer method for surface enhanced Raman scattering,” *J. Colloid Interface Sci.*, vol. 499, pp. 54–61, 2017, doi: 10.1016/j.jcis.2017.03.098.
- [255] R. Bhatt *et al.*, “Urbach tail and bandgap analysis in near stoichiometric LiNbO₃ crystals,” *Phys. Status Solidi Appl. Mater. Sci.*, vol. 209, no. 1, pp. 176–180, 2012, doi: 10.1002/pssa.201127361.
- [256] K. A. Curtis, D. Miller, P. Millard, S. Basu, F. Horkay, and P. L. Chandran, “Unusual Salt and pH Induced Changes in Polyethylenimine Solutions,” *PLoS One*, vol. 11, no. 9, p. e0158147, 2016, doi: 10.1371/journal.pone.0158147.
- [257] Y. W. Naguib and Z. Cui, *Nanomedicine: The Promise and Challenges in Cancer Chemotherapy*, vol. 811. Dordrecht: Springer, 2014. doi: 10.1007/978-94-017-8739-0.
- [258] T. Pham, J. B. Jackson, N. J. Halas, and T. R. Lee, “Preparation and characterization of gold nanoshells coated with self-assembled monolayers,” *Langmuir*, vol. 18, no. 12, pp. 4915–4920, 2002, doi: 10.1021/la015561y.
- [259] Z. Liu *et al.*, “Synthesis of polyethylenimine (PEI) functionalized silver nanoparticles by a hydrothermal method and their antibacterial activity study,” *Mater. Sci. Eng. C*, vol. 42, pp. 31–37, 2014, doi: 10.1016/j.msec.2014.05.007.
- [260] A. Sharif, N. Farid, and G. M. O’Connor, “Ultrashort laser sintering of metal nanoparticles: A review,” *Results Eng.*, vol. 16, p. 100731, 2022, doi: 10.1016/j.rineng.2022.100731.
- [261] A. Brown, M. Kai, A. DuRoss, G. Sahay, and C. Sun, “Biodistribution and Toxicity of Micellar Platinum Nanoparticles in Mice via Intravenous Administration,” *Nanomaterials*, vol. 8, no. 6, p. 410, 2018, doi: 10.3390/nano8060410.
- [262] C. Zhang, H. He, and K. ichi Tanaka, “Catalytic performance and mechanism of a Pt/TiO₂ catalyst for the oxidation of formaldehyde at room temperature,” *Appl. Catal. B Environ.*, vol. 65, no. 1–2, pp. 37–43, 2006, doi: 10.1016/j.apcatb.2005.12.010.
- [263] M. Haruta, T. Kobayashi, H. Sano, and N. Yamada, “Novel Gold Catalysts for the Oxidation of Carbon Monoxide at a Temperature far Below 0 °C,” *Chem. Lett.*, vol. 16, no. 2, pp. 405–408, 1987, doi: 10.1246/cl.1987.405.
- [264] M. Singh, P. Weerathunge, P. D. Liyanage, E. Mayes, R. Ramanathan, and V. Bansal, “Competitive Inhibition of the Enzyme-Mimic Activity of Gd-Based Nanorods toward Highly Specific Colorimetric Sensing of l -Cysteine,” *Langmuir*, vol. 33, no. 38, pp. 10006–10015, 2017, doi: 10.1021/acs.langmuir.7b01926.
- [265] J. Hu *et al.*, “A facile label-free colorimetric aptasensor for ricin based on the peroxidase-like activity of gold nanoparticles,” *RSC Adv.*, vol. 5, no. 21, pp. 16036–16041, 2015, doi: 10.1039/C4RA17327A.
- [266] R. Walther *et al.*, “Identification and Directed Development of Non-Organic Catalysts with Apparent Pan-Enzymatic Mimicry into Nanozymes for Efficient Prodrug Conversion,” *Angew. Chemie - Int. Ed.*, vol. 58, no. 1, pp. 278–282, 2019, doi: 10.1002/anie.201812668.

- [267] D. Josephy, T. Eling, and R. Mason, "The Horseradish Peroxidase-catalyzed Oxidation of 3,5,3',5'- Tetramethylbenzidine," *J. Biol. Chem.*, vol. 257, no. 7, pp. 3669–3675, 1982.
- [268] M. Drozd, M. Pietrzak, P. G. Parzuchowski, and E. Malinowska, "Pitfalls and capabilities of various hydrogen donors in evaluation of peroxidase-like activity of gold nanoparticles," *Anal. Bioanal. Chem.*, vol. 408, no. 29, pp. 8505–8513, 2016, doi: 10.1007/s00216-016-9976-z.
- [269] C. Moreno-Castilla, Á. Naranjo, M. Victoria López-Ramón, E. Siles, J. J. López-Peñalver, and J. M. R. de Almodóvar, "Influence of the hydrodynamic size and ζ potential of manganese ferrite nanozymes as peroxidase-mimicking catalysts at pH 4 in different buffers," *J. Catal.*, vol. 414, pp. 179–185, 2022, doi: 10.1016/j.jcat.2022.09.010.
- [270] J. R. Crowther, *The ELISA Guidebook*, vol. 516. Totowa, NJ: Humana Press, 2009. doi: 10.1007/978-1-60327-254-4.
- [271] P. Xiao *et al.*, "Polymeric carbon nitride/mesoporous silica composites as catalyst support for au and pt nanoparticles," *Chem. - A Eur. J.*, vol. 20, no. 10, pp. 2872–2878, 2014, doi: 10.1002/chem.201303741.
- [272] J.-G. You, Y.-W. Liu, C.-Y. Lu, W.-L. Tseng, and C.-J. Yu, "Colorimetric assay of heparin in plasma based on the inhibition of oxidase-like activity of citrate-capped platinum nanoparticles," *Biosens. Bioelectron.*, vol. 92, pp. 442–448, 2017, doi: 10.1016/j.bios.2016.10.082.
- [273] M. M. Schubert, S. Hackenberg, A. C. Van Veen, M. Muhler, V. Plzak, and J. J. Behm, "CO oxidation over supported gold catalysts - 'Inert' and 'active' support materials and their role for the oxygen supply during reaction," *J. Catal.*, vol. 197, no. 1, pp. 113–122, 2001, doi: 10.1006/jcat.2000.3069.
- [274] G. Lopes *et al.*, "Ag-Fe₃O₄ dimer colloidal nanoparticles: Synthesis and enhancement of magnetic properties," *J. Phys. Chem. C*, vol. 114, no. 22, pp. 10148–10152, 2010, doi: 10.1021/jp102311u.
- [275] M. D. Scanlon, P. Peljo, M. A. Méndez, E. Smirnov, and H. H. Girault, "Charging and discharging at the nanoscale: Fermi level equilibration of metallic nanoparticles," *Chem. Sci.*, vol. 6, no. 5, pp. 2705–2720, 2015, doi: 10.1039/c5sc00461f.
- [276] S. M. Kim, H. Lee, and J. Y. Park, "Charge Transport in Metal–Oxide Interfaces: Genesis and Detection of Hot Electron Flow and Its Role in Heterogeneous Catalysis," *Catal. Letters*, vol. 145, no. 1, pp. 299–308, 2015, doi: 10.1007/s10562-014-1418-y.
- [277] H. Niu, Y. Zheng, S. Wang, L. Zhao, S. Yang, and Y. Cai, "Continuous generation of hydroxyl radicals for highly efficient elimination of chlorophenols and phenols catalyzed by heterogeneous Fenton-like catalysts yolk/shell Pd@Fe₃O₄@metal organic frameworks," *J. Hazard. Mater.*, vol. 346, pp. 174–183, 2018, doi: 10.1016/j.jhazmat.2017.12.027.
- [278] X. Peng, G. Wan, L. Wu, M. Zeng, S. Lin, and G. Wang, "Peroxidase-like activity of Au@TiO₂ yolk-shell nanostructure and its application for colorimetric detection of H₂O₂ and glucose," *Sens. Act. B Chem.*, vol. 257, pp. 166–177, 2018, doi: 10.1016/j.snb.2017.10.146.
- [279] S. Nanda and K. K. Nanda, "Identifying the Accuracy of Various Approaches for Determining the Fraction of Surface Atoms in a Nanoparticle to Deepen Students' Understanding of Size-Dependent Properties," *J. Chem. Educ.*, vol. 98, no. 6, pp. 1982–1987, 2021, doi: 10.1021/acs.jchemed.0c01247.

- [280] H. Jia *et al.*, “Site-Selective Growth of Crystalline Ceria with Oxygen Vacancies on Gold Nanocrystals for Near-Infrared Nitrogen Photofixation,” *J. Am. Chem. Soc.*, vol. 141, no. 13, pp. 5083–5086, 2019, doi: 10.1021/jacs.8b13062.
- [281] W. Chen, S. Li, J. Wang, K. Sun, and Y. Si, “Metal and metal-oxide nanozymes: Bioenzymatic characteristics, catalytic mechanism, and eco-environmental applications,” *Nanoscale*, vol. 11, no. 34, pp. 15783–15793, 2019, doi: 10.1039/c9nr04771a.
- [282] A. Tumuluri, K. Lakshun Naidu, and K. C. James Raju, “Band gap determination using Tauc’s plot for LiNbO₃ thin films,” *Int. J. ChemTech Res.*, vol. 6, no. 6, pp. 3353–3356, 2014.
- [283] L. Zhou, F. Liu, J. Wang, R. Chen, and Y. Chen, “Effects of ligand functionalization on the band gaps and luminescent properties of a Zr₁₂O₁₀-cluster based metal-organic framework,” *CrystEngComm*, vol. 23, no. 16, pp. 2961–2967, 2021, doi: 10.1039/d0ce01843k.
- [284] Y. Zhang *et al.*, “Sensing the charge state of single gold nanoparticles via work function measurements,” *Nano Lett.*, vol. 15, no. 1, pp. 51–55, 2015, doi: 10.1021/nl503782s.
- [285] S. A. Ansari, M. M. Khan, M. O. Ansari, and M. H. Cho, “Gold nanoparticles-sensitized wide and narrow band gap TiO₂ for visible light applications: A comparative study,” *New J. Chem.*, vol. 39, no. 6, pp. 4708–4715, 2015, doi: 10.1039/c5nj00556f.
- [286] D. Reyes-Coronado, G. Rodríguez-Gattorno, M. E. Espinosa-Pesqueira, C. Cab, R. De Coss, and G. Oskam, “Phase-pure TiO₂ nanoparticles: Anatase, brookite and rutile,” *Nanotechnology*, vol. 19, no. 14, p. 145605, 2008, doi: 10.1088/0957-4484/19/14/145605.
- [287] A. W. Dweydari and C. H. B. Mee, “Work function measurements on (100) and (110) surfaces of silver,” *Phys. Status Solidi*, vol. 27, no. 1, pp. 223–230, 1975, doi: 10.1002/pssa.2210270126.
- [288] W. M. H. Sachtler, G. J. H. Dorgelo, and A. A. Holscher, “The work function of gold,” *Surf. Sci.*, vol. 5, no. 2, pp. 221–229, 1966, doi: 10.1016/0039-6028(66)90083-5.
- [289] A. B. Posadas, A. O’Hara, S. Rangan, R. A. Bartynski, and A. A. Demkov, “Band gap of epitaxial in-plane-dimerized single-phase NbO₂ films,” *Appl. Phys. Lett.*, vol. 104, no. 9, pp. 1–6, 2014, doi: 10.1063/1.4867085.
- [290] D. R. Lide, *CRC Handbook of Chemistry and Physics*, vol. 85. Boca Raton: CRC Press, 2016. doi: 10.1201/9781315380476.
- [291] R. R. Nazarewicz, A. Bikineyeva, and S. I. Dikalov, “Rapid and specific measurements of superoxide using fluorescence spectroscopy,” *J. Biomol. Screen.*, vol. 18, no. 4, pp. 498–503, 2013, doi: 10.1177/1087057112468765.
- [292] Y.-M. Wang *et al.*, “Single Nano-Sized Metal–Organic Framework for Bio-Nanoarchitectonics with *In Vivo* Fluorescence Imaging and Chemo-Photodynamic Therapy,” *Nanomaterials*, vol. 12, no. 2, p. 287, 2022, doi: 10.3390/nano12020287.
- [293] A. M. Carmona-Ribeiro and L. D. de Melo Carrasco, “Cationic antimicrobial polymers and their assemblies,” *Int. J. Mol. Sci.*, vol. 14, no. 5, pp. 9906–9946, 2013, doi: 10.3390/ijms14059906.
- [294] L. Wang, C. Hu, and L. Shao, “The antimicrobial activity of nanoparticles: present situation and prospects for the future,” *Int. J. Nanomedicine*, vol. 12, pp. 1227–1249, 2017, doi: 10.2147/IJN.S121956.
- [295] M. Arakha *et al.*, “Antimicrobial activity of iron oxide nanoparticle upon modulation of

- nanoparticle-bacteria interface,” *Sci. Rep.*, vol. 5, pp. 1–12, 2015, doi: 10.1038/srep14813.
- [296] M. Roth *et al.*, “Transcriptomic Analysis of *E. coli* after Exposure to a Sublethal Concentration of Hydrogen Peroxide Revealed a Coordinated Up-Regulation of the Cysteine Biosynthesis Pathway,” *Antioxidants*, vol. 11, no. 4, p. 655, 2022, doi: 10.3390/antiox11040655.
- [297] M. N. Karim *et al.*, “Visible-Light-Triggered Reactive-Oxygen-Species-Mediated Antibacterial Activity of Peroxidase-Mimic CuO Nanorods,” *ACS Appl. Nano Mater.*, vol. 1, no. 4, pp. 1694–1704, 2018, doi: 10.1021/acsanm.8b00153.
- [298] N. R. Asad, L. M. B. O. Asad, C. E. B. de Almeida, I. Felzenszwalb, J. B. Cabral-Neto, and A. C. Leitão, “Several pathways of hydrogen peroxide action that damage the *E. coli* genome,” *Genet. Mol. Biol.*, vol. 27, no. 2, pp. 291–303, 2004, doi: 10.1590/S1415-47572004000200026.
- [299] M. Grundmann, *The Physics of Semiconductors*, 3rd ed. Cham: Springer International Publishing, 2016. doi: 10.1007/978-3-319-23880-7.
- [300] Liu, Tseng, Wang, Dai, and Shih, “The Study of an Ultraviolet Radiation Technique for Removal of the Indoor Air Volatile Organic Compounds and Bioaerosol,” *Int. J. Environ. Res. Public Health*, vol. 16, no. 14, p. 2557, 2019, doi: 10.3390/ijerph16142557.
- [301] S. J. Blanksby and G. B. Ellison, “Bond dissociation energies of organic molecules,” *Acc. Chem. Res.*, vol. 36, no. 4, pp. 255–263, 2003, doi: 10.1021/ar020230d.
- [302] Q. Zhou *et al.*, “TiO₂ as a Nanozyme Mimicking Photolyase to Repair DNA Damage,” *J. Phys. Chem. Lett.*, vol. 13, no. 47, pp. 10929–10935, 2022, doi: 10.1021/acs.jpcclett.2c02717.
- [303] K. Hermann, *Crystallography and surface structure: an introduction for surface scientists and nanoscientists*. Weinheim: John Wiley & Sons, 2017.
- [304] C. Thierfelder, S. Sanna, A. Schindlmayr, and W. G. Schmidt, “Do we know the band gap of lithium niobate?,” *Phys. Status Solidi Curr. Top. Solid State Phys.*, vol. 7, no. 2, pp. 362–365, 2010, doi: 10.1002/pssc.200982473.
- [305] V. Mansfeldova *et al.*, “Work Function of TiO₂ (Anatase, Rutile, and Brookite) Single Crystals: Effects of the Environment,” *J. Phys. Chem. C*, vol. 125, no. 3, pp. 1902–1912, Jan. 2021, doi: 10.1021/acs.jpcc.0c10519.

Appendix

Batch-to-batch synthesis reproducibility

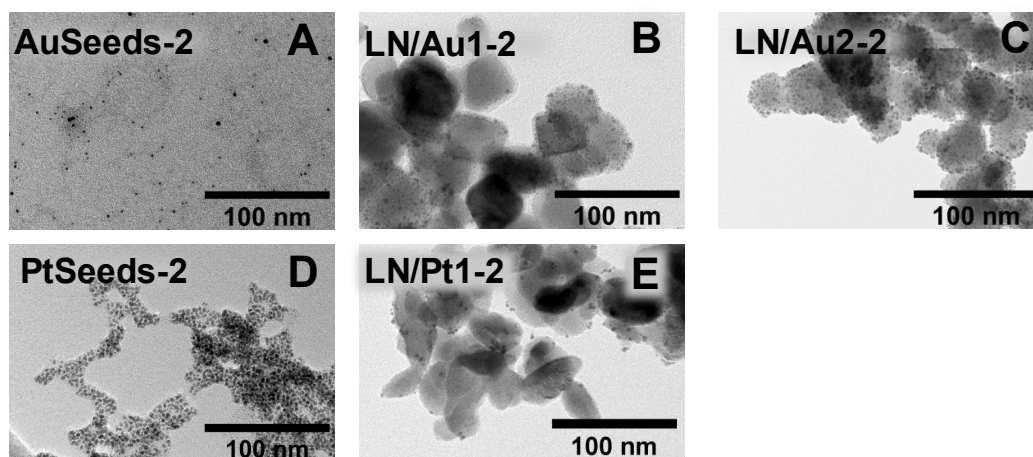


Figure A1. (A) TEM image of an independent batch of AuSeeds. (B) TEM image of independent batch of LN/Au1. (C) TEM image of an independent batch of LN/Au2. (D) TEM image of an independent batch of PtSeeds. (E) TEM image of independent batch of LN/Pt1.

TiO₂ NPs characterization

X-Ray diffractogram (XRD) was obtained using a Bruker D8 X-ray diffractometer in Bragg Brentano configuration with Cu K α radiation (wavelength 1.5405 Å).

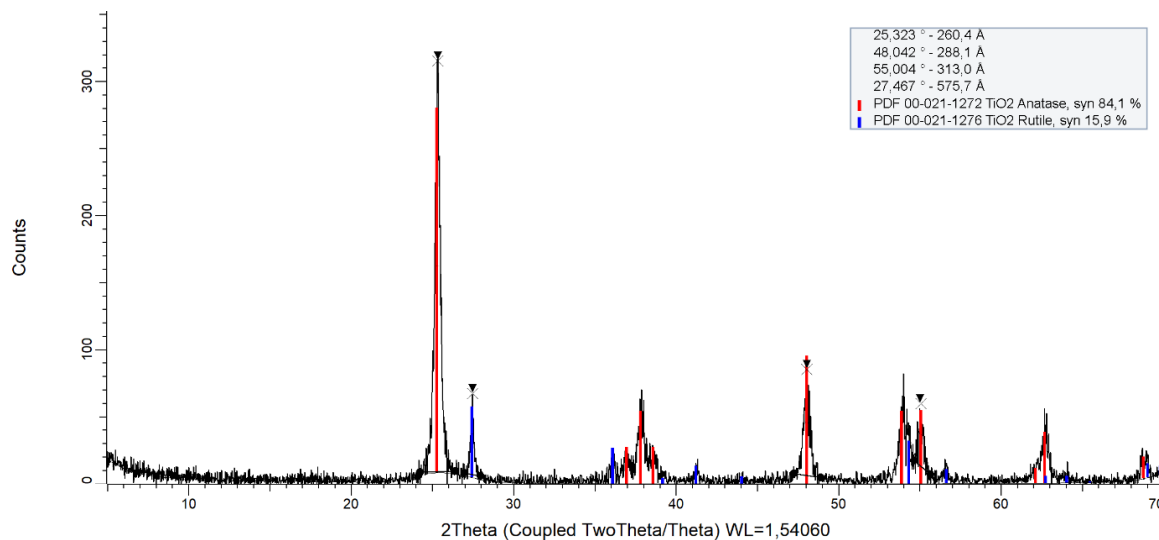


Figure A2. X-Ray diffractogram of commercial TiO₂ (Degussa P25).

TiO₂/Au synthesis for different volume ratios

For the synthesis of TiO₂/Au hybrid NPs, we varied the volumes of the AuSeeds (0.037 g/L) and TiO₂ NPs (0.35 g/L) and we compared the EDS atomic of Ti and Au of the hybrids (**Figure A3**).

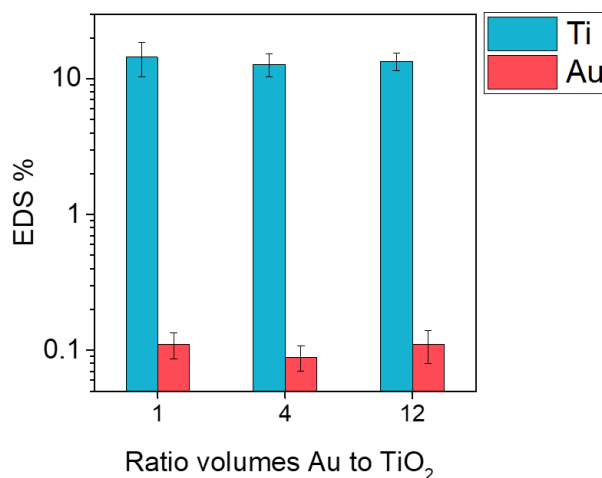


Figure A3. EDS atomic percentage of Ti and Au for three different TiO₂/Au hybrid NPs.

Figure A3 shows that no difference is observed in the loading of Au on TiO₂ when the volume ratio of AuSeeds to TiO₂ is changed.

Calculation of metal seeds in one LN NP

The volume of one LN nanoparticle, one AuSeed and one PtSeed was calculated using the average diameter obtained from TEM images assuming the nanoparticles are spherical. With the bulk density of LiNbO₃ (4.65 g/cm³), Au (19.3 g/cm³) and Pt (21.4 g/cm³), it is then possible to obtain the mass per nanoparticle. Then, we divided the concentration obtained by ICP/AES by the mass of each nanoparticle to obtain the number of nanoparticles per mL. We finally divided the number of metal seeds per mL by the number of LN NPs per ml, obtaining the number of metal seeds per LN NP. The calculations also assumed that all the metal seeds employed in the reaction were bound to LN, as no free metal seeds were observed during TEM imaging.

Number of surface metal atoms calculation

The surface metal atoms calculations follow Nanda et al.'s recommendations [279]. The approach considers that the shell thickness of a nanoparticle with a diameter D corresponds to half of the lattice parameter ($l/2$). The lattice parameter for Au (fcc) and Pt (fcc) is 0.408 nm and 0.392, respectively [303]. Thus, the volume of the core (V_{core}) is:

$$V_{core} = \frac{4}{3}\pi \left(\frac{D}{2} - \frac{l}{2}\right)^3$$

The calculation of the volume of the shell (V_{shell}) is then:

$$V_{shell} = V_{total} - V_{core} = \frac{4}{3}\pi \left(\frac{D}{2}\right)^3 - \frac{4}{3}\pi \left(\frac{D}{2} - \frac{l}{2}\right)^3$$

where V_{total} is the total volume of the nanoparticle.

By dividing the volume of the shell by the volume of the unit cell (V_{cell}), l^3 , one can find the number of unit cells in the shell. Then multiplying by the number of atoms per unit cell (4 in fcc for Au and Pt), n_l , the number of atoms can be estimated. We followed the calculation by multiplying the number of atoms by the number of nanoparticles per litre, obtaining the

concentration of surface atoms per litre. Finally, dividing by Avogadro's number, we get the molar concentration of surface atoms per litre.

Indirect band gaps

For the indirect band gap calculation, there are two linear parts, as shown in **Figure A0.4**, which correspond to the energy of the indirect electron transition ($E_{g,i}$) and the phonon energy (E_p). The lowest energy obtained through extrapolation corresponds to the $E_{g,i}-E_p$ and the highest to the $E_{g,i}+E_p$ [246].

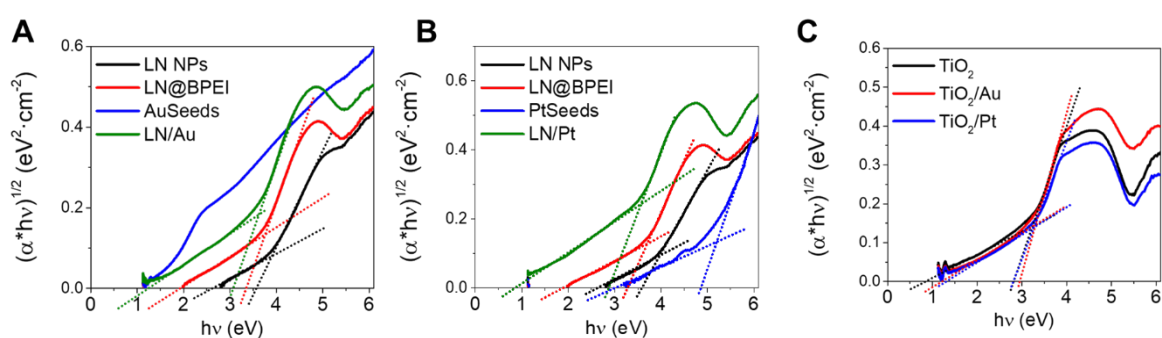


Figure A4. (A) Tauc plot for indirect band gap obtained from the percentage of transmittance of LN (black), LN@BPEI (red), AuSeeds (blue) and LN/Au (green) (B) Tauc plot for indirect band gap (B) obtained from the percentage of transmittance of LN (black), LN@BPEI (red), PtSeeds (blue) and LN/Pt (green). (C) Tauc plot for indirect band gap obtained from the percentage of transmittance of TiO₂ (black), TiO₂/Au (red) and TiO₂/Pt (blue).

Table A1. Indirect band gap energies of the different materials obtained from extrapolation in the Tauc plot.

| Sample | Indirect band gap (eV) |
|----------------------|------------------------|
| LN NPs | 3.11 |
| LN@BPEI NPs | 2.64 |
| AuSeeds | - |
| LN/Au | 2.17 |
| PtSeeds | 4.02 |
| LN/Pt | 1.23 |
| TiO ₂ | 1.86 |
| TiO ₂ /Au | 2.10 |
| TiO ₂ /Pt | 2.12 |

The indirect band gap of LN NPs has an energy of 3.11 eV, which slightly differs from the reported values of 3.48-3.61 eV, although it has been less investigated than the direct transition [304]. The deposition of BPEI produces an energy decrease of the indirect band gaps of 14%. This effect may be caused by the tendency of -NH₂ groups, abundant in BPEI, to donate electrons, causing a shift of LN NPs' valence band [283]. LN/Au indirect band gap is reduced by 30% with respect to LN NPs. In the case of the LN/Pt, the reduction is 60%. The electron transfer and the possible vacancies creation in LN NPs upon metal deposition may explain these results [285].

XPS/UPS characterization of TiO₂, and TiO₂/Au

First, an XPS analysis at room temperature on TiO₂ shows the presence of C 1s, O 1s, and Ti 2p core levels with atomic concentrations reaching 54%, 36%, and 10%, respectively. Subsequently, the combined UPS and XPS study revealed a chemical state of Ti⁴⁺. **Figure A5** highlights the valence of TiO₂ mainly characterized by the O 2p-Ti 3d hybridized band located between 10 eV and 2 eV along with a measured work function approx. 4.4 eV [305] and a maximum valence band of 2.8 eV, privileging thus the anatase phase at the surface [246]. The $V_{B_{max}}$ was calculated by applying the second derivative to the UPS spectrum. All the states in UPS have been calibrated thanks to the reminiscent Fermi level of Ag used as support (**insert Figure A5A**).

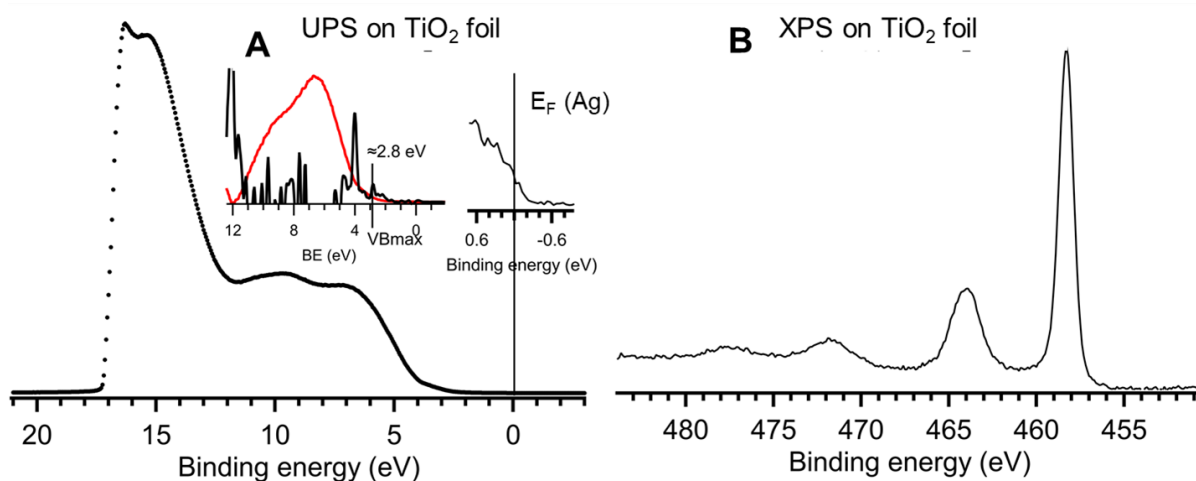


Figure A5. (A) UPS analysis on TiO₂. (insert: Calculation of the V_{bmax} and reminiscent Fermi Level of Ag foil). (B) Ti 2p core level of TiO₂ corresponding to Ti⁴⁺.

Figure A6 shows the UPS and XPS analysis on TiO₂ decorated with gold nanoparticles. XPS revealed a low concentration of gold at the surface, reaching approx. 0.2% in the detection limit. However, the presence of Au(0) was visible with a concentration of 95%. The valence band remains essentially the same as TiO₂ pristine, with no traces of d states of Au. However, its work function decreased to 3.7 eV relative to TiO₂ support. The maximum of the valence band is located at 2.7 eV.

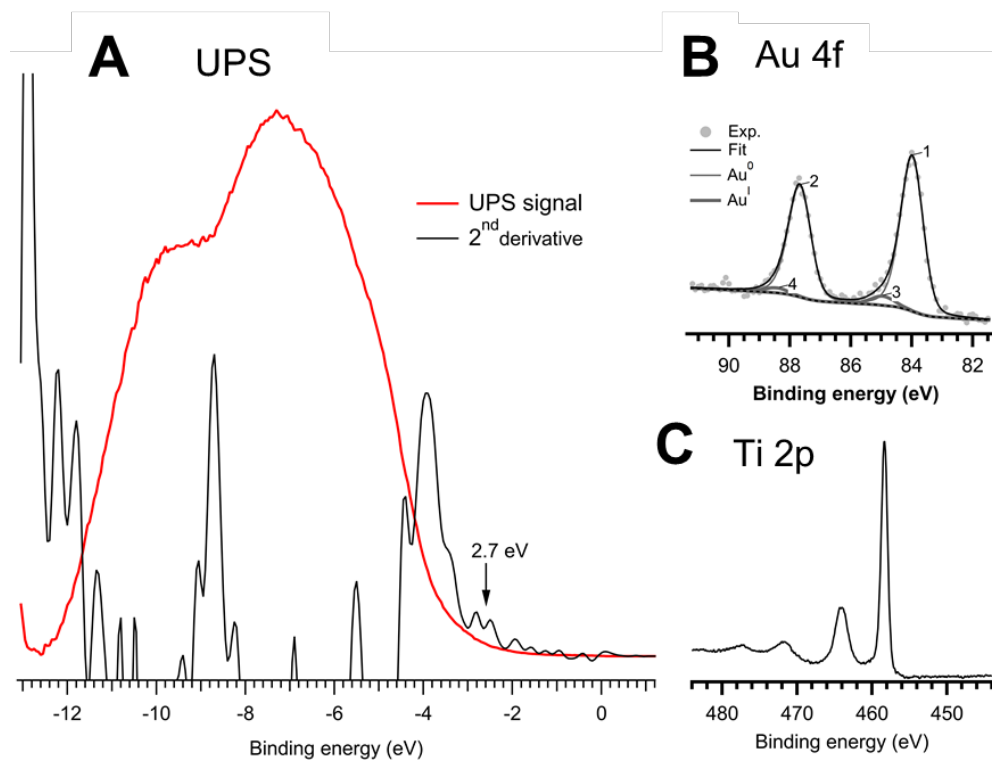


Figure A6. (A) UPS analysis on TiO₂-Au. (insert: Calculation of the VB_{max}). (B) Au 4f core level and (C) Ti 2p core level of TiO₂-Au.

Table A2. Work function ϕ and valence band maximum (VB_{max}) values for the samples determined by XPS/UPS analysis. The absolute energy of the valence band maximum is equal to the sum of VB_{max} relative to the Fermi level and the Ag foil work function (4.2 eV as determined previously).

| Sample | Work function relative to the Fermi level of Ag (eV) | VB _{max} (eV) relative to the Fermi level of Ag |
|----------------------|--|--|
| Ag foil | 4.2 | / |
| Au foil | 5.3 | / |
| TiO ₂ | 4.4 | 2.8 |
| TiO ₂ /Au | 3.7 | 2.5 |

Résumé de la thèse en français

Nanoparticules de niobate de lithium décorées par des germes métalliques pour la réalisation de Nanozymes hybrides mimant une activité biologique

Introduction

Les Nanozymes sont des nanomatériaux qui miment le comportement des enzymes naturelles et offrent plusieurs avantages par rapport à elles : un coût moins élevé, une plus grande surface spécifique, une grande variété de forme, taille, nature de matériaux, fonctionnalisation de surface et également la possibilité de moduler leurs propriétés physiques sous l'effet de stimuli externes, comme par exemple une excitation lumineuse. De nombreuses applications dans le domaine de l'environnement et des biotechnologies sont donc envisagées à partir des Nanozymes. Parmi elles, on peut citer les biocapteurs à base de Nanozymes, permettant par exemple de se substituer aux tests type ELISA, et l'effet thérapeutique des Nanozymes grâce à leur possibilité d'augmenter ou d'inhiber la production d'espèces réactives oxydantes (ROS).

Les Nanozymes à base de métaux nobles sont des candidats intéressants pour ce type d'applications, grâce à leur synthèse bien maîtrisée, la possibilité de les fonctionnaliser facilement et leurs différentes activités enzymatiques (peroxydase, oxydase, catalase et dismutase). Cette activité enzymatique dépend fortement de la taille des nanoparticules (elle est fortement améliorée pour des diamètres inférieurs à 5 nm) et de leur état d'agrégation. Pour limiter l'agrégation, les nanoparticules métalliques peuvent être déposées à la surface d'oxydes métalliques. Ceci permet également, grâce aux propriétés semi-conductrices des oxydes métalliques, de produire un effet synergétique sur les propriétés catalytiques grâce à un transfert de charge amélioré, une stabilisation de la structure de bandes et la création de défauts.

Dans ce travail de thèse, nous avons utilisé le niobate de lithium (LiNbO_3 ou LN) en tant qu'oxyde métallique, en combinaison avec des germes métalliques d'or et de platine. Lors de travaux précédents, la synthèse de ces nanoparticules hybrides avait été réalisée à l'aide de polyéthylèneimine branché (BPEI) en tant que lien chimique entre les deux composants. Nous

souhaitons ici montrer que ces nanoparticules hybrides ont des propriétés en tant que Nanozymes et que la combinaison du LN et des métaux nobles permet d'obtenir un effet catalytique synergétique. Enfin, nous nous intéresserons à leur capacité à produire ou à inhiber les ROS.

Le **Chapitre 1** présente les concepts de base sur les Nanozymes et les avantages des Nanozymes métalliques. Nous introduisons également le principe théorique de l'effet catalytique synergétique entre les métaux et les oxydes métalliques, ainsi que son effet sur l'activité enzymatique. Enfin, nous présentons l'état de l'art sur les Nanozymes métalliques et leur capacité à amplifier ou à inhiber la production de ROS en vue d'applications thérapeutiques. Une attention spécifique est portée sur les Nanozymes hybrides métal-oxyde métallique et leur interaction avec la lumière. Enfin, les objectifs de la thèse sont présentés.

Le **Chapitre 2** donne un aperçu des différentes techniques de caractérisation utilisées dans ce travail. Les techniques pour la caractérisation des nanoparticules sont la microscopie électronique en transmission, la diffusion dynamique de la lumière, la zétamétrie, la spectroscopie d'absorption UV-Visible et la spectrométrie à plasma à couplage inductif. Les techniques pour la caractérisation de l'activité des Nanozymes et l'élucidation de leur mécanisme catalytique sont la spectroscopie UV-Visible, la spectroscopie de fluorescence et la spectroscopie de photoélectrons X et UV. Enfin, l'interaction des nanoparticules avec les bactéries est étudiée par mesure de densité optique.

Le **Chapitre 3** présente la synthèse et la caractérisation des nanoparticules hybrides. Tout d'abord, nous détaillons les protocoles de synthèse des blocs de construction de départ, c'est-à-dire les nanoparticules de LN, de LN@BPEI (nanoparticules de LN fonctionnalisées par le BPEI) et des germes métalliques. Puis la synthèse des nanoparticules hybrides est présentée. La caractérisation des nanoparticules est enfin discutée en termes de taille et de propriétés colloïdales.

Le **Chapitre 4** concerne l'optimisation de l'activité enzymatique des nanoparticules hybrides. Des paramètres tels que le substrat, le pH et la température sont étudiés et ajustés. L'activité peroxydase des Nanozymes est démontrée et comparée à celle des composants isolés. Ensuite, le modèle de Michaelis-Menten valable pour les enzymes naturelles est vérifié et comparé pour les Nanozymes hybrides et les germes métalliques. Enfin, une tentative d'élucidation du

mécanisme catalytique est proposée à l'aide d'une étude de la structure de bandes, de tests catalytiques supplémentaires et de tests de capture de ROS.

Le **Chapitre 5** se concentre sur l'étude de la croissance bactérienne en présence des Nanozymes et du stress oxydatif induit par l'eau oxygénée et par la lumière UV. La croissance bactérienne est d'abord étudiée seulement en présence des Nanozymes puis après ajout de quantités optimisées d'eau oxygénée et d'une irradiation UV. Enfin, l'effet résultant de la combinaison de ces deux sources de stress oxydatif en présence des Nanozymes est étudié.

Chapitre 1 : Etat de l'art

1.1. Enzymes artificielles : Nanozymes

Les enzymes sont définies par l'IUPAC comme des macromolécules, principalement des protéines, qui augmentent la vitesse d'une réaction biochimique d'un facteur pouvant atteindre 10^{14} par rapport à la réaction non catalysée. Généralement une enzyme catalyse une seule réaction spécifique et fonctionne avec un seul type de substrat spécifique. Elles sont utilisées à l'échelle industrielle dans de nombreux domaines (pharmacie, agro-alimentaire, bio-carburants par exemple). Il existe cependant quelques inconvénients à leur utilisation : coût élevé, conditions physiologiques, faible stabilité, stockage seulement à court terme, impossibilité de changer de substrat ainsi que leur nombreuses étapes de purification. Ainsi la fabrication d'enzymes artificielles ne présentant pas ces limitations représente un intérêt considérable.

Les Nanozymes peuvent être définis comme des matériaux organiques ou inorganiques avec au moins une de leur dimension comprise entre 1 et 100 nm, et possédant une capacité intrinsèque leur permettant de catalyser des réactions biochimiques selon le même mécanisme (cinétique de Michaelis-Menten) que les enzymes naturelles. Leurs avantages par rapport aux enzymes naturelles sont les suivants : faible coût, grande stabilité, stockage possible à long terme, facilité de fabrication et meilleure résistance aux différents milieux dans lesquels ils sont dispersés. De plus, leur activité et leur sélectivité peut être ajustée en fonction de leur nanostructure. Enfin, les Nanozymes peuvent avoir une activité enzymatique multiple, les rendant plus versatile, et leurs propriétés physico-chimiques particulières peuvent être utilisées pour réguler l'activité enzymatique et diversifier leurs applications.

Comme les enzymes, les Nanozymes peuvent être classées selon le type de réaction qu'ils catalysent. L'activité peroxydase est la plus courante pour les Nanozymes. Cette réaction implique l'eau oxygénée en tant qu'oxydant et un substrat en tant que réducteur. Pour mettre en évidence cette réaction on utilise un substrat qui se colore lorsqu'il est oxydé. L'activité catalase, qui consiste en la décomposition de H_2O_2 en O_2 est aussi fréquemment observée pour les Nanozymes. Enfin, certains Nanozymes possèdent une activité type oxydase, c'est-à-dire qu'ils catalysent l'oxydation d'un substrat en présence de O_2 .

Le modèle de Michaelis-Menten permet de déterminer la cinétique enzymatique, notamment la vitesse maximale V_{max} et la constante K_m , liée à l'affinité de l'enzyme pour son substrat. Dans le cas des Nanozymes, ce modèle doit être appliqué avec précaution car les Nanozymes sont moins flexibles en termes de conformation des molécules au niveau du site actif que les enzymes naturelles.

Les Nanozymes de métaux nobles ont une activité enzymatique modulable grâce à leurs différentes caractéristiques présentées sur la Figure 1.

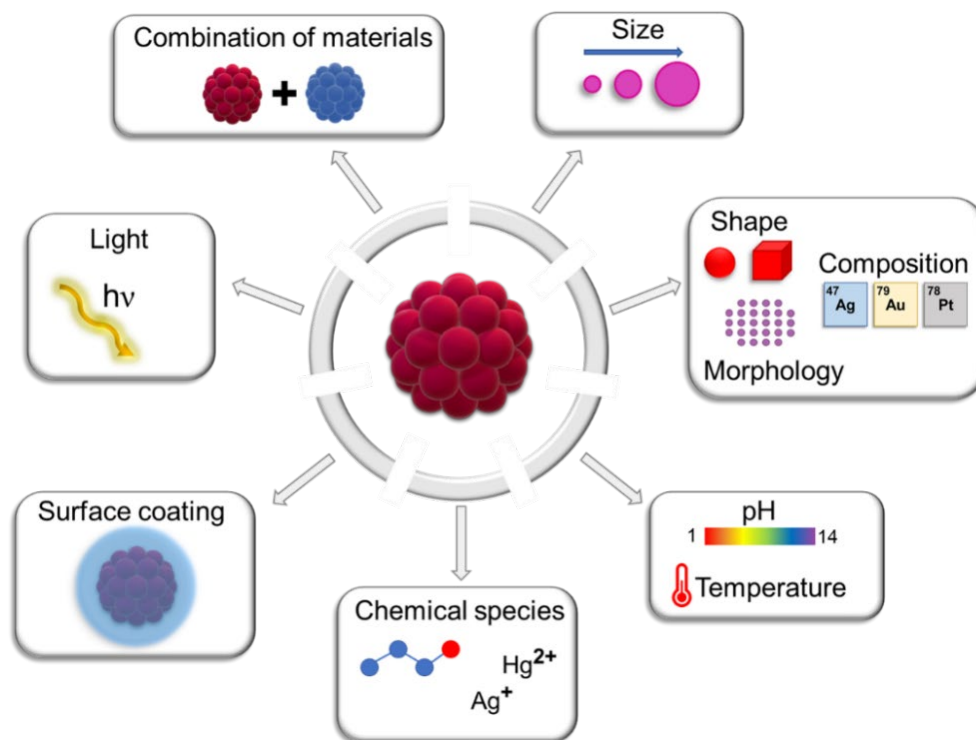


Figure 1. Différentes manières de modifier l'activité enzymatique de Nanozymes métalliques.

En particulier, l'action de la lumière sur l'activité catalytique est une caractéristique spécifique des Nanozymes de métaux nobles à cause de leur résonance plasmon localisée qui entraîne une

absorption de la lumière dans le domaine UV-Visible. Enfin, différentes études ont montré que la combinaison de matériaux différents permettait d'augmenter l'activité catalytique. Nous allons maintenant nous intéresser à l'effet de germes métalliques combinés à des nanoparticules d'oxyde métallique.

Cette combinaison fait apparaître une jonction métal-semiconducteur (oxyde métallique) qui facilite le transfert de charge ainsi que la création de lacunes d'oxygène. Le transfert de charge amélioré conduit à une diminution de l'énergie d'activation tandis que la création de lacunes permet une meilleure adsorption des réactifs. Ces effets peuvent être amplifiés sous l'action de la lumière (photocatalyse), en produisant des électrons de haute énergie à cause de l'excitation du plasmon du métal.

De nombreux exemples dans la littérature montrent l'intérêt de Nanozymes hybrides métal-oxyde métallique pour obtenir un effet catalytique synergétique. Plusieurs hypothèses sont proposées pour expliquer leur mécanisme catalytique, comme par exemple la formation de ROS intermédiaires du type $\text{OH}\cdot$, $^1\text{O}_2$ et $\text{O}_2\cdot^-$ qui favorisent l'oxydation du substrat dans le cas de l'activité peroxydase.

Les nanostructures hybrides combinant un métal et oxyde métallique sont variées. Parmi elles, on peut citer les dimères, les particules type Janus, les cœur-coquilles et la décoration par des germes. Cette dernière nanostructure, que nous avons sélectionné dans ce travail, présente plusieurs avantages : une minimisation de l'agrégation des nanoparticules métalliques, une grande surface spécifique et une grande densité de jonctions métal-oxyde métallique. Plusieurs méthodes permettent de synthétiser des nanostructures de ce type (Figure 2).

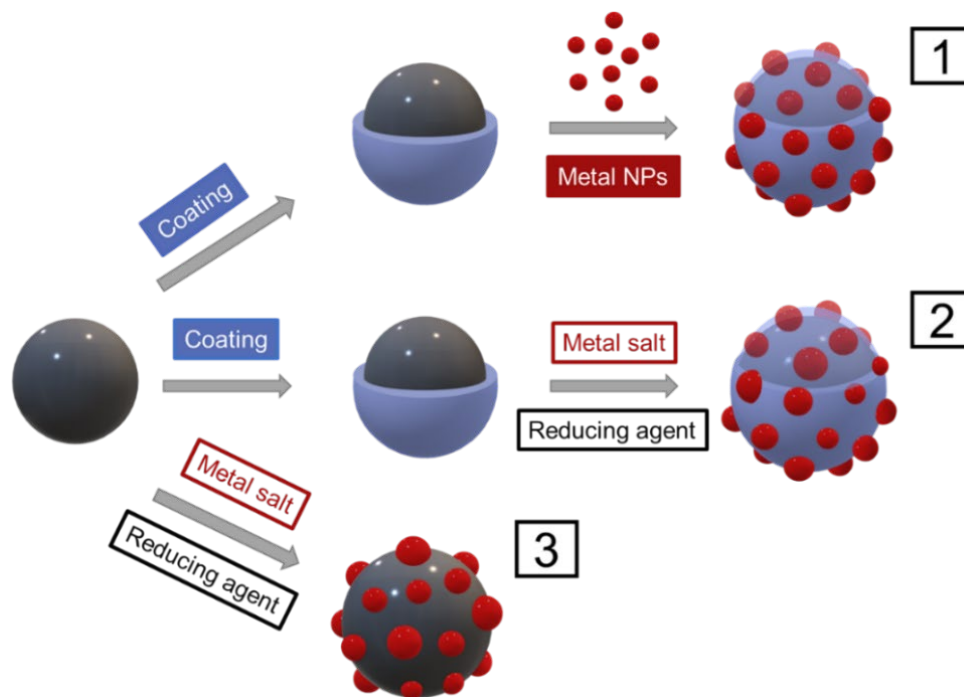


Figure 2. Différentes approches pour synthétiser des nanoparticules hybrides par décoration de germes.

La méthode 1 consiste dans le dépôt d'une couche d'accroche sur le cœur d'oxyde métallique permettant d'immobiliser ensuite les germes métalliques. La méthode 2 démarre de la même manière mais une réaction de réduction est utilisée pour faire croître les germes métalliques sur l'oxyde. Enfin la méthode 3 utilise aussi cette méthode de réduction mais sans couche d'accroche. Nous avons sélectionné ici la méthode 1 qui permet un meilleur contrôle en taille et en forme des nanoparticules afin de mieux pouvoir mettre en évidence l'effet synergétique en comparant avec les matériaux de départ séparés.

Dans ce travail de thèse, nous nous intéressons plus particulièrement aux nanoparticules hybrides LN/Métal. Les nanoparticules de LN présentent de nombreuses propriétés notamment en optique non linéaire mais également en tant que semiconducteur et matériau ferroélectrique. Ces deux dernières propriétés favorisent la séparation des charges et l'adsorption d'espèces sous l'effet de la polarisation, ce qui rend ces nanoparticules potentiellement intéressantes en catalyse et en photocatalyse. Ici ces nanoparticules ont été préparés par une méthode solvothermale. Quant aux germes métalliques, ils sont synthétisés par la réduction de sels de ces métaux.

1.2. Génération d'espèces réactives oxydantes par les Nanozymes

Dans la littérature, on trouve trois effets principaux faisant intervenir les Nanozymes, les ROS et les organismes vivants : une production augmentée, une inhibition ou une régulation des ROS (Figure 3).

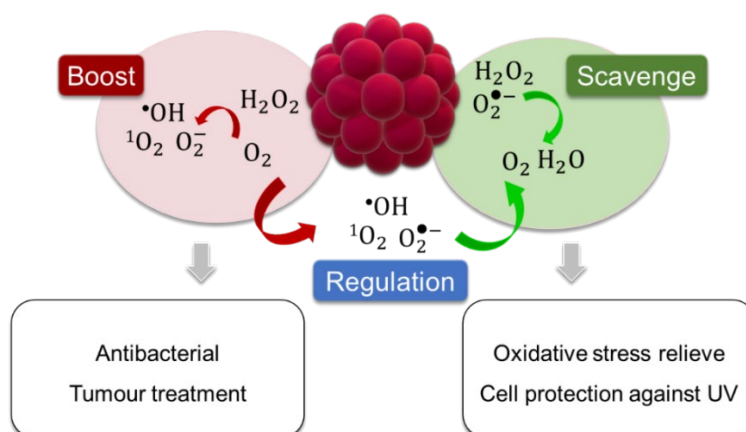


Figure 3. Exemples de réactions faisant intervenir des ROS et des Nanozymes et applications biomédicales associées.

Ces effets sont associés à différentes applications biomédicales. Ainsi, la production augmentée de ROS entraîne la destruction et la mort cellulaire, ce qui permet d'élaborer des agents antimicrobiens et des thérapies anti-tumorales. L'inhibition est quant à elle utilisée pour les thérapies anti-oxydantes pour protéger les cellules de l'excès de ROS produits dans l'organisme, par exemple pour éviter la dégradation des neurones dans le cas de maladies neuro-dégénératives, ou pour éviter le stress généré par des agents externes (blessures, polluants par exemple).

Au vu de cet état de l'art, les objectifs de ce travail de thèse sont les suivants :

- Maîtriser la synthèse des nanoparticules hybrides LN/Métal ;
- Tester et optimiser l'activité enzymatique de ces nanoparticules ;
- Mettre en évidence l'effet catalytique synergétique ;
- Comparer l'activité selon la nature du métal ajouté sur LN ;
- Elucider le mécanisme catalytique synergétique ;
- Tester l'effet des Nanozymes sur des bactéries ;
- Etudier cet effet en présence de conditions de stress oxydant (ajout de H_2O_2 et irradiation UV).

Chapitre 2 : Techniques de caractérisation

La **microscopie électronique en transmission (TEM)** a été utilisée pour caractériser la taille et la forme des nanoparticules. Cette technique est basée sur l'interaction entre des électrons émis par une source portée à une haute tension (> 100 kV) et la matière. Elle fournit des images de l'échantillon avec une précision inférieure au nanomètre. Dans ce travail, le microscope utilisé est un JEOL-2100HT muni d'une source LaB_6 portée à 200 kV. Les images TEM ont été analysées à l'aide du logiciel ImageJ.

En complément, pour avoir accès à la composition chimique, nous avons utilisé la **spectroscopie de rayons X à dispersion d'énergie (EDX/EDS)**. Cette technique permet une caractérisation des éléments chimiques d'un échantillon en analysant la fluorescence X émise par ces éléments sous excitation électronique. Elle n'est cependant pas adaptée aux éléments légers et ne permet pas l'analyse de traces. Dans ce travail, la spectroscopie EDX a été réalisée pendant les mesures TEM avec un détecteur EDX XMAX en silicium en focalisant le faisceau d'électrons sur différentes régions de l'échantillon. Des cartographies chimiques ont également été obtenues avec un microscope TITAN ETEM FEI. Le logiciel Aztec (Oxford Instruments) a été utilisé pour l'analyse des spectres.

La **diffusion dynamique de la lumière (DLS)** utilise les fluctuations de l'intensité lumineuse diffusée par des particules en solution soumises au mouvement Brownien. Ces fluctuations permettent de déterminer le coefficient de diffusion des particules qui est lié au à leur rayon hydrodynamique. La conversion de la distribution des intensités mesurées en distribution en nombre ou en volume de particules est basée sur la théorie de Mie qui suppose que les particules sont sphériques, homogènes et que leurs propriétés optiques sont connues. Dans ce travail, un appareil Malvern Nanoseries Zetasizer ZS a été utilisé. Les mesures ont été réalisées à un angle de rétrodiffusion de 173° .

La **vélocimétrie laser combinée à l'électrophorèse** permet d'extraire le potentiel zeta, en déterminant la vitesse de migration des particules soumise à un champ électrique. Autour d'une particule dispersée en milieu liquide se forme une double couche électrique composée de la couche de Stern, constituée de charges opposées à la charge de surface de la particule, suivie de la couche diffuse dans laquelle les espèces chargées sont moins liées à la particule. Le potentiel zeta est le potentiel électrique mesuré au niveau d'un plan appelé plan de cisaillement situé dans la couche diffuse qui sépare la région du liquide mobile et la région du liquide qui

reste attachée à la particule. Dans ce travail, un appareil Malvern Nanoseries Zetasizer ZS a été utilisé avec des cuves capillaires munies d'électrodes en or pour appliquer le champ électrique.

La **spectrométrie à plasma à couplage inductif (ICP-AES)** est une technique de quantification élémentaire basée sur la digestion acide de l'échantillon et l'injection de la solution résiduelle dans un plasma. L'interaction des atomes de l'échantillon avec les particules chargées du plasma provoque des pertes d'électrons et des recombinaisons entraînant l'émission d'un rayonnement caractéristique des éléments présents. Les concentrations détectables sont de l'ordre du $\mu\text{g/L}$. Les appareils utilisés sont ceux du laboratoire CREALINS de Lyon, ICP-AES ICAP 6300 et ICAP 6500 de Thermofisher Scientific. Le milieu de digestion acide utilisé est composé de 4% de H_2SO_4 , 4% de HNO_3 et 4% de HCl .

La **spectroscopie d'absorption UV-Visible** a été utilisée dans ce travail : 1) pour caractériser les propriétés plasmoniques des nanoparticules, 2) pour étudier leur activité catalytique, 3) pour déterminer leur bande interdite et 4) pour mesurer la croissance bactérienne. Cette technique de caractérisation optique permet d'étudier les transitions entre les niveaux d'énergie électronique de molécules en solution sous excitation lumineuse. L'absorbance mesurée est reliée à la concentration par la loi de Beer-Lambert. Dans le cas des nanoparticules, il faut également tenir compte de la diffusion de la lumière. Le spectre mesuré correspond donc au spectre d'extinction, qui tient compte de l'absorption et de la diffusion. Le type d'appareil utilisé pour chaque caractérisation est résumé dans le Tableau 1.

Tableau 1. Résumé des appareils utilisés pour la spectroscopie d'absorption UV-Visible.

| Objectifs | Interaction lumière-matière | Loi physique appliquée | Technique utilisée | Type d'appareil |
|-------------------------|------------------------------------|-------------------------------|---------------------------|--|
| Activité catalytique | Absorption | Beer-Lambert | Transmission | Lecteur de plaques UV-Vis |
| Croissance bactérienne | Diffusion | Beer-Lambert | Transmission | Lecteur de plaques UV-Vis |
| Propriétés plasmoniques | Absorption, diffusion | | Transmission | Spectrophotomètre UV-Vis standard |
| Bande interdite | Absorption | Tauc | Transmission | Spectrophotomètre UV-Vis muni d'une sphère d'intégration |

Les **spectroscopies de photoélectrons X (XPS) et UV (UPS)** sont basées sur l'interaction entre un rayonnement X ou UV et la surface de l'échantillon. Lors de la photo-excitation, des photoélectrons provenant des différents niveaux d'énergie des éléments chimiques contenus dans l'échantillon sont émis. Il est possible de mesurer leur énergie cinétique et d'en déduire leur énergie de liaison. Dans le cas de la spectroscopie XPS, les photoélectrons sont issus des niveaux de cœur, tandis qu'en spectroscopie UPS, ils proviennent des niveaux de valence. Dans ce travail, les analyses ont été réalisées à l'IRCELYON à l'aide d'un spectromètre Kratos muni d'une source de rayons X $AlK\alpha$ à 1486,6 eV et d'une source UV He I à 21,2 eV.

La **spectroscopie de fluorescence** a été utilisée pour caractériser la production ou l'inhibition de ROS à l'aide de substrats produisant un changement de l'émission de fluorescence. Dans ce travail, les mesures ont été réalisées à l'aide d'un lecteur de plaques CLARIOstar (BMG Labtech).

Chapitre 3 : Synthèse et caractérisation des Nanozymes hybrides

Dans ce chapitre, nous détaillons le protocole de synthèse (Figure 4) et les caractérisations structurales des nanoparticules hybrides composées de $LiNbO_3$ et germes d'or (LN/Au) et $LiNbO_3$ et germes de platine (LN/Pt). Une tentative a également été réalisée avec des germes d'argent. Enfin, des nanoparticules de TiO_2/Au et TiO_2/Pt ont également été élaborées.

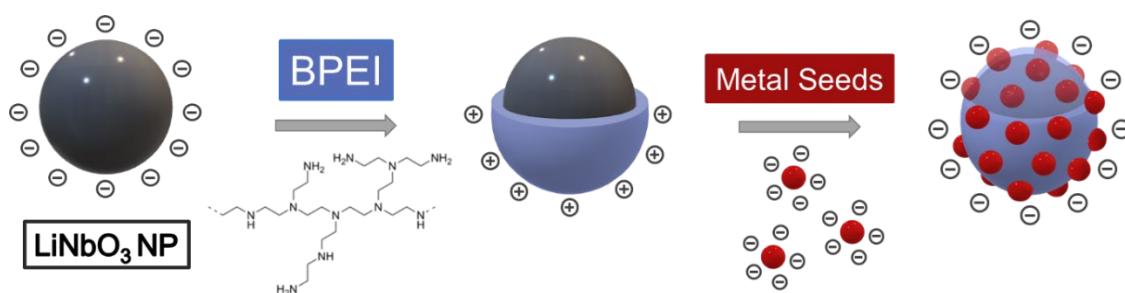


Figure 4. Synthèse des nanoparticules LN/Métal par la méthode de décoration de germes.

3.1. Matériels et méthodes

Les nanoparticules de LN ont été synthétisées au laboratoire SYMME d'Annecy par un procédé solvothermal en faisant réagir l'éthoxyde de lithium niobium en présence de butane-1,4-diol. Les nanoparticules de LN obtenues ont été dispersées dans l'eau à une concentration de 1 g/L. Ensuite le polyéthylèneimine ramifié (BPEI) à 25 kDa a été déposé à la surface des

nanoparticules à 90°C pendant 4 h puis l'excès de BPEI a été éliminé par 4 étapes de centrifugation/lavage dans l'eau à 10°C et 9100g. Puis les nanoparticules résultantes (LN@BPEI) ont été dispersées dans l'eau à 0,35 g/L. Les germes d'or, de platine et d'argent ont été synthétisés par la réduction de sels métalliques par le THPC en milieu basique. Enfin les nanoparticules hybrides ont été élaborées par l'interaction électrostatique de ces germes avec LN@BPEI. Pour les nanoparticules TiO₂/Métal, la synthèse a été réalisée sans BPEI à cause de la charge de surface positive des nanoparticules de TiO₂.

3.2. Résultats et discussion

Le Tableau 2 présente les caractéristiques structurales des nanoparticules de départ permettant de synthétiser LN/Au et LN/Pt.

Tableau 2. Diamètres TEM et hydrodynamique, et potentiel zeta de LN, LN@BPEI et des germes Au et Pt.

| Echantillon | Diamètre TEM (nm) | Diamètre hydrodynamique (nm) | Potentiel zeta (mV) |
|-------------|-------------------|------------------------------|---------------------|
| LN | 30.4 ± 8.6 | 114.2 ± 1.7 | -42.5 ± 0.8 |
| LN@BPEI | 29.6 ± 8.4 | 147.6 ± 2.8 | +39.4 ± 3.6 |
| Germes Au | 2.0 ± 0.8 | 36.0 ± 8.5 | -12.1 ± 6.0 |
| Germes Pt | 3.1 ± 0.6 | 135.7 ± 6.6 | -14.7 ± 2.4 |

Les caractérisations montrent des charges de surfaces opposées pour LN@BPEI et les germes métalliques permettant la formation des nanoparticules hybrides par interaction électrostatique. Plusieurs nanoparticules hybrides LN/Au et LN/Pt ont été élaborées en faisant varier le rapport volumique germes métalliques/LN@BPEI. Les densités croissantes de germes à la surface de LN observées par TEM et mesurées par EDS, sont corrélées avec une diminution progressive du potentiel zeta des nanoparticules hybrides (Tableau 3).

Tableau 3. Diamètres TEM des germes métalliques sur LN@BPEI, diamètre hydrodynamique et potentiel zeta des nanoparticules hybrides et pourcentage molaire en métal des hybrides déterminé par EDS.

| Echantillon | Diamètre TEM des germes métalliques sur LN@BPEI (nm) | Diamètre hydrodynamique des NPs hybrides (nm) | Potentiel zeta des NPs hybrides (mV) | Pourcentage molaire déterminé par EDS (%) |
|-------------|--|---|--------------------------------------|---|
| LN/Au1 | 2.4 ± 0.8 | 233.7 ± 8.6 | $+24.6 \pm 1.0$ | 5.7 (Au) |
| LN/Au2 | 2.5 ± 0.7 | 164.2 ± 0.5 | -28.7 ± 0.3 | 11.2 (Au) |
| LN/Au3 | 3.1 ± 0.8 | 160.5 ± 2.1 | -32.1 ± 0.4 | 16.2 (Au) |
| LN/Pt1 | 2.5 ± 0.6 | 176.4 ± 3.3 | $+23.2 \pm 1.5$ | 3.9 (Pt) |
| LN/Pt2 | 2.5 ± 0.5 | 366.9 ± 2.1 | -12.6 ± 0.5 | 6.8 (Pt) |

Les cartographies chimiques de la Figure 5 obtenues pour les plus fortes densités de germes, confirment la présence des 2 matériaux.

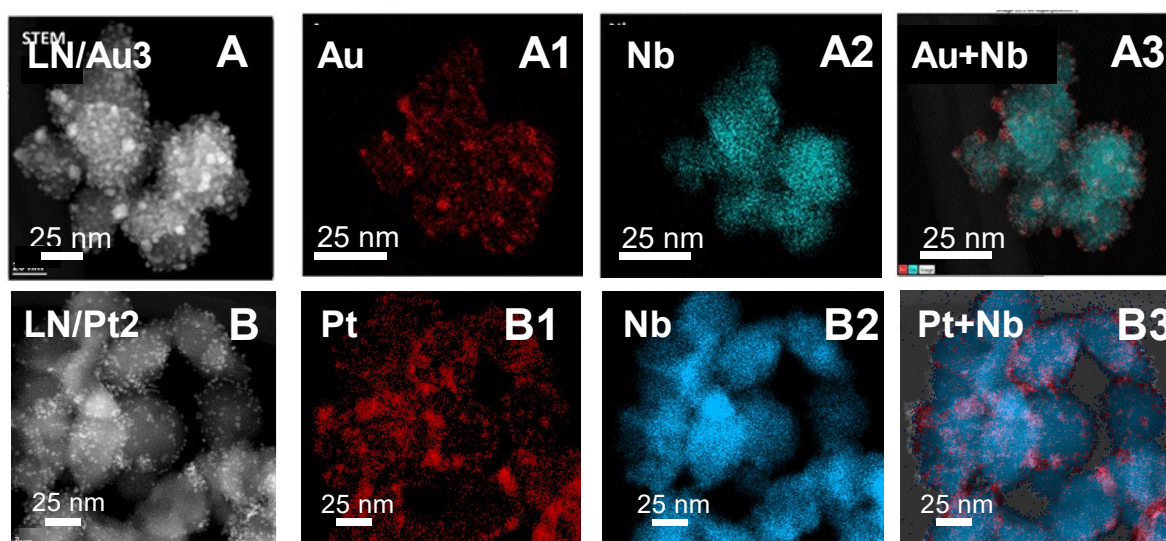


Figure 5. (A, B) Image STEM des nanoparticules hybrides, (A1, A2, B1, B2) cartographies chimiques des éléments Au, Pt et Nb, (A3, B3) tous les éléments chimiques superposés.

A haute résolution au TEM, on observe également la présence de facettes de la famille {111} pour les germes métalliques à la surface de LN/Au et LN/Pt. Le même protocole de synthèse a été testé pour élaborer des nanoparticules LN/Ag. Cependant, l'hétérogénéité en taille et en forme des germes d'argent obtenus ne permet pas de comparer ces hybrides à LN/Au et LN/Pt. Une étude de reproductibilité et de vieillissement a été menée sur LN/Au et LN/Pt montrant

que les différents lots étaient bien similaires et que l'ajout des germes sur LN permettait de diminuer leur coalescence par rapport aux germes isolés. Enfin, les nanoparticules TiO₂/Métal élaborées par simple interaction électrostatique montrent également une charge opposée du TiO₂ par rapport aux hybrides (Tableau 4).

Tableau 4. Diamètre hydrodynamique et potentiel zeta des nanoparticules de TiO₂, TiO₂/Au et TiO₂/Pt.

| Echantillon | Diamètre hydrodynamique (nm) | Potentiel zeta (mV) |
|----------------------|------------------------------|---------------------|
| TiO ₂ | 292.8 ± 20.0 | +20.2 ± 0.2 |
| TiO ₂ /Au | 184.9 ± 2.1 | -21.5 ± 0.1 |
| TiO ₂ /Pt | 261.7 ± 10.8 | -4.97 ± 0.6 |

3.3. Conclusion

Les nanoparticules hybrides LN/Au et LN/Pt présentent une densité contrôlée de germes en surface et des caractéristiques structurales similaires. De plus leur synthèse est reproductible et elles peuvent être stockées sur le long terme. Leurs activités catalytiques pourront donc être étudiées et comparées, ce qui n'est pas le cas des LN/Ag. L'effet de l'oxyde métallique pourra également être étudié à l'aide des nanoparticules hybrides à base de TiO₂.

Chapitre 4: Activité enzymatique peroxydase des nanoparticules LN/Au et LN/Pt. Optimisation et élucidation de leur mécanisme catalytique

4.1. Matériels et méthodes pour la caractérisation de l'activité peroxydase

Un lecteur de plaques UV-Visible Multiskan Go de ThermoFisher a été utilisé pour mesurer l'évolution de l'absorbance au cours du temps lors des réactions catalytiques. L'absorbance a été mesurée à 405, 450 et 650 nm, correspondant respectivement aux 3 substrats colorés, ABTS, OPD et TMB. Le volume total dans chaque puits de la plaque était de 150 µL, la température a été variée de 20 à 45°C et le pH de 2 à 7. Les données ont été analysées à l'aide d'un ajustement non linéaire d'OriginPro 2016. La détermination des bandes interdites a été réalisée par spectroscopie UV-Vis avec une sphère d'intégration en mesurant le pourcentage de transmittance entre 1100 et 200 nm dans des cuvettes de 10, 5 et 1 mm d'épaisseur. Les

ROS ont été mesurées en utilisant les molécules de TA pour la production de $\text{OH}\cdot$ par fluorescence, de DHE pour la production de $\text{O}_2\cdot^-$ par fluorescence et d'ABDA pour la production de $^1\text{O}_2$ par absorbance, dans un lecteur de plaque CLARIOSTAR.

4.2. Optimisation de l'activité peroxydase des nanoparticules LN/Au et LN/Pt

Cette étude a été réalisée avec uniquement les nanoparticules hybrides présentant les densités de germes en surface les plus importantes, LN/Au3 et LN/Pt2, qui seront nommées ici respectivement LN/Au et LN/Pt. Ces densités correspondent à 40 germes d'or par LN et 73 germes de Pt par LN.

Leur activité catalytique peroxydase a d'abord été optimisée en termes de substrat, température et pH. Pour les deux types de nanoparticules, le substrat permettant de maximiser l'activité catalytique est le TMB, la température optimale est de 37°C et le pH optimal de 4 dans un tampon acétate. Aucune activité oxydase n'a été observée pour LN/Au, contrairement au LN/Pt qui présente une activité oxydase non négligeable. Les deux types de nanoparticules hybrides ont également une certaine activité catalase qui se manifeste par l'observation de bulles. Les concentrations optimales en LN/Au et LN/Pt ont également été déterminées, montrant que pour une concentration en Pt 10 fois plus petite qu'en Au, l'activité peroxydase de LN/Pt est 8 fois plus rapide que celle de LN/Au. Enfin, il n'a pas été constaté d'activité due aux ions métalliques isolés restant en solution, que ce soit pour LN/Au ou LN/Pt.

L'effet synergétique des nanoparticules hybrides a ensuite été étudié en comparant leur activité catalytique à celle de leurs composants isolés (Figure 6).

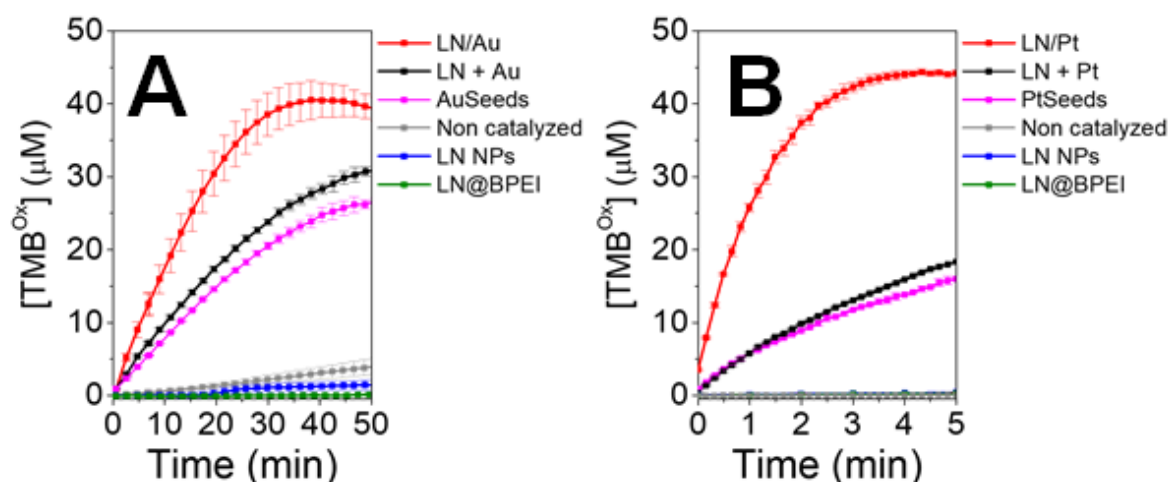


Figure 6. Activités peroxydases de LN/Au (A) et LN/Pt (B) comparées à celles de leurs composants individuels. Les concentrations ont été déterminées par ICP-AES. LN+Au et LN+Pt correspondent à un simple mélange, sans ajout de BPEI.

Il apparaît clairement que les activités de LN/Au et LN/Pt sont supérieures à celles de leurs composants isolés, montrant un effet synergétique qui peut être attribué à un meilleur transfert de charges et à la présence de lacunes d'oxygène. La reproductibilité entre lots est satisfaisante et le stockage à long terme entraîne une légère diminution de l'activité catalytique. Par comparaison avec TiO₂/Au et TiO₂/Pt pour des concentrations identiques en métal, l'activité peroxydase de LN/Au et LN/Pt est supérieure.

4.3. Calcul des paramètres cinétiques enzymatiques

Les paramètres cinétiques enzymatiques ont été déterminés en étudiant l'effet d'une variation des concentrations de H₂O₂ et TMB sur l'activité peroxydase. Les courbes obtenues permettent ainsi, à l'aide du modèle de Michaelis-Menten, de calculer et de comparer les paramètres cinétiques présentés dans le Tableau 5.

Tableau 5. Paramètres cinétiques K_m , V_{max} , K_{cat} et K_{eff} calculés pour LN/Au, les germes Au, LN/Pt et les germes Pt.

| Nanozyme | Substrat | K_m (10^{-3} M) | V_{max} (10^{-8} M·s ⁻¹) | K_{cat} (s ⁻¹) | K_{eff} (M ⁻¹ ·s ⁻¹) |
|----------|-------------------------------|----------------------|---|------------------------------|---|
| LN/Au | H ₂ O ₂ | 20.43 | 4.9 | 5.2×10^{-3} | 26×10^{-2} |

| | | | | | |
|-----------|-------------------------------|-----------------------|------|-----------------------|----------------------|
| | TMB | 3.08×10^{-2} | 3.7 | 3.9×10^{-3} | 128.8 |
| Germes Au | H ₂ O ₂ | 44.26 | 2.8 | 2.1×10^{-3} | 4.7×10^{-2} |
| | TMB | 1.34×10^{-2} | 3.1 | 2.3×10^{-3} | 173.6 |
| LN/Pt | H ₂ O ₂ | 8.81 | 56.1 | 55.9×10^{-2} | 63.5 |
| | TMB | 20×10^{-2} | 97.9 | 97.6×10^{-2} | 5.0×10^4 |
| Germes Pt | H ₂ O ₂ | 12.31 | 3.6 | 3.1×10^{-2} | 2.5 |
| | TMB | 3.82×10^{-2} | 5.9 | 5.1×10^{-2} | 1.3×10^3 |

Ces résultats suggèrent une préférence des Nanozymes pour l'adsorption de TMB par rapport à celle de H₂O₂, avec des valeurs de K_m nettement plus faibles. L'affinité des hybrides pour H₂O₂ est meilleure que celle des germes, tandis qu'un comportement inverse est observé pour TMB, ceci peut être expliqué par son encombrement stérique. La vitesse de la réaction catalytique est toujours plus grande pour les hybrides que pour les germes. Il est à noter aussi que les nanoparticules LN/Pt présentent des valeurs particulièrement élevées de K_{cat} et K_{eff}, ce qui confirme leur effet synergétique remarquable par rapport aux composants isolés.

4.4. Elucidation du mécanisme

Une étude menée en parallèle par UPS/XPS et spectrométrie UV-Visible a permis de déterminer la position des niveaux de Fermi ainsi que les valeurs des bandes interdites, respectivement, pour les différents Nanozymes. Les diagrammes énergétiques de la Figure 7 ont ainsi pu être tracés.

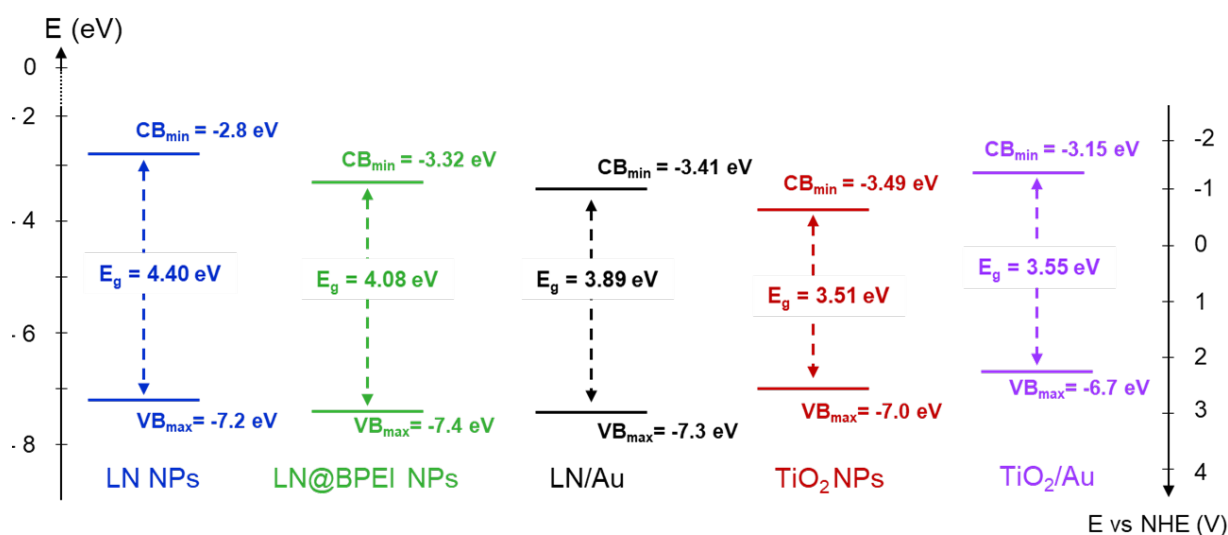


Figure 7. Position des niveaux d'énergies pour les nanoparticules de LN (bleu), LN@BPEI (vert), LN/Au (noir), TiO₂ (rouge) et TiO₂/Au (violet) déterminée à partir des mesures UPS/XPS et UV-Vis.

Ce diagramme montre que la bande interdite de LN/Au est considérablement réduite par rapport à celle de LN, ce qui pourrait favoriser le transfert d'électrons dans les hybrides.

Une étude complémentaire a également été réalisée pour comprendre l'effet du BPEI sur l'activité catalytique. Ainsi des germes d'or et de platine ont été mélangés au BPEI et leur activité peroxydase a été étudiée. Cette étude montre des résultats opposés pour les germes d'or et les germes de platine, et permet uniquement de formuler des hypothèses sur l'effet de la taille des germes (modifiée en présence de BPEI) et des affinités différentes Au-BPEI et Pt-BPEI.

Enfin, la caractérisation de la production de ROS montre que les Nanozymes ne génèrent pas de radicaux OH· ni de radicaux ¹O₂, et même si les germes d'or produisent des radicaux O₂^{·-} de façon significative à partir du O₂ dissout, ce n'est pas le cas pour LN/Au. On peut donc conclure que la production de ROS par LN/Au et LN/Pt reste négligeable.

4.5. Conclusion

Pour conclure, LN/Au et LN/Pt présentent une activité peroxydase avec un effet synergétique, et également une activité catalase, particulièrement pour LN/Pt. Seul LN/Pt présente une activité oxydase. La tentative d'élucidation du mécanisme a essentiellement montré une réduction de la bande interdite pour LN/Au.

Chapitre 5: Production et inhibition d'espèces réactives oxydantes par les Nanozymes et interaction avec les bactéries

5.1. Matériels et méthodes pour la culture bactérienne et la caractérisation des espèces réactives oxydantes

Des monocolonies de la bactérie *E. Coli* ont été sélectionnées et mises en culture. La densité des bactéries est contrôlée par mesure de densité optique (OD) et ajustée de façon à avoir une OD mesurée à 600 nm (OD₆₀₀) égale à 0,05, ce qui correspond à 4×10^7 CFU/mL. Les tests avec les Nanozymes sont réalisés dans une plaque à puits avec un volume total de 150 µL dans chaque puits. Le rayonnement UV choisi est issu d'une lampe UVB à 302 nm. Avant toute mesure, les minimas de cytotoxicité de H₂O₂ et d'irradiation d'UV sont déterminés. La production et l'inhibition des ROS sont mesurées à l'aide des trois sondes, TA, DHE et ABDA, présentées au Chapitre 4.

5.2. Effet des Nanozymes et des nanoparticules sur la croissance de *E. Coli*

Cette première étude montre que toutes les nanoparticules présentent un effet probiotique sur les bactéries. Cependant, la présence de BPEI semble réduire cet effet, ce qui est en accord avec ses propriétés anti-bactériennes en tant que polymère cationique. Le potentiel zeta joue également un rôle sur l'interaction avec les bactéries. Enfin l'effet différent des Nanozymes à base de platine et d'or peut être expliqué par leurs activités enzymatiques différentes.

5.3. Effet des Nanozymes et de H₂O₂ sur la croissance de *E. Coli*

La concentration minimale pour laquelle H₂O₂ présente un effet toxique sur les bactéries se situe entre 1 et 5 mM. Ainsi une concentration de 1 mM a été choisie pour les études suivantes. On constate que les nanoparticules de LN en présence de H₂O₂ induisent une diminution de la croissance bactérienne, ce qui n'est pas observé pour LN@BPEI. L'effet le plus remarquable est obtenu pour LN/Au. Cet effet est également observé pour LN/Pt, les germes Au et les germes Pt (Figure 8). Ajouter H₂O₂ en présence des Nanozymes pourrait donc promouvoir la production de ROS.

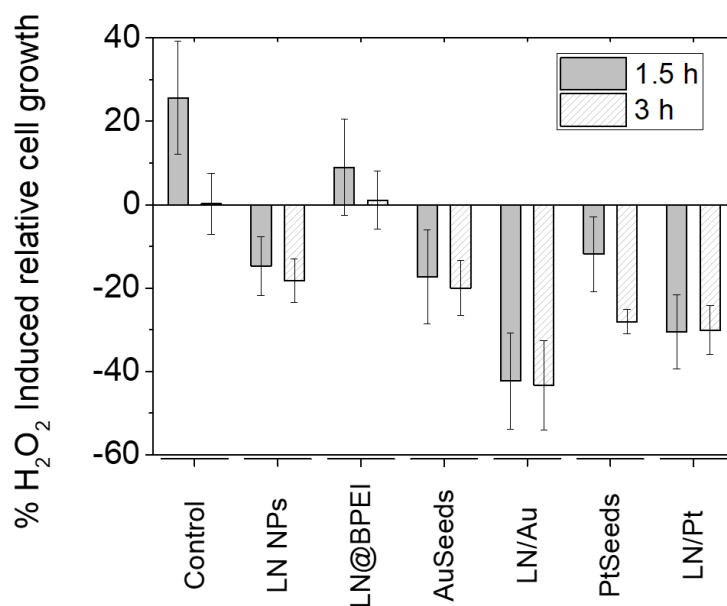


Figure 8. Effet de H₂O₂ sur la croissance bactérienne en présence des différents types de nanoparticules et Nanozymes.

5.4. Effet des Nanozymes et du rayonnement UV sur la croissance de *E. Coli*

L'énergie du rayonnement UV choisi est proche de celle correspondant à la bande interdite des Nanozymes. Un temps d'exposition de 1 min est sélectionné car il n'induit pas de toxicité sur les bactéries. Les résultats montrent qu'en présence des Nanozymes et d'une irradiation UV la croissance bactérienne est favorisée, en particulier pour LN/Pt au bout de 1,5 h après l'exposition. Une étude complémentaire sur la production de ROS dans ces conditions a permis de montrer que LN/Au et LN/Pt limitaient la production de ROS et par conséquent possèdent un effet protecteur vis-à-vis du rayonnement UV.

5.5. Effet des Nanozymes, de H₂O₂ et du rayonnement UV sur la croissance de *E. Coli*

L'effet combiné de H₂O₂ et du rayonnement UV provoque une diminution importante de la croissance bactérienne que ce soit pour LN/Au, LN/Pt, les germes d'or ou les germes de platine (Figure 9).

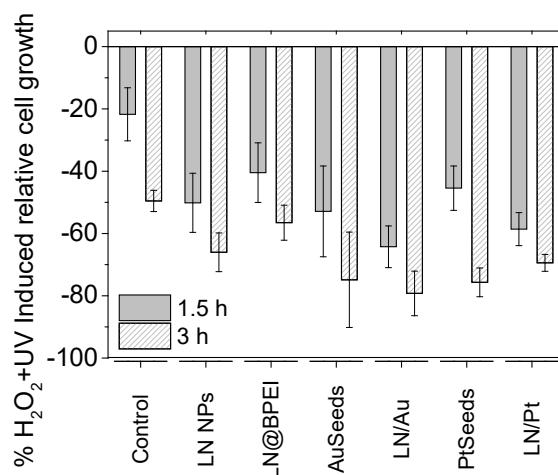


Figure 9. Effet combiné de H₂O₂ et du rayonnement UV sur la croissance bactérienne en présence des différents types de nanoparticules et Nanozymes.

5.6. Effet des traitements par stress oxydatif en fonction du matériau

La comparaison des effets des différents traitements par les nanoparticules et les Nanozymes montre un effet prononcé des nanoparticules à base de platine qui de façon générale, ont tendance à protéger les bactéries, que ce soit seules ou en présence de rayonnement UV. Par contre, les effets combinés de H₂O₂ et de l'UV en présence de LN/Pt ont plutôt tendance à inhiber la croissance bactérienne (Figure 10).

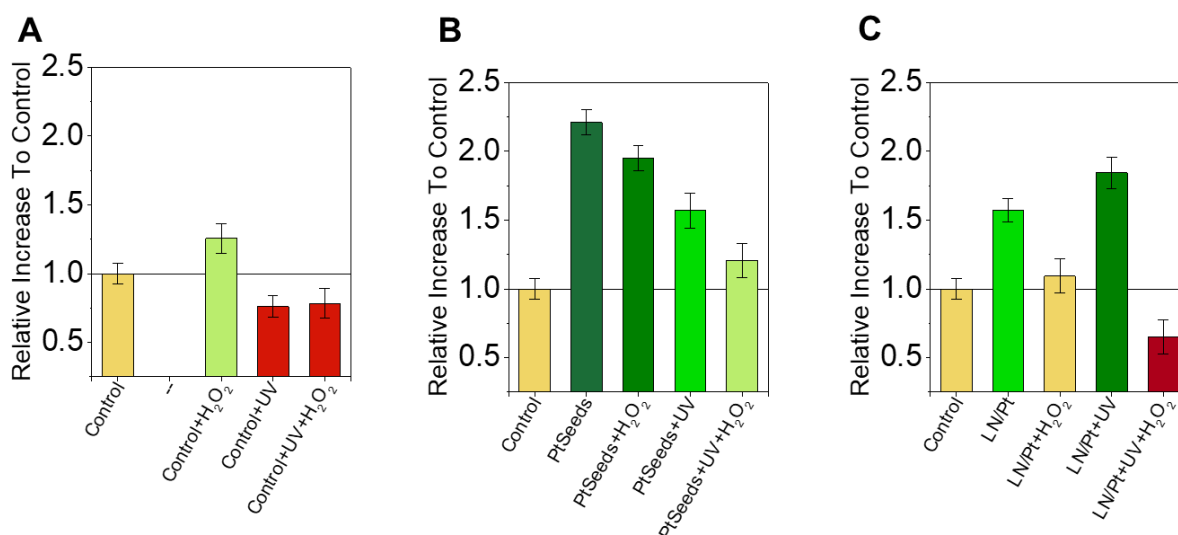


Figure 10. Réponse des bactéries vis-à-vis des différents traitements par les nanoparticules à base de Pt: (A) échantillon de contrôle, (B) échantillon traité par les germes de Pt, (C) échantillon traité par LN/Pt.

5.7. Conclusion

Les résultats présentés dans ce chapitre montrent la versatilité des différents matériaux et des différents stress oxydants pour promouvoir ou inhiber la croissance bactérienne (Tableau 6). LN/Au présente un effet protecteur vis-à-vis du rayonnement UV, et LN/Pt protège non seulement les bactéries mais permet aussi d'amplifier leur viabilité. Ces expériences préliminaires montrent aussi la capacité des Nanozymes pour capturer différents ROS.

Tableau 6. Résumé des pourcentages de croissance bactérienne relative induits par les différents stress oxydants (H₂O₂, UV, H₂O₂+UV) en présence des différentes nanoparticules et Nanozymes.

| NPs ou Nanozymes | Source de stress oxydant | | |
|------------------|-------------------------------|-----|------------------------------------|
| | H ₂ O ₂ | UVB | H ₂ O ₂ +UVB |
| Aucune | +26 | -24 | -22 |
| LN NPs | -15 | -46 | -50 |
| LN@BPEI | +9 | -45 | -40 |
| Germes Au | -17 | -35 | -53 |
| LN/Au | -42 | -19 | -64 |
| Germes Pt | -12 | -29 | -45 |
| LN/Pt | -31 | +17 | -59 |

Conclusions et perspectives

Des Nanozymes hybrides LiNbO₃/Au et LiNbO₃/Pt ont été synthétisés par une méthode basée sur des interactions électrostatiques. Cette méthode a aussi été étendue à des nanoparticules TiO₂/Au et TiO₂/Pt. L'activité peroxydase de ces Nanozymes a été établie et optimisée, et cette activité est reproductible et stable sur le long terme. Les Nanozymes LN/Pt présentent en plus une activité oxydase. L'effet catalytique synergétique de ces Nanozymes a été mis en évidence, et quantifié en calculant les paramètres cinétiques avec le modèle de Michaelis-Menten. Le mécanisme de cet effet synergétique a été étudié par XPS/UPS et UV-Visible, l'effet de l'ajout

de BPEI a permis de formuler différentes hypothèses et l'analyse de la production de ROS a permis d'exclure un mécanisme gouverné par les espèces oxydantes. Enfin, l'étude en présence de bactéries et de stress oxydatifs (H_2O_2 et UV) montre la versatilité des différents Nanozymes pour promouvoir ou inhiber la croissance bactérienne.

Les perspectives de ce sujet sont nombreuses. Actuellement, les propriétés enzymatiques nanohybrides Fe_3O_4/Au , Fe_3O_4/Pt et Fe_3O_4/Pd sont étudiées, ceux-ci présentant, grâce à leurs propriétés magnétiques, une capacité de séparation intéressante. Nous investiguons également l'effet de l'ajout d'autres métaux nobles (Pd) sur LN. En plus des applications thérapeutiques des Nanozymes présentées dans ce manuscrit, on peut envisager aussi d'élaborer des biocapteurs grâce à l'adsorption sur les Nanozymes d'aptamères inhibant leur activité catalytique et capables de la restaurer en présence de la cible biologique. A plus long terme, l'étude de la production de ROS et de la croissance bactérienne devra être poursuivie. Enfin, la possibilité de moduler les propriétés des Nanozymes en fonction de l'excitation lumineuse est attractive, notamment en déplaçant la bande plasmon des Nanozymes vers le proche infrarouge, fenêtre de transparence biologique, permettant d'envisager des applications thérapeutiques *in vivo*.

Metal-seeded lithium niobate nanoparticles as hybrid nanozymes for mimicking bioactivity

Nanozymes are a new class of artificial enzymes, which allow their customization in terms of intrinsic and extrinsic parameters. Among them, metal Nanozymes are well-established nanomaterials which allow easiness of modification and functionalization. Their outstanding properties in catalysis requires a reduced size, but the risk of aggregation increases. To overcome this their deposition onto an oxide is a potent approach, which produces a synergetic catalytic effect and generates a hotspot for catalysis. We synthesized noble-metal lithium niobate nanoparticles with branched-polyethyleneimine as an intermediate linker. Au and Pt nanoseeds were deposited onto LiNbO₃. Then we studied their ability to mimic peroxidase activity using a redox probe and we optimized the conditions to maximize the colorimetric response. The hybrid nanoparticles possess better peroxidase-mimics than the separated counterparts and a simple mixture of them. The Nanozymes were applied to *Escherichia Coli* culture under different sources of oxidative stress, *i.e.*, hydrogen peroxide and ultraviolet light. The hybrid Nanozymes and the separated counterparts cause different response to bacterial growth depending on the source of oxidative stress. Moreover, the hybrid Nanozymes composed of LiNbO₃/AuSeeds and LiNbO₃/PtSeeds protected the bacteria from UV-light induced damage.

Keywords: Hybrid Nanozyme, lithium niobate, noble metal, peroxidase, ROS, synergetic effect.

Nanoparticules de niobate de lithium décorées par des germes métalliques pour la réalisation de Nanozymes hybrides mimant une activité biologique

Les Nanozymes sont une nouvelle classe d'enzymes artificielles, permettant une mise en forme à façon de leurs paramètres intrinsèques et extrinsèques. Parmi eux, les Nanozymes métalliques sont des nanomatériaux facilement modifiables et fonctionnalisables. Leurs remarquables propriétés catalytiques sont dues à leur faible diamètre mais en contre-partie, cette petite taille augmente leur risque d'agrégation. Pour limiter cet effet, leur immobilisation sur un oxyde est une méthode intéressante, qui produit en plus un effet catalytique synergétique et génère des "points chauds" pour la catalyse. Nous avons synthétisé des nanoparticules hybrides de niobate de lithium-métal noble avec un polyéthylèneimine branché en tant que lien chimique entre les deux composants. Des nanogermes d'or et de platine ont été déposés sur LiNbO₃. Ensuite leur capacité à mimer l'activité peroxydase a été étudiée en utilisant une sonde rédox et nous avons optimisé les conditions pour maximiser la réponse colorimétrique. Les nanoparticules hybrides possèdent une meilleure activité peroxydase que leurs composants séparés et un simple mélange d'entre eux. Les Nanozymes ont été mis en présence de bactéries *Escherichia Coli* sous différentes sources de stress oxydatifs, *i.e.* du peroxyde d'hydrogène et un rayonnement ultraviolet. Les Nanozymes hybrides et leurs composants séparés causent différents effets sur la croissance bactérienne selon la source de stress oxydatif. De plus, les Nanozymes hybrides LiNbO₃/Au et LiNbO₃/Pt protègent les bactéries contre la dégradation due aux UV.

Mots-clés: Nanozymes hybrides, niobate de lithium, metal noble, peroxydase, espèces réactives de l'oxygène, effet synergique.

AUTORISATION DE SOUTENANCE

Vu les dispositions de l'arrêté du 25 mai 2016 modifié par l'arrêté du 26 août 2022,

Vu la demande du directeur de thèse

Madame, V. MONNIER-VILLAUME, Messieurs Y. CHEVOLOT et V. BANSAL

et les rapports de

Mme A. AMIENS
Professeure, Laboratoire de Chimie de Coordination, 205 Route de Narbonne,
31400 TOULOUSE

et de

Mme N. MILLOT
Professeure, Laboratoire Interdisciplinaire Carnot de Bourgogne, Département Nanosciences,
9 avenue Alain Savary, BP 47870, 21078 Dijon Cedex

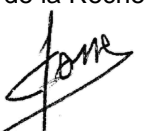
Madame PABLO SAINZ-EZQUERRA Ana Maria

est autorisée à soutenir une thèse pour l'obtention du grade de **DOCTEUR**

Ecole doctorale ELECTRONIQUE, ELECTROTECHNIQUE, AUTOMATIQUE

Fait à Ecully, le 21 mars 2023

Pour le directeur de l'Ecole centrale de Lyon
Le directeur de la Recherche



Christophe CORRE